The accuracy of a Varian 600CD LINAC and the Pinnacle^3 (v6.2b) treatment planning system with regard to IMRT implementation

Tim Crabtree, B.App.Sci.(Hons)

Supervisors:

Mr. Martin Pracy
Dr. Eva Bezak

A thesis submitted for the degree of
Master of Science
in the Department of Physics and Mathematical Physics
University of Adelaide
~ October 2006 ~

Table of Contents

TABLE OF CONTENTS *iii*

LIST OF ABBREVIATIONS AND ACRONYMS *ix*

LIST OF FIGURES *xi*

LIST OF TABLES *xviii*

ABSTRACT *xxi*

THESIS STATEMENT *xxiv*

ACKNOWLEDGEMENTS *xxv*

1 Introduction 1

1.1 General introduction 1

1.1.1 3D conformal radiation therapy 2

1.1.2 Intensity modulated radiation therapy 3

1.2 Aims of current investigation 4

1.3 Thesis outline 4

2 Pinnacle^3 radiotherapy planning software and beam delivery system 7

2.1 Introduction 7

2.2 Photon beam modelling and the Pinnacle^3 planning system 9

2.2.1 Superposition / Convolution dose algorithm 9

2.2.2 Pinnacle^3 and the multi-leaf collimator 14

2.2.2.1 Introduction 14

2.2.2.2 Pinnacle^3 model for fields defined by the MLC 16

2.2.4 Inverse planning 19

2.2.4.1 Introduction 19

2.2.4.2 Pinnacle^3 and inverse planning 20

2.2.5 Beam parameter optimisation methods 21

2.2.5.1 Traditional IMRT optimisation 21

2.2.5.2 Direct machine parameter optimisation 22

2.2.5.3 Pinnacle^3 optimisation process 23

2.2.6 Leaf sequencing algorithms for accurate IMRT dose calculation employing the "step-and-shoot" approach 25

2.2.6.1 Introduction 25

2.2.6.2 Multi-level approximation distribution 26

2.2.6.3 K-means Clustering 26

2.2.7 Head geometry for the Varian 600C/D Linac 29

2.2.8. Limiting factors of the MLC as a primary shield 33

2.2.8.1 Transmission 33

2.2.8.2 Rounded leaf effect 34

2.2.8.2.1 Beam penumbra 34

2.2.8.2.2 Match-line 35

2.2.8.3 Tongue-and-groove effect 36

2.2.8.4 Overshoot effect 36

3 Dosimetric Methods 38

3.1 Introduction 38

3.2 Film Dosimetry 38

3.2.1 Introduction 38

3.2.2 Kodak EDR2 film calibration 41

3.2.2.1 Introduction 41

3.2.2.2 Method 42

3.2.2.3 Results 43

3.2.2.4 Conclusion 45

3.3 Ion Chamber theory 46

3.3.1 Introduction 46

3.3.2 Pin Point ion chamber 48

3.4 Gamma Index 52

3.4.1 Introduction 52

3.4.2 The Van Dyke criteria 52

3.4.3 Definition of Gamma Index 53

3.4.4 Pinnacle^3 scripts for profile data extraction 57

4. Comparison of the Pinnacle^3 planning system with measurement 59

4.1 Introduction 59

4.2 Small field data collection 59

4.2.1 Method 59

4.2.2 Results and discussion 60

4.2.3 Conclusion 64

4.3 Output factor determination for small MLC fields 65

4.3.1 Method 66

4.3.2 Results and discussion 67

4.3.3 Conclusion 74

4.4 Off-axis segments defined by the MLC with varying secondary collimators 74

4.4.1 Method 75

4.4.2 Results and discussion 78

4.4.3 Conclusion 82

5. Characterisation of the Varian millennium multi-leaf collimator 84

5.1 Introduction 84

5.2 Transmission 84

5.2.1 Method 84

5.2.2 Results and discussion 86

5.2.3 Conclusion 87

5.3 Rounded leaves 88

5.3.1 Beam penumbra 88

5.3.1.1 Method 88

5.3.1.2 Results and discussion 89

5.3.1.3 Conclusion 97

5.3.2 Match-line 98

5.3.2.1 Method 98

5.3.2.2 Results and discussion 100

5.3.2.3 Conclusion 105

5.4 Tongue and groove 105

5.4.1 Method 105

5.4.2 Results and discussion 108

5.4.3 Conclusion 110

5.5 Varian 600CD characteristics and the "Overshoot" effect 111

5.5.1 Method 111

5.5.2 Results and discussion 112

5.5.3 Conclusion 119

5.6 Machine limits applied to IMRT planning 119

5.6.1 Method 119

5.6.2 Results and discussion 121

5.6.3 Conclusion 124

6 Conclusion 125

6.1 Summary / Conclusion 125

6.2 Future work 127

References 128

Appendix 137

A. Small field profile measurements for the Pinnacle model (Jaws only) 137

B. Small field profile measurements (MLC only – off CAX) 143

I. Profile comparisons 144

II. Output Factor measurements 148

C. Small field profile measurements (MLC only – on CAX) 156

D. Multi-leaf collimator characterisation measurements 160

I. Match-line effect 161

II. Tongue-and-groove effect 168

E. 600CD characterisation measurements 175

Abbreviations and Acronyms

ACPSEM	Australasian College of Physical Scientists and Engineers in Medicine
CAX	Central axis
CC	Collapsed cone convolution
CRT	Conformal radiation therapy
cpd	Computed scan data
CT	Computed tomography
CTV	Clinical target volume
DTA	Distance-to-agreement
DVH	Dose volume histogram
EDR	Extended dose range
FWHM	Full width half maximum
γ	Gamma index
OD	Optical density
ODM	Open density matrix
MLC	Multileaf collimator
Linac	Linear accelerator
IMRT	Intensity modulated radiation therapy
MLC	Multi-leaf collimator
msd	Measured scan data
MU	Monitor unit
NPSOL	Nonlinear Programming Systems Optimization Laboratory
P^3	Pinnacle 3D radiotherapy treatment planning system
PP	PinPoint ion chamber
PTV	Planning target volume

ROI	Region of interest
SAD	Source-axis-distance
SSD	Source-surface-distance
SQP	Sequential quadratic programming
3D CRT	Three dimensional conformal radiation therapy
TPS	Treatment planning system
Z	Atomic number

List of Figures

Figure 2.1. Vector representation for the convolution / superposition method of dose calculation........10

Figure 2.2. Multi-leaf schematic illustrating leaf terminology........15

Figure 2.3. Multi-leaf collimator position relative to the secondary collimator. 15

Figure 2.4. Schematic showing the ray lines that form the radiation and the light field edges due to the curved construction of the MLC leaf........18

Figure 2.5. Techniques for decomposition of fluences into smaller elements... 24

Figure 2.6. Scheme tree of IMRT planning process........25

Figure 2.7. One-dimensional intensity distribution with the multi-level approximation........26

Figure 2.8. (a) Individual beam intensity levels (b) Intensity levels within a defined error tolerance grouped into *k* clusters........28

Figure 2.9. A schematic representation of the treatment head of the 600CD linear accelerator........30

Figure 2.10. Effect on the dose distribution with and without the flattening filter. 31

Figure 2.11. Inter- and intra-leaf transmission through the Varian Millennium MLC. 34

Figure 2.12. Varian Millennium Rounded leaf junction effect.................... 35

Figure 2.13. Varian Millennium tongue-and-groove effect........................ 36

Figure 2.14. Overshoot effect and the impact on MU delivery.................... 37

Figure 3.1. Electron micrograph showing silver halide grains evenly dispersed in gelatin substrate... 39

Figure 3.2. Ratio of mass energy-absorption coefficient of radiotherapy film as a function of photon energy...40

Figure 3.3. In-plane profile of the MLC step wedge calibration film........... 44

Figure 3.4. Optical density for EDR2 film versus scanner A/D characteristic curve...45

Figure 3.5. Optical density versus dose calibration curve........................ 45

Figure 3.6. Schematic of the basic construction of an ion chamber..............46

Figure 3.7. Ionization chamber type 31006 with build up cap....................49

Figure 3.8. Output factors for a Varian 600CD / 6 MV Clinac measured with the PTW type 31002 PinPoint chamber and PTW 60003 Diamond............ 50

Figure 3.9. Ratio of the response of the PTW type 31006 PinPoint chamber to a 0.125 cm^3 ion chamber...51

Figure 3.10. (a) Level of acceptability determined as a percentage dose difference. (b) Level of acceptability determined as a distance to agreement...........53

Figure 3.11. One-dimensional representation of the dose distribution evaluation criteria using both DTA and dose difference checks..........................54

Figure 3.12. Two-dimensional representation of the dose distribution evaluation criteria using both DTA and dose difference checks..........................56

Figure 3.13. Pinnacle scripts used for the extraction of computed and measured profile data from within the Pinnacle 'Physics Photon Tool'................57

Figure 4.1. (a) Depth dose curves for field sizes 1x1 cm^2, 1.5x1.5 cm^2, 2x2 cm^2, 3x3 cm^2, 4x4 cm^2 defined by fixed jaws and measured with PinPoint ion chamber (b) Expanded depth dose curve from 15cm onwards showing the increase in dose at depth with increasing field size...........................61

Figure 4.2. PinPoint ion chamber measured and Pinnacle computed half profiles (a) cross-plane 5 cm deep (b) in-plane 5 cm deep (c) cross-plane 10 cm deep (d) in-plane 10 cm deep (e) cross-plane 20 cm deep (f) in-plane 20 cm deep. 62

Figure 4.3. % $\gamma < 1$ than one as a function of field size for (a) Cross-plane (b) In-plane...63

Figure 4.4. γ as a function of distance from CAX for a 4x4 cm^2 field at 5 cm, 10 cm and 20cm...64

Figure 4.5. Dose at depth as a function of increasing equivalent field size for 6 MV x-rays...65

Figure 4.6. 6 MV output factors for the Varian 600CD Linac at 100 cm SSD corrected back to a 10x10 cm^2 reference field plotted against uncorrected output factors...68

Figure 4.7. 6 MV output factors for Varian 600CD Linac at 100 cm SSD and 10 cm depth in water……69

Figure 4.8. The ratio of the output factor for MLC segments (a) 1x1 cm^2 (b) 2x2 cm^2 (c) 3x3 cm^2 with a varying secondary collimator setting (OF'), and the output factor for fixed secondary collimator setting of (a) 1x1 cm^2 (d) 2x2 cm^2 (g) 3x3 cm^2 (OF), plotted as a function of the percentage of the secondary collimators blocked by the MLC segment……71

Figure 4.9. % deviations between the Pinnacle computed outputs and the ion chamber measured outputs for small segments with varying fixed secondary jaw positions at depths (a) 5 cm depth (b) 10 cm depth (c) 20 cm depth……72

Figure 4.10. Schematics of small MLC segments delivered off-axis (a) 1x1 cm^2 10x10 cm^2 (b) 1x1 cm^2 15x15 cm^2 (c) 2x2 cm^2 10x10 cm^2 (d) 2x2 cm^2 15x15 cm^2 (e) 3x3 cm^2 10x10 cm^2 (f) 3x3 cm^2 15x15 cm^2……77

Figure 4.11. Film exposure of 9 1x1 cm^2 MLC segments delivered statically….78

Figure 4.12. Ion chamber (msd) and Pinnacle (cpd) profile comparisons with γ for 1x1 cm^2 segments with secondary collimators set to 10x10 cm^2 at 5 cm depth for (a) Cross-plane segment a (b) In-plane segment a (c) Cross-plane segment *i* (d) In-plane segment *i*……80

Figure 4.13. Half profiles through a 1x1 cm^2 segment on the side closer to the secondary collimator. Plots show the reduction in the penumbra for the segments on the field boundary defined by the secondary collimators (a) Segments *a, b, c* (b) Segments *d, e, f* (c) Segments *g, h, i*……81

Figure 4.14. % deviation calculated between the dose/MU determined from PinPoint ion chamber measurements and that determined by Pinnacle for depths 5 cm, 10 cm and 20 cm as a function of segment equivalent field size for secondary collimator settings of (a) 10x10 cm^2 (b) 15x15 cm^2 82

Figure 5.1. (a) Scan set-up for Intra- and Interleaf transmission measurements for the Varian 120 leaf Millennium MLC. (b) Set-up for the transmission measurement using Farmer Chamber 85

Figure 5.2. The normalized transmission profiles for a Varian 120 leaf Millennium MLC measured for a 6 MV photon beam. Half field profiles were measured at 5 cm and 10 cm from central axis for both A and B carriages and normalized and averaged 87

Figure 5.3. Scan set-up for beam penumbra measurements for the Varian 120 leaf Millennium MLC for segments (a) 1x1 cm^2 (b) 2x2 cm^2 (c) 3x3 cm^2 88

Figure 5.4. 1x1 cm^2 half beam profiles measured with film and PinPoint ion chamber compared with Pinnacle generated (a) (c) cross-plane at 5 cm and 10 cm depth respectively (b) (d) In -plane at 5 cm and 10 cm depth respectively. 92

Figure 5.5. PinPoint ion chamber and Pinnacle generated cross-plane half beam profiles of small MLC defined segments with secondary collimators set to 10x10 cm^2 and 15x15 cm^2 and at 10 cm depth (a) 1x1 cm^2 (b) 2x2 cm^2 (c) 3x3 cm^2 96

Figure 5.6. Schematic of the scan method for investigating the match-line effect produced by the Varian 120-leaf Millennium multi-leaf collimator 98

Figure 5.7. The MLC leaf positions of a 1x4 cm^2 strip propagating in the cross-plan direction to determine the rounded leaf effect 99

Figure 5.8. Film results showing the match-line effect for (a) 1x4 cm^2 segments (b) 2x4 cm^2 segments (c) 3x4 cm^2 segments..101

Figure 5.9. Profiles showing the increased dose as a result of the rounded leaf effect measured for 6 MV photons at 5 cm deep in water. Profiles generated by delivering via step-and-shoot (a) 11 sequential 1x4 cm^2 segments (b) 6 sequential 2x4 cm^2 segments (c) 4 sequential 3x4 cm^2 segments...........101

Figure 5.10. Dose error as a function of (a) (b) field size and (c) (d) depth, where dose error is given as the percentage overdose caused by the match-line effect. (a) (c) Junction of 2 pair of adjacent leaves (b) (d) Junction of 1 pair of adjacent leaves...103

Figure 5.11. Varying magnitude and width of the hotspot at CAX at 5 cm deep for X jaw setting of 1 cm, 2 cm and 3 cm...104

Figure 5.12. Schematic of the scan method for investigating the tongue-and-groove effect produced by the Varian 120-leaf Millennium multi-leaf collimator. 106

Figure 5.13. The MLC leaf positions to determine the tongue-and-groove leaf effect. 107

Figure 5.14. Film results showing the tongue-and-groove effect for (a) 5x1 cm^2 segments (b) 5x2 cm^2 segments (c) 5x3 cm^2 segments.......................108

Figure 5.15. Profile showing the decreased dose as a result of the tongue-and-groove effect measured for 6 MV photons at 5 cm deep in water. Profile generated by delivering 12 sequential 5x1cm^2 segments dynamically (step-and-shoot)..109

Figure 5.16. Film results showing the overshoot effect resulting from delivering segments via step-and-shoot. (a) Segments propagating in-plane (b) Segments propagating cross-plane..112

Figure 5.17. Step-and-shoot profile overlaid with static profile to demonstrate the overshoot effect seen for the Varian 600CD Linac, for scan direction (a) In-plane (b) Cross-plane..114

Figure 5.18. The ratio of the calculated percent dose of the last segment delivered and the measured percent dose of the last segment subtracted from unity as a function of machine dose rate..115

Figure 5.19. (a) Change in MU delivered for all MU/segment settings as a function of machine dose rate. (b) Average change in the MU delivered for machine dose rates as a result of the overshoot effect..................................116

Figure 5.20. (a) Normalised dose profiles in the cross-plane direction through the overdose and under dose regions, shown by the white dotted lines in Figure 5.16b. (b) Normalised dose profiles in the cross-plane direction through the overdose and underdose regions for dose rate 400 MU/min with different delivered MU/segment..117

Figure 5.21. Example IMRT fields delivered (a) and (c) without limits (b) and (d) with limits..123

Figure 5.22. Profiles through IMRT example shown in Figures 5.21 (a) and (b). 124

Figure 5.23. Profiles through IMRT example shown in Figures 5.21 (c) and (d). 124

List of Tables

Table 2.1 Physical properties of the Varian 120-leaf Millennium MLC system. 32

Table 3.1. Measured ion chamber doses corresponding to each individual MLC segment of the step wedge.......... 44

Table 3.2. Van Dyk criteria for levels of Photon beam acceptability......52

Table 4.1. % $\gamma < 1$ calculated for comparison between measured and Pinnacle modelled profiles and depth dose for small fields (Distance and Dose tolerance of 2% and 2 mm respectively).......... 62

Table 4.2. Comparison of PinPoint ion chamber and Pinnacle output factors for small segments defined by the MLC and an increasing secondary collimator setting. Fixed MLC segment (a) 1x1 cm^2 (b) 2x2 cm^2 (c) 3x3 cm^2..........72

Table 4.3. Percent $\gamma < 1$ for the comparison of Pinnacle and measured profiles for small MLC defined segments off-axis..........78

Table 5.1. Transmission and leakage values for the Varian 120 leaf Millennium MLC measured for a 6 MV photon beam..........87

Table 5.2. Penumbra widths for 1x1 cm^2 MLC defined square field on central axis at 100 cm SSD measured in water for (a) cross-plane (b) in-plane..........91

Table 5.3. FWHM difference from expected penumbra width for 1x1 cm^2, 2x2 cm^2 and 3x3 cm^2 MLC defined square fields on central axis at 100 cm SSD measured in water and with the secondary collimators set to 10x10 cm^2 for (a) cross-plane PinPoint chamber (b) cross-plane Pinnacle generated (c) in-plane PinPoint chamber (d) in-plane Pinnacle generated............................93

Table 5.4. Penumbra widths for 1x1 cm^2, 2x2 cm^2 and 3x3 cm^2 MLC defined square fields on central axis at 100 cm SSD measured in water and with the secondary collimators set to 10x10 cm^2 for (a) cross-plane PinPoint chamber (b) cross plane Pinnacle generated (c) in-plane PinPoint chamber (d) in-plane Pinnacle generated..94

Table 5.5. 80%-20% penumbra width difference from Pinnacle generated penumbra width for 1x1 cm^2, 2x2 cm^2 and 3x3 cm^2 MLC defined square fields on central axis at 100 cm SSD measured in water and with the secondary collimators set to 10x10 cm^2 for (a) cross-plane (b) in-plane................95

Table 5.6. The difference between the penumbra width determined with secondary collimators set to 15x15 cm^2 and those with secondary collimators set to 10x10 cm^2 for 1x1 cm^2, 2x2 cm^2 and 3x3 cm^2 MLC defined square fields on central axis at 100 cm SSD measured in water for (a) cross-plane PinPoint chamber (b) cross-plane Pinnacle generated (c) in-plane PinPoint chamber (d) in-plane Pinnacle generated.....................................97

Table 5.7. Summary of the percent dose increase as a result of the rounded leaf effect at the leaf junction for opposing leaves for the Varian 120 leaf Millennium MLC system and 6 MV..102

Table 5.8. Summary of FWHM data for overdose peaks resulting from the rounded leaf effect for the Varian 120 leaf Millennium MLC system.......104

Table 5.9. Summary of the percent dose decrease as a result of the tongue-and-groove effect for the Varian 120 leaf Millennium MLC system and 6 MV......... 109

Table 5.10. Summary of percent difference seen for the sum of the first and last segments and that of the expected dose for both segments.................. 114

Table 5.11. $\gamma < 1$ for the comparison of profile overlays of static and step-and-shoot profiles for the determination of optimum machine settings for IMRT delivery. 118

Table 5.12. Pinnacle settings for optimal IMRT delivery......................... 120

Table 5.13. Summary of the impact on IMRT planning when machine limits are applied...121

Abstract

With IMRT now the future for the accurate delivery of radiation therapy, an investigation into the beam delivery system and the radiotherapy planning system has been undertaken to determine the accuracy and limitations of both systems. Pinnacle^3 (v6.2b) allows the delivery of sub-millimetre field segments and fractions of monitor units in delivering the ideal fluence, posing the question of delivery accuracy. As electronic equilibrium breaks down for the small field segments employed in IMRT delivery it is crucial to have an understanding of Pinnacle^3 generated segments and their comparison with reality. Small field sizes 1x1 cm^2, 2x2 cm^2 and 3x3 cm^2 at water depths 5 cm, 10cm and 20 cm were investigated. Field sizes smaller than 1x1 cm^2 posed measurement accuracy issues, and were also thought not realistic in accurate IMRT delivery, thus, were not investigated. The PTW PinPoint ion chamber and Kodak extended dose range (EDR2) film were employed in the study, with a Varian 600CD Linear accelerator equipped with the Millennium 120 leaf multi-leaf collimator system with dynamic capabilities used to generate a 6 MV x-ray beam. All Pinnacle^3 calculations were performed using the convolution algorithm with a dose grid size of 0.3 cm.

Results outlined in the following investigation have shown limitations in the beam delivery system as a result of the individual leaf construction and the Linac mechanics. The match-line effect resulting from the rounded leaf design was shown to be marginally lower for step-and-shoot delivery rather than static delivery with overall hotspots shown to increase sharply with increasing field size and only slightly decrease with increasing depth in water. Hot spots showed no pattern with distance off-axis, with a maximum hot spot

of 23.3% measured for a 3x4 cm^2 field size at 5 cm depth. Cold spots as a result of the tongue-and-groove effect were shown to increase with increasing field size and decrease with increasing depth. Cold spots showed no real pattern with distance off-axis, with a maximum cold spot of -13.6% measured for a 3x4 cm^2 field size at 5 cm depth.

With IMRT the small segments used to deliver the optimum fluence block the secondary collimators, which for IMRT are usually much larger than the individual segments. Output factor measurements showed that for a 2 cm equivalent field size, blocking the secondary collimators by 50% resulted in an approximate -2% error between the output from Pinnacle and that measured for depths 5 cm, 10 cm and 20 cm. With increasing blocked secondary collimators up to 99%, the error increased to approximately -4.0% for the three depths. This was also shown to be very similar for a 3 cm equivalent segment size. However, for a 1 cm equivalent segment size the error for 75% blocked secondary collimators was approximately -10% for all three depths and increased above -11% for 5 cm and 10cm depth , and >-14% for 20 cm depth.

Small segments off-axis comparisons showed output for a 1x1 cm^2 segment increases with increasing depth and has a maximum error of 8% and 12.3% at 20 cm depth for 10x10 cm^2 and 15x15 cm^2 secondary collimator setting respectively. For segment field sizes 2x2 cm^2 and 3x3 cm^2 the errors show an almost linear error over increasing depth, with average errors of 3.6% and 2.3% for the two segment sizes blocking a 10x10 cm^2 secondary collimator setting. For a 15x15 cm^2 secondary collimator setting errors of 4% and 2.3% for 2x2 cm^2 and 3x3 cm^2 segment sizes was obtained. Results confirm the use of segments 1x1 cm^2 and smaller are not recommended as the dosimetry accuracy is unreliable. Profile comparisons for small segments off-axis did not show any major differences other than the expected penumbra widening in the cross-plan direction as a result of the rounded leaf ends. With distance off-axis it was shown that the profile comparisons compared well, with FWHM difference between measured and expected were less than 1mm for in-plane scans for all three segment sizes, depths and secondary collimator settings, with the exception of the 3x3 cm^2 at 20 cm depth showed a difference of approximately 1.5 mm. For cross-plane scans, differences were shown to increase with depth due to beam divergence and the rounded leaf effect with average differences for all segments shown to be 0.5 mm for segments 5 cm deep, 1.1 mm for segments 10 cm deep and 2.2 mm for segments 20 cm deep.

Overshoot measurements were performed to determine machine characteristics with regard to the delivery of small number of MU's with varying dose rates. Results have shown the optimum combination to be 4 MU/segment at a dose rate of 400 MU/minute.

In conclusion, results from this investigation have shown limitations applied to the IMRT fluence conversion and machine delivery process must include a minimum 2 cm equivalent segment size with the smallest possible secondary collimator setting encompassing all segments, 400 MU/min dose rate and 4MU/segment to provide optimum IMRT delivery employing the Pinnacle^3 planning system and the Varian 600CD Linac. Applying these limitations was also shown to minimize the effects due to the leaf construction.

Thesis Statement

Declaration

For a Thesis that does not contain work already in the public domain

NAME: Tim Crabtree PROGRAM: MSc (Medical Physics)

This work contains no material which has been accepted for the award of any other degree or diploma in any university or other tertiary institution and, to the best of my knowledge and belief, contains no material previously published or written by another person, except where due reference has been made in the text.

I give consent to this copy of my thesis, when deposited in the University Library, being made available for loan and photocopying, subject to the provisions of the Copyright Act 1968.

SIGNATURE: .. DATE: 25/9/2007

Acknowledgements

Thank you to my supervisors Mr Martin Pracy and Dr Eva Bezak for their long distance support and providing valuable feed back on this manuscript.

Thanks also to my wife Lisa who kept me on track over the years, and to my son Max who came along at the end of the project and inspired me to finish.

Chapter 1

1.1 General Introduction

The aims in the treatment of malignant disease are the complete eradication of a primary tumour, control of regional lymph nodes, and the eradication of disease that has migrated to distant sites from the primary volume. The latter complication is generally treated via chemotherapy methods, whereas primary tumour control can be treated by a combination of surgical techniques and radiation therapy. The aim of radiation therapy is to deliver a lethal dose to a tumour volume whilst sparing the surrounding healthy tissue. This can be greatly enhanced over conformal radiation therapy by employing intensity modulated radiation therapy (IMRT), a treatment technique that enables beam conformation around a tumour volume by delivering a prescribed dose through many beam segments. Small field segments play a crucial role in IMRT in that they provide a way of modulating the intensity of the treatment beams and forming a relatively uniform dose distribution around regular or irregular target volumes. This modulation of beam intensity can enable significant dose escalation to the tumour volume whilst avoiding the deposition of high dose to surrounding critical structures. It is thought 6 MV x-rays will be employed for IMRT treatments at the W. P. Holman Clinic at the Launceston General Hospital, Tasmania. Studies have shown that lower energy photons provide a tighter dose distribution surrounding the target volume at the expense of a higher dose deposition to the areas superficial to the beams entry (Webb, 2005). Conversely, other authors have shown no difference in calculations performed at 6 MV and 18 MV indicating 18 MV is not required for IMRT (Dong, 2003, O'Brien, 2002, Wierzbicki, 2003). Initially only head and neck cases, suited to IMRT due to complex tumour volumes, will be treated via IMRT. This was decided purely due to greater immobilization of the patient, as well as the limited movement of the tumour volume over the treatment period.

The two combined systems for IMRT delivery at the W. P. Holman Clinic and used in this investigation is the Philips Pinnacle treatment planning system (Philips Radiation Oncology Systems, Milpitas, CA) and the Varian 600CD linear accelerator (Varian

Medical Systems, Palo Alto, CA) equipped with the 120-leaf Millennium multileaf collimator (MLC).

1.1.1 3D conformal radiation therapy

Conformal radiation therapy (CRT) using an MLC is a technique pioneered in the 1960s by Shinji Takahashi (Takahashi, 1965). A rotating MLC with large leaves was employed to shield critical structures while conforming the planning target volume (PTV) to the clinical target volume (CTV) in position, shape and size (Bomford, 2004). As the prescribed dose to a tumour is limited by the dose tolerance of surrounding tissues, conformal therapy enables higher doses to be delivered by reducing the treatment volume through shaping to the PTV (Williams, 1993).

Three dimensional conformal radiation therapy (3D CRT) utilizes computed tomography (CT) images, and powerful computing software, in conjunction with complex dose algorithms, generate dose distributions that overlay the CT images, providing a visual guide of what is occurring inside a patient with regard to a specific treatment. 3D CRT involves outlining and correctly orientating the patient, the target and any organs of interest as 3D structures. Multiple beams are then positioned such that each individual beam conforms to the PTV, and attacks from multiple angles, assuring an homogenous dose is distributed within the tumour.

The MLC is a crucial tool in 3D CRT, first appearing commercially in 1984 (Webb, 2005) and since has taken over the role of the hazardous, heavy and time-consuming alloy blocks previously used for shielding. In 3D CRT the MLC is primarily employed to shield critical structures from the primary beam of radiation. This shielding is achieved within Pinnacle by outlining the area to be treated and instructing the software to position the leaves to form the digitised shape. The fixed secondary collimators are then positioned as close as possible to the treatment field edge defined by the multi-leaves. The manual placement of the secondary collimators is required due to Pinnacle determining dose from the secondary collimators and not the field shape defined by the MLC.

1.1.2 Intensity modulated radiation therapy

As a result of a homogenous dose across the beam, complex tumour structures irradiated using conformal therapy generally lack the ability to spare surrounding critical structures from unacceptably high doses.

IMRT is a treatment modality designed to deliver an inhomogenous dose distribution around a target volume whilst sparing surrounding critical structures. This is achieved through beam modulation; not a completely new concept, as beam modulation has been performed using compensators that correct for patient shape and heterogeneities (Williams, 2004). However, IMRT is different in that it can modulate the dose such that high doses can be conformed to a complex shaped PTV, while sparing closely placed critical structures.

In the implementation of IMRT a comprehensive investigation into the dosimetry of small beams is required if an accurate IMRT program is to be achieved. Individual IMRT fields consist of multiple small beam segments that are combined to deliver a desired dose distribution. These segments are confined within a minimum fixed jaw setting that is initially set, such that the jaws completely cover the contoured target volume. During the calculation process to generate an IMRT plan, the jaw settings are optimised during the conversion to field segments so they accurately match the generated intensity-modulated fields.

The overall benefits of IMRT as a treatment modality outweigh the disadvantages resulting from the complexity of implementing the technique. Early evidence has shown that by generating superior dose distributions, complications resulting from radiation exposure can be reduced, for example, reduced xerostomia, reduced rectal toxicity, reduced dry-eye syndrome, and reduced paediatric complications (Webb, 2005). From these results, any benefit to patient outcome should be considered worthwhile.

1.2 Aims of current investigation

In most IMRT cases, the optimised jaw setting for each treatment field will be significantly larger than individual segments defined by the MLC, and as many small segments are combined in a treatment field, the Pinnacle planning system will overestimate the dose calculation. This dose overestimation will apply to all segments within the treatment field, and therefore, it is thought a compound effect will be seen.

The MLC is constructed of interlocking leaves that are driven into position by a screw mechanism. The leaf banks are positioned horizontally inside the head of the Linac and as a result have a round construction on the end that is positioned in the radiation beam to follow beam divergence as the field opens and closes. The dosimetric impact resulting from the construction of the MLC requires investigation to determine any limitations that may impact on the accuracy of IMRT treatment.

The aims of this research are:

- the characterisation of the Pinnacle planning system with regard to the dosimetric accuracy of small fields defined by the Varian Millennium MLC.

- a comprehensive characterisation of the Varian Millennium MLC for small fields delivered via the step-and-shoot technique.

- determination of limits applicable to accurate IMRT delivery employing the Pinnacle planning system and a Varian 600CD Linac equipped with the Millennium MLC.

1.3 Thesis Outline

Chapter 2 covers the theory and provides a general background of the Pinnacle planning system and the algorithm employed for dose calculation as well as the affiliation between Pinnacle and the Millennium MLC. As this investigation concerns IMRT planning, a brief discussion on inverse planning as well as beam parameter optimisation techniques and the leaf-sequencing algorithm employed are also discussed. An in depth discussion on the MLC and the factors that limit its use as a primary shielding technique is also covered.

Chapter 3 covers the dosimetric techniques employed for this investigation, that being, radiographic film dosimetry and ionometric measurements. Radiographic film dosimetry is a method of measuring relative or absolute dose distributions through capturing a snapshot of ionising radiation through a chemical reaction when the radiation encounters the film. Ionometric measurement involves the measurement of ionising radiation through the use of an ion chamber. As the radiation passes through the ion chamber, ionisation of the air within the chamber cavity occurs, resulting in a generated current which is measured and used to characterise the radiation beam. Chapter 3 also describes the Gamma Index, a useful parameter used for dose profile comparisons through incorporating a dose tolerance and distance to agreement tolerance in a simple formula that generates a pass or fail index.

Chapter 4 is the first chapter of experimental results. The chapter focuses on the small field data collection for the Pinnacle model associated with IMRT commissioning. Data for field sizes 1x1 cm^2, 2x2 cm^2 and 3x3 cm^2 will be collected and imported into Pinnacle, and the best model of this data has been created. Output factors have been measured using a small volume ion chamber and entered into Pinnacle as required for dose calculation. Output factors for fields defined by the MLC, and the changes seen between those measured for fields defined by the secondary collimators are presented. The variation between Pinnacles generated and measured outputs for small MLC defined segments off central axis and with varying secondary collimator settings are finally discussed.

Chapter 5 focuses primarily on the characterisation of the Varian Millennium MLC system. The limitations of the MLC as a result of the leaf construction are addressed with respect to accurate IMRT delivery. Measured inter- and intra-leaf radiation transmission through the MLC is discussed, followed by discussions on the impact on IMRT treatment planning as a result of the rounded leaf and tongue-and-groove effects. The Pinnacle beam model is defined using data for fields defined by the secondary collimators, therefore, comparisons between the penumbra defined by the secondary collimators and that by the MLC is investigated. The overshoot effect resulting from communication delays between the MLC and beam controllers is investigated, with outcomes providing information of possible machine limits that can be applied to reduce not only the overshoot effect, but other inherent MLC effects.

Chapter 2

Pinnacle^3 radiotherapy planning software and beam delivery system

2.1 Introduction

The planning process of a course of radiotherapy involves choosing beams of a selected energy, collimated to a desired field size, and arranged around the patient to provide a lethal dose to the tumour volume whilst sparing the surrounding healthy tissue. Historically, radiotherapy treatment planning consisted of manually combining data on superimposed isodose charts (Tsien, 1955). Such manual methods provided limited accuracy, due to the limited degree of complexity, and also the lack of dose distribution optimisation (Metcalfe, 1997). Progressive enhancement followed by aid of the computer, with methods employing punch cards used to determine dose distributions (Tsien, 1955). As computer technology advanced, so did radiotherapy treatment planning. Rudimentary corrections for heterogeneities where first introduced in the early seventies that took account of the primary radiation whilst neglecting the scattered component. Milan *et al.* first introduced the effective depth method that corrected for heterogeneities by applying a correction factor to the geometrical depth to a point within the patient (Milan, 1974). This neglect of scattered radiation was found to underestimate or overestimate the correction factor (Tatcher, 1981), depending on the density of the heterogenious material. An underestimate in the correction factor would result from higher than unity density material, due to the increased scatter produced, and likewise an overestimate produced from the reduced scatter of the lower than unity density materials.

The introduction of the CT scanner in the late seventies (Goiten, 1979) provided a breakthrough in treatment planning due to the accurate delineation of the extent of disease relative to normal tissue (Goiten, 1979). Previous conventional techniques were inadequate in providing tumour coverage, and Goiten *et al.* demonstrated that from a study of 77 patients, 52% required plan alterations as a result of a CT scan (Goiten, 1979). The CT was not only seen as beneficial for tumour delineation, but also provided a way of obtaining the varying tissue electron densities within the patient, providing for the first time a practical method of correcting for varying densities in the dose calculation (Fraass, 1995). Compton scattering is the primary photon interaction for mega-voltage x-rays (Johns, 1983), and the absorbed dose to tissue is dependent on the irradiated tissue volumes distribution of electron densities (Sontag, 1977). It was therefore necessary to match tissue electron densities to the generated attenuation coefficients that resulted from the mathematical image reconstruction technique pioneered by Cormack (Cormack, 1973), which relates incident and transmitted radiation to attenuation coefficients of tissue elements that are traversed by the x-ray projection through the medium (Cormack, 1973). Hounsfield (Hounsfield, 1973) then defined the CT number scale that provided a manageable system for describing attenuation coefficients, and thus electron densities. Not only did CT now provide excellent target volume delineation from surrounding structures, but also provided greater accuracy in dose calculations in treatment planning by providing quantitative data that could be utilized in heterogeneity corrections.

McShan *et al.* (McShan, 1979) in the late seventies introduced the first interactive treatment planning computer with 3D colour graphics that enabled input of multiple transverse contours that could be viewed 3-dimensionally with varying colours differentiating anatomical structures. Machine parameters could be adjusted and changes in the isodose distributions could be viewed on screen. It wasn't until 1986 that the first 3-D treatment planning system was routinely used clinically (Fraass, 1995), and over the next ten years numerous other planning systems appeared, with CT image data sets eventually incorporated to individualized each patient's anatomical composition.

Other advances in radiotherapy delivery were introduced that change the way radiotherapy was planned and delivered. Such design features as dynamic wedge implementation and the introduction of dynamic therapy employing a computer controlled multi-leaf collimator (MLC) provided alternative ways of delivering specific dose distributions, and provided new tools in the planning process.

Dynamic wedge techniques were first realized in 1978 (Kijewski, 1978) and provided an alternative to the manual placement of lead blocks and physical wedges, however, as the computer was not at that time commercially integrated with the linear accelerator the benefit of the technique was not available clinically (Varian, 1991). In the late 1980's when the computer had become fully integrated with the linear accelerator, Leavitt *et al.* (Leavitt, 1989) confirmed the work performed early by Kiljewski *et al.* and the technique was implemented for clinical treatments.

The introduction of the MLC has been a revolution in radiotherapy treatment. The MLC provided an alternative to fabricated beam blocks used historically, and paved the way for improving the efficiency of treatment delivery. The advantages of the MLC over custom blocks include (i) removes the time-consuming processes of block fabrication and mounting during treatment (ii) removes the handling and exposure to toxic fumes and materials, and (iii) removes the risk of heavy blocks falling on the patient inadvertently. The dosimetry investigation of the MLC has been widely undertaken and is well understood with respect to patient planning. The present investigation involves the combination of the Pinnacle planning system and a Varian 600CD linear accelerator, equipped with the 120-leaf millennium MLC system.

2.2 Photon beam modelling and the Pinnacle planning system

2.2.1 Superposition / Convolution dose algorithm

At the heart of the Pinnacle 3D radiotherapy planning system is the collapsed cone superposition convolution algorithm, which provides, in most situations, dose distribution accuracy to within 3% (Sharp, 1993). The convolution superposition method is a model-based algorithm; in that, it takes into account beam energy, beam modifiers, patient contours, tissue heterogeneities, and electron density distribution (Mackie, 2001). This is achieved by generating an incident fluence model, determined from the characterisation of a photon beam from inputted treatment machine data. If we consider the vector representation shown in Figure 2.1, the absorbed dose $D(\boldsymbol{r})$, to a volume element at a point with vector magnitude $\boldsymbol{r}$, from a monoenergetic photon beam of energy *hv*, originating at interaction site with a vector magnitude ***r′***, is expressed as the convolution integral:

$$D(\mathbf{r}) = \int_V \Phi(\mathbf{r}')G_T(\mathbf{r}-\mathbf{r}')dV \qquad (2.1)$$

This is true assuming that all the incident photons are parallel with beam central axis (Sharpe, 1993) and the medium of propagation is homogenous (Boyer, 1985). Broken down the equation consists of the primary photon fluence distribution Φ, incident at the volume element *dV*, located at a point with vector magnitude ***r′***, convolved with the integral kernal $G_T(\boldsymbol{r}-\boldsymbol{r}')$, which describes the deposited energy at the point with vector magnitude ***r***, by charged particles originating from interaction site with vector magnitude ***r′*** (Metcalfe, 1989).

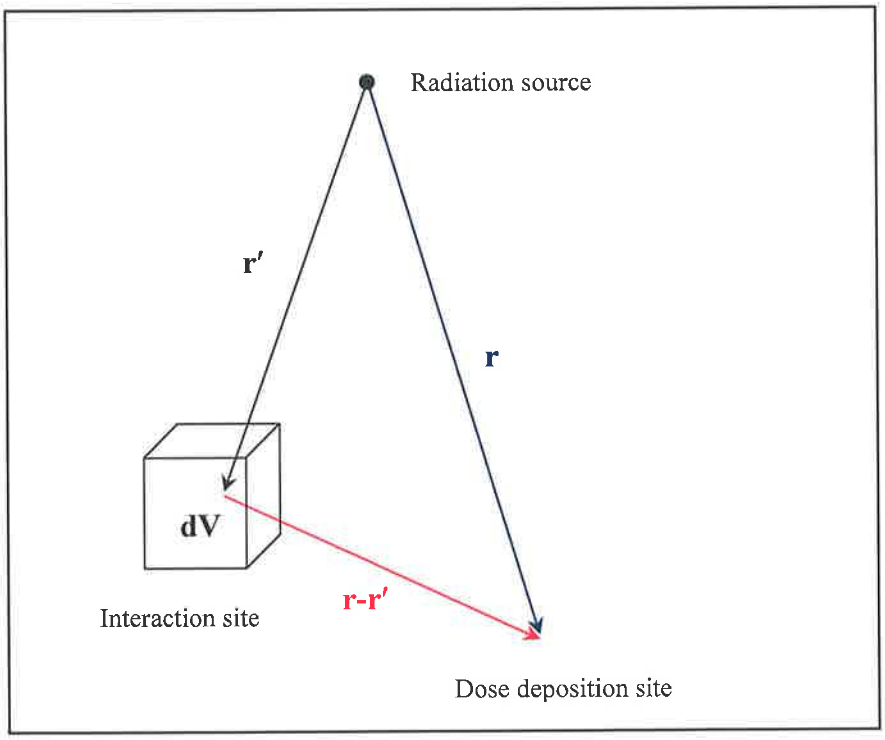

Figure 2.1: Vector representation for the convolution / superposition method of dose calculation.

The integral kernel or energy spread function $G_T(\boldsymbol{r}-\boldsymbol{r}')$ (Metcalfe, 1989), can be further broken down into the sum of constituent components that account for scatter from primary interactions $G_e(\mathbf{r}-\mathbf{r}')$, first scatter interactions $G_s(\mathbf{r}-\mathbf{r}')$, and that from multiple scatter interactions $G_{sm}(\mathbf{r}-\mathbf{r}')$ (Metcalfe, 1989). The energy spread function $G_T(\mathbf{r}-\mathbf{r}')$, are pre-computed from the energy spectrum of the beam, using a database of monoenergetic kernels (Ahnesjö, 1989) and employing Monte Carlo simulations, the only practical method considering the large number of charged particle interactions involved. The function $(\mathbf{r}-\mathbf{r}')$ represents the displacement vector between the primary interaction site and the dose deposition site. By multiplying the energy spread function by the mass attenuation coefficient $(\mu/\rho)_o$ and the photon beam energy E_o, the fluence units of photons per cm^2 are converted to energy per unit mass.

$$G_T(\mathbf{r}-\mathbf{r}') = \left(\frac{\mu}{\rho}\right)_o E_o H_T(\mathbf{r}-\mathbf{r}') \tag{2.2}$$

H_T is the dose spread function, which represents the fractional energy deposited at the volume element at vector magnitude $\mathbf{r}$, from the energy liberated from the primary interaction at volume element dV (Murray, 1989). If the primary photon fluence distribution is multiplied by the product of the mass attenuation coefficient $(\mu/\rho)_o$ and photon beam energy E_o, the total energy liberated per unit mass or TERMA $T(\mathbf{r}')$ is obtained.

$$T(\mathbf{r}') = \left(\frac{\mu}{\rho}\right)_o E_o \Phi(\mathbf{r}') \tag{2.3}$$

The TERMA originates from the primary photon energy fluence, and is defined as the energy that is liberated by a photon during an interaction with a unit mass, and also the kinetic energy of resultant secondary electrons (Hoban, 1990). Combining equations 2.1, 2.2, and 2.3 the following expression is obtained for the dose at the volume element at vector magnitude $\mathbf{r}$:

$$D(\mathbf{r}) = \int_V T(\mathbf{r}') H_T(\mathbf{r}-\mathbf{r}') dV \tag{2.4}$$

Equation 2.4 is an integration over the volume element dV. The dose spread function H_T is a dimensionless quantity (Murray, 1989), and the TERMA has the units of energy per unit mass, and thus must be multiplied by the density of the volume element at vector magnitude $\boldsymbol{r}'$ to convert TERMA to energy per unit volume (Metcalfe, 1997). It is also required to divide the resultant integration by the density of the volume element located at vector magnitude $\boldsymbol{r}$, to convert the result to dose units. Therefore, equation 2.4 converts to:

$$D(\mathbf{r}) = \frac{1}{\rho(\mathbf{r})} \int_V T(\mathbf{r}')\rho(\mathbf{r}')H_T(\mathbf{r}-\mathbf{r}')dV \tag{2.5}$$

For homogenous media it is shown that equation 2.5 is valid, as both densities will cancel. Homogenous media is of little use when it comes to radiotherapy treatment planning as structures of varying densities are scattered throughout the body, which the photon beam interacts with, causing vast differences to the beam attenuation and lateral scattering effects. Equation 2.5 requires adjustment to account for the presence of structures of varying density. This is achieved by a ray tracing technique between the TERMA primary interaction site and the dose deposition site (Philips, 2001). Three- dimensional rays are projected from the dose deposition site, which is tilted on its axis to align with the divergent primary beam to account for the changing direction of the incident particle (Sharpe, 1993). The dose spread function in equation 2.5 is then modified to account for this tilting, and equation 2.5 is written as:

$$D(\mathbf{r}) = \frac{1}{\rho(\mathbf{r})} \int_V T(\mathbf{r}')\rho(\mathbf{r}')H_T(\mathbf{r}',\mathbf{r}-\mathbf{r}')dV \tag{2.6}$$

Metcalfe *et al.* state that the total energy deposited in individual volume elements along a ray traced from volume element at vector magnitude $\boldsymbol{r}'$ to volume element at vector magnitude $\boldsymbol{r}$ is proportional to the density within each volume element (Metcalfe, 1997). The dose spread function is then obtained from the expression:

$$H(\mathbf{r}',\mathbf{r}-\mathbf{r}') = H(\rho_{ave},\mathbf{r}-\mathbf{r}')\frac{\rho_e^w(\mathbf{r})}{\rho_{ave}} \tag{2.7}$$

where $H(\rho_{ave},\boldsymbol{r}\text{-}\boldsymbol{r}')$ is the dose spread per unit energy interval (Metcalfe, 1989), and $\rho_{ew}(\boldsymbol{r})$ is the electron density relative to water for the unit volume element with average density ρ_{ave}. The use of electron density in equation 2.7 is due to the fact the energy lost is predominantly through electron-electron interactions, and thus, is incorrect to assume the mass density can be used to quantify electron energy loss (Metcalfe, 1997). As the average density ρ_{ave} is determined between two points with a displacement of $\boldsymbol{r}\text{-}\boldsymbol{r}'$, it can be calculated from the line integral:

$$\rho_{ave} = \frac{1}{|\mathbf{r}-\mathbf{r}'|}\int_{r'}^{r} \rho(\mathbf{r}'')dr'' \tag{2.8}$$

where $\rho(\boldsymbol{r}'')$ is the density of the volume element located at vector magnitude $\boldsymbol{r}''$ along the projected line. By substituting equation 2.7 into equation 2.6 the equation for dose within a medium containing heterogeneities is given by the following expression:

$$D(\mathbf{r}) = \frac{1}{\rho(\mathbf{r})}\int_V T(\mathbf{r}')\rho_e^w(\mathbf{r}')H_T(\rho_{ave},\mathbf{r}-\mathbf{r}')\frac{\rho_e^w(\mathbf{r})}{\rho_{ave}}dV \tag{2.9}$$

It is shown that the TERMA is now multiplied by the electron density relative to water for the volume element at vector magnitude $\boldsymbol{r}'$. This is because the TERMA is the energy imparted per unit mass. So to determine the TERMA for a material of unit volume, other than water, *s* the TERMA multiplied by the number of electrons per volume relative to water (Metcalfe, 1997).

2.2.2 Pinnacle^3 and the multi-leaf collimator

2.2.2.1 Introduction

The multi-leaf collimator has been designed primarily to replace the conventional method of beam shielding using low melting point alloy blocks. This is not due to a way of improving the dosimetry of blocked fields, but a more efficient method of delivering radiotherapy, as the casting of alloy blocks is a time consuming and hazardous process. The MLC attached to the Varian 600C/D Linac is the Millennium type equipped with 120 leaves consisting of an A and B carriage of 60 leaves each. The construction is such that each carriage has a maximum retract and extend position of 20.1 cm and –20.1 cm respectively, allowing a maximum shaped field size of 40x40 cm^2 obtainable. Individual leaves have a varying width with leaf pairs 1 and 60 at 1.4 cm, leaf pairs 2-10 and 51-59 at 1.0 cm, and all other leaf pairs at 0.5 cm. At machine isocentre the varying thickness of leaf widths provides higher accuracy in conforming to the block defined by the planning therapist, one would expect then, were there are more leaves, leaf effects will be more prominent.

The leaves are constructed of a high-density tungsten alloy with a baked on Molybdenum disulfide coating, which provides an acceptable amount of attenuation of the primary photon beam. Tungsten alloy is the ideal material, not only because of the high density (17.0 g/cm^3 – 18.5 g/cm^3), but the low coefficients of expansion (Boyer, 2001), which allows machining to exact tolerances that are unobtainable with other high-density materials. Figure 2.2 illustrates a single generic leaf with terminology used to describe all leaves. The length is the distance from the centre of the leaf tip to the end of the leaf; the leaf end refers to the end of the leaf that is moving into the field; the leaf sides are the surfaces that make contact with the neighbouring leaves; the leaf height refers to the dimension of the leaf parallel to the incident x-ray beam, and the leaf width refers to the dimension of the leaf perpendicular to the incident x-ray beam.

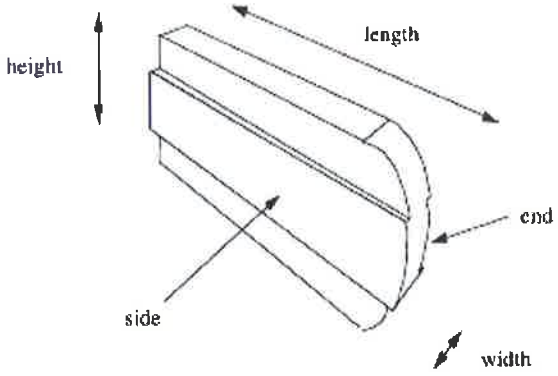

Figure 2.2: Multi-leaf schematic illustrating leaf terminology (Taken from AAPM, 2001).

The use of the MLC with the Varian 600C/D accelerator is as a tertiary collimator, where Figure 2.3 shows the positioning of the MLC relative to the upper and lower secondary collimator.

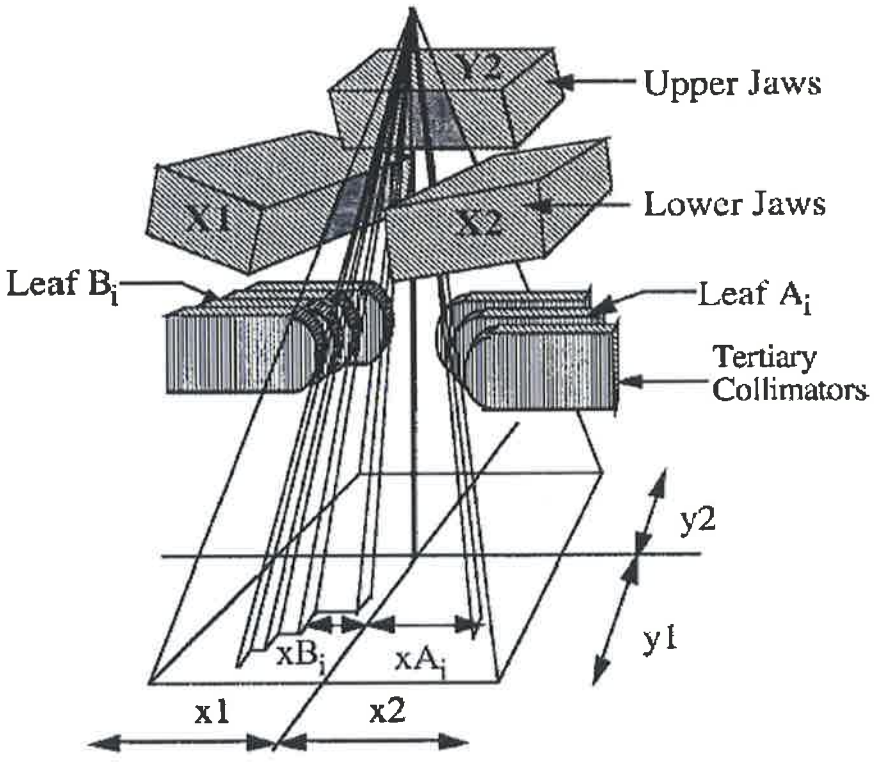

Figure 2.3: Multi-leaf collimator position relative to the secondary collimator (Taken from AAPM, 2001).

The installation of the MLC on the 600C/D does not have an effect on the dosimetry for the secondary collimators, and therefore, scattered radiation for changing collimator setting does not change following MLC attachment. Investigation has shown that the presence of the MLC is equivalent to alloy blocking (Boyer, 1992), this then enables the parameters corresponding to the equivalent field size defined by the MLC to be used in the monitor unit calculations, and as the secondary collimator setting is set just beyond the blocked field the collimator scatter factor will only be affected slightly (Boyer, 2001). Boyer *et al.* (Boyer, 1992) showed that agreement in dose calculation for small fields blocked to 50% by the MLC agreed within 1.7% and 2.5% for 6 MV and 18 MV x-rays respectively. Beyond 50% blocking it has been found that the errors become unacceptable due to the high overestimated output factor. Pinnacle therefore, overestimates the dose for small fields defined by the MLC with secondary collimators set greater than the treatment field.

2.2.2.2 Pinnacle^3 model for fields defined by the MLC

The rounded leaf construction of the individual leaves of the MLC is designed to follow beam divergence as the field size is adjusted, and is termed as a "focused" collimator type (Boyer, 2001). From the schematic displayed in Figure 2.4, Boyer *et al.* (Boyer, 1997) showed that the projected leaf tip travel, W_i at machine isocenter for an individual leaf is given by,

$$W_i = w_i \cdot \frac{SAD}{SCD} \tag{2.10}$$

where, w_i is the leaf tip travel at the source to the center of the leaf distance, SCD, and SAD is the source to machine isocenter distance. The equation is derived from similar triangles, and represents the geometric projection of the radiation field edge at machine isocenter; it does not represent the light field edge, as this differs due to the light field edge being defined from a tangent intersecting a point at the leaf end. It is shown in Figure 2.4 that this ray tangent differs as the leaf shifts off central axis, which is the position whereby the radiation and field edges coincide. Boyer *et al.* (Boyer, 1997) show that the light field edge, X_i, at the machine isocenter is given by,

$$X_i = \frac{W_i \cdot SCD \pm SAD \cdot R \cdot \left(1 - \frac{SAD}{\sqrt{SAD^2 + W_i^2}}\right)}{SCD \pm \frac{R \cdot W_i}{\sqrt{SAD^2 + W_i^2}}} \tag{2.11}$$

The plus and minus signs indicate the position of the leaf insertion relative to the x-axis, with plus indicating when the leaf travel originates from the positive x direction, and negative indicating when the leaf travel originates from the negative x direction. Equation 2.11 represents a simplified two-dimensional situation with two approximations.

1. The y or leaf lateral coordinates are assumed the same for the tip point of intersection between the leaf and radiation edge, and that of the light tangent point of intersection. Boyer *et al.* (Boyer, 1997) show this difference is given as:

   $$y - y_o = \frac{Y_i R \sin\theta}{SAD} \tag{2.12}$$

   where Y_i is the y-coordinate in the isocenter plane. It is shown that the maximum difference calculated by equation 2.12 is 1.2 mm (Boyer, 1997).

2. From Figure 2.4, the second approximation is that $\theta = \theta'$, where, θ and θ' are the angles *ctd* and *cte* respectively.

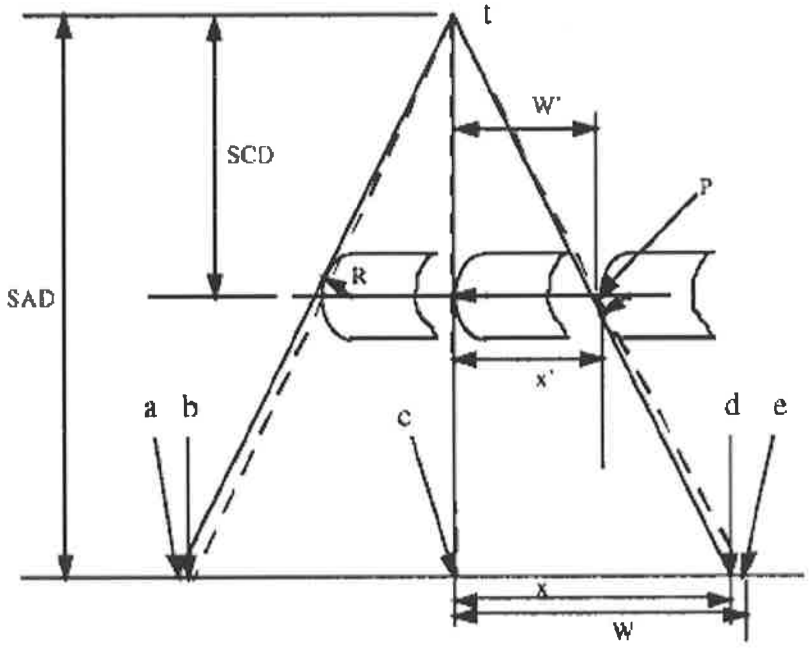

Figure 2.4: Schematic showing the ray lines that form the radiation (a) and the light (b) field edges due to the curved construction of the MLC leaf. *SAD* is the source to isocenter distance, *SCD* is the source to leaf center distance, and *R* is the radius of curvature of the leaf (Taken form Boyer *et al.* 2001).

Leaf construction is not taken into account during beam modelling by Pinnacle. The limiting factor of radiation and light field edge mismatch, as shown in Figure 2.4, will result in an underestimate of the penumbra width and overall field width for the MLC defined field. The profile for the fixed jaws in the in-plane direction is used by Pinnacle for the MLC defined field, and the profiles are assumed to be identical. This however has been shown to be incorrect, with significant discrepancies between MLC and fixed jaw defined fields (Lydon, 2005). In two-dimensions in the isocentric plane, the discrepancy is equal to the difference between Equation 2.10 and 2.11. Also, as X_i and W_i are directly proportional the discrepancy will increase with an increasing field size.

From Figure 2.4, the expression for the difference between radiation and light field projections, δ_{W1} in two-dimensions is given as:

$$\delta_{Wi} = \frac{\left(R - \sqrt{R^2 - \frac{HVT^2}{4}} \right) \cdot \sqrt{SAD^2 + W_i^2}}{SCD \pm \frac{R \cdot W_i}{\sqrt{SAD^2 + W_i^2}}} \tag{2.13}$$

where, *HVT* is the half-value thickness of the leaf material.

As the x-ray field displacement is directly proportional to both the *SAD* and the angle of field edge projection, it is expected that the difference will increase with both depth in water and increasing field size.

2.2.4 Inverse planning

2.2.4.1 Introduction

The general goals of treatment planning is the delivery of low doses outside a treatment volume, high dose gradients in the direction of organs at risk, and provide an homogenous dose inside the target volume. Inverse planning is a technique that enables a desired dose distribution to be produced from a known solution, thus enhancing the probability of satisfying these goals. With conventional planning, a desired clinical plan is obtained through the manual adjustment of beam parameters, such as beam direction, beam weights, wedge angle, collimation, and beam shielding. This trial and error process is time consuming as well as limiting, in that the final distribution is restricted to the collimated boundaries. Inverse planning eliminates, to a degree, the manual adjustment of beam parameters through assigning dose constraints and/or objectives, which include minimum, maximum or uniform dose to selected regions of interest.

2.2.4.2 Pinnacle^3 and inverse planning

There are basically four steps in generating an IMRT plan using Pinnacle:

- Create a standard plan.
- Set the objectives and/or constraints.
- Run the optimization (Section 2.2.5).
- Run the conversion (Section 2.2.6).

When creating an IMRT plan using Pinnacle a standard treatment plan needs to be planned and have an assigned dose grid, prior to entering the IMRT module. The assigned dose grid must completely cover the regions of interest (ROI) that will be used as objectives. The process of inverse planning using the Pinnacle system is very straight forward and requires only a few steps to be manually adjusted. Following the importation of the patient data set, ROIs are defined to delineate target and critical structure volumes. Appropriate safety margins can be incorporated in the ROIs to account for organ motion, patient movement and setup uncertainties that are unavoidable during multiple treatments. Plan optimization speed can be greatly decreased through the careful setup of beams and jaws. This can be achieved by angling the beams such that they avoid critical structures and set the jaws to block critical structures, this will reduce the complexity of the plan and reduce the overall time for optimization. The total number of beams selected is also a crucial factor in limiting plan complexity and reducing optimisation time. To generate an acceptable plan 5 - 9 beams can be used, and by using an odd number of beams will make it easier to avoid creating opposing beams (Philips, 2002). Beam weights, collimator rotation and beam sizes should also be set optimally. Beam weights should be set equally prior to optimization to provide a better starting point for the algorithm (Philips, 2002). To provide optimal blocking on the critical structures the collimators should be rotated such that the MLC leaves are approximately perpendicular to the long tumour axis. Beam sizes should be initially set so that the critical structures are blocked as much as possible, but still fully exposing the target ROIs with a 1.5 cm margin (Philips, 2002).

Once the standard plan has been produced the objectives and constraints are assigned to the ROIs within the P^3IMRT module. An objective is a desired goal which can be weighted to give the software an indication of the importance relative to all other objectives. A constraint on the other hand cannot be weighted and informs the software that it must satisfy the goal, regardless of the outcome of the set objectives. To assign objectives and constraints at least one ROI has to be included in the plan, and at least one objective or constraint has to be assigned as a target objective or constraint (Philips, 2002). Following optimization a value of zero is obtained for the objective value only if the objective has been met, however, if an objective is not met an objective value relative to the difference between the computed and assigned dose, and proportional to the objective weight is assigned. The smaller the objective value the better the overall optimized plan has met the objectives. Following optimization a composite objective value is displayed and provides an indication of the overall value of the plan optimization as it is the sum of the individual objective values.

Once the objectives and constraints have been assigned with appropriate weighting for the objectives, the plan can be optimized then converted. The two processes of beam optimization and conversion are discussed in sections 2.2.5 and 2.2.6 respectively.

2.2.5 Beam parameter optimisation methods

2.2.5.1 Traditional IMRT optimisation

Optimisation is the process by which the optimum beam weight or intensity distribution is determined that can best satisfy an objective function specified by the planner. The Pinnacle planning system employs the NPSOL[#] (Philips, 2001) method that utilizes sequential quadratic programming (SQP) to achieve, via iteration, the minimization of a function subject to user defined constraints (Gill, 1998). The SQP algorithm used by Pinnacle is very effective in the case of non-linear problems that would otherwise require vast computational time (Löf, 2003).

[#] NPSOL - Nonlinear Programming Systems Optimization Laboratory

In the case of IMRT the function minimized is the sum of user-defined objectives F_k,

$$F(\tau) = \sum_{k=1}^{n} F_K \qquad (k = 1......n) \tag{2.14}$$

where an objective could represent any combination of, a minimum dose, maximum dose, minimum dose to a given volume, maximum dose to a given volume, and uniform dose (Löf, 2003). The IMRT optimisation problem is expressed mathematically as:

$$\begin{aligned} &\min_{\tau} \ F(\tau) \\ &s.t. \begin{cases} C(\tau) \leq 0 \\ \tau \quad \geq 0 \end{cases} \end{aligned} \tag{2.15}$$

where $F(\tau)$ represents the objective vector function, $C(\tau)$ the constraints vector function, and τ the parameters to be optimised. The condition $\tau \geq 0$ guarantees that negative fluences will be discarded (Hårdemark, 2004). The results of the optimisation routine are in the form of a fluence and require conversion to control points before delivery to the patient. However, the conversion of the fluence to control points does not take into account the Oncologists treatment preferences, and consequently an undesirable outcome may result (Hårdemark, 2004).

2.2.5.2 Direct machine parameter optimisation

The limitation of traditional IMRT optimisation is overcome by direct machine parameter optimisation, which, given a beam model, control points can be calculated for a fluence, τ, from the actual leaf positions, x, and the weight of each segment, w.

The optimisation problem stated in equation 2.15 can now be expressed as:

$$\min_{x,w} \; F(x,w) \qquad (2.16)$$

$$s.t. \begin{cases} C(x,w) \leq 0 \\ Ax \leq b \\ w \geq 0 \end{cases}$$

With the segment weight constraint w set as greater than or equal to zero, non-negative fluences are again avoided. A_x represents the machine-specific and user leaf position requirements, where b is a particular set constraint that could be, amongst others, minimum leaf gap, interdigitation, maximum tip differences, or segment areas (Hårdemark, 2004).

2.2.5.3 Pinnacle^3 optimisation process

Once the optimisation process has been selected the software begins a set number of iterations, where an optimal solution for Pinnacle should be found within 25 - 40 iterations (Philips, 2002). The first few iterations, involves searching for the optimum solution via applying the Delta Pixel Beam method, which is a hybrid of the collapsed cone (CC) convolution superposition method (Philips, 2002). Being substantially faster than collapsed cone, the Delta Pixel method determines the intermediated dose between iterations until the optimum solution is found (Philips, 2002). Once this is achieved, all beam doses are calculated using the collapsed cone approach which is used to minimize the error introduced through dose calculation using the Delta Pixel approach (Hårdemark, 2004); further iterations are performed with the dose calculated via the Delta Pixel method, with each successive dose difference compared to the open density matrix (ODM) determined via collapsed cone convolution superposition (Philips, 2002). These dose differences are then applied to the dose calculated for each successive iteration (Philips, 2002). The final dose is then calculated for all beams using the CC method. The end result is an ideal ODM that undergoes conversion to decompose the fluence values into a number of acceptable smaller segments. Bortfield *et al.* (Bortfield, 1994) discuss MLC leaf trajectory techniques that Pinnacle employs for fluence decomposition. Figure 2.5 demonstrates the two techniques employed; 'Closed in' and 'Leaf sweep'. The 'Close in' technique produces a profile with a single maximum through the movement of the leaves either towards or from a single point (Convery, 1992), and the 'Leaf sweep' technique is a more simple approach, whereby leaf positions are sorted regarding magnitude (Bortfield, 1994).

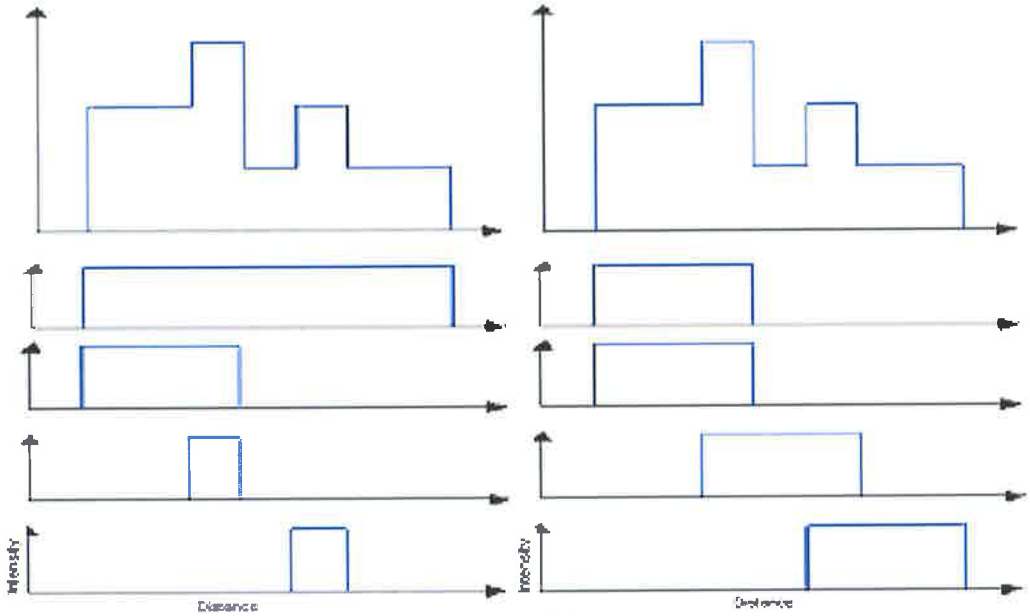

(a) (b)

Figure 2.5: Techniques for decomposition of fluences into smaller elements (a) 'Close in' technique (b) 'Leaf sweep' technique (Taken from Wu *et al.*, 2001).

The end product of the optimisation process is an ideal ODM, this however is not a deliverable ODM as corrections for the effects of head scatter and leaf transmission are not taken into account. The physical limitations of the MLC are also neglected during the optimisation process.

2.2.6 Leaf sequencing algorithms for accurate IMRT dose calculation employing the "step-and-shoot" approach

2.2.6.1 Introduction

Dose calculation with regard to IMRT planning is a complex problem due to the number of segments or control points involved in supplying the ideal dose distribution. This project involves investigating the accuracy of the Pinnacle radiotherapy treatment planning system in calculating the dose for static small fields defined by the multi-leaf collimator; and as only static fields are under investigation, the "step-and-shoot" approach to IMRT delivery will be investigated. With the "step-and-shoot" approach, a combination of MLC defined segments is mathematically generated to produce the desired dose distribution, achieved via the conversion of the ideal ODMs. The ODMs are determined from specified dose objectives and/or constraints, as well as set beam parameters; the software then applies optimising routines to provide the optimum treatment outcome. See Figure 2.6 for the sequential steps to deliver an IMRT plan.

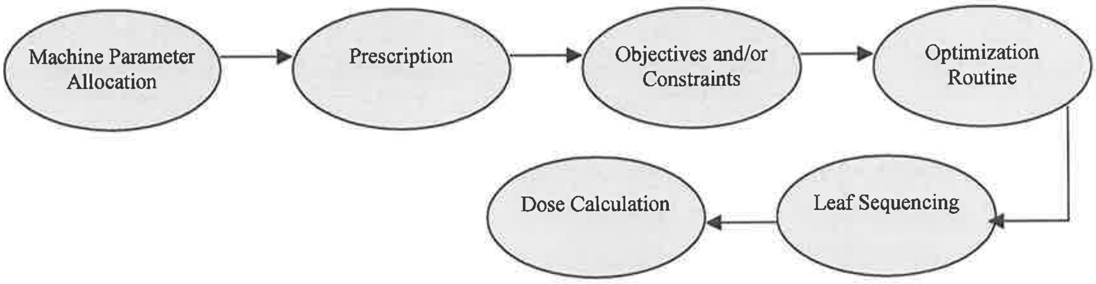

Figure 2.6: Scheme tree of IMRT planning process.

The Pinnacle system has two built-in "step-and-shoot" conversion algorithms: K-means clustering and IMFAST. The IMFAST method is for the Siemens linear accelerator, and therefore, will not be covered here.

2.2.6.2 Multi-level approximation distribution

The overall intensity of an optimised intensity modulated beam Φ_o, or primary ODM can be grouped into a multi-level approximation distribution Φ (Wu, 2001), or ideal ODM. This is simply determining similar intensity levels and grouping these levels into clusters such that a preset objective function relative to the "centroids" of the clusters is minimized. Figure 2.7 illustrates the grouping of a one-dimensional intensity distribution formed by a single intensity modulated beam consisting of multiple beamlets. The dashed line in the figure represents the multi-level approximation distribution.

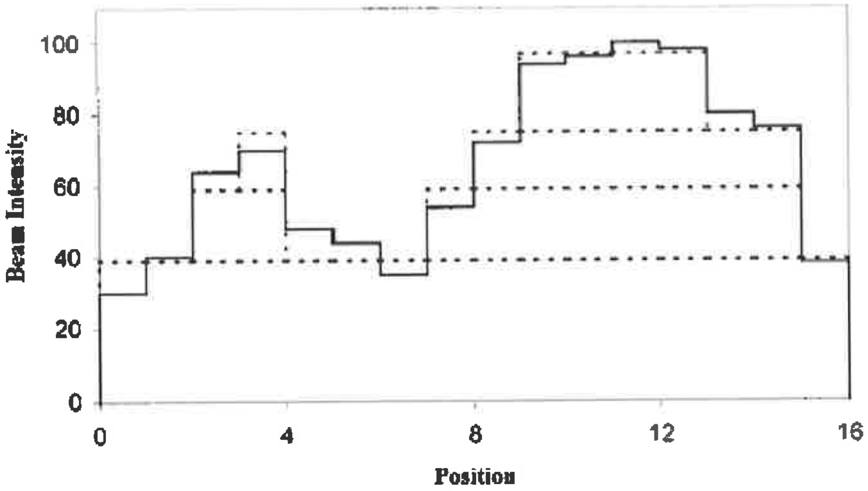

Figure 2.7: One-dimensional intensity distribution (solid line) with the multi-level approximation (dashed line) (Taken from Wu *et al.* 2001).

2.2.6.3 K-means Clustering

Following the optimisation step in the process of IMRT planning, the ideal ODM requires conversion to a deliverable beam. This conversion takes the ideal ODM, determined through optimisation and converts it to a deliverable ODM that takes into account MLC leaf transmission, head scatter and the physical limitations of the MLC (Philips, 2002). The deliverable ODM is then converted into a multilevel approximation distribution using the K-means Clustering method (Wu, 2001). This approach is a non-hierarchal method that takes the intensity of individual beam segments and maps them to a fixed number of predefined intensity levels (Wu, 2001), enabling a large amount of data to be grouped into clusters of smaller sets of similar data. This 'sorting' of intensity levels into clusters is determined by a set error tolerance between intensity levels (Hartigan, 1975). From these clustered intensity levels, MLC segments are formed to accurately deliver the optimum dose to the target volume. The Pinnacle system has several parameter settings that enable the intensity levels to be user defined: Jaw settings, error tolerance, minimum segment area, minimum equivalent square, leaf/field edge overlap, number of segments, minimize tongue and groove effect, ODM filter, and correction for head scatter.

Following the grouping of the intensity values within a minimum set of K clusters the ideal ODM is expressed as:

$$\Phi = \{(\phi_1,\phi_1,\ldots,\phi_1);(\phi_2,\phi_2,\ldots,\phi_2);\ldots;(\phi_j,\phi_j,\ldots,\phi_j)\} \tag{2.17}$$

Each bracketed term in 2.17 represents the grouping of averaged intensities ϕ_j,

$$\phi_j = \frac{1}{n_j} \sum_{i=1}^{n} \phi^o_{ji} \tag{2.18}$$

where, the clustered original beam intensity distribution Φ_o with n total intensity values is expressed as:

$$\Phi^o = \{(\phi^o_{11},\phi^o_{12},\ldots,\phi^o_{1n_1});(\phi^o_{21},\phi^o_{22},\ldots,\phi^o_{2n_1});\ldots;(\phi^o_{k1},\phi^o_{k2},\ldots,\phi^o_{kn_k})\} \tag{2.19}$$

Figure 2.8 (a) demonstrates the intensity pattern with all intensity levels Φ_o marked by the dashed lines, and Figure 2.8 (b) illustrates the clustering represented by expression 2.17, where each bracketed term corresponds to a dashed line.

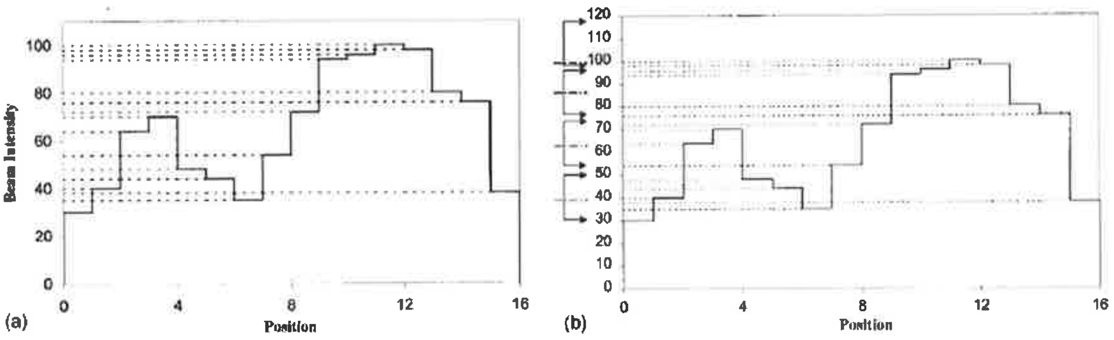

Figure 2.8: (a) Individual beam intensity levels (b) Intensity levels within a defined error tolerance grouped into *k* clusters (solid line indicates the span of the cluster and dashed line indicates the cluster centre). (Taken from Wu *et al.* 2001).

An error tolerance is required as the algorithm uses this to insure the difference between expressions 2.19 and 2.17 is less than twice this error tolerance:

$$\Phi^0_{jn_j} - \Phi^0_{j1} \le 2e_{\max} \quad \text{for } j = 1,\ldots,k \tag{2.20}$$

$$\Phi^0_{(j+1)1} - \Phi^0_{j1} \le 2e_{\max} \quad \text{for } j = 1,\ldots,(k-1) \tag{2.21}$$

where the overall difference between the original beam intensity and the approximation distribution is expressed as:

$$E = \{(e_{11}, e_{12}, \ldots., e_{1n_1}); (e_{21}, e_{22}, \ldots., e_{2n_2}); \ldots.; (e_{k1}, e_{k2}, \ldots., e_{kn_k})\} \tag{2.22}$$

with individual error differences given by:

$$e_{ji} = \phi_j - \phi^o_{ji} \quad \text{for } 1 \le j \le k, 1 \le i \le n_j \tag{2.23}$$

Once the intensity values have been correctly "clustered" and the constraints outlined in expression 2.23 satisfied, the clusters are optimized such that:

$$\left|e_{ij}\right| \le e_{\max} \quad \text{for } 1 \le j \le k, 1 \le i \le n_j \tag{2.24}$$

and the total squared error, *J* or objective function is kept to a minimum:

$$J = \sum_{j=1}^{k} \sum_{i=1}^{n_j} e_{ji}^2 \tag{2.25}$$

Wu *et al.* (Wu, 2001) established, through employing the K-means clustering algorithm on 10 clinical prostate cases, the total number of segments per beam was influenced by the user specified error tolerance, *e*, whereby for tolerances less than 6% segment numbers rapidly increased, resulting also in segments with small monitor unit settings. This becomes an issue due to beam delivery system limitations on the accuracy of beam stability and symmetry when delivering a small number of monitor units (MU). DVH matching also showed significant improvement, as would be expected when the number of segments increases.

2.2.7 Head geometry for the Varian 600C/D Linac

The output and dose distribution from a linear accelerator is primarily influenced by the photon beam interaction with the beam flattening filter, and various other components that comprise the collimator assembly. Figure 2.9 shows a schematic of the head construction for the Varian 600CD machine used in this investigation for all data acquisition. From the figure, it is shown that the exiting electron beam *(a)* from the waveguide collides with the target *(b)*, located 100 cm upstream from beam isocenter. The 600CD model linear accelerator has the waveguide in line with the treatment head, eliminating the need for a bending magnet to bend the electron beam prior to entry into the head. As a result the target is permanently attached to the accelerating waveguide via the flight tube. The 600CD electron target is constructed from thick tungsten, which provides a photon spectrum with higher beam penetration.

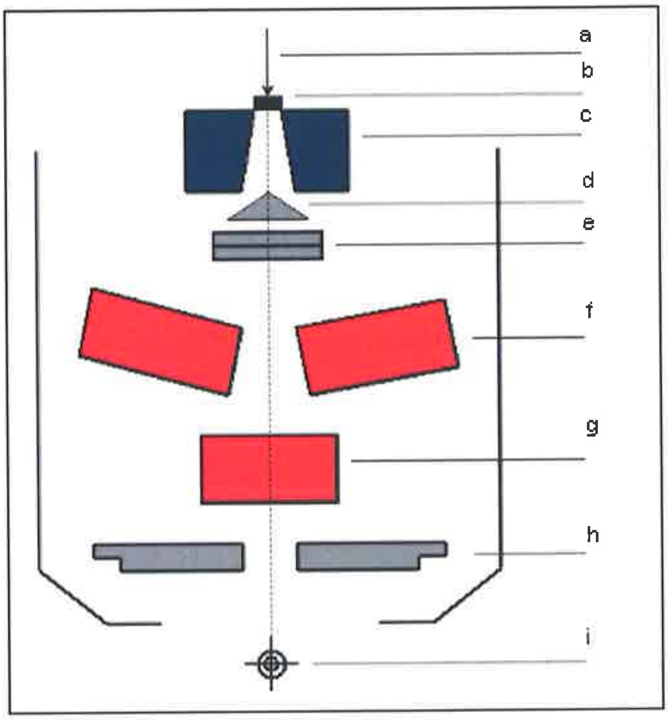

Figure 2.9: A schematic representation of the treatment head of the 600CD linear accelerator. Components labelled are: (a) electron beam exiting accelerating waveguide (b) target (c) primary collimator (d) photon flattening filter (e) monitor ionisation chamber (f) upper collimator jaw pair (g) lower collimator jaw pair (only 1 jaw visible) (h) multi-leaf collimator (i) machine isocentre.

Following interaction with the target material the photon fluence emanating from the distal surface of the target is shaped as a cone by the primary collimator *(c)*, which is used to limit the angular distribution of the photons.

Upon exiting the primary collimator the photon beam interacts with the flattening filter *(d)*. The construction of the flattening filter is a combination of high Z alloys, and is of a circular cone construction. The x-rays generated from the incident electrons are predominately produced along the electron line of travel at central axis (CAX) rather than the field outer edges. For an unfiltered beam this results in a sharply peaked dose distribution about CAX, shown as plot *A* in Figure 2.10. The flattening filter thereby creates a uniform beam intensity across the field by differentially absorbing the high-energy photons, shown as plot *B* in Figure 2.10.

The ionisation chambers *(e)* lie distal to the flattening filter and are constructed of two sealed circular multiple-electrode ion chambers whose function is to constantly monitor the Linacs output. Backscatter to the chambers is minimised by an anti-backscatter plate placed directly below the chambers.

The collimator pairs *(f) (g)* are motorized jaws constructed of a sufficient thickness of tungsten and whose main function is to shape the exiting photon beam to a desired rectangular shape and size. To provide an optimal penumbra the collimators move in an arc about the target whereby the face of the jaw remains parallel to the ray-line from the photon source. For the Varian 600CD the upper jaws are called Y1 and Y2, and the lower jaws are X1 and X2. The Y jaw position limits are +20 cm to –10 cm from CAX and X jaw limits are +20 cm to –2 cm from CAX.

The MLC system *(h)* lies below the lower X jaws and acts as a tertiary jaw and consists of two banks of independent tungsten leaves, which are used to shape a desired treatment field. As well as being thick enough to attenuate the beam it is essential the leaves are sufficiently narrow to provide adequate spatial resolution with respect to the direction of leaf travel. Table 2.1 lists the physical properties of the Varian 120 leaf Millennium MLC system.

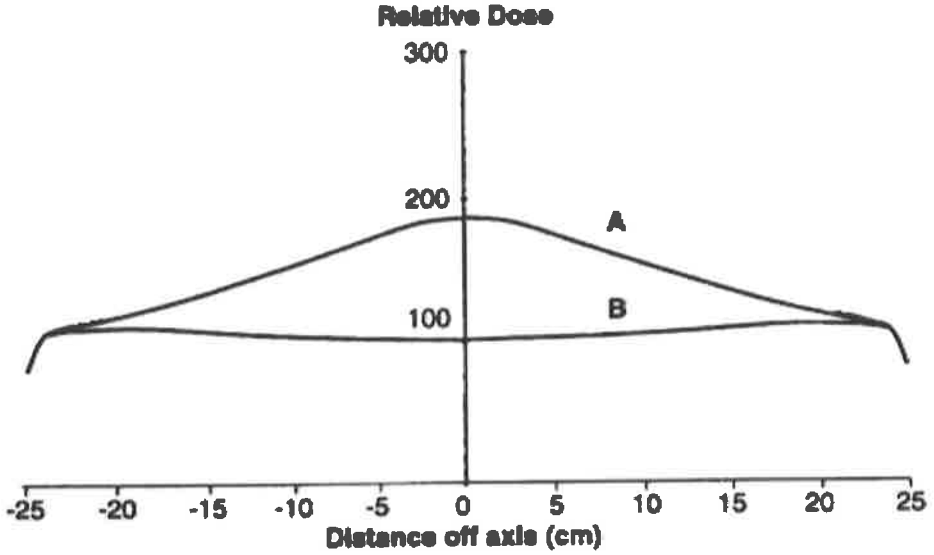

Figure 2.10: Effect on the dose distribution with and without the flattening filter (Taken from Green, 1997).

Number of leaves	2 x 60
Leaf width at Iso.	Central 20 leaves : 5mm Leaf pairs 2-10, 51-59: 10mm Leaf pairs 1-40: 1.4cm
Leaf thickness	55.3mm
Source to midleaf distance	50.7mm
Material	WHA
Patient clearance to accessory mount	33.5cm
Direction of leaves (coll. 0)	cross-plane
Collimator rotation	330
Maximum field size	40x40cm
Over-travel	19.7cm
Max. single leaf extension	14.5cm
Inter-digitised	yes
Minimum leaf gap	0cm
Verification method	encoder and soft pot
Motion control	motor and gearbox
Speed	2.5cm/sec

Table 2.1: Physical properties of the Varian 120-leaf Millennium MLC system.

2.2.8 Limiting factors of the MLC as a primary shield

2.2.8.1 Transmission

As the Millennium MLC acts as a tertiary collimator system, the leaves are limited to a certain construction height (5.53 cm for the Varian Millennium MLC) to enable adequate fixture to the machine head. This limitation and the fact that the composition of the leaves will not fully attenuate the radiation, results in a certain amount of radiation transmission. As the primary function of IMRT beam delivery is to provide dose escalation to the tumour volume, a greater number of MUs is delivered over a course of treatment, resulting in an increased significance in the patient dose due to transmission.

Transmission radiation can be split into two components, inter- and intraleaf transmission, as shown in Figure 2.11. Interleaf transmission is a result of the diverging leaf design of the MLC leaves. As the radiation beam is diverging, leakage occurs between each leaf and results in the local maxima in the percent radiation transmitted as a function distance off-axis plot, Figure 2.11. The minima seen in Figure 2.11 are due to the intraleaf transmission, and this is the radiation that is not completely attenuated by the leaf length. Varian medical systems quote inter-leaf leakage < 4.0%, and intra-leaf leakage < 2.5%. Butson *et al.* (Butson, 2003) have shown, for the Varian Millennium MLC system, inter- and intraleaf leakage < 4.0%.

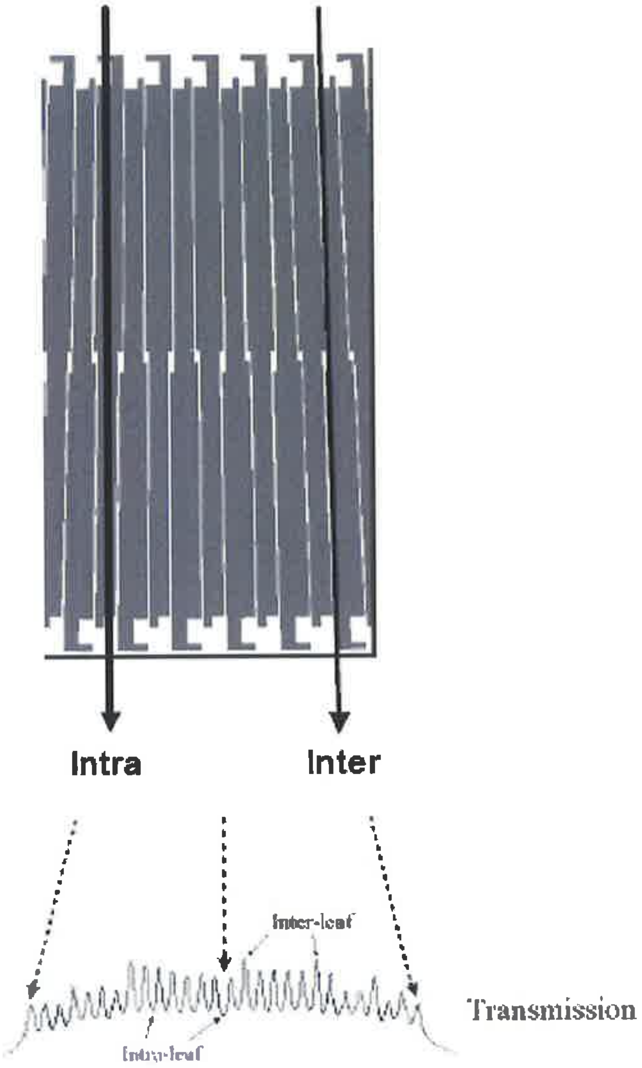

Figure 2.11: Inter- and intra-leaf transmission through the Varian Millennium MLC (Taken from Arnfield *et al.*, 2001).

2.2.8.2 Rounded leaf effects

2.2.8.2.1 Beam Penumbra

As discussed in 2.2.2.2, the Millennium MLC is of the focused variety and is constructed such that the individual leaves follow beam divergence and produce a constant penumbra for different displacements. The side effect of the rounded leaf design is the partial attenuation of the primary fluence in the rounded end along chords of the circle defining the leaf curvature. As displayed in Figure 2.4 distance *d*→ *e* describes the discrepancy in the penumbra edge caused by the rounded leaf design.

2.2.8.2.2 Match-line

With multiple segments overlapping in the delivery of IMRT, rounded leaf effects can be quite significant in that multiple hotspots can be produced, introducing discrepancies between what is planned and what is delivered. Match-line is the effect of two adjacent fields of radiation delivered with a common central edge defined by one jaw in one field and the opposing jaw in the subsequent field. Figure 2.12 (a) represents leaf positions shifted either side of CAX that produce a field edge defined by abutting leaves, and as a result, penumbra overlap occurs resulting in a radiation hot spot as shown in Figure 2.12 (b).

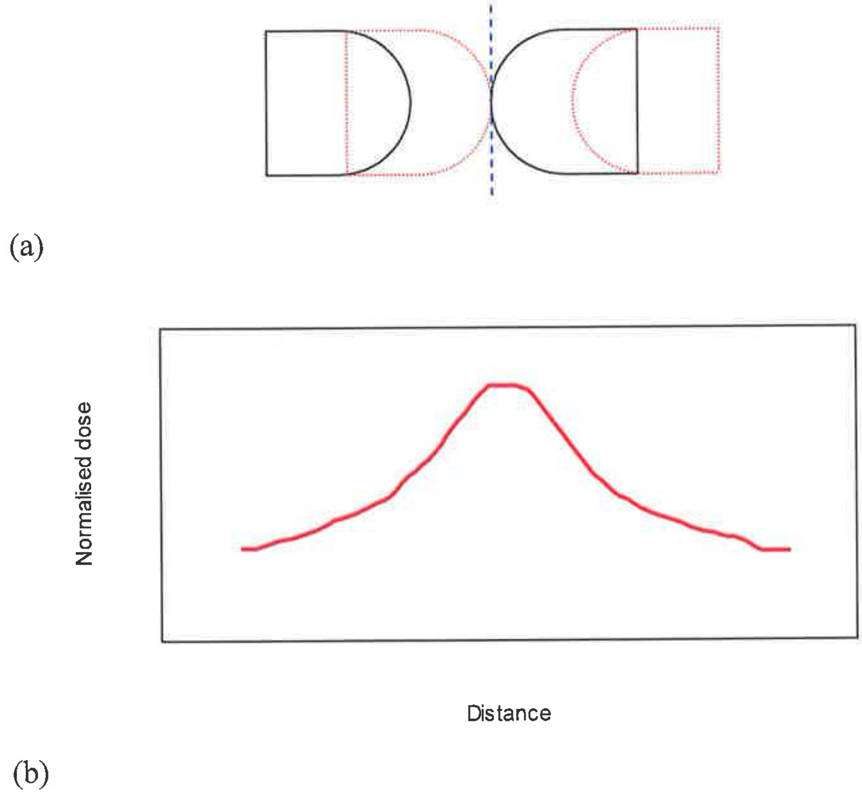

Figure 2.12:Varian Millennium Rounded leaf junction effect (a) Leaf positions of two 5x5 cm^2 segments mirrored either side of CAX to produce a 10x10 cm^2 segment (b) Expected dose spike produced at the leaf end junctions.

2.2.8.3 Tongue-and-groove effects

In addition to the rounded leaf design the construction of the individual leaves results in another important design feature, the leaf edge. As the construction of the MLC is of a divergent design any gap between adjacent leaves could result in an unhindered path of radiation to patient. This is the reasoning to why the leaves are not constructed with flat sides and edge to edge. To prevent this transmission of radiation the construction of the MLC edge is of an interlocking tongue-and-groove design as displayed in Figure 2.11. This design limits, to a degree, the amount of radiation that is transported through the MLC to the patient by providing a physical barrier that attenuates the beam.

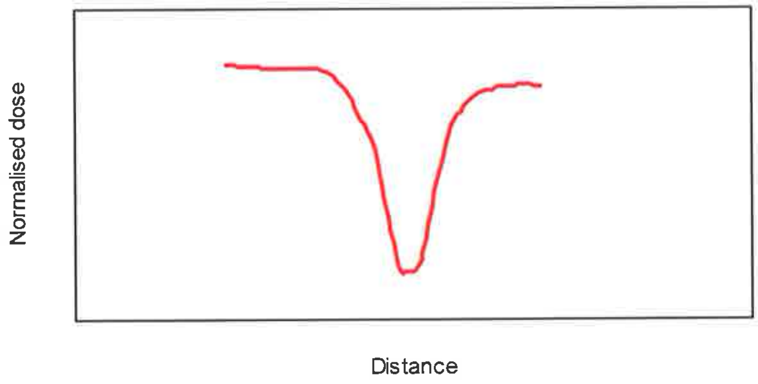

Figure 2.13: Expected dose cold spot produced as a result of the tongue-and-groove effect.

Figure 2.13 demonstrates how the tongue-and-groove design of the MLC leaf edge may result in an underdose through the partial shielding at the field edge when two adjacent fields are delivered.

2.2.8.4 Overshoot effect

With the delivery of small MUs per segment with varying dose rates the control loop of the Varian MLC system requires ~65 msec to monitor and halt the delivery of the set MUs (Ezzell, 2001). The irradiation from the Linac requires a certain time to stabilise, and with the delivery of small MUs an "overshoot" effect is seen, whereby during step-and-shoot delivery the first segment receives more dose and the last segment receives less (Figure 2.14 a). Figure 2.14 also shows other variations of the effect with intermediate segments delivering differing number of MUs. Ezzell *et al.* (Ezzell, 2001) state that the total MU for a delivered plan is correct, therefore, for the example shown in Figure 2.14 (a) the difference seen between the overdose at the first delivered segment (ΔD_{first}) and the planned dose (D), where D is the same for each segment, results in the missing dose seen for the final segment (ΔD_{last}).

$$\Delta D_{last} = \Delta D_{first} - D \tag{2.26}$$

The dose fraction for individual segments is therefore given as,

$$fD_i = \frac{\Delta D_i}{D} \tag{2.27}$$

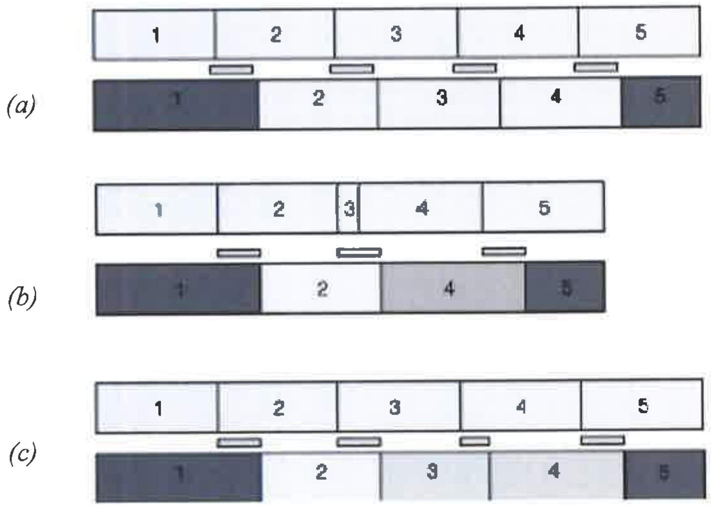

Figure 2.14: Overshoot effect and the impact on MU delivery. (a) Segment 1 high, 5 is low and intermediate are constant. (b) Segment 3 missed as overshoot exceeded. (c) Segment 3 lower, 4 higher (Taken from Ezzel *et al.* 2001).

Chapter 3

Dosimetric Methods

3.1 Introduction

This chapter introduces the concepts that are used in this investigation for measurements of beam profiles and machine outputs for comparisons with Pinnacle generated data. Film dosimetry is discussed with an outline of the method employed to generate a calibration file for use in film and Pinnacle distribution comparison for IMRT plan quality assurance. The majority of measurements included in this investigation involve the use of an ion chamber; therefore, the theory of ion chamber operation is discussed as well as an in depth background discussion on the small volume PinPoint chamber used in this study.

The chapter also contains a description of the concept of the Gamma Index, γ, a parameter utilized for beam profile and IMRT dose distribution comparisons. γ is a single parameter, calculated using a simple expression that incorporates both a dose and a distance tolerance limit.

3.2 Film Dosimetry

3.2.1 Introduction

Radiographic film is an ideal tool employed in the study of high-energy radiation therapy. It has several advantages over other conventional methods in that it has a low cost, speed of data collection, high spatial resolution, ease of handling, and the ability to produce two dimensional dose maps in the film plane (Suchowerska, 1997), which is very attractive with regard to the study of dynamic field delivery, particularly IMRT plan verification. The mechanism of film developing is well understood and the basis of the process involves creating a latent image within potato shaped silver halide crystals, through exposure to ionising radiation (Khan, 1998). Generally, the film consists of a transparent material base of cellulose acetate, thinly coated with an emulsion consisting of gelatin (Khan, 1998). Gelatin is an ideal substrate as it keeps the non-uniform grains of silver halide finely dispersed (Figure 3.1), preventing clumping and sedimentation (Das, 2002). It also protects unexposed grains from reduction by the developer agent and chemically neutral to the crystals in terms of fogging and loss of sensitivity (Das, 2002).

Figure 3.1: Electron micrograph showing silver halide grains evenly dispersed in gelatin substrate (Taken from Das *et al.*, 2002).

Upon exposure to ionising radiation the silver halide directly or indirectly ionises, releasing energetic electrons that produce electron and hole pairs, which subsequently disperse through the silver halide crystals trapping electrons in the impurity atoms leading to the production of free silver ions. During the film developing process the free silver ions are reduced to silver atoms, which is unaffected by the fixing solution and therefore, remains behind, as the emulsion that has not undergone a chemical reaction is removed by the fixing solution. The metallic silver produces a darkened area on the transparent base material.

The degree of film darkening can be measured from the optical density (OD) of the film (Williams, 1993). This is achieved by using a film densitometer, which measures the amount of absorption of light transmitted through an exposed film. The *OD* is defined as:

$$OD = \log\frac{I_o}{I_t} \tag{3.1}$$

where I_t and I_o are the amount of light collected by the densitometer with and without the film respectively. Unexposed base material will have a certain OD value, which is termed background or fog. This fog OD value is subtracted from the OD values obtained from the exposed film to provide a corrected response.

Energy independence and tissue equivalence are ideal qualities in detector materials. In the case of radiographic film, the silver content of the film emulsion has an atomic number, Z, of 47, which is vastly greater than the Z of tissue 7.64 (Johns, 1983). The high atomic number of the silver results in a higher cross-section for low energy photon interactions. Figure 3.2 displays the ratio of the mass-energy absorption coefficient for radiographic film as a function of photon energy, and illustrates the high-energy dependence of film below approximately 400 keV, especially below 200 keV due to photoelectric interactions.

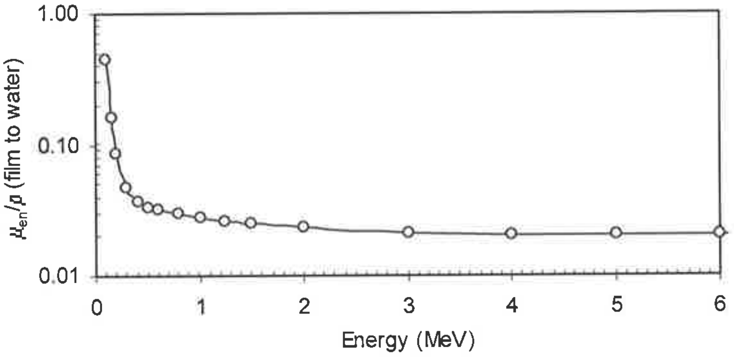

Figure 3.2: Ratio of mass energy-absorption coefficient of radiotherapy film as a function of photon energy (Data taken from Hubbell *et al.*, 1997).

This is a serious disadvantage of radiographic film as a radiotherapy dosimeter. Palm *et al.* (Palm, 2004) state that film sensitivity to low energy photons increases with an increase in the ratio of scattered and primary radiation. This infers that film over response will increase with depth as well as field size and distance off axis due to the higher amount of low energy photons present under these conditions. So in the case for IMRT plan verification the variation in the photon fluence may vary across a field (Palm, 2004) comprising multiple segments. However, Martens *et al.* (Martens, 2002) have shown that film over response due to field size and dose rate does not rule out film for characterizing intensity modulated beams. Response with increasing field size was shown to increase, but for fields up to 15x15 cm^2 a 3% difference between film and diamond detector was seen (Martens, 2002). Comparisons for film response with dose rate variations for beams in regions of high dose gradient are within 1%, and for shielded regions 3% (Martens, 2002). As for response with changing depth, several authors have investigated this with no consensus as to the extent of the effect (Burch, 1997, Sykes, 1999).

3.2.2 Kodak EDR2 film calibration

3.2.2.1 Introduction

Kodak Extended Dose Range (EDR2) type radiographic film is a relatively new option for film dosimetry. In replacing the Kodak XV film the EDR2 film provides the ease of use as a film dosimeter without some of the disadvantages seen with the XV type film. Dose saturation with the XV film has been quoted by the manufacturer at 200 cGy (Kodak, Rochester NY) and in the literature between 100 cGy (Dogan, 2002) and 200 cGy (Zhu, 2002). Literature states for EDR2 film a saturation point at 700cGy (Kodak, Rochester NY, Zhu 2002) and 500 cGy (Dogan, 2002). Generally a saturation point of 100 cGy would not be an issue for single intensity modulated beam verification, but in the case of a global plan check, were it is possible for many beams; such a low saturation point is impractical, as the total dose would exceed 100 cGy as the whole purpose of IMRT is to provide dose escalation to a tumour volume.

EDR2 film comes as a ready pack form of the original EC (Porous Ethylcellulose) type film used for portal localization (Zhu, 2002). The two types of film differ in that EDR2 film is composed of uniform cubic crystals of silver halide finely dispersed in a double emulsion layer, coated on a 0.18 mm ester base. The silver halide crystals are approximately 10 times smaller than those found in the XV emulsion (Das, 2002), rendering the film much less sensitive than the XV film, resulting in a low noise level and higher contrast (Zhu, 2002). Zhu *et al.* (Zhu, 2002) state that the EDR2 film is rendered developable as a result of the double hit process, dominant for mega-voltage x-ray beams. The sensitometric curve is then described by a third order polynomial function of OD and dose, given by,

$$OD = OD_1\left(1 - e^{-\alpha_1 D}\right) + OD_2\left[1 - e^{-\alpha_{21} D}\left(1 + \alpha_2 D\right)\right] \qquad (3.2)$$

where, OD is the optical density corresponding to dose D in cGy, OD_1 and OD_2 are the maximum optical densities achieved by single and double hit processes respectively, and α_1 and α_2 are the factors that describe the sensitivity of the film for single and double hits respectively and have the units of reciprocal dose. In the case for XV film the single hit process renders the film developable (Williamson, 1981), and hence equation 3.2 reduces to,

$$OD = OD_1\left(1 - e^{-\alpha_1 D}\right) \qquad (3.3)$$

3.2.2.2 Method

In the current work, the RIT113 film dosimetry software version 4.1 (Radiological Imaging Technology Inc, Colorado Springs, Colorado) and the VIDAR VXR-16 Dosimetry Pro film scanner (Vidar Systems Corp., USA) were used for all film analysis. For IMRT film verification a calibration file is required for film and plan comparison. An MLC step wedge calibration was used in this investigation and involved exposing EDR2 film to a 13 segment MLC file provided by Radiological Imaging Technology Inc. The 600CD Linac equipped with 120-leaf millennium MLC was used to generate 6 MV photon beam. The film was placed at a clinically representative depth of 5 cm in a Solid Water® phantom (Gammex RMI, Middleton USA). The MLC segments were set-up such that they produced an asymmetric field in the cross-plane direction and symmetric in the in-plane direction, i.e. X1 = 15 cm, X2 = 0 cm and Y = 26 cm. The Linac couch was raised such that the film was at machine isocenter of 100 cm. Total MU of 300 were delivered at a dose rate of 400 MU / min. The Linac output was calibrated to deliver 1 cGy / MU at isocenter at depth of maximum dose and 10x10 cm^2 collimator setting. The file was delivered as a step-and-shoot technique to a single film and then repeated by replacing the film with a Farmer chamber, type 2571 positioned at 5 cm depth and SAD of 100 cm. The calibration file was delivered 13 times, corresponding to longitudinal shifts to the centre of the Farmer chamber under each individual segment. Placement of the

Farmer chamber under each individual segment in effect took into account the effects of scatter from all segments providing an accurate and simple way of producing a calibration file.The exposed film was then processed in a Kodak processor used for medical imaging, providing constant chemistry conditions, and then digitised into the RIT software using the VXR-16 scanner. Provided with the RIT software is a step wedge of known OD values. This was scanned and an OD versus scanner A/D characteristic curve generated, which enables association of the scanner signal to a unique OD, and from the calibration file, a dose. To produce the dose calibration file the step wedge was scanned into the RIT software and a certain region of interest was selected such that edge field effects are not included in the overall calibration file. Each segment of the step wedge was then associated with the dose calculated by measurements performed with the Farmer ion chamber. The dose was measured using the ACPSEM protocol of photon dose determination (ACPSEM, 1998). The use of the recommended TRS-398 was not used as at the time was not implemented at the W. P. Holman Clinic, Launceston. The dose is given as,

$$D_{W,Q} = M_Q N_{D,air} (S_{W,air})_Q P_Q \tag{3.4}$$

where, $D_{W,Q}$ is the absorbed dose to water, M_Q is the charge reading taken from the dosimeter and corrected for the effects of temperature and pressure, $N_{D,air}$ is the calibration factor to convert the reading into dose to water and traceable to a national standard, $(S_{W,air})_Q$ is the ratio of stopping powers in water and air, and P_Q is the global perturbation factor that accounts for the presence of the chamber in the primary beam.

3.2.2.3 Results

Figure 3.3 shows an in-plane profile through the central axis of the digitised MLC step wedge film. Ion chamber measurements performed with the chamber positioned at the centre of each step in the profile is tabulated in Table 3.1.

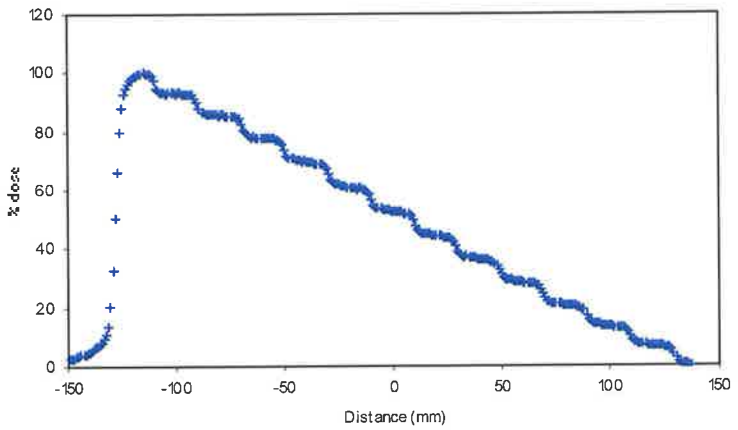

Figure 3.3: In-plane profile of the MLC step wedge calibration film.

Position No.	1	2	3	4	5	6	7	8	9	10	11	12	13
Dose, cGy	27.4	49.3	72.2	94.9	117	139	162	184	207	227	249	268	282

Table 3.1: Measured ion chamber doses corresponding to each individual MLC segment of the step wedge.

Figure 3.4 is the characteristic curve for the VXR-16 scanner used for all film scans. The provided OD step wedge was scanned and the associated scanner values plotted against the known OD values. It is shown that the characteristic curve has a sharp drop from OD 3.74 to 1.44, which from the calibration curve shown in Figure 3.5 corresponds to approximately 500 cGy and 200 cGy respectively. The calibration curve shown in Figure 3.5 provides the way to associate the film dose to an OD value from the scanner signal. The OD value of 0.209 at a zero dose, represents the background or fog reading, and indicates the importance of including a fog reading, especially in the low dose regions.

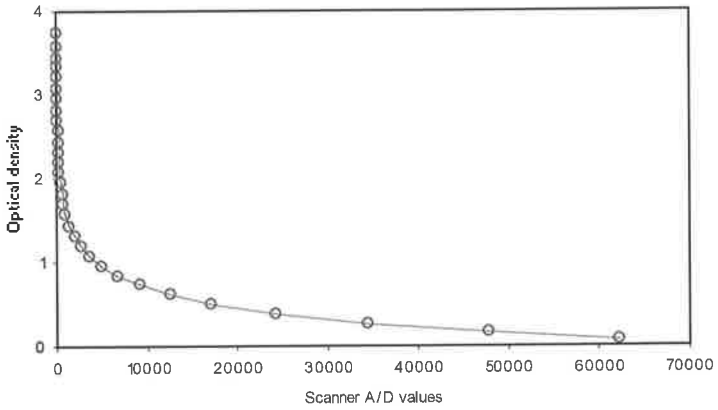

Figure 3.4: Optical density for EDR2 film versus scanner A/D characteristic curve.

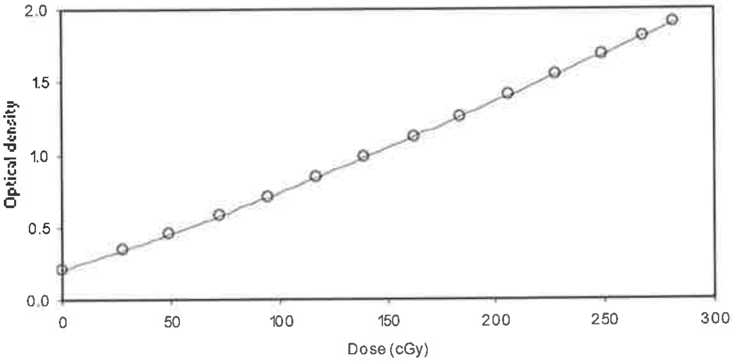

Figure 3.5: Optical density versus dose calibration curve.

3.2.2.4 Conclusion

A simple method of film calibration has been discussed using an MLC step wedge for dose determination from a films measured OD. The created calibration file can be applied to the same type of film, and preferably a film from the same batch as the calibration film and under the same development conditions. For film analysis in the RIT113 dosimetry package a calibration file is required for comparisons between measured and calculated distributions, and the method outlined in this investigation and suggested by Radiological Imaging Technology as one method of calibration file generation, this is the most accurate method, due to the direct association of the film measured OD and the absolute dose determined by a reference standard ion chamber whose measurements are performed at the same time as the film exposure.

3.3 Ion chamber theory

3.3.1 Introduction

When radiation passes through or is stopped within a medium, free positive and negative charge carries are produced. This process is termed ionization and can be measured with an ionization chamber. An ionization chamber consists of a gas filled cavity containing two oppositely charged electrodes, such that when the gas is ionized by the presence of ionizing radiation, the ions formed are drawn to the electrode of opposite charge. This creates an ionization current that can be measured and related to the intensity of the ionizing radiation. Ion chambers have become the standard instrument for clinical dosimetry measurements due to their long-term stability, high precision, direct readout, and relative ease of use. Figure 3.6 represents the construction of a basic ion chamber consisting of a central electrode, which is insulated from the wall enclosing the gas cavity, and the chamber stem that carries the high polarizing voltage, typically set to ±300 V. A high voltage is required so that the charge produced is collected, but not so high that the accelerated electrons themselves create more ionization.

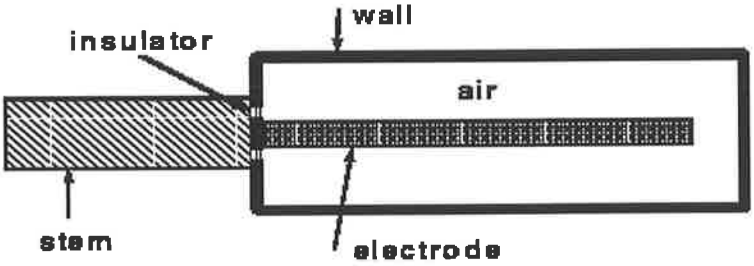

Figure 3.6: Schematic of the basic construction of an ion chamber.

The theory of absorbed dose calculation employing an ion chamber was first introduced by Bragg (Bragg, 1912) and later adapted by Gray (Gray, 1936) to form the Bragg-Gray cavity theory. Consider a small gas-filled cavity in a large volume of absorbing medium that is uniformly irradiated. The cavity is assumed to be sufficiently small so that its introduction does not alter the number or distribution of the secondary electrons that would exist in the medium without the cavity. Bragg-

Gray theory states that the absorbed dose produced in the cavity, D_{cav}, is related to the absorbed dose in the surrounding medium, D_{med}, as follows:

$$D_{med} = D_{cav}\left(\frac{\bar{S}}{\rho}\right)_{med,cav} \tag{3.5}$$

where, $(\bar{S}/\rho)$ is the ratio of the averaged unrestricted mass collision stopping power of the medium and cavity. The cavity dose is the product of the ionization charge of one sign per unit mass of cavity gas, J_g, and the average energy absorbed per unit charge of ionization produced, $(\bar{W}/e)$. For the Bragg-Gray theory to be applied two criteria must be satisfied:

The cavity volume must be smaller than the range of charged particles incident on it to prevent perturbation of the fluence within the medium. The cavity-absorbed dose is produced solely from charge particle interactions, and photon interactions are negligible. Secondary delta electrons are produced within the chamber volume as a consequence of the slowing down of the primary electrons. These δ-electrons are not taken into account in the Bragg-Gray theory and as they contain sufficient energy have been shown to contribute to further ionization (Podgorsak, 2003). Spencer and Attix (Spencer, 1955) developed a theory to take into effect the δ-electrons with the following assumptions:

i) The energy lost by an electron in a collision with an atomic electron is immediately transformed into imparted energy if the energy loss is less than a given energy Δ.

ii) If the energy loss is larger than Δ, it is carried away as kinetic energy of a δ-electron and no energy is absorbed. The δ-electron generated with kinetic energy > Δ are added to the fluence of electrons.

The Spencer-Attix formalism is given as:

$$D_{med} = D_{cav}\left(\frac{\bar{L}}{\rho}\right)_{med,cav} \qquad (3.6)$$

where, $(\bar{L}/\rho)$ is the ratio of the averaged restricted mass collision stopping power of the medium and cavity with cut-off energy Δ, and is defined as follows:

$$\frac{\bar{L}}{\rho} = \frac{\int_{\Delta}^{E_o} \Phi(E).\frac{L}{\rho}(E)dE}{\int_{\Delta}^{E_o} \Phi(E)dE} \qquad (3.7)$$

Equation 3.7 takes into account the effect of ionization produced from the δ-electrons by setting the arbitrary maximum energy limit, Δ. Eo is the initial kinetic energy of the secondary electrons, $\Phi(E)$ is the distribution of electron fluence in energy, and (L/ρ) is the restricted mass collision stopping power with cut-off energy, $\tilde{\Delta}$.

3.3.2 Pin Point ion chamber

Due to the narrow fields under investigation an ionisation chamber able to measure accurate profiles and depth dose information down to a 1x1 cm^2 field size was required. The PinPoint chamber manufactured by PTW Freiburg (PTW, Freiburg), was employed as the construction of the type 31006 chamber (Figure 3.7) consists of a vented air cavity with a sensitive volume of 0.015 cm^3 and inner diameter of 2 mm. The small volume is satisfactory for measurements of relative beam profiles (PTW, 2002), but is not suitable for absolute dose measurements due to the loss of sensitivity as a result of the small electrode current (IAEA #398, 2000). This lack of charge particle equilibrium can also provide limitations in measurements performed on remote IMRT segments, and thus would rule it out for verification measurements (Leybovich, 2003).

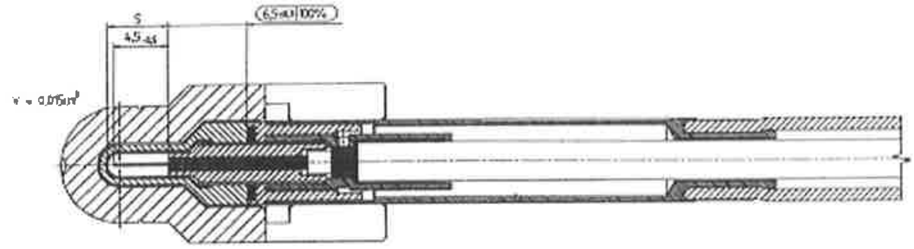

Figure 3.7: Ionization chamber type 31006 with build up cap (Taken from PTW, 2002).

Figure 3.7 is a schematic representation of the PinPoint type 31006 ion chamber which consists of a 0.18 mm diameter steel central electrode, with a length of 4.5 mm from tip to guard ring. Chamber response is quoted to be 4×10^{-10} C/Gy, with a maximum leakage of ±4x10-15 A (PTW, 2002). The wall material is composed of 0.56 mm of PMMA ($C_5H_8O_2$) and 0.15 mm of carbon (PTW, 2002). Polarizing voltage was set for all measurements to –300 Volts, which corresponds to an ion collection time of 20 μs. The chamber also has a nominal useful energy range of ^{60}Co to 50 MV. As the central electrode is of a steel composition, photoelectric interactions occur resulting in an over-response to low energy scattered radiation (Martens, 2000), resulting in a detector comparable to radiographic film (Burch, 1997). The response of the PinPoint chamber has also been shown to overestimate machine output above field size 10x10 cm^2, and underestimate the outputs for small fields below approximately 2x2 cm^2 (Martens, 2000). Figure 3.8 shows results taken from Stasi *et al.* (Stasi, 2004), which demonstrates this underestimation and overestimation for small and large fields respectively. Outputs for the PinPoint chamber are normalised to the output of a 10x10 cm^2 field, and are compared to those measured with a PTW 60003 diamond detector.

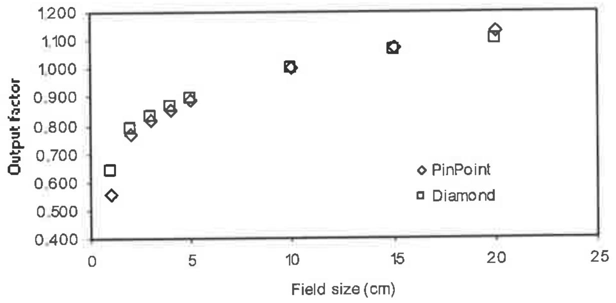

Figure 3.8: Output factors for a Varian 600CD / 6 MV Clinac measured with the PTW type 31002 PinPoint chamber and PTW 60003 Diamond detector as measured by Stasi *et al.* (Data taken from Stasi, 2004).

The fact that the PinPoint chamber over-responds to low energy photons, it would be assumed that this effect would be enhanced with increasing field size and depth in water as a result of the increased amount of low energy photons present under these conditions. Figure 3.9 is a graph of the measured data by Martens *et al.* (Martens, 2000) that characterises the energy response of the PinPoint chamber relative to a PTW 0.125 cm^3 chamber, which has a useful range of 30 kV to 50 MV photons. The relative response is determined from the ratio of the readings performed using the PinPoint chamber and that of the 0.125 cm^3 chamber. As displayed in Figure 3.9 the change in sensitivity with increasing water depth shows an approximate linear relationship. For field sizes 5x5 cm^2 and 6x6 cm^2 the change in sensitivity is negligible over a water depth range of 2 cm – 30 cm. A 10x10 cm^2 field is shown to increase in sensitivity beyond a depth of 10 cm and reach a maximum change of 3.4% at 30 cm deep; this would be a consequence of a larger amount of low energy scatter radiation present at this depth. The sensitivity increases unacceptably for larger field sizes, and as much as approximately 20% for a 40x40 cm^2 field at 30 cm depth.

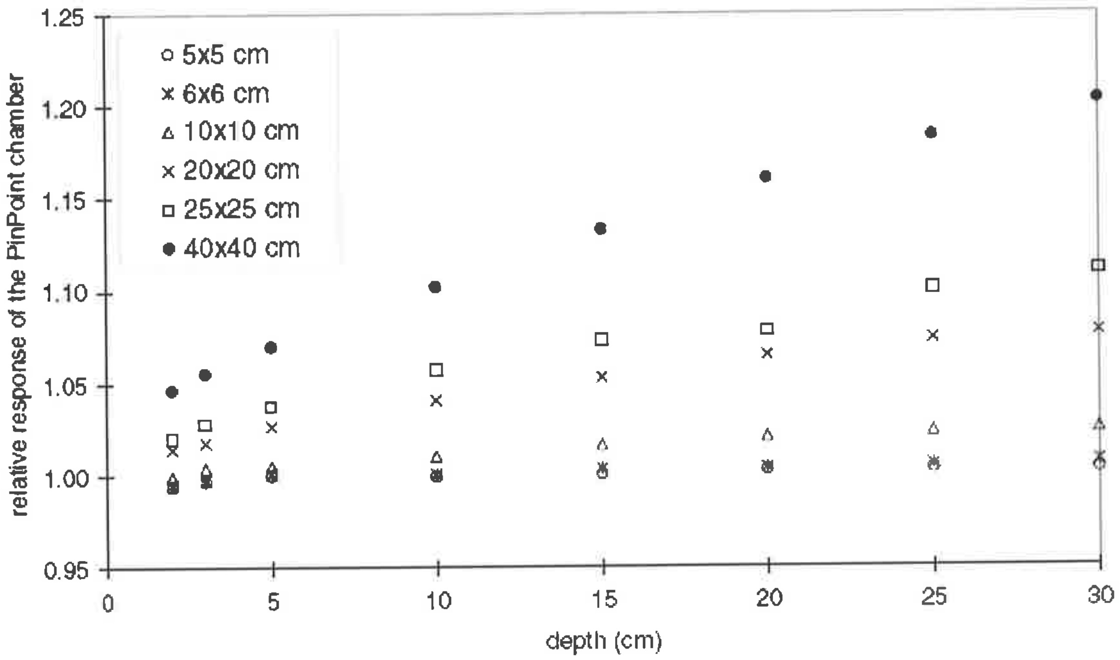

Figure 3.9: Ratio of the response of the PTW type 31006 PinPoint chamber to a 0.125 cm^3 ion chamber (Taken from Martens *et al.*, 2000).

Martens *et al.* (Martens, 2000) concluded from this study that the PinPoint chamber is suitable for relative output factor measurements for fields in the range 5x5 cm^2 and 2x2 cm^2, and ideally at a reference depth of 5 cm. For fields below 2x2 cm^2 the PinPoint chamber is not suitable due to the small collecting volume, resulting in an underestimation of the output, and in this instance a diamond detector should be used (Martens, 2000). As shown in Figure 3.9 a depth of 10 cm is showing negligible change in sensitivity and therefore should provide accuracy in measured output factors within 0.5%. A depth of 10 cm is desired as this is of clinical significance. A change in sensitivity with field offset from central axis also showed negligible change with an overall average of 0.23% seen for a 5x5 cm^2 field offset up to 10 cm deep (Martens, 2000).

3.4 Gamma Index

3.4.1 Introduction

The W. P. Holman Clinic, Launceston employs the Pinnacle treatment planning system (TPS) for all external beam planning. Pinnacle utilizes a Collapsed Cone Convolution Superposition algorithm to generate a dose distribution within a patient. A set of model parameters defined during physics data matching, and accelerator geometries determines this dose distribution. Auto-modelling scripts embedded within Pinnacle drive an iterative process that parameterises the model. These scripts are determined by sets of two-dimensional measured data for varying physical parameters. The model generated by Pinnacle, characterizes the radiation that exits the head of the linear accelerator, which is then overlayed with the actual measured data from the accelerator. Tools are available within Pinnacle that allows the adjustment, to a certain extent, of computed data and measured data. The Gamma Index is a tool that allows a comparison of computed and measured profile data.

3.4.2 The Van Dyk criteria

Comprehensive quality assurance of both hardware and software is an essential ingredient in the accurate delivery of radiation. Many complex steps are involved and each of these steps requires thorough scrutiny to provide confidence in delivered tumour doses. Van Dyk et al. provide guidelines for reasonable levels of acceptability in the case of measured photon beam data and that computed by a TPS (Van Dyk, 1993). Table 3.2 summarises levels of acceptability for photon beams.

Central axis data (excluding the build-up region	High dose region - Low dose gradient	Low dose region - Small dose gradient	Large dose gradient
2%	3%	3%	4 mm

Table 3.2: Van Dyk criteria for levels of Photon beam acceptability.

It is shown that the levels of acceptability are specified as either a percentage of the dose difference at a certain point for measured and computed data (Figure 3.10 a), or the distance to agreement (DTA) of two points that receive the same dose (Figure 3.10 b).

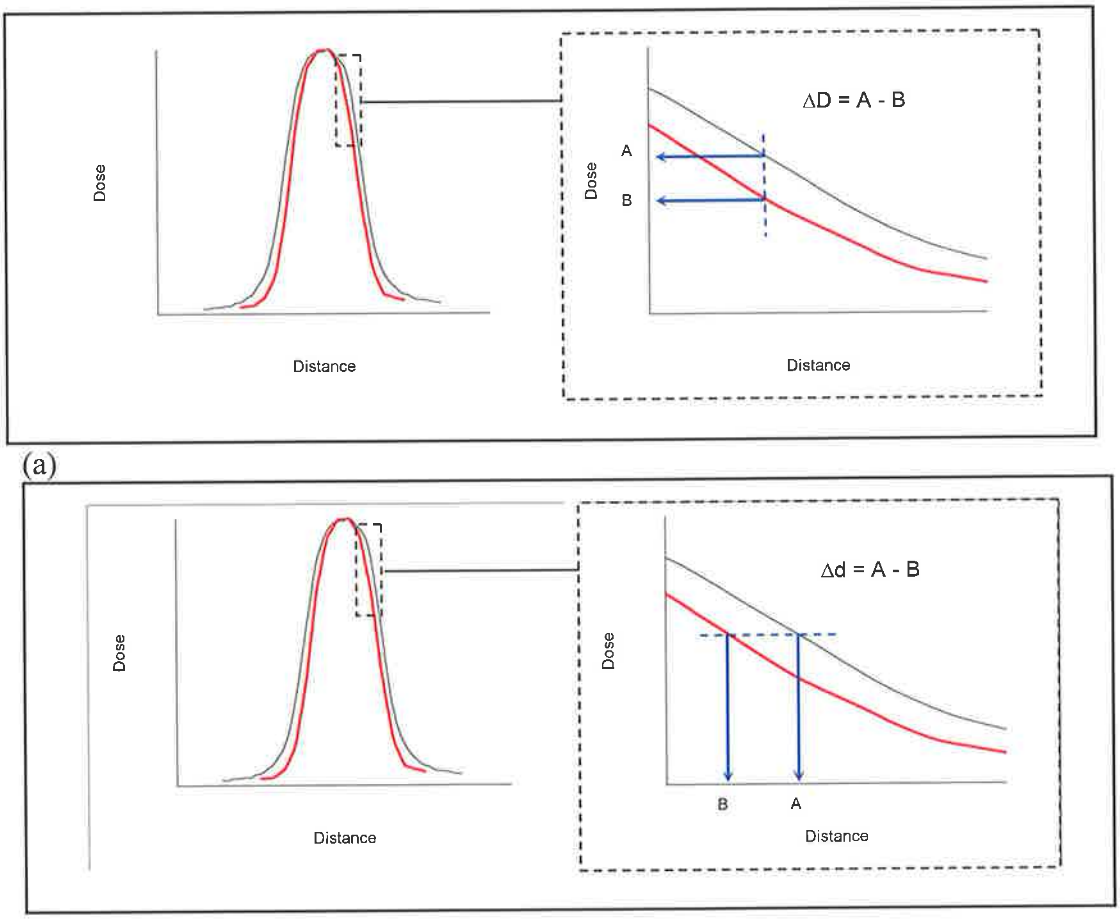

(b)

Figure 3.10: (a) Level of acceptability determined as a percentage dose difference. (b) Level of acceptability determined as a distance to agreement.

3.4.3 Definition of Gamma Index

By combining the dose-difference and DTA methods of dose distribution analysis, Harms et al. provide a software tool that utilizes the criteria outlined by Van Dyk, resulting in a 'quality index', γ (Harms 1998, Low 1998), defined as the magnitude of the minimum vector difference between one dose surface and another (Hugo, 2003).

Combining the two analytical methods eliminates the over sensitivity seen in high- and low-dose gradients for the dose-difference and DTA, respectively (Harms, 1998). Consider the dose D_m, at a point r_m, positioned on a measured dose distribution (Figure 3.11). A dose limit for acceptability ΔD_m, and a spatial limit for acceptability Δd_m is defined, where the dose tolerance is expressed as a percentage of the dose on central axis at the reference depth of 100 mm. The depth of 100 mm is chosen over the normalisation depth of depth of dose maximum as it closely represents the clinical situation (Chappell, 2000). The spatial tolerance, Δd_m, is expressed in millimetres and reflects assessment of experimental error and clinical importance (Chappell, 2000).

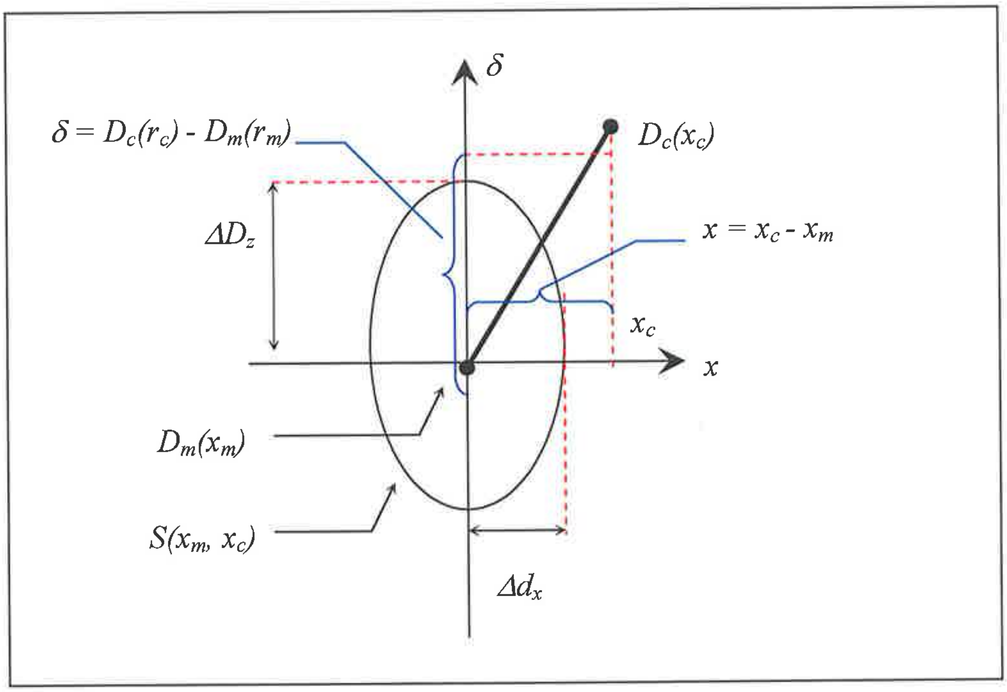

Figure 3.11: One-dimensional representation of the dose distribution evaluation criteria using both DTA and dose difference checks.

Likewise, consider a dose D_c, at a point r_c, positioned on a calculated dose distribution (Figure 3.11). Low *et al.* state that an ellipsoid can be selected as the surface that characterizes the acceptance criterion (Low, 1998). Therefore, the surface representing a one-dimensional ellipsoid in the xz-plane, that encloses the x-axis with a radius of Δd_m, and the z-axis with a radius of ΔD_m, is given by:

$$1=\sqrt{\frac{d(x_m,x_c)^2}{\Delta d_m^2}+\frac{\delta(x_m,x_c)^2}{\Delta D_m^2}} \tag{3.8}$$

where the d and δ parameters are the distance and dose differences between points x_m and x_c respectively.

$$d(x_m,x_c)=x_c-x_m \tag{3.9}$$

and

$$\delta(x_m,x_c)=D_c(x_c)-D_m(x_m) \tag{3.10}$$

Equation 3.8 is a one-dimensional representation of the surface area of the ellipsoid shown in Figure 3.11, and represents the stated acceptance criteria for two dose distributions. For a two-dimensional representation (Figure 3.12) the x- and y-axis coordinates represent the vector point r_c of the calculated dose distribution D_c relative to the measured distribution D_m (Low, 1998).

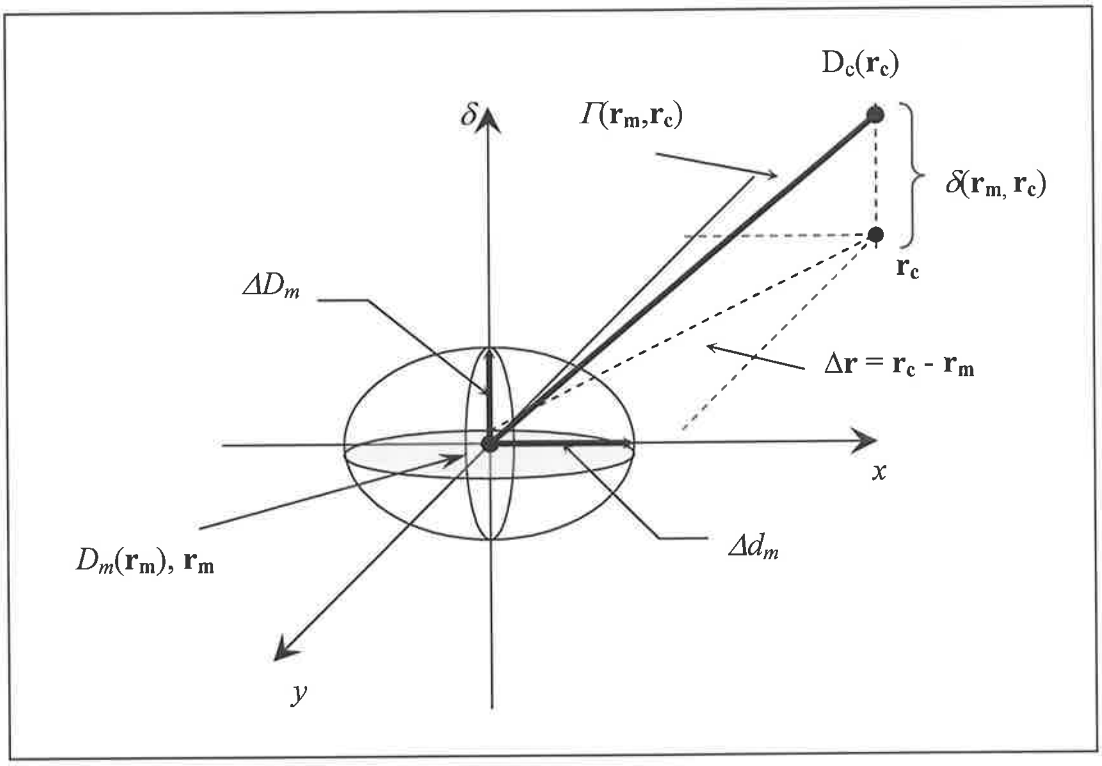

Figure 3.12: Two-dimensional representation of the dose distribution evaluation criteria using both DTA and dose difference checks.

From Figure 3.12 it is shown that incorporating the y-axis the new distance to agreement criteria term Δr is obtained, and from Pythagorean Theorem it is shown to be equal to,

$$\Delta r = \left|\mathbf{r}_c - \mathbf{r}_m\right| = (x_c - x_m)^2 + (y_c - y_m)^2 \tag{3.11}$$

and the new dose difference criteria at point r_m has the form:

$$\delta(\mathbf{r}_c, \mathbf{r}_m) = D_c(\mathbf{r}_c) - D_m(\mathbf{r}_m) \tag{3.12}$$

Substitution of equations 3.11 and 3.12 into equation 3.8, results in the equation for the surface area of a two-dimensional ellipsoid represented in Figure 3.12.

$$S(\mathbf{r}_m,\mathbf{r}_c)=\sqrt{\frac{\Delta r^2(\mathbf{r}_m,\mathbf{r}_c)}{\Delta d_m^2}+\frac{\delta^2(\mathbf{r}_m,\mathbf{r}_c)}{\Delta D_m^2}}=1 \tag{3.13}$$

We now have an expression for an ellipsoid that covers the stated acceptance criteria for two-dimensions, where the right–hand side of equation 3.13 is termed the γ index, and is expressed in the formulae:

$$\gamma(\mathbf{r}_m)=\min\{S(\mathbf{r}_m,\mathbf{r}_c)\} \tag{3.14}$$

γ is thus defined as the minimum distance located between the dose point $D_m(r_m)$ and that found on the comparison data set $D_c(r_c)$.

3.4.4 Pinnacle^3 scripts for profile data extraction

Two scripts (Figure 3.13) obtained from Pinnacle technical support where used to export measured and computed files for a profile shown in the 'Detail' window within the Pinnacle 'Photon Physics Tool'. The scripts are located in the Pinnacle directory /usr/local/adacnew/PinnacleSiteData/Scripts. The exported files are written to the destination directory /rtpx/Physics/600CD as an ASCII file.

```
MachineList.Current.PhotonEnergyList.Current.PhysicsData.MeasureGeometryList.Mark3.CompareList.Mark3.MeasuredProfile.Curve.WriteToFile="PrX015.msd";

MachineList.Current.PhotonEnergyList.Current.PhysicsData.MeasureGeometryList.Mark3.CompareList.Mark3.ComputedProfile.Curve.WriteToFile="PrX015.cpd";
```

Figure 3.13: Pinnacle scripts used for the extraction of computed and measured profile data from within the Pinnacle 'Physics Photon Tool'.

Files are then exported into in-house software package ‘Gamma” written in Visual Basic and run in the Excel environment (Pracy, 2001). ‘Gamma’ processes a series of measured and computed profiles from Pinnacle generating a set of graphs and saving worksheets files showing how well the measured and computed profiles agree (Pracy, 2001).

Files were assumed to be named according to the following convention:

File name *aabbsd* where *aa* is the x-collimator size in centimetres (X< 10 is coded as "0x"), *bb* is the y-collimator size in centimetres (i.e. "1" is coded as "01"), s is the scan direction, *z* is the depth dose, x="x", y="y", *d* is the depth (for photons 1=>5 cm, 2=>10 cm, 4=>20 cm (Pracy, 2001).

Chapter 4

Comparison of the Pinnacle^3 planning system with measurement

4.1 Introduction

The Pinnacle planning system calculates dose distributions within the patient employing a model-based algorithm. Through the adjustment of model parameters the radiation emanating from the Linear Accelerator is accurately characterized through finding the optimal association between measured and calculated beam data. This chapter focuses on the comparison between Pinnacle generated outputs and those measured.

4.2 Small field data collection

Small fields play a vital part in IMRT. Multiple small segments combined provide an overall dose fluence that enables excellent tumour coverage with dose escalation whilst sparing critical structures. With the implementation of IMRT, the investigation of the planning system accuracy is crucial with regard to small beam delivery.

4.2.1 Method

The measured data requirement for an IMRT investigation includes depth dose and profile measurements for field sizes less than 4x4 cm^2. The data measured for this investigation and entered into Pinnacle for beam modelling included depth doses and profiles for field sizes 1x1 cm^2, 1.5x1.5 cm^2, 2x2 cm^2, 3x3 cm^2, and 4x4 cm^2.

Small field data was measured using the waterproof type 31006 PinPoint thimble chamber from PTW, positioned horizontally in a 50x50cm^2 Scanditronix water tank, and controlled by the RFA*plus* version 5.3 beam data acquisition software. A collecting potential of –400 V was applied to the ion chamber, and a measurement step size of 1 mm was used to provide an adequate number of points within the small fields. In conjunction with the PinPoint ion chamber, the RFD type Scanditronix reference diode detector with a 2 mm active diameter and 0.06 mm^3 active volume was employed. The reference diode required accurate placement within the field to eliminate possible beam perturbation. This was especially critical with the 1x1 cm^2 field size. All profiles collected for entry into Pinnacle were performed with the water surface at isocenter and chamber depths of d_{max}, 5 cm, 10 cm, and 20 cm. All measurements extended more than 2 cm from the field boundary. Only data measured at 5 cm, 10 cm, and 20 cm is discussed in this investigation as all other measurements performed are at these depths.

Special care was taken with the tank set-up to ensure confidence that the chamber was centred perfectly within the field. As scan batch files were used to collect profiles, centring scans were performed prior to actual measurements to assess the chamber centring at all depths as well as the positioning of the reference diode. Chamber shifts and tank levelling were applied until any chamber drift with depth was eliminated.

The small data collected for the Pinnacle model was added to the machine file for the 600CD previously modelled. All scans were converted to a simple ASCII format and imported into Pinnacle via floppy disc. Measured and Pinnacle computed depth doses and profiles were then exported using the scripts outlined in Chapter 3.4.4 and compared using the Gamma Index.

4.2.2 Results and discussion

Figure 4.1 (a) shows measured percent depth dose curves for field sizes 1x1 cm^2, 1.5x1.5 cm^2, 2x2 cm^2, 3x3 cm^2, and 4x4 cm^2 defined by the secondary collimators and at an SSD of 100 cm. All curves have been normalised to their d_{max} value. Figure 4.1 (b) shows the depth dose curves in Figure 4.1 (a) between depths 15 cm and 26 cm, to highlight the dose increase seen with an increasing field size, resulting from a higher scattered dose due to the higher area of medium exposed.

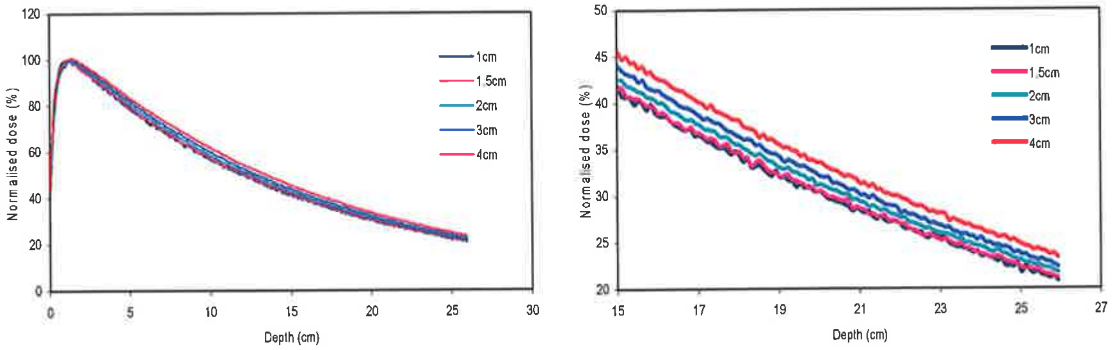

(a) (b)

Figure 4.1: (a) Depth dose curves for field sizes 1x1 cm^2, 1.5x1.5 cm^2, 2x2 cm^2, 3x3 cm^2, 4x4 cm^2 defined by fixed jaws and measured with PinPoint ion chamber (b) Expanded depth dose curve from 15cm onwards showing the increase in dose at depth with increasing field size.

Half beam profiles measured at 5 cm deep are displayed in Figure 4.2. The complete set of profiles for all depths with calculated γ are shown in Appendix A. Figure 4.2 (a) and (b) show the measured (msd) and Pinnacle computed (cpd) dose profiles for field sizes 1x1 cm^2, 1.5x1.5 cm^2, 2x2 cm^2, 3x3 cm^2, and 4x4 cm^2. All profiles are normalised to the centre of the field. Good agreement is seen between the measured and computed profiles with measured dose values tending to slightly exceed that of the calculated doses approximately above the 50% dose point for scans in the cross-plane orientation. Below the 50% dose point the calculated doses slightly exceeds the measured doses. This indicates a much sharper penumbra is obtained with ion chamber measurement over the Pinnacle model. It would be thought, due to the lower spatial resolution of the PinPoint chamber, the computed profiles would have a shaper penumbra and may indicate slight inaccuracies in modelling the source and extra-focal radiation (Williams, 2006). At 5cm depth, in-plane profiles show a similar result in the penumbra region to that obtained for cross-plane scans. However, beyond 5 cm the in-plane Pinnacle computed profiles seem to show the expected sharper penumbra over measurement. Overall the differences from expected can be attributed to both chamber spatial resolution and modelling inaccuracies. Interestingly, Sohn *et al.* has shown similar results modelling small fields using the Corvus treatment planning system (Sohn, 2003). The profile roundness seen for 1x1 cm^2, 1.5x1.5 cm^2, 2x2 cm^2 fields can be attributed to the lack of electron equilibrium resulting from the small field sizes.

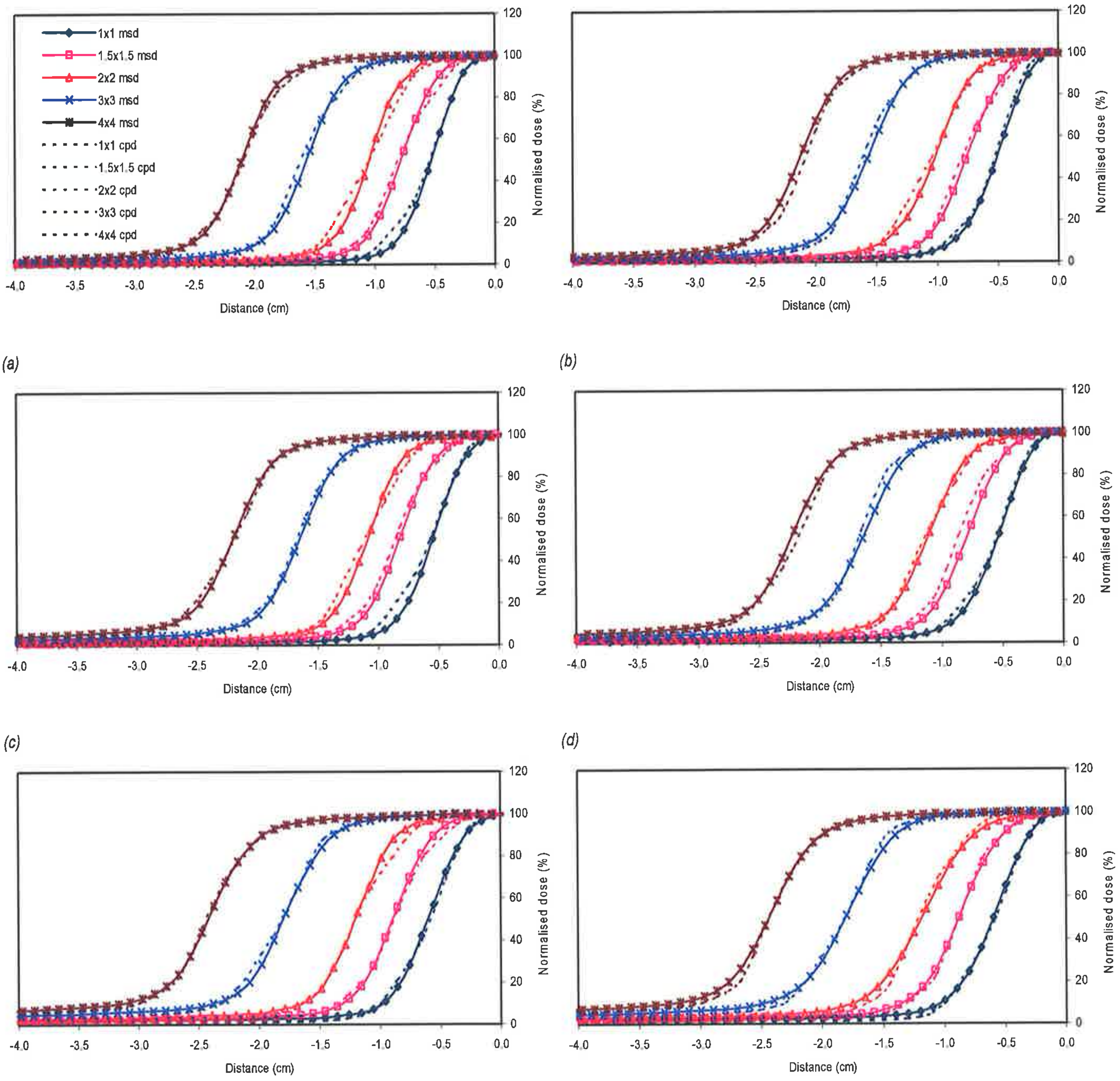

(a) *(b)*

(c) *(d)*

(e) *(f)*

Figure 4.2: PinPoint ion chamber measured and Pinnacle computed half profiles (a) cross-plane 5 cm deep (b) in-plane 5 cm deep (c) cross-plane 10 cm deep (d) in-plane 10 cm deep (e) cross-plane 20 cm deep (f) in-plane 20 cm deep. (The legend in (a) is the same for all plots in this series).

The γ plots shown in Appendix A for comparison of Pinnacle modelled and measured profiles show very good agreement over all field sizes and depths. Calculated γ values for each comparison used a dose tolerance of 2% and a distance tolerance of 2 mm. Table 4.1 summarizes the results obtained, showing the percentage of $\gamma < 1$ one. Results show 100% $\gamma < 1$ for depth doses and profiles at 5 cm and 10 cm. Profiles at 20 cm depth do show γ values greater than one, but does not seem to show a trend with increasing field size, as shown in Figure 4.3.

Field Size (cm^2)	Scan plane	Profiles at depth (cm)			PDD
		5	10	20	
1x1	Cross	100.0%	100.0%	100.0%	100.0%
	In	100.0%	100.0%	97.3%	
1.5x1.5	Cross	100.0%	100.0%	100.0%	100.0%
	In	100.0%	100.0%	98.0%	
2x2	Cross	100.0%	100.0%	96.9%	100.0%
	In	100.0%	100.0%	94.7%	
3x3	Cross	100.0%	100.0%	88.6%	100.0%
	In	100.0%	100.0%	87.8%	
4x4	Cross	100.0%	100.0%	94.6%	100.0%
	In	100.0%	100.0%	96.6%	

Table 4.1: % $\gamma < 1$ calculated for comparison between measured and Pinnacle modelled profiles and depth dose for small fields (Distance and Dose tolerance of 2% and 2 mm respectively).

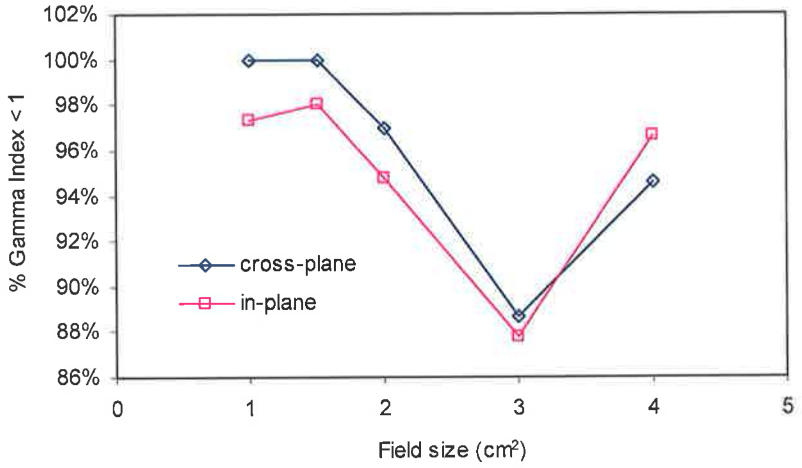

Figure 4.3: % $\gamma < 1$ than one as a function of field size for (a) Cross-plane (b) In-plane.

However, as Figure 4.4 shows, the γ increases significantly outside the field for increasing depth. This can be attributed to over response of the PinPoint ion chamber to the low energy scattered radiation. Figure 4.4 represent γ values for the comparison of Pinnacle calculated and measured profiles for a 4x4 cm^2 field. These results show that for the 4x4 cm^2 field at 20 cm depth, agreement in the primary field is accurate but the outer edges are approaching a fail condition, this is extremely important with regard to critical structures just beyond the field edge. As it has been shown that the PinPoint chamber should not be employed for measuring field sizes greater than 5x5 cm^2 (Martens 2000), these results would seem to support this.

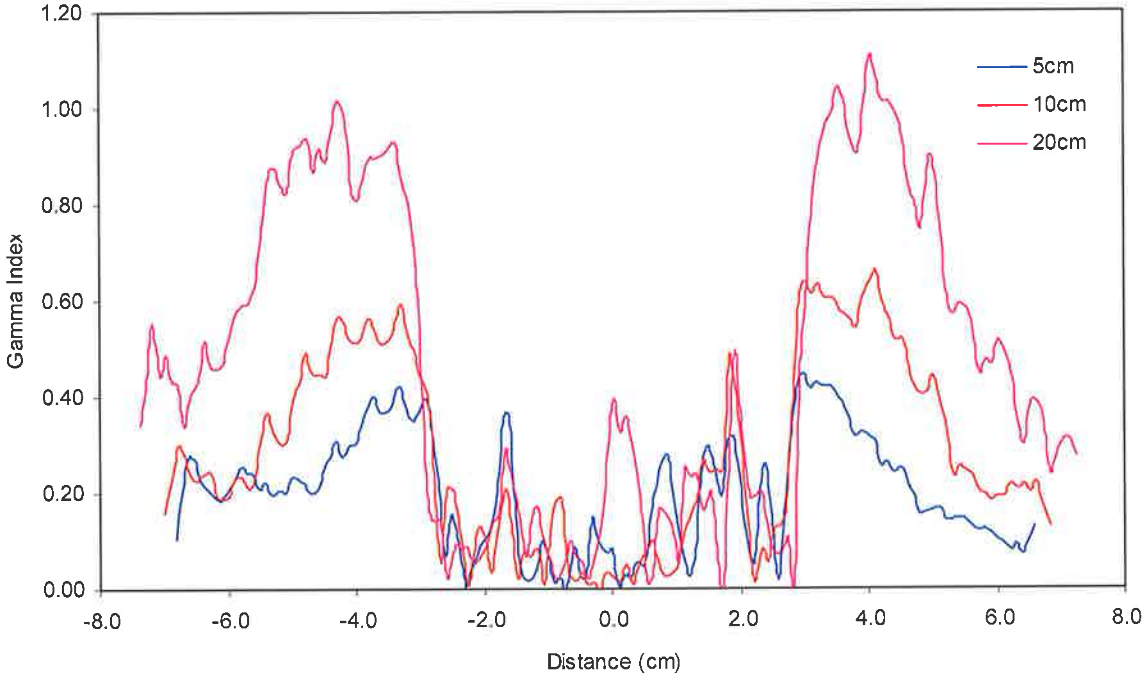

Figure 4.4: γ as a function of distance from CAX for a 4x4 cm^2 field at 5 cm, 10 cm and 20cm.

4.2.3 Conclusion

The results for the small fields modelled in Pinnacle show a good comparison between those measured, with 100% of $\gamma < 1$ for all small fields measured for depths ≤ 10 cm. A depth of 20 cm shows slight movement away for 100% and is attributed to the ion chamber over response to low energy radiation, which increases with depth, and evident in the γ plots showing fail conditions at the profile edges. Slight discrepancies noted for the penumbra edges were attributed to possible inaccuracies in the model; however, these differences are quite small and would not have a significant impact clinically.

4.3 Output factor determination for small MLC fields

When the treatment field size is increased or decreased, and the monitor units kept constant, the dose deposited at a point within the field will also vary. This is due to a change in the scattering conditions in both the Linac head and the medium being irradiated. As the field size increases the contribution of both Linac head scatter and medium scatter increases due to a greater amount of exposure of the head components, as well as a greater area of medium. Figure 4.5 shows this effect taken from data generated from the Pinnacle planning system at varying depths in water.

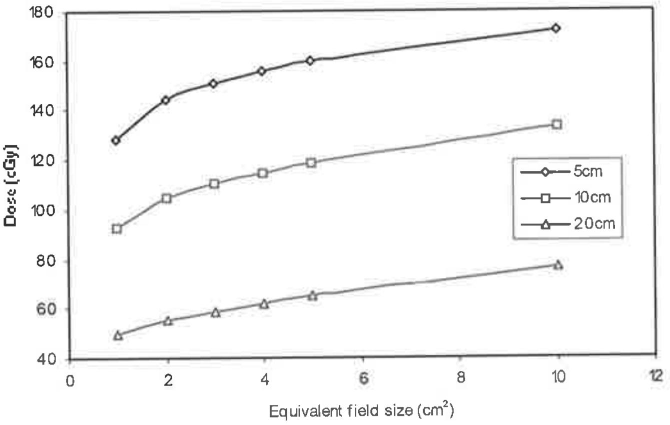

Figure 4.5: Dose at depth as a function of increasing equivalent field size for 6 MV x-rays.

As the dose varies with field size, it is not a result of a change in the machine output, but a change in the scatter conditions associated with a varying field size; therefore, Pinnacle applies an output factor correction to account for the changes in scattering conditions. The determination of the output factor is achieved from the ratio of the collected ion chamber signal for a field size *nxn*, $S_{pp}(nxn)$, and the signal collected for a reference field size, usually 10x10 cm^2, $S_{pp}(10x10)$ positioned at a reference depth.

$$OF_{PP} = \frac{S_{PP}(n \times n)}{S_{PP}(10 \times 10)} \tag{4.1}$$

The measured output factors are then manually entered into Pinnacle, which then employs a lookup table of factors and applies them to the dose calculation where required.

4.3.1 Method

6 MV x-rays for output factor measurements were generated by a Varian Clinac 600C/D. The absolute dose calibration of the 600CD was performed as outlined in the ACPSEM protocol of photon dose calculation (ACPSEM, 1998). Machine output is calibrated to deliver 1 cGy/MU at the depth of maximum dose 1.5 cm for a field size of 10x10 cm^2 at an SSD of 100 cm. Field sizes were shaped by the fixed secondary collimators and by the Millennium 120 leaf MLC. All MLC fields were generated using the MLC text editor within the Pinnacle planning software. Generated MLC files were exported to the treatment machine for exposure. Output factors where determined for the following field sizes, defined by both the fixed secondary jaws and the MLC: 1x1 cm^2, 2x2 cm^2, 3x3 cm^2, 4x4 cm^2, 5x5 cm^2, and 10x10 cm^2. All small field measurements were performed using the waterproof type 31006 PinPoint thimble chamber from PTW, positioned vertically in a 50x50 cm^2 Scanditronix water tank, and controlled by the RFA*plus* version 5.3 beam data acquisition software. A collecting potential of –400 V was applied for all output measurements. To account for possible chamber drift effects, the output for the reference field 5x5 cm^2 was frequently remeasured. The PinPoint chamber displays an over-response to low-energy scattered photons for field sizes greater than 5x5 cm^2 (Martens, 2000), however, this scatter has been shown to not influence output factor measurements for fields of 5x5 cm^2 or smaller (Martens, 2000), therefore in this investigation all output factors have been determined by replacing the reference field size in the denominator of Equation 4.1 to 5x5 cm^2 and multiplying by a factor to correct back to the 10x10 cm^2 field size. Pinnacle requires output factors normalized to a 10x10 cm^2 field Philips (Philips 2001). Therefore, output factors corrected back to a 10x10 cm^2 field and measured using the pinpoint chamber are given by,

$$OF_{PP} = \frac{S_{PP}(n \times n)}{S_{PP}(5 \times 5)} x \frac{OF_{RK}(5 \times 5)}{OF_{RK}(10 \times 10)} \tag{4.2}$$

where, $OF_{RK}(5x5)$ and $OF_{RK}(10x10)$ are the output factors determined by using a type RK 8304 ionization chamber, which is not prone to over-respond to low energy photons for larger field sizes as the smaller PinPoint chamber demonstrates. Output factors were measured at 10 cm water depth and an SSD of 100 cm. A depth of 10cm is the recommendation of Philips (Philips, 2001) and is also a depth of clinical significance and where electron contamination is minimized. Depth of maximum dose, d_{max}, was not used for the measurement depth, as there is uncertainty of absolute dose computation and deviations in measurement at d_{max} (Philips 2001).

As well as measuring output factors for fixed field sizes defined by the secondary collimators, which is required for the Pinnacle model, it is important to characterise the outputs generated from fields defined by the MLC, crucial to determine the accuracy of the Pinnacle planning system with respect to IMRT delivery. PinPoint chamber measurements were repeated for small fields defined by the MLC on central axis, in water at depth 10 cm and 100 cm SSD. Measurements were also performed with the same experimental set-up for small MLC fields with an increasing secondary collimator setting. Fields sizes of 1x1 cm^2, 2x2 cm^2 and 3x3 cm^2 fields had secondary collimator settings up to 15x15 cm^2.

4.3.2 Results and discussion

Martens *et al.* (Martens, 2000) showed discrepancies due to sensitivity changes with depth in water as well as field size (Figure 3.9). Results revealed that for a 10x10 cm^2 field at depths 5 cm, 10 cm, 20 cm in water the sensitivity increase between the PinPoint chamber and a reference 0.125 cm^3 chamber showed approximately 0.5%, 0.9% and 1.5% for the respective depths. Output factors using the PinPoint chamber where measured up to a 5x5 cm^2 field (Figure 4.6). Correcting back to a 10x10 cm^2 reference field showed deviations between corrected and uncorrected output factors of 1.0%, 0.95% and 1.48% for depths 5 cm, 10 cm and 20 cm respectively. The uncorrected output factors were determined from the ratio of chamber signal collected for field size *n*x*n* cm^2 and 10x10 cm^2 measured with the PinPoint chamber.

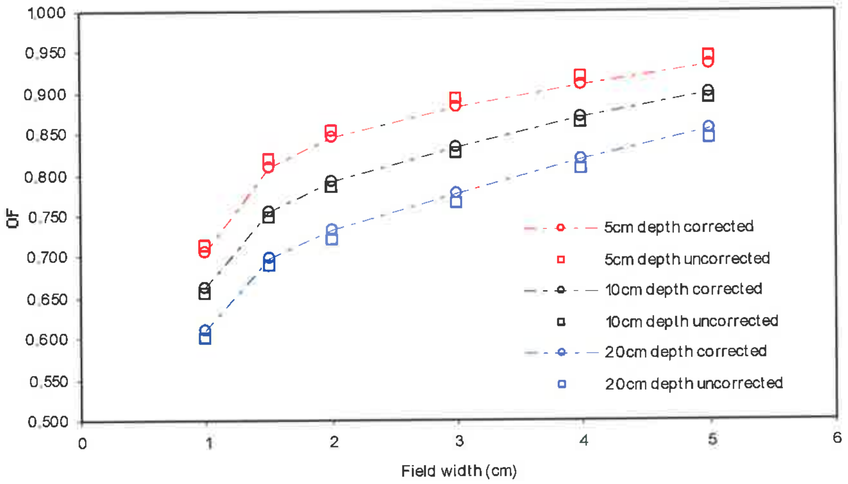

Figure 4.6: 6 MV output factors for the Varian 600CD Linac at 100 cm SSD corrected back to a 10x10 cm^2 reference field plotted against uncorrected output factors.

Output factors measured for fields defined by the MLC and normalised to a 5x5 cm^2 reference are shown in Figure 4.7, and are plotted against output factors for secondary collimator defined fields. The secondary collimators were set to 10x10 cm^2 for the measurement of output factors for MLC fields. As can be seen the difference between output factors increases with a decreasing field size, and up to 12.7% for a 1x1 cm^2 field size. With conventional planning employing the MLC where the output factor is primarily dependant on the secondary collimators, the jaws are set just beyond the furthest most retracted leaf on each bank. This eliminates, to a degree, the overestimation of the collimator scatter factor applied to the MLC field. The large differences seen in Figure 4.7 can be attributed to the differences in the radiation transmission through the leaves, and differencc in the scattering in the air from the linac head. Higher deviations are seen with decreasing MLC field due to increased transmission, resulting also, in a higher scatter component.

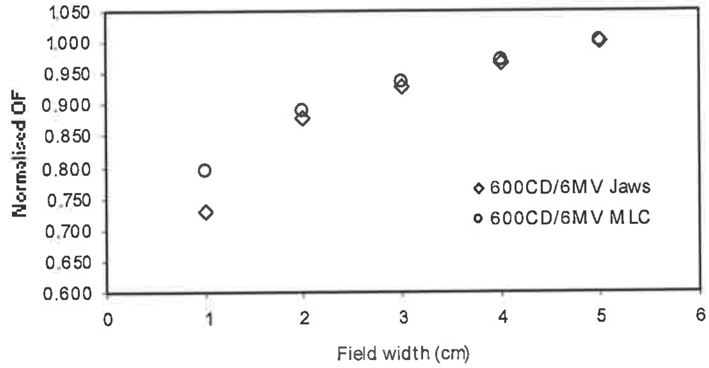

Figure 4.7: 6 MV output factors for Varian 600CD Linac at 100 cm SSD and 10 cm depth in water.

Output factors measured for small fields 1x1 cm^2, 2x2 cm^2, and 3x3 cm^2 with varying secondary collimator settings are shown in Figure 4.8 with results summarised in Table 4.2. The deviation for the dose calculated by Pinnacle at depths 5 cm, 10 cm, and 20 cm for a 1x1 cm^2, 2x2 cm^2, and 3x3 cm^2 is plotted against increasing secondary collimator setting (Figure 4.9). The deviations were determined by calculating the dose for field sizes 1x1 cm^2, 2x2 cm^2, and 3x3 cm^2 defined by the secondary collimator at depths 5 cm, 10 cm, and 20 cm, and with the MLC fully retracted. This calculated dose was then compared to the dose calculated with the MLC used to define the fixed field settings of 1x1 cm^2, 2x2 cm^2, and 3x3 cm^2 with an increasing secondary collimator setting. As can be seen in the plots, the deviation does not show a dependence on depth but does show a significant dependence on secondary collimator setting. This is due to Pinnacle not taking into account the presence of the MLC, and therefore overestimating the collimator scatter, resulting in a lower delivered dose as the MUs needed are underestimated. Phantom scatter is taken into account, as this factor is determined from the projected field at the depth of interest, determined as the percentage of the secondary collimator blocked due to the MLC. The overestimate in collimator scatter however, is significant, especially when the secondary collimator is much greater than the set MLC field. Beyond 50% blocked of the field defined by the secondary collimators deviations are greater than 2% and greatest for a 99% blocked 20x20 cm^2 by a 2x2 cm^2 field and 97.8% blocked 20x20 cm^2 by a 3x3 cm^2 field, with approximately –4.5% and -4.2% respectively. The results for the 1x1cm^2 field size are alarming, with deviations ranging from approximately –10% for 75% field blocked to –14.4% for 99.8% blocked, and is most probably a result of the lack of charged particle equilibrium and volume averaging effects of the PinPoint chamber. Stasi *et al.* (Stasi, 2004) and Martens *et al.* (Martens, 2000) have also shown the PTW PinPoint chamber suffers from these effects below a 2x2 cm^2 field size and recommend not employing the PinPoint chamber for measurements below 2x2 cm^2. In fact Stasti *et al.* (Stasi, 2002) has shown the output factor for the PTW PinPoint chamber is 12% lower than that determined by a Diamond detector.

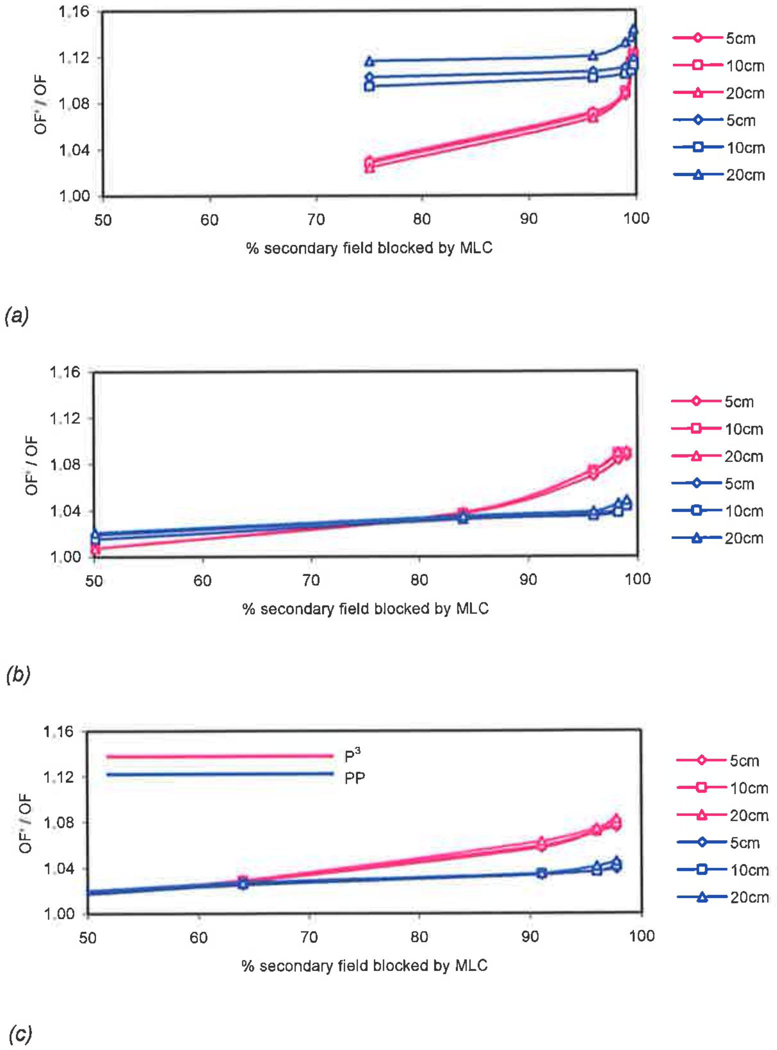

Figure 4.8: The ratio of the output factor for MLC segments (a) 1x1 cm^2 (b) 2x2 cm^2 (c) 3x3 cm^2 with a varying secondary collimator setting (OF'), and the output factor for fixed secondary collimator setting of (a) 1x1 cm^2 (d) 2x2 cm^2 (g) 3x3 cm^2 (OF), plotted as a function of the percentage of the secondary collimators blocked by the MLC segment.

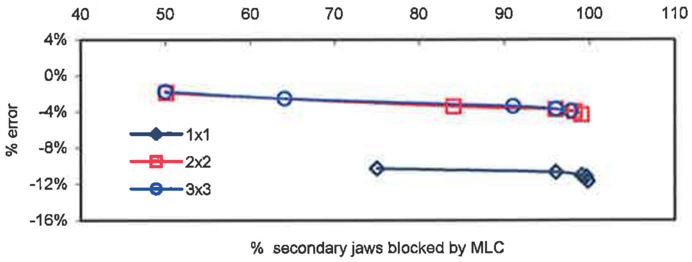

(a)

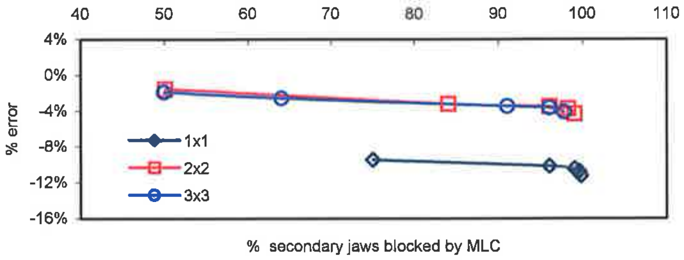

(b)

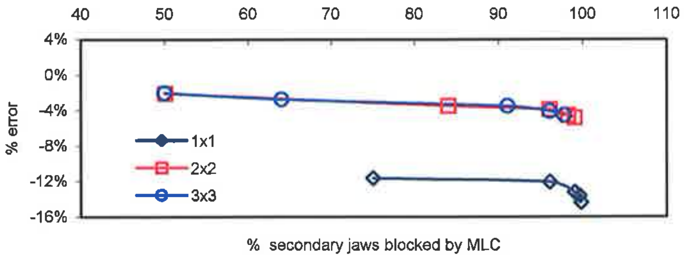

(c)

Figure 4.9: % deviations between the Pinnacle computed outputs and the ion chamber measured outputs for small segments with varying fixed secondary jaw positions at depths (a) 5 cm depth (b) 10 cm depth (c) 20 cm depth.

Secondary Jaws (cm^2)	MLC (cm^2)	% Blocked	Output factor (OF_{PP}) defined as the ion chamber reading normalised to the reading for a 1x1cm^2 field defined by secondary collimators			Output factor (OF_{P3}) defined as the P^3 calculated dose normalised to the P^3 dose for a 1x1cm^2 field defined by secondary collimators			% error between OF_{P3} and OF_{PP}		
			Depth (cm)								
			5	10	20	5	10	20	5	10	20
1x1	retracted	0.0	1.000	1.000	1.000	1.000	1.000	1.000	-	-	-
1x1	1x1	0.0	0.998	0.993	1.001	1.000	1.000	1.000	0.2%	0.7%	-0.1%
2x2		75.0	1.103	1.095	1.116	1.030	1.028	1.024	-10.3%	-9.5%	-11.6%
5x5		96.0	1.107	1.102	1.121	1.072	1.070	1.067	-10.7%	-10.2%	-12.1%
10x10		99.0	1.111	1.105	1.132	1.086	1.090	1.089	-11.1%	-10.5%	-13.2%
15x15		99.6	1.112	1.107	1.136	1.110	1.115	1.117	-11.2%	-10.7%	-13.6%
20x20		99.8	1.117	1.112	1.144	1.123	1.122	1.121	-11.7%	-11.2%	-14.4%

(a)

Secondary Jaws (cm^2)	MLC (cm^2)	% Blocked	Output factor (OF_{PP}) defined as the ion chamber reading normalised to the reading for a 2x2cm^2 field defined by secondary collimators			Output factor (OF_{P3}) defined as the P^3 calculated dose normalised to the P^3 dose for a 2x2cm^2 field defined by secondary collimators			% error between OF_{P3} and OF_{PP}		
			Depth (cm)								
			5	10	20	5	10	20	5	10	20
2x2	retracted	0.0	1.000	1.000	1.000	1.000	1.000	1.000	-	-	-
2x2	2x2	0.0	1.000	0.995	0.998	1.000	1.000	1.000	0.0%	0.5%	0.2%
2.83x2.83		50.1	1.019	1.015	1.021	1.007	1.007	1.007	-1.9%	-1.5%	-2.1%
5x5		84.0	1.034	1.032	1.035	1.037	1.038	1.038	-3.4%	-3.2%	-3.5%
10x10		96.0	1.037	1.035	1.039	1.069	1.074	1.074	-3.7%	-3.5%	-3.9%
15x15		98.2	1.040	1.038	1.045	1.083	1.089	1.090	-4.0%	-3.8%	-4.5%
20x20		99.0	1.043	1.043	1.048	1.086	1.089	1.091	-4.3%	-4.3%	-4.8%

(b)

Secondary Jaws (cm^2)	MLC (cm^2)	% Blocked	Output factor (OF_{PP}) defined as the ion chamber reading normalised to the reading for a 3x3cm^2 field defined by secondary collimators			Output factor (OF_{P3}) defined as the P^3 calculated dose normalised to the P^3 dose for a 3x3cm^2 field defined by secondary collimators			% error between OF_{P3} and OF_{PP}		
			Depth (cm)								
			5	10	20	5	10	20	5	10	20
3x3	retracted	0.0	1.000	1.000	1.000	1.000	1.000	1.000	-	-	-
3x3	3x3	0.0	0.999	0.997	0.997	1.000	1.000	1.000	0.1%	0.3%	0.3%
4.24x4.24		49.9	1.017	1.019	1.020	1.019	1.020	1.020	-1.7%	-1.9%	-2.0%
5x5		64.0	1.025	1.026	1.027	1.028	1.029	1.029	-2.5%	-2.6%	-2.7%
10x10		91.0	1.034	1.035	1.035	1.057	1.059	1.063	-3.4%	-3.5%	-3.5%
15x15		96.0	1.037	1.037	1.041	1.071	1.072	1.074	-3.7%	-3.7%	-4.1%
20x20		97.8	1.039	1.041	1.045	1.075	1.078	1.082	-3.9%	-4.1%	-4.5%

(c)

Table 4.2: Comparison of PinPoint ion chamber and Pinnacle output factors for small segments defined by the MLC and an increasing secondary collimator setting. Fixed MLC segment (a) 1x1 cm^2 (b) 2x2 cm^2 (c) 3x3 cm^2.

4.3.3 Conclusion

The differences between the output factors determined for fields defined by secondary collimators and those defined by the MLC with secondary collimators set to 10x10 cm^2 have been shown to increase with a decreasing field size, and as high as 12.7% for a 1x1 cm^2 field defined by the MLC. The assumption drawn from this is the high difference seen with decreasing field size is the higher transmission of radiation through the leaves as more leaves are exposed with a decreasing field size, as well as the differing scatter conditions as a result of fields defined by the MLC.

As a larger secondary collimator setting with a small field defined by the MLC is generally common in IMRT plans, results showed that for output factors measured and calculated for this condition there was no real trend with an increasing depth, but a significant dependence on the actual secondary collimator setting was shown. For a 2x2 cm^2 field it was shown there was a 2% deviation for secondary collimators blocked by >50% and for >99% blocked the deviation increased beyond 4%. These results are very similar with the MLC field set to 3x3 cm^2. The 1x1 cm^2 field did however show a large deviation with 10% and 12.5% differences calculated for 75% and 99.8% blocked secondary collimators respectively. The conclusion made regarding the large difference found with the 1x1 cm^2 field is the lack of charged particle equilibrium for such a small field and volume averaging effect associated with the small volume ion chamber.

4.4 Off-axis Segments defined by the multi-leaf collimator with varying secondary collimators

For IMRT treatment many small segments are combined to provide an optimal dose fluence. These small segments are generally not located on the CAX, and are enclosed within an area defined by the secondary collimators, generally much larger than individual segments. The accuracy in how Pinnacle calculates dose in this situation is vital in understanding any limitations in the planning system as well as the delivery system.

4.4.1 Method

Small MLC segment profiles off-axis with varying secondary collimators were measured using the waterproof type 31006 PinPoint thimble chamber from PTW, positioned horizontally in a 50x50 cm^2 Scanditronix water tank, and controlled by the RFA*plus* version 5.3 beam data acquisition software. A collecting potential of –400 V was applied to the ion chamber, and a measurement step size of 1mm was used to provide an adequate number of points within the small fields. In conjunction with the PinPoint ion chamber, the RFD type Scanditronix reference diode detector with a 2 mm active diameter and 0.06 mm^3 active volume was employed. The reference diode required accurate placement within the field to eliminate possible beam perturbation. This was especially critical with the 1x1 cm^2 field size. All profiles collected for comparison with Pinnacle generated profiles were performed with the water surface at isocenter and chamber depths of 5 cm, 10 cm, and 20 cm.

Special care was taken with the tank set-up to ensure confidence that the chamber was centred perfectly within the field. The beam divergence seen with collecting profiles off-axis at varying depths posed a problem, as batch files for data collection could not be used due to limitations of the beam data acquisition system. This meant all profiles collected required individual centring and scanning to assure accurate measurement. The reference diode also required repositioning for each segment. Field centring of the PinPoint chamber required an initial rough scan to find the field centre, then if required the chamber was shifted. Tank levelling was also crucial as the water level was set to isocentre at the CAX and any unevenness could result in a significant SSD shift for points off-axis.

Figure 4.10 displays schematics for the set-ups used to assess small off-axis segments enclosed by varying secondary collimator settings. Segment sizes of 1x1 cm^2, 2x2 cm^2, and 3x3 cm^2 were positioned in the top left quadrant of the area defined by the secondary collimators and in-plane and cross-plane scans were performed for each segment. For all scans the collimators were set to 0°, and the chamber positioned identically for in-plane and cross-plan scans to assure the same active volume for both scan directions. This required measuring in-plane and cross-plane scans independently.

As well as measuring profiles, point measurements were performed for each segment with the chamber positioned at the centre of each segment. Point measurements were measured at the same time as the profile scan was performed for a certain segment to assure the correct centring of the chamber within the field. The measurements were performed for each segment and the average found. All point measurements were enclosed by a set of reference measurements at the same depth for a 10x10 cm^2 field defined by the MLC. This enabled any chamber drift to be observed.

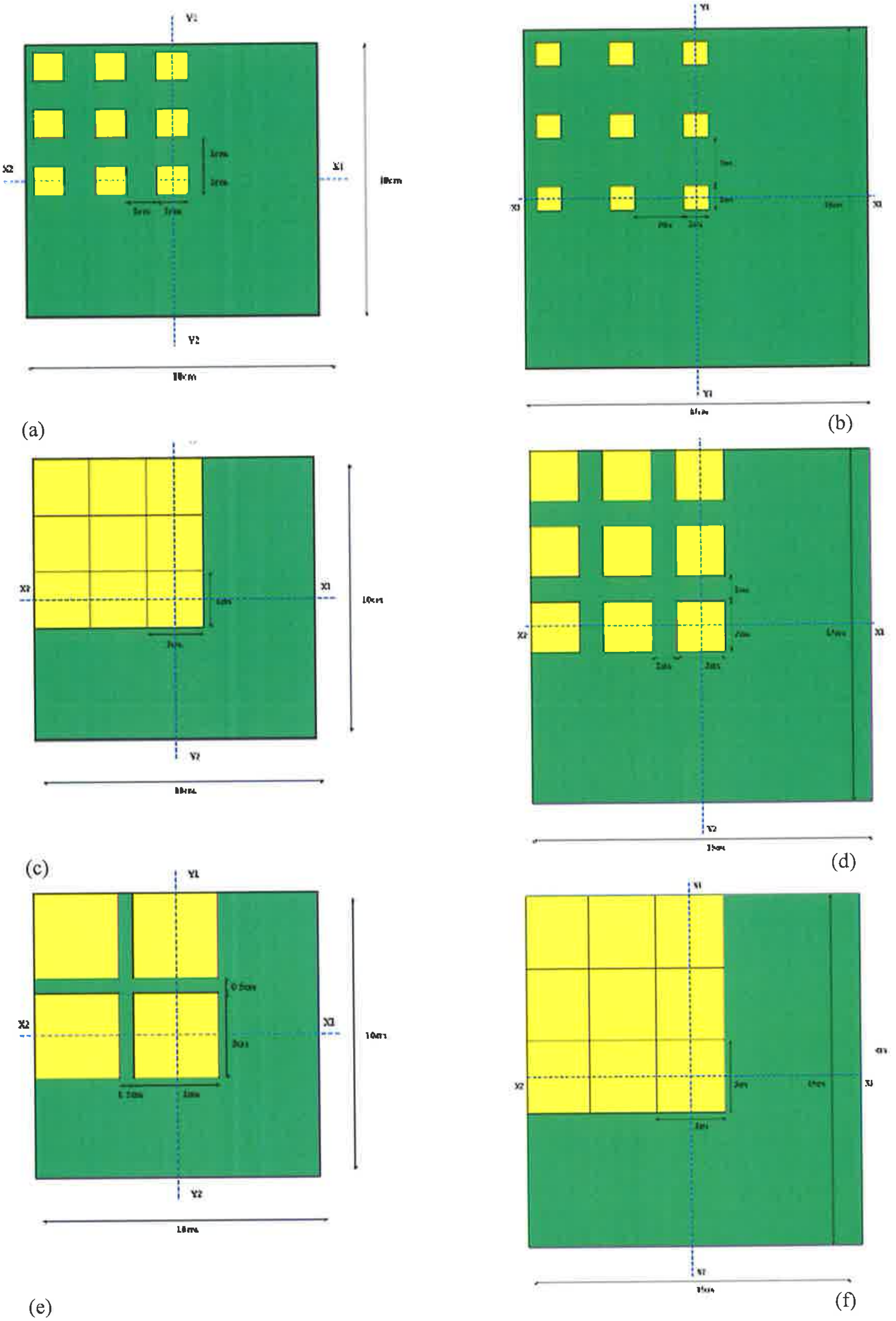

Figure 4.10: Schematics of small MLC segments delivered off-axis (a) 1x1 cm^2 10x10 cm^2 (b) 1x1 cm^2 15x15 cm^2 (c) 2x2 cm^2 10x10 cm^2 (d) 2x2 cm^2 15x15 cm^2 (e) 3x3 cm^2 10x10 cm^2 (f) 3x3 cm^2 15x15 cm^2. Green indicates the area defined by the secondary collimator and yellow defines the MLC segments. Segments are labelled as *a* → *i* for 9 segments and *a* → *d* for 4 segments starting at the top most segment and moving towards the segment at CAX, as displayed in (f).

4.4.2 Results and discussion

Figure 4.11 displays a film exposed to the set-up shown in Figure 4.10 (a). Kodak X-Omat V film was placed 5 cm under a solid water phantom, with the phantom surface set to isocentre. 70 MU were delivered for each individually delivered segment. The film was processed in a Kodak automatic processor. The dark dose band on the far right of the film is the MLC junction of opposing leaf banks, and clearly evident on the film is the leakage radiation between the leaves.

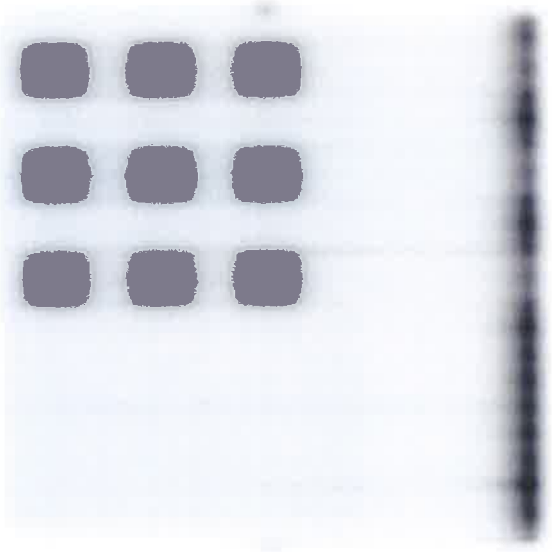

Figure 4.11: Film exposure of 9 1x1 cm^2 MLC segments delivered statically. All segments are located in the upper left quadrant of a 10x10 cm^2 field defined by the fixed jaws.

Cross-plane and in-plane scans at depths 5 cm, 10 cm, and 20 cm were performed for each segment and secondary collimator setting as defined in the schematics outlined in Figure 4.10. Six scans were performed for each segment resulting in a total of 294 scans. It is unrealistic to display that number of scans; therefore, a sample of these scans is displayed in Figure 4.12, with the results for all scans tabulated in Table 4.3.

The small segments investigated have been labelled *a* → *i* for set-ups containing nine segments as shown in Figure 4.10. Figure 4.10 (e) contains only four segments due to limitations on fitting 3x3 cm^2 segments within a single 5x5 cm^2 quadrant of a 10x10

cm^2 secondary collimator setting, therefore, in this situation segments have been labelled $a \rightarrow d$.

Figure 4.12 displays example comparisons for Pinnacle computed and measured profiles for 1x1 cm^2 segments with secondary collimators set to 10x10 cm^2. Figures 4.12 (a) and (c) are cross-plane profiles through segment a and i respectively, and Figures 4.12 (b) and (d) are in-plane profiles through segment a and i respectively. The γ for each profile comparison has been generated and results show an excellent match for the in-plane scans with 100% $\gamma < 1$ with distance and dose tolerances of 2 mm and 2% respectively. Cross-plane results are not as good as would be expected as a result of the rounded leaf end design of the leaves, so we expect a broadening of the penumbra due to the transmitted radiation through the leaf ends. Values of $\gamma < 1$ are 98% and 70.6% for segment a and i respectively. Looking at the profiles in Figure 4.12 (a) and (d) it would seem to not indicate such a large difference, however, by zooming in on the profiles that are closer to the field defined by the secondary collimators (Figure 4.13), it is shown that the penumbra is reduce and if the γ distance tolerance is reduced to 1 mm the percent $\gamma < 1$ becomes more comparable, at 66.7% and 56.9% for segments a and i respectively. This is a probable indicator that for the 1x1cm^2 field size a distance tolerance of 2 mm is too large.

MLC segment size (cm^2)	Secondary collimators (cm^2)	Depth (cm)					
		5		10		20	
		Cross-plane	In-plane	Cross-plane	In-plane	Cross-plane	In-plane
1x1	10x10	79.1%	99.6%	80.6%	98.1%	62.1%	90.4%
	15x15	75.5%	100.0%	59.3%	99.6%	59.3%	91.6%
2x2	10x10	77.1%	98.5%	70.8%	93.2%	67.9%	81.0%
	15x15	79.1%	99.1%	75.3%	94.8%	66.6%	83.0%
3x3	10x10	81.8%	99.3%	75.5%	88.3%	63.7%	74.1%
	15x15	81.7%	97.8%	76.7%	90.3%	72.5%	79.5%

Table 4.3: Percent $\gamma < 1$ for the comparison of Pinnacle and measured profiles for small MLC defined segments off-axis (Distance and Dose tolerance of 2% and 2 mm respectively).

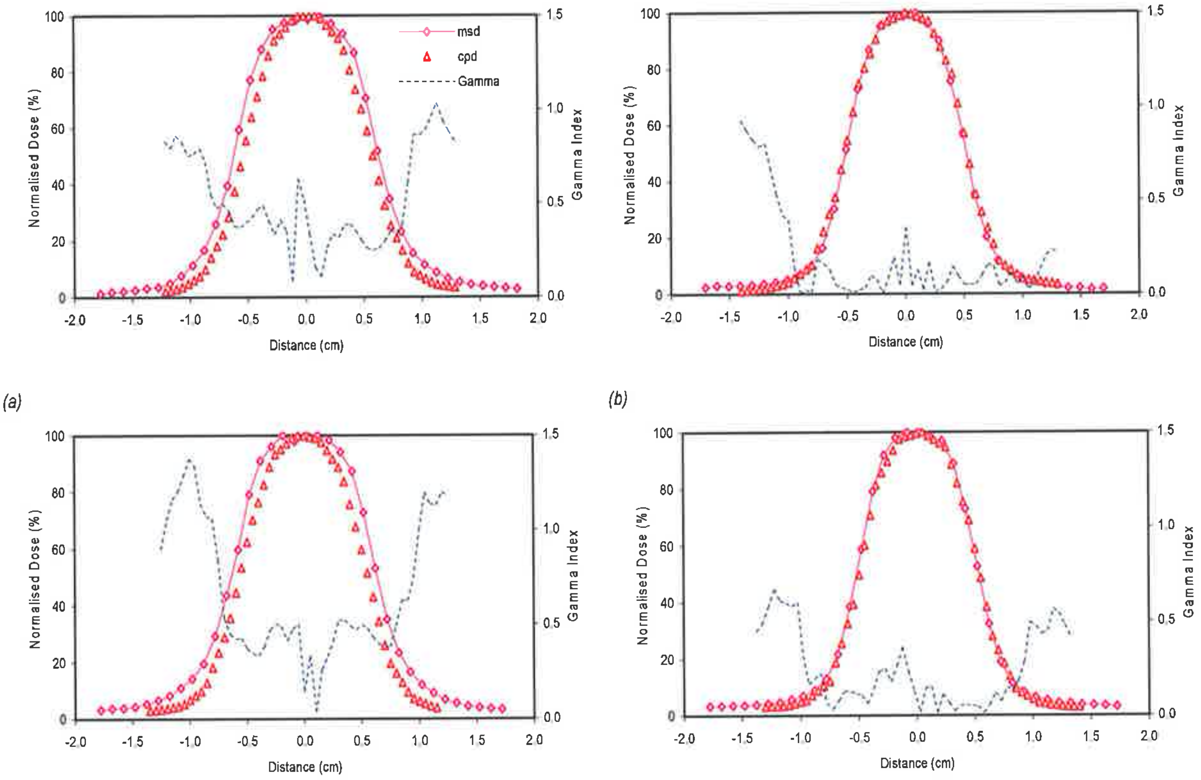

(a) (b) (c) (d)

Figure 4.12: Ion chamber (msd) and Pinnacle (cpd) profile comparisons with γ for 1x1 cm^2 segments with secondary collimators set to 10x10 cm^2 at 5 cm depth for (a) Cross-plane segment a (b) In-plane segment a (c) Cross-plane segment *i* (d) In-plane segment *i* (The legend in (a) is the same for all plots in this series).

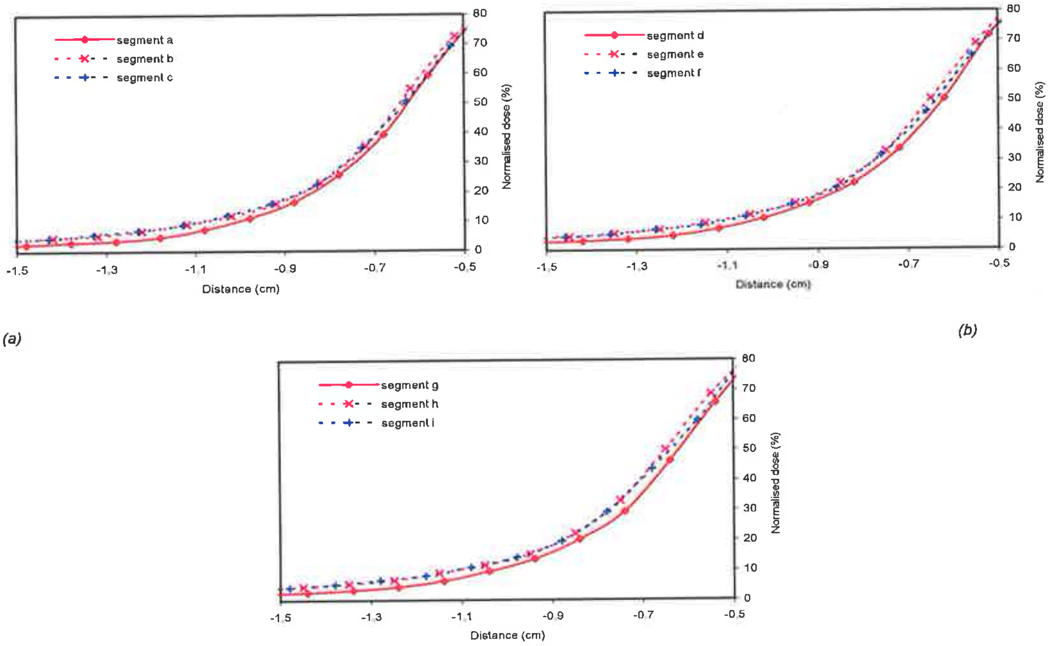

(a)

(b)

(c)

Figure 4.13: Half profiles through a 1x1 cm^2 segment on the side closer to the secondary collimator. Plots show the reduction in the penumbra for the segments on the field boundary defined by the secondary collimators (a) Segments *a, b, c* (b) Segments *d, e, f* (c) Segments *g, h, i.*

The machine output in dose/MU was measured with the PinPoint chamber for all combinations of segment size and secondary collimator setting, and at 5 cm, 10 cm and 20 cm deep. Appendix B (II) displays the results obtained, and shows the percentage deviation of the measured output to the Pinnacle calculated output. What is immediately noticeable is the increase in magnitude of the deviation with an increase in depth, as well as the much larger deviations seen for the 1x1 cm^2 segment with both secondary collimator settings.

Figure 4.14 shows the plots obtained for the averaged percent deviation calculated for the difference in measured dose/MU and that calculated by Pinnacle, and plotted as a function of segment equivalent field size for secondary collimator settings at 10x10 cm^2 and 15x15 cm^2. Results show that for segments 2x2 cm^2 and 3x3 cm^2 there is very little variation with increasing fixed jaw setting with Pinnacle overestimating the dose by approximately 4% for 2x2 cm^2 and 2% for 3x3 cm^2 for both fixed jaw settings. Conversely the 1x1 cm^2 segment shows a variation in the dose/MU deviation, with an approximately linear increase in deviation seen with increasing depth, with up to 8% and 12.3% at 20 cm deep with secondary collimators at 10x10 cm^2 and 15x15 cm^2 respectively. The large discrepancies seen for the 1x1 cm^2 segment could possibly be attributed to inaccuracies in the chamber positioning for such a small field size. Slight shifts off from central axis will result in a lower chamber signal. The lower Dose/MUs measured compared to higher Pinnacle values more than likely confirm this as the most probable reason. With such a small field the lack of charged particle equilibrium could also contribute to the overall discrepancies.

In any case the results suggest large discrepancies in the measured and calculated dosimetry for the 1x1 cm^2 segment, and indicate a 2x2 cm^2 segment be set as the minimum segment size for IMRT, especially in the case when treating at depths greater than 5 cm.

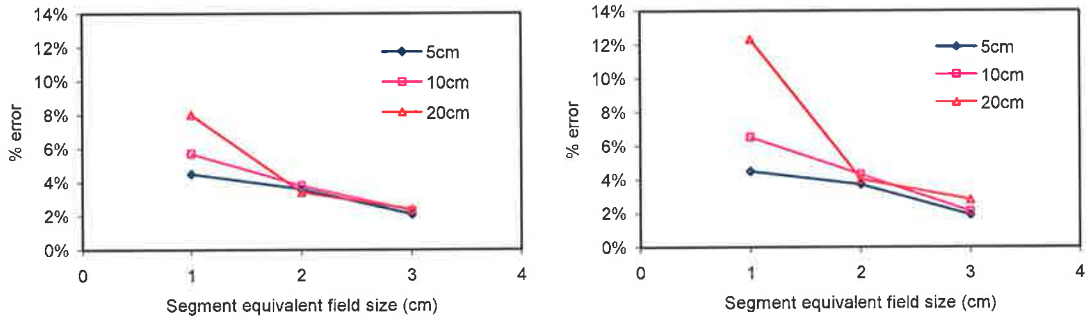

(a)　　*(b)*

Figure 4.14: % deviation calculated between the dose/MU determined from PinPoint ion chamber measurements and that determined by Pinnacle for depths 5 cm, 10 cm and 20 cm as a function of segment equivalent field size for secondary collimator settings of (a) 10x10 cm^2 (b) 15x15 cm^2.

4.4.3 Conclusion

The average differences between the output factors determined for small MLC defined segments off-axis with varying secondary collimator settings have been shown to increase with a decreasing field size, and as high as 8% and 12.3% for a 1x1 cm^2 segment with secondary collimators set to 10x10 cm^2 and 15x15 cm^2 respectively, and at 20 cm deep. For field sizes > 1x1 cm^2 and for both secondary collimator settings the deviations are approximately 4% and 2%, for 2x2 cm^2 and 3x3 cm^2 respectively. Therefore it is suggested that a minimum segment size setting for IMRT planning should be set to > 1x1 cm^2, as the dosimetry of the 1x1 cm^2 field seems very unreliable. There does not seem to be any noticeable effect on the output with regard to secondary collimator setting with a segment size set > 1x1 cm^2.

Chapter 5

Characterisation of the Varian millennium multi-leaf collimator

5.1 Introduction

The MLC is an important tool in accurate IMRT planning and its complete characterisation is required to determine the impact on the accuracy capable through IMRT. This chapter focuses on the characterisation of the MLC through ion chamber and film measurements. Areas covered include inter- and intra-leaf radiation transmission through the leaves, beam penumbra and match-line effects as a result of the rounded leaf design, tongue-and-groove effects, and finally the overshoot and undershoot of dose, resulting from the communication lag between the MLC controller and the linac beam control.

5.2 Transmission

5.2.1 Method

The transmission of radiation through the MLC system due to the limitations of the construction design was investigated using a silicon diode detector placed at 10 cm deep in water. The fixed jaws were set to the maximum field size of 40x40 cm^2 and the MLC were fully closed. The diode was scanned perpendicular to the direction of leaf propagation for both A and B carriages, and at 5 cm and 10 cm from central axis, Figure 5.1 (a).

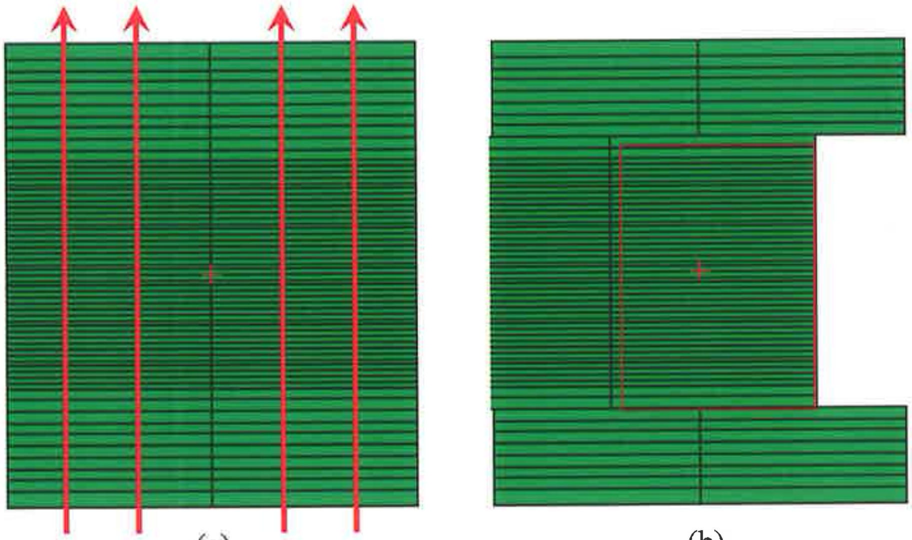

(a) (b)

Figure 5.1: (a) Scan set-up for Intra- and Interleaf transmission measurements for the Varian 120 leaf Millennium MLC. The red arrows indicate the scan direction. (b) Set-up for the transmission measurement using Farmer Chamber. The red box indicates the fixed jaw settings.

Pinnacle accepts a single value for MLC transmission for a given energy. The overall transmission was measured using a NE Technology 0.6cc graphite guarded stem Farmer Ion Chamber model 2571, connected to a NE dosemeter model 2570, set to low range and -240 Volt polarizing voltage. The fixed jaw setting as well as the measurement depth of 10 cm was chosen such that they approximated an average clinical situation. Figure 5.1 (b) shows graphically the position of the chamber (centre cross) relative to the field size defined by the fixed jaws. As shown in Figure 5.1 (b), the leaf junction is positioned under one side of the fixed jaw setting to eliminate transmission through the leaf ends, which would otherwise overestimate the transmission measurement. With the MLC fully closed and the fixed jaws set to X=8 cm and Y=12 cm, 2000 MUs were delivered. The Farmer chamber was positioned in a solid water phantom such that the stem was parallel in the in-plane direction to enable an average of several leaf junctions. The transmission readings were then normalised to the output determined with the MLC fully retracted. Calculated transmission was determined using the following equation:

$$T = \frac{M^*}{M} \tag{5.1}$$

where M^* is the measured output with the MLC closed, and M is the measured output with the MLC fully retracted.

5.2.2 Results and discussion

The transmission will obviously be altered with varying field settings and chamber depth, therefore, for this setup, which represents an average clinical setup the total transmission was determined to be 1.53%. This compares well with 1.5% transmission determined by Venencia *et al.* (Venencia, 2004) for the same delivery system. The plot displayed in Figure 5.2 shows the normalized average readings for distance off CAX, and Table 5.1 shows the results as a whole for the measured transmission and average, maximum and minimum intra- and interleaf transmission. The peaks and valleys of the curve shown in Figure 5.2 are termed the inter-leaf and intra-leaf transmission respectively, where interleaf resulting from the transmission through the gaps between adjacent leafs and intra-leaf from the transmission through the leaf itself. From diode measurements performed the average inter- and intra-leaf transmission was determined to be 1.07% ± 0.07 and 1.01 ± 0.1 respectively. It would be thought that the average of the inter- and intra-leaf transmission would be indicative of the overall measured transmission. This is however not the case, but from Figure 5.2 it can be seen from the fitted curve the intensity of the transmission is decreasing with increasing distance from central axis, producing a distinctive rounded shape. This can be explained, as there is greater transmission radiating from the 40 central leaves with isocentric widths of 0.5 cm than is radiating from the outer leaves with width 1.0 cm. Beam divergence will also influence the transmission intensity at distance off-axis. Also, the scatter contribution at depth is greatest at the centre of the field. As a result of the rounded transmission curve the average inter- and intra-leaf transmission are not going to represent the true transmission as was measured at a single point at field centre. A depth closer to depth maximum may have resulted in a more flat transmission curve, but would not have been a good representation of an average clinical treatment situation with a 6 MV beam.

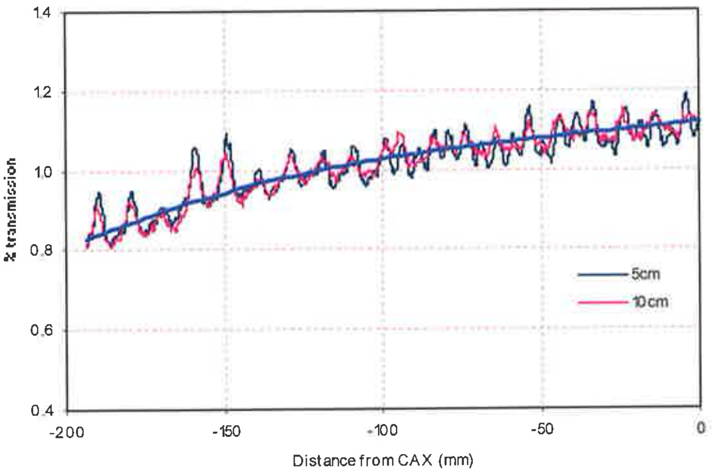

Figure 5.2: The normalized transmission profiles for a Varian 120 leaf Millennium MLC measured for a 6 MV photon beam. Half field profiles were measured at 5 cm and 10 cm from central axis for both A and B carriages and normalized and averaged. The blue fitted curve is a cubic fit that illustrates the trend of MLC transmission.

Measured transmission	1.53%
Average Interleaf	1.07% ± 0.07
Maximum Interleaf	1.16%
Average Intraleaf	1.01% ± 0.1
Minimum Intraleaf	0.81%

Table 5.1: Transmission and leakage values for the Varian 120 leaf Millennium MLC measured for a 6 MV photon beam.

5.2.3 Conclusion

Transmission measurements on the Varian MLC have been performed using ion chamber and film measurements. A single overall transmission value of 1.53% was measured for entry into Pinnacle. This measured transmission value has been shown to be a good match to that found in the literature. Inter- and intra-leaf transmission was measured using film, with results showing 1.07% ± 0.7 and 1.01% ± 0.1 for inter- and intra-leaf respectively. No significant difference was seen in the overall magnitude for the transmission measurements at depths 5 cm and 10 cm.

5.3 Rounded Leaves

5.3.1 Beam penumbra

5.3.1.1 Method

As small segments play a crucial part in the delivery of IMRT, the beam penumbra for small fields was investigated to see the effect on penumbra size as a result of the rounded leaf ends. The penumbra at the tongue side of the leaf was also measured for completeness by measuring a profile in the in-plane direction perpendicular to leaf propagation. All measurements were performed using the PinPoint ion chamber in water depths 5 cm, 10 cm and 20 cm. Figure 5.3 shows the leaf set-up to achieve profiles defined by the MLC for field sizes 1x1 cm^2, 2x2 cm^2, and 3x3 cm^2 respectively, with all MLC files generated using the Pinnacle system. The water level was set to 100 cm SSD and the leaves were positioned such that the junction caused by the convergence of the leaf banks was obscured by the fixed jaws set to 10x10 cm^2, thus, limiting unnecessary radiation leakage.

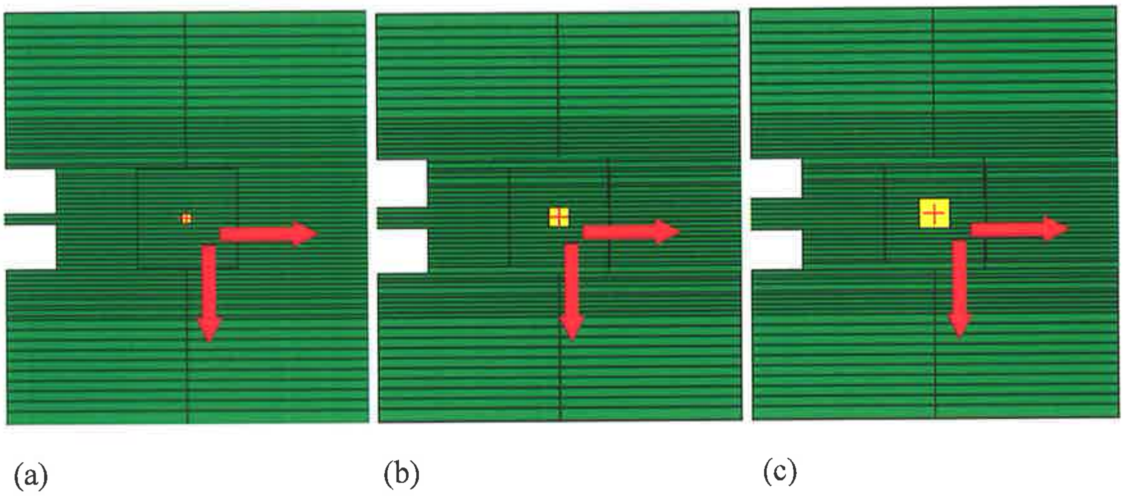

Figure 5.3: Scan set-up for beam penumbra measurements for the Varian 120 leaf Millennium MLC. The red arrows indicate the scan directions for field sizes (a) 1x1 cm^2 (b) 2x2 cm^2 (c) 3x3 cm^2.

The Scanditronix beam data acquisition system RFA*plus* version 5.3 (Scanditronix Wellhöfer, Germany) was used to collect profile data, which was then sub-sequentially analysed in Excel. The measurement step size was set to 1 mm increments and a potential of –400 V applied to the ion chamber. An RFD type Scanditronix reference diode detector (Scanditronix Wellhöfer, Germany) with 2 mm active diameter and 0.06 mm^3 active volume was used in conjunction with the PTW PinPoint ion chamber. The reference diode required accurate placement within the field to eliminate possible beam perturbation. This was especially critical with the 1x1 cm^2 field size. Film measurements were also performed for the 1x1 cm^2 field size to assess the volume averaging effect of the PinPoint chamber at such a small field size. Ready pack Kodak EDR2 radiographic film was used (Eastman Kodak Inc., USA), and processed with a Kodak automatic processor used for medical imaging, providing constant chemistry conditions. All experimental films and corresponding calibration films were taken from a single batch, minimizing any variations between film batches. All films were digitized using a VIDAR VXR-16 Dosimetry Pro film scanner, and analysed using the RIT113 film dosimetry software version 4.1 in conjunction with a calibration film generated by the technique discussed in Chapter 3.1. All experimental films were exposed perpendicular to the primary beam direction, and firmly sandwiched between slabs of the RMI certified therapy grade solid water.

To generate the profiles in Pinnacle to match those measured using the beam data acquisition system, the contour tool within Pinnacle was used to construct a patient contour that had matching dimensions of the water tank used for measurements. Once the contour was constructed a density of unity was assigned to define the water within the tank. A beam was positioned with the gantry set to zero, and secondary collimators at 10x10 cm^2. MLC fields were set by initially setting the secondary collimators to the small field size, then conforming the MLC to the jaw size. The Pinnacle profiles for the MLC fields were extracted using the planar dose tool. This tool provides a way of generating a dose distribution for a beam setup at a desired depth. The exported distribution is in the form of a dose map that can be imported in the RIT software for profile extraction.

5.3.1.2 Results and discussion

In characterising the penumbra effect as a result of the Millenium MLC, it is important to look at both the penumbra formed by the leaf ends and the leaf edges.

Half beam profiles for a 1x1 cm^2 field defined by the MLC with a 10x10 cm^2 secondary collimator setting are shown in Figure 5.4 for the Pinnacle model (Jaws), film and PinPoint ion chamber. Results are summarised in Table 5.2. The radiation field edges measured with the PinPoint chamber and the EDR2 film both show a higher 50% (FWHM) dose point to that of the digital readout of the Linac itself due to the radiation transmission through the rounded leaf ends. At depths 5 cm and 10 cm there is very good agreement between film and ion chamber, both cross-plane and in-plane, with approximately 1.2 mm difference seen from expected and measured FWHM for cross-plane and approximately 0.1 mm for in-plane, and for both depths. Pinnacle generated profiles show a slight disagreement with expected FWHM with approximately 0.5 mm for both depths and scan plans. The expected FWHM for the half-beam profiles is given by the expression:

$$FWHM_{\text{expected}} = \frac{s}{2} \times \left(\frac{SSD + d}{SSD} \right) \tag{5.2}$$

where, *s* is the field size, *SSD* is the source-to-surface distance and *d* is the scan depth.

Lydon (Lydon, 2005) has also shown disagreement in the Pinnacle radiation edge and expected edge of about 0.4 mm and 2 mm for cross-plane and in-pane respectively (for the Varian Mark II 80 leaf MLC). As the secondary collimators are set to 10x10 cm^2 the MLC radiation transmission through the leaves will have an effect on the Pinnacle FWHM, and may explain the overestimation seen.

The 80%-20% penumbral widths for the Pinnacle calculated profiles and ion chamber measured shows no significant change with depth, whilst the film penumbra width does show a significant increase with depth for both scan planes for this small field size. The 80%-20% penumbra widths for film positioned at 5 cm depth, is 3.2 mm and 2.5 mm for cross-plane and in-plane respectively. At 10 cm depth the film penumbra width becomes more consistent with the Pinnacle and ion chamber penumbra widths, but still displays a sharper penumbra.

The sharpening of the penumbra seen with the film at 5 cm depth is due to the fact that the ion chamber volume effect underestimated the true dose inside the field and overestimated it outside the field; therefore the higher resolution obtained from the film provides a profile with enhanced shoulders and lower tailing edges. The lower dose seen at the profile edge is also a result of the film being more tissue equivalent than the PinPoint chamber electrode, and hence, does not display the over response to the low energy radiation. This is the case at 5 cm depth; however, at 10 cm depth it is shown the film matches the ion chamber quite closely at the profile edge, indicating that at larger depth the film is showing signs of over responding to the low energy scattered radiation. The in-field profile shoulder at approximately 80% dose is still showing a higher response than the ion chamber due to less lower energy radiation being present in-field, nevertheless as the over response at the tail edges is present at depth 10 cm, the film penumbra is consistent with that of the ion chamber.

Depth	FWHM (mm)			80% - 20% penumbra (mm)			90% - 10% penumbra (mm)		
(cm)	P3	PP	Film	P3	PP	Film	P3	PP	Film
5	*5.44*	*6.42*	*6.55*	*4.11*	*4.03*	*3.24*	*6.09*	*7.26*	*5.71*
10	*5.73*	*6.73*	*6.65*	*4.15*	*4.48*	*4.29*	*6.49*	*7.87*	*8.45*

(a)

Depth	FWHM (mm)			80% - 20% penumbra (mm)			90% - 10% penumbra (mm)		
(cm)	P3	PP	Film	P3	PP	Film	P3	PP	Film
5	*5.29*	*5.19*	*5.23*	*3.34*	*3.25*	*2.52*	*5.66*	*5.56*	*4.40*
10	*5.54*	*5.47*	*5.61*	*3.41*	*3.48*	*3.16*	*5.83*	*6.21*	*6.27*

(b)

Table 5.2: Penumbra widths for 1x1 cm^2 MLC defined square field on central axis at 100 cm SSD measured in water for (a) cross-plane (b) in-plane.

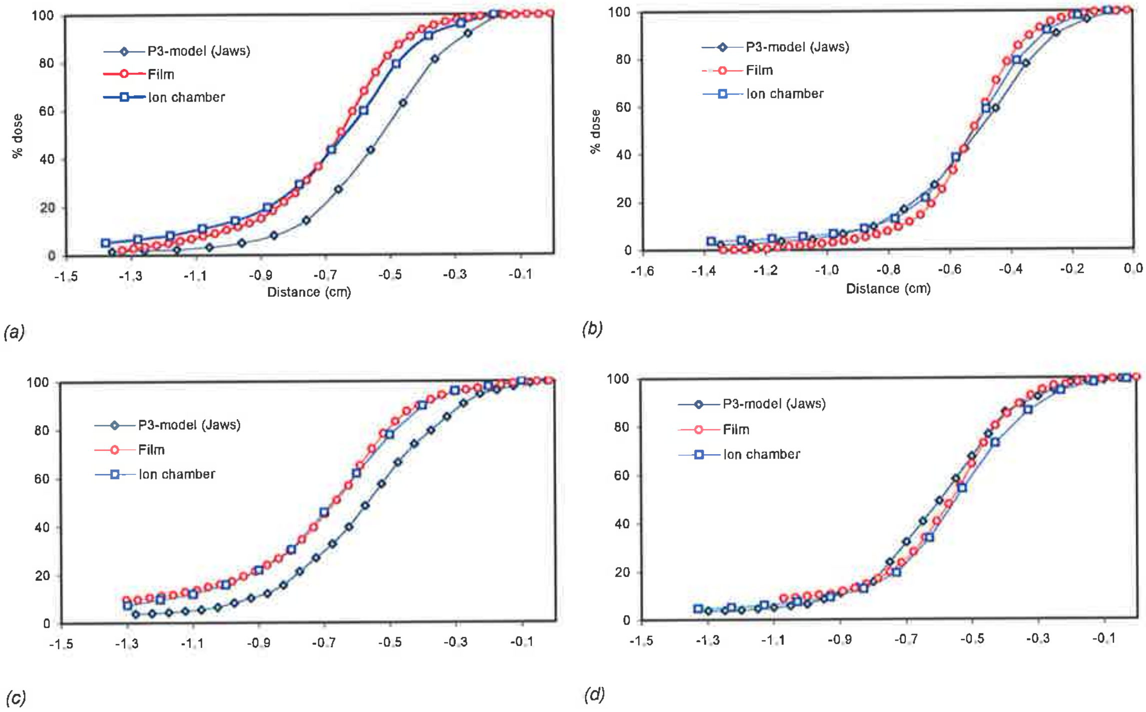

Figure 5.4: 1x1 cm^2 half beam profiles measured with film and PinPoint ion chamber compared with Pinnacle generated (a) (c) cross-plane at 5 cm and 10 cm depth respectively (b) (d) In -plane at 5 cm and 10 cm depth respectively.

Appendix B (I) shows a complete summary of the penumbra characterisation data collected from the measured profiles for field sizes 1x1 cm^2, 2x2 cm^2, and 3x3 cm^2, with varying secondary collimator settings. Table 5.4 summarizes the results obtained from the scans performed at 5, 10 and 20 cm depth with a secondary collimator setting of 10x10 cm^2.

Table 5.3 (a) shows the difference calculated between the ion chamber measured FWHM and the expected FWHM. In the cross-plane scan direction a definite dependence with increasing depth is seen, but not with field size. This would indicate that chamber over response does not have an influence on the FWHM, due to the fact that with increasing field size a greater amount of low energy scattered radiation will be present, but because no increase with field size is seen in the cross-plane direction the increasing deviation seen with increasing depth can be attributed solely to the rounded leaf construction. Because chamber over response is known to be a contributing factor with an increasing depth (Martens, 2000), Table 5.3 (c) shows that there is no trend seen for either increasing field size or depth for scans in the in-plane direction, and because the rounded leaf construction is not a factor in the in-plane direction affirms that it is the contributing factor in the differences seen in the cross-plane direction.

Depth (cm)	Field size (cm^2)		
	1x1	2x2	3x3
5	1.17	1.16	0.96
10	1.28	1.29	1.18
20	1.51	1.44	1.42

(a)

Depth (cm)	Field size (cm^2)		
	1x1	2x2	3x3
5	0.19	0.82	0.64
10	0.23	0.77	0.78
20	0.16	1.00	0.78

(b)

Depth (cm)	Field size (cm^2)		
	1x1	2x2	3x3
5	-0.06	-0.08	-0.09
10	-0.03	-0.03	-0.01
20	0.07	-0.12	0.02

(c)

Depth (cm)	Field size (cm^2)		
	1x1	2x2	3x3
5	0.04	0.48	0.47
10	0.04	0.27	0.52
20	-0.15	0.25	0.61

(d)

Table 5.3: Difference between measured and expected FWHM width for 1x1 cm^2, 2x2 cm^2 and 3x3 cm^2 MLC defined square fields on central axis at 100 cm SSD measured in water and with the secondary collimators set to 10x10 cm^2 for (a) cross-plane PinPoint chamber (b) cross-plane Pinnacle generated (c) in-plane PinPoint chamber (d) in-plane Pinnacle generated.

Table 5.3 (b) and (d) show the FWHM differences between the expected widths and the widths calculated from the Pinnacle generated scans. No real trends are seen for either increasing depth or field size, but the deviations are slightly higher than would be expected. As Pinnacle does not account for the presence of the MLC it is expected to not only underestimate the radiation field edge but also underestimate the penumbra width. Results displayed in Table 5.3 suggests that Pinnacle is overestimating the 50% penumbra width for all field sizes in the cross-plane direction and for the 2x2 cm^2 and 3x3 cm^2 field sizes in the in-plane direction. As discussed previously Lydon (Lydon, 2005) has also shown this Pinnacle overestimation in penumbra width with results ranging from 4 mm to 2 mm. This investigation shows a maximum of 1mm difference between the Pinnacle and expected FWHM, with all other difference ranging from 0.16 mm to 0.82 mm. The 1x1 cm^2 in-plane results do show an underestimate in the FWHM at depths 5 cm and 20 cm, but an overestimate of 0.45 mm at 10 cm.

Depth (cm)	Field size (cm^2)								
	FWHM (mm)			80% - 20% penumbra (mm)			90% - 10% penumbra (mm)		
	1x1	2x2	3x3	1x1	2x2	3x3	1x1	2x2	3x3
5	6.42	11.66	16.71	4.03	5.04	5.33	7.26	8.92	9.60
10	6.78	12.29	17.68	4.48	5.39	5.77	7.87	9.70	10.85
20	7.51	13.44	19.42	5.05	5.93	6.68	8.91	10.99	12.58

(a)

Depth (cm)	Field size (cm^2)								
	FWHM (mm)			80% - 20% penumbra (mm)			90% - 10% penumbra (mm)		
	1x1	2x2	3x3	1x1	2x2	3x3	1x1	2x2	3x3
5	5.44	11.33	16.39	4.11	4.38	4.16	6.09	6.91	7.18
10	5.73	11.77	17.28	4.15	4.50	4.66	6.49	7.25	7.89
20	6.16	13.00	18.78	4.28	4.78	4.95	7.00	7.92	8.69

(b)

Depth (cm)	Field size (cm^2)								
	FWHM (mm)			80% - 20% penumbra (mm)			90% - 10% penumbra (mm)		
	1x1	2x2	3x3	1x1	2x2	3x3	1x1	2x2	3x3
5	5.19	10.42	15.66	3.25	3.80	4.01	5.56	7.21	7.64
10	5.47	10.98	16.49	3.48	4.12	4.21	6.21	8.05	8.91
20	6.07	11.89	18.02	3.84	4.71	4.70	7.01	9.35	11.09

(c)

Depth (cm)	Field size (cm^2)								
	FWHM (mm)			80% - 20% penumbra (mm)			90% - 10% penumbra (mm)		
	1x1	2x2	3x3	1x1	2x2	3x3	1x1	2x2	3x3
5	5.29	10.98	16.22	3.34	4.00	3.87	5.66	6.39	6.52
10	5.54	11.27	17.02	3.41	3.80	4.09	5.83	6.89	7.21
20	5.85	12.25	18.61	3.75	4.18	4.54	6.00	6.80	7.82

(d)

Table 5.4: Penumbra widths for 1x1 cm^2, 2x2 cm^2 and 3x3 cm^2 MLC defined square fields on central axis at 100 cm SSD measured in water and with the secondary collimators set to 10x10 cm^2 for (a) cross-plane PinPoint chamber (b) cross plane Pinnacle generated (c) in-plane PinPoint chamber (d) in-plane Pinnacle generated.

The 80%-20% penumbra widths obtained suggest that with an increasing depth and increasing field size the penumbra edge sharpness decreases for ion chamber measured profiles in the cross-plane direction, with differences (Table 5.5) ranging from 1.2 mm to 1.7 mm for a 3x3 cm^2 field for depths 5 cm, 10 cm and 20 cm. Differences are reduced down to 0.5 mm for in-plane scans and is due to removing the influence of the rounded leaves.

Depth (cm)	80% - 20% penumbra difference (mm)		
	Field size (cm^2)		
	1x1	2x2	3x3
5	-0.08	0.67	1.16
10	0.33	0.90	1.11
20	0.77	1.15	1.73

(a)

Depth (cm)	80% - 20% penumbra difference (mm)		
	Field size (cm^2)		
	1x1	2x2	3x3
5	-0.09	-0.20	0.13
10	0.07	0.32	0.12
20	0.09	0.53	0.17

(b)

Table 5.5: 80%-20% penumbra width difference from Pinnacle generated penumbra width for 1x1 cm^2, 2x2 cm^2 and 3x3 cm^2 MLC defined square fields on central axis at 100 cm SSD measured in water and with the secondary collimators set to 10x10 cm^2 for (a) cross-plane (b) in-plane.

As IMRT involves delivering small segments with larger set secondary collimators, it is important to investigate the effect this has on the beam penumbra. Figure 5.5 shows half beam profiles at 10 cm deep for small MLC defined segments with secondary collimators set to 10x10 cm^2 and 15x15 cm^2. Table 5.6 summarizes results obtained from the plots shown in Figure 5.5 as well as the full set of scans shown in Appendix C. Results show no significant difference in beam penumbra with changing secondary collimating setting. The main differences seen are for the ion chamber cross-plane 1x1 cm^2 scans with an approximate 1 mm difference for the 80%-20% penumbra and up to 2 mm for the 90%-10% penumbra widths. Cross-plane Pinnacle 1x1 cm^2 profiles show less than 1 mm differences for all penumbra widths and all in-plane scans have differences less than 0.5 mm.

Chow *et al.* (Chow, 2005) have investigated this effect with the Varian 120 Millennium MLC with results indicating a penumbra width increase "saturation" when the secondary collimator setting is beyond 1-2 cm from the field edge defined by the MLC. Such "saturation" would explain the results obtained in this investigation, and as far as IMRT delivery is concerned, secondary collimation 2 cm from each individual segment is not possible with current delivery systems, moreover, a single secondary collimator setting is defined in the planning process and is for the most part much larger than individual segments.

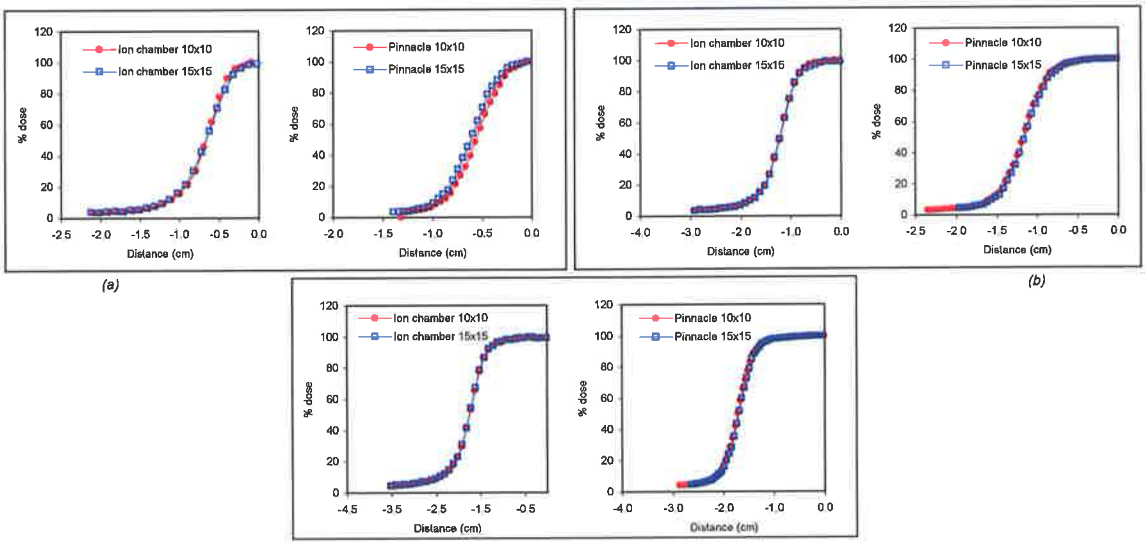

(a)

(b)

(c)

Figure 5.5: PinPoint ion chamber and Pinnacle generated cross-plane half beam profiles of small MLC defined segments with secondary collimators set to 10x10 cm^2 and 15x15 cm^2 and at 10 cm depth (a) 1x1 cm^2 (b) 2x2 cm^2 (c) 3x3 cm^2.

Depth (cm)	FWHM (mm)			80%-20% penumbra (mm)			90%-10% penumbra (mm)		
	1x1	2x2	3x3	1x1	2x2	3x3	1x1	2x2	3x3
5	-0.11	-0.02	0.09	1.17	0.04	0.04	1.62	-0.15	-0.04
10	-0.12	0.12	-0.03	1.25	-0.03	0.10	2.24	-0.06	0.08
20	0.05	0.05	0.03	1.37	-0.06	-0.04	2.90	0.21	1.60

(a)

Depth (cm)	FWHM (mm)			80%-20% penumbra (mm)			90%-10% penumbra (mm)		
	1x1	2x2	3x3	1x1	2x2	3x3	1x1	2x2	3x3
5	0.06	-0.08	0.04	0.35	-0.02	-0.08	0.80	-0.02	0.08
10	-0.51	-0.38	-0.16	0.08	-0.25	-0.06	0.86	0.06	-0.02
20	0.05	-0.17	0.09	0.33	-0.20	-0.01	0.78	-0.22	0.00

(b)

Depth (cm)	FWHM (mm)			80%-20% penumbra (mm)			90%-10% penumbra (mm)		
	1x1	2x2	3x3	1x1	2x2	3x3	1x1	2x2	3x3
5	0.03	-0.08	0.04	0.06	-0.07	-0.06	0.05	-0.10	0.00
10	-0.05	-0.09	0.00	-0.04	0.06	-0.01	0.02	0.16	0.08
20	0.04	0.06	-0.07	-0.11	-0.03	0.11	0.14	0.55	-0.02

(c)

Depth (cm)	FWHM (mm)			80%-20% penumbra (mm)			90%-10% penumbra (mm)		
	1x1	2x2	3x3	1x1	2x2	3x3	1x1	2x2	3x3
5	0.72	0.09	-0.26	0.28	-0.31	-0.15	0.07	0.07	0.36
10	-0.19	0.19	-0.16	0.04	0.21	0.05	0.16	-0.51	-0.19
20	0.48	0.22	-0.28	-0.28	-0.27	-0.71	-0.01	0.35	-0.16

(d)

Table 5.6: The difference between the penumbra width determined with secondary collimators set to 15x15 cm^2 and those with secondary collimators set to 10x10 cm^2 for 1x1 cm^2, 2x2 cm^2 and 3x3 cm^2 MLC defined square fields on central axis at 100 cm SSD measured in water for (a) cross-plane PinPoint chamber (b) cross-plane Pinnacle generated (c) in-plane PinPoint chamber (d) in-plane Pinnacle generated.

5.3.1.3 Conclusion

The rounded leaf effect has been shown to impact on the penumbra of small fields in the cross-plane direction only. The difference between measured and expected penumbra widths for the three small fields investigated has been shown to increase with an increasing depth, but no trend seen with changing field size. Very good agreement in the in-plane direction was found when the influence of the rounded leaves was removed. Results reveal that the penumbra broadening seen for cross-plane profiles resulting from the rounded leaf effect is significant and requires addressing during IMRT commissioning. As the effect is currently unavoidable, it is important to understand the effect and any impact it has on accurate IMRT delivery.

5.3.2 Match-line

5.3.2.1 Method

To investigate the match-line effect as a result of the rounded leaf construction, small 1x5 cm^2, 2x5 cm^2 and 3x5 cm^2 segments were delivered sequentially such that the leaves defining the X1 and X2 field edges propagate in the cross-plane direction (Figure 5.7). Each field edge is defined by adjacent leaves and opposite adjacent leaves. Figure 5.6 shows the scan directions through leaf positions to assess the clinical impact of rounded leaf junctions. All measurements were performed using Kodak X-Omat V film 5 cm deep in RMI certified therapy grade solid water. All films were processed with a Kodak automatic processor used for medical imaging, providing constant chemistry conditions. All experimental films and corresponding calibration films were taken from a single batch, minimizing any variations between film batches. All films were digitized using a VIDAR VXR-16 Dosimetry Pro film scanner, and analysed using the RIT113 film dosimetry software version 4.1. All experimental films were exposed perpendicular to the primary beam direction, and firmly sandwiched between the slabs of solid water.

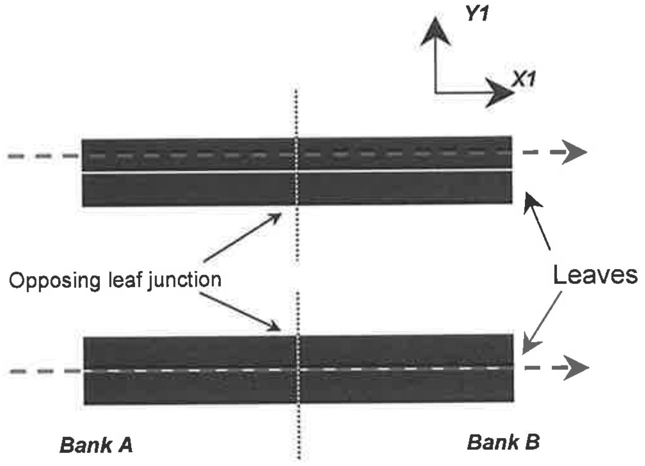

Figure 5.6: Schematic of the scan method for investigating the match-line effect produced by the Varian 120-leaf Millennium multi-leaf collimator. The red line indicates the scan direction.

Secondary collimators were set to 12x4 cm^2 such that the leaves beyond the edges of the propagating segment were shielded to eliminate any unnecessary transmitted and scattered radiation.

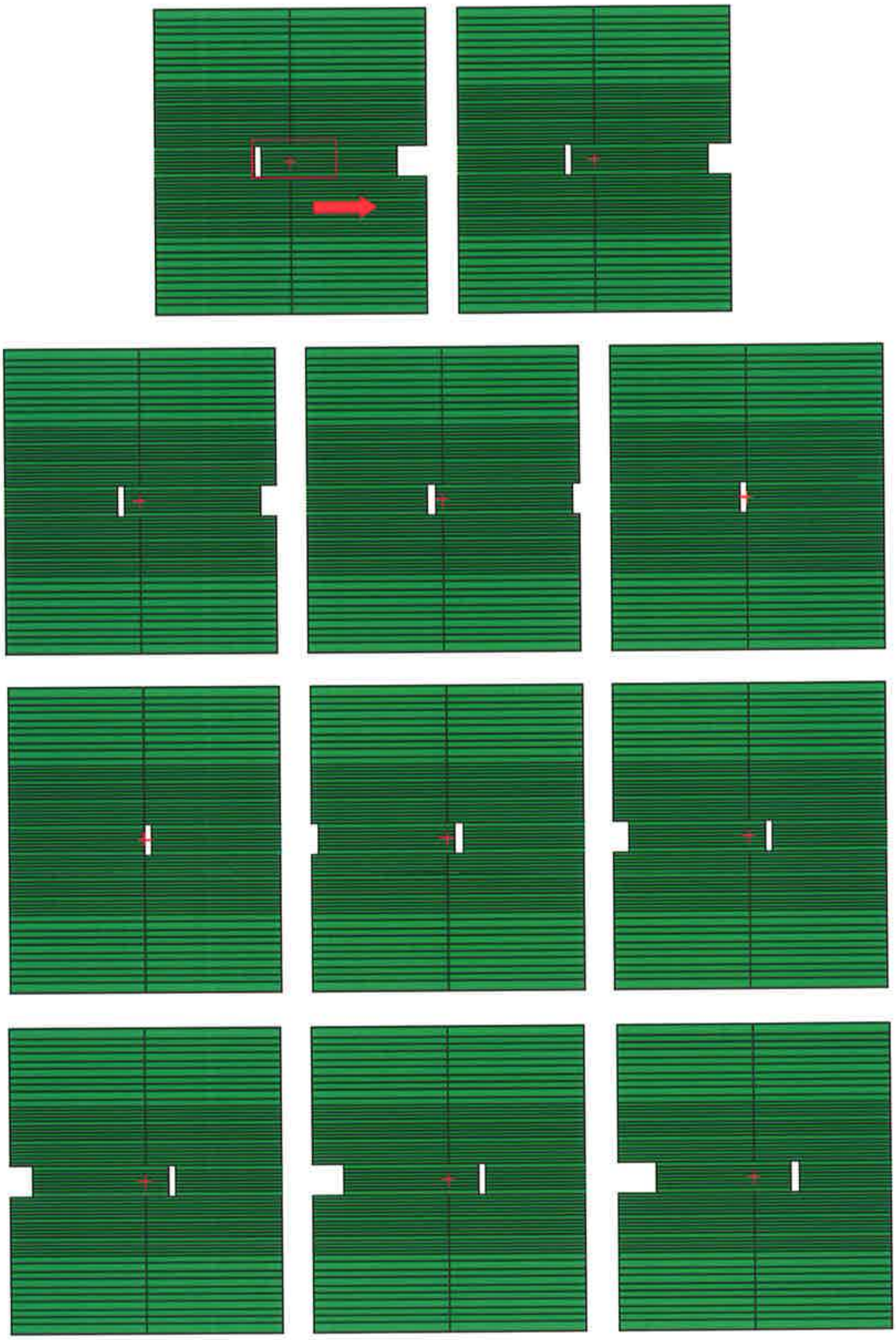

Figure 5.7: The MLC leaf positions of a 1x4 cm^2 strip propagating in the cross-plan direction to determine the rounded leaf effect. The arrow indicates the direction of leaf propagation. The red rectangle on the first image represents the jaw settings.

5.3.2.2 Results and discussion

To investigate the impact of the match-line effect, two scan planes were looked at; (i) the junction between one pair of adjacent leaves (ii) the junction between two pair of adjacent leaves (Figure 5.6). Films taken quantify the dosimetry impact of the produced match-lines (Figure 5.8) and were obtained by exposing sequential segments delivered via step-and-shoot for both scan planes mentioned above. Fields were also delivered statically for comparison. For the three different segment sizes investigated (1x4 cm^2, 2x4 cm^2, 3x4 cm^2), the same field edge was defined by opposite leaf banks eleven times, six times and three times respectively. These field edges are displayed as the dark bands in Figure 5.8. Figure 5.9 shows the profiles obtained for both scan plans. The dose was normalised to an open corresponding field and at the corresponding exposure depth. As can be seen at each adjacent field junction the leaves fell short resulting in an overdose, and in the case of Figure 5.9, the overdose seen for 2 pair and 1 pair of adjacent leaves delivered via step-and-shoot is 13.6 ± 0.93% and 11.4 ± 0.97% respectively for 1x4 cm^2, 23.7 ± 0.83% and 21.4 ± 0.89% respectively for 2x4 cm^2, and 26.2 ± 0.85% and 23.3 ± 0.46% respectively for 3x4 cm^2. Percent deviations were determined from the mean dose peaks produced for each scan. Appendix D (II) shows all the results obtained for match-line characterisation with Table 5.7 summarizing the results obtained from the scans displayed. For the same delivery system, Tangboonduangjit *et al.* showed a hotspot peak of 131%+-5% using Kodak XO-mat V film, EDR2 radiographic film and MD-55-2 Radiochromic film at 0cm offset (Tangboonduangjit, 2004).

The results displayed in Table 5.7 have been plotted and are shown in Figure 5.10. The difference seen between static and step-and-shoot delivery is slightly increased, with this increase showing a decrease with depth for both scan planes. Figure 5.10 (b) shows that for the scan plane through one pair of adjacent leaves, for depths 5cm and 10cm the agreement between static for both depths and step-and-shot for both depths compares quite well, with results at 20 cm deep showing that static and step-and-shot compare well except for the larger field size of 3x4 cm^2. Figure 5.10 (a) shows that for the scan plane through two pair of adjacent leaves a similar pattern is seen, however, overall deviationss are slightly higher as would be expected due to the transmission resulting from the tongue-and-groove effect.

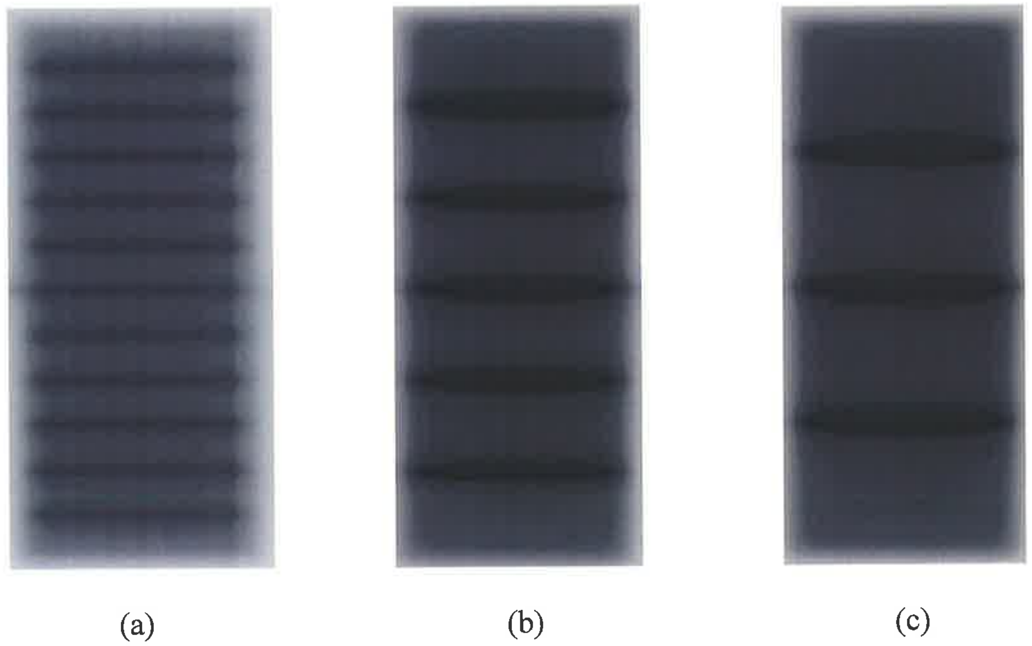
(a) (b) (c)

Figure 5.8: Film results showing the match-line effect for (a) 1x4 cm^2 segments (b) 2x4 cm^2 segments (c) 3x4 cm^2 segments.

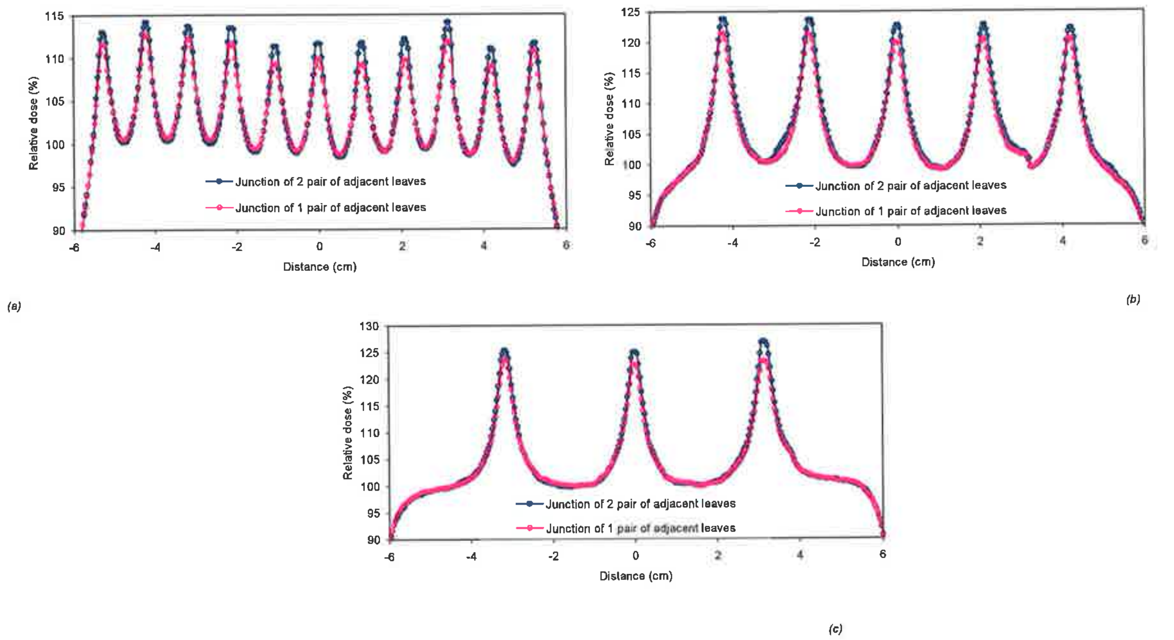

(a) (b) (c)

Figure 5.9: Profiles showing the increased dose as a result of the rounded leaf effect measured for 6 MV photons at 5 cm deep in water. Profiles generated by delivering via step-and-shoot (a) 11 sequential 1x4 cm^2 segments (b) 6 sequential 2x4 cm^2 segments (c) 4 sequential 3x4 cm^2 segments.

From Table 5.7 it is shown that the difference seen between static and step-and-shot delivery is slightly increased, with this increase showing a decrease with depth for both scan planes. Figure 5.10 (b) shows that for the scan plane through one pair of adjacent leaves, for depths 5 cm and 10 cm the agreement between static for both depths and step-and-shot for both depths compares quite well, with results at 20 cm deep showing that static and step-and-shot compare well except for the larger field size of 3x4 cm^2. Figure 5.10 (a) shows that for the scan plane through two pair of adjacent leaves a similar pattern is seen, however, overall deviations are slightly higher.

Field size (cm^2)	Delivery technique	Depth (cm)					
		5		10		20	
		2 leaves	4 leaves	2 leaves	4 leaves	2 leaves	4 leaves
1x4	static	13.0%	14.8%	13.0%	14.3%	11.0%	12.5%
	± standard deviation	0.94	0.84	1.03	1.00	1.22	1.33
	step & shoot	11.4%	13.6%	11.8%	13.0%	10.6%	12.4%
	± standard deviation	0.97	0.93	0.67	0.58	0.81	0.90
2x4	static	22.7%	25.2%	22.7%	25.2%	18.7%	20.7%
	± standard deviation	0.56	0.89	0.56	0.87	0.61	0.83
	step & shoot	21.4%	23.7%	21.5%	23.7%	18.6%	20.3%
	± standard deviation	0.89	0.83	1.02	1.00	0.52	1.07
3x4	static	25.8%	28.2%	25.4%	27.0%	23.5%	26.2%
	± standard deviation	1.03	0.72	0.39	1.17	0.95	0.38
	step & shoot	23.3%	26.2%	23.3%	25.6%	21.9%	25.8%
	± standard deviation	0.46	0.85	1.01	1.01	0.88	1.46

Table 5.7: Summary of the percent dose increase as a result of the rounded leaf effect at the leaf junction for opposing leaves for the Varian 120 leaf Millennium MLC system and 6 MV.

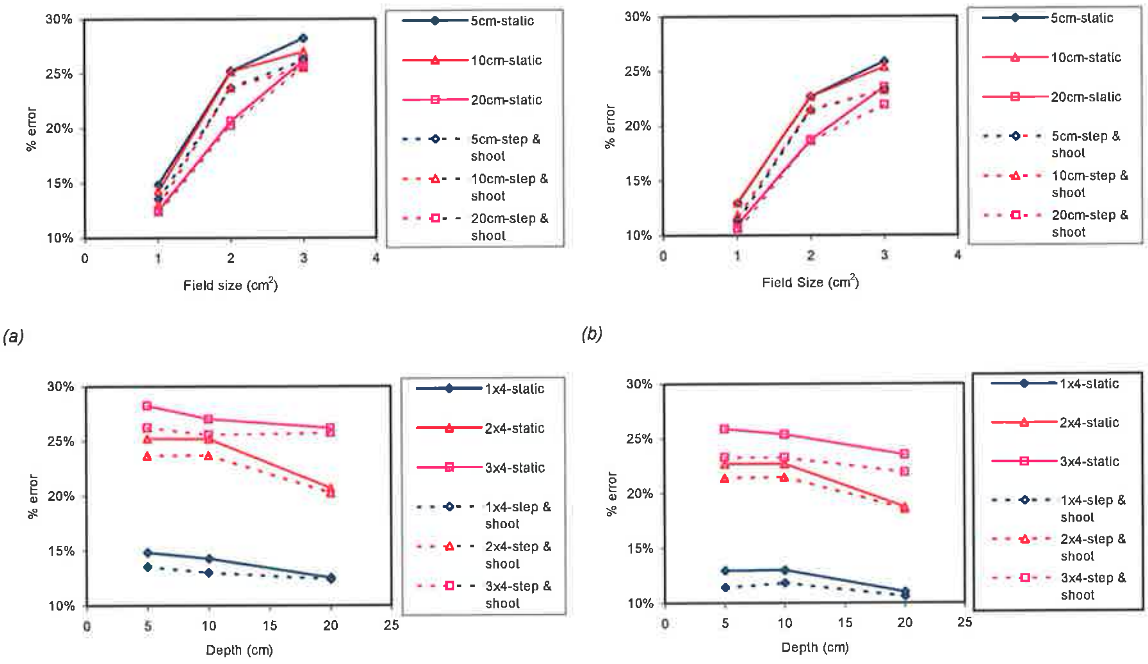

(a) *(b)*

(c) *(d)*

Figure 5.10: Dose error as a function of (a) (b) field size and (c) (d) depth, where dose error is given as the percentage overdose caused by the match-line effect. (a) (c) Junction of 2 pair of adjacent leaves (b) (d) Junction of 1 pair of adjacent leaves.

Table 5.8 summarizes the average FWHM for the overdose peaks for each field size delivered via step-and-shoot with corresponding measurement depth. For the calculated standard deviation the overall FWHM does not seem to show any change with distance off-axis or a significant change between 5 cm and 10 cm. The FWHM of the overdose peaks does however show an increase with increasing MLC defined X field size and at a depth of 20 cm. The increase with increasing depth can be explained by the penumbra broadening seen in section 5.2. It has been shown that with an increasing depth the penumbra broadens and hence more penumbra overlap of the leaf end will be present at greater depth, and with this increasing penumbra overlap the resulting dose spike will be seen to decrease.

Field size (cm^2)	**Depth (cm)**					
	5		**10**		**20**	
	FWHM (mm)	**Std. Dev. (mm)**	**FWHM (mm)**	**Std. Dev. (mm)**	**FWHM (mm)**	**Std. Dev. (mm)**
1x4	3.2	0.29	3.4	0.22	4.4	0.10
2x4	4.9	0.11	5.1	0.10	5.9	0.11
3x4	5.1	0.51	5.2	0.18	6.3	0.22

Table 5.8: Summary of FWHM data for overdose peaks resulting from the rounded leaf effect for the Varian 120 leaf Millennium MLC system.

As Figure 5.11 shows, not only does the dose spike resulting from the match-line effect increase with increasing field size, but the FWHM of the dose spike also increases with an increasing field size. The attributing factor to this is the increasing scatter component that will be present with an increasing field size.

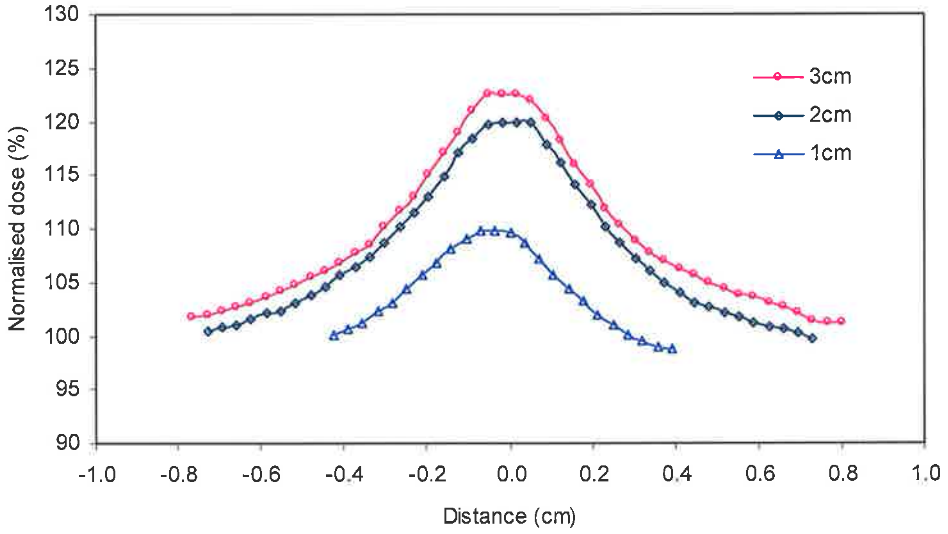

Figure 5.11: Varying magnitude and width of the hotspot at CAX at 5 cm deep for X jaw setting of 1 cm, 2 cm and 3 cm.

To account for the match-line effect it has been shown that a shift in individual leaves provides a method to limit the effect. Literature shows a variety of leaf offsets for the Millennium MLC system. Lydon (Lydon, 2005) has shown a leaf shift of 0.06 cm gave best agreement between measurement and Pinnacle calculated for multiple segment fields. Arnfield *et al.* (Arnfield, 2000), Cadman *et al.* (Cadman 2002), LoSasso *et al.* (LoSasso, 1998), from calculation of the integral fluence and film measurements shown optimum leaf offsets of 0.06 cm, 0.07 cm and 0.085 cm respectively. Tabgboonduangjit *et al.* (Tabgboonduangjit, 2004) showed an offset of 0.07 cm most appropriate, and Boyer *et al.* (Boyer, 2001) showed an offset of 0.05 cm produces the difference between the least over- and under-dose.

5.3.2.3 Conclusion

The match-line effect as a result of the rounded leaf construction has been investigated with results showing dose hotspots at the junctions of opposing leaves. For the three small field sizes investigated the hotspot magnitude was shown to increase with field size, with the highest hotspot of 23.3% found for the larger field size of 3x4 cm^2 at 5 cm deep. With a change in depth it was shown that for 5 cm and 10 cm there was no significant change in the magnitude of the hotspot, but at 20 cm depth the hotspot was shown to decrease a further approximate 2% from that seen at 5 cm and 10 cm. As IMRT will be delivered via step-and-shoot results were compared to results obtained by the static delivery of small segments. Results show that the hotspot magnitude is increased by approximately 1.5% for 5 cm and 10 cm and approximately 0.7% for 20 cm depth.

5.4 Tongue and groove

5.4.1 Method

To investigate the tongue and groove effect as a result of radiation transport between adjacent neighbouring leaves, small 5x1 cm^2, 5x2 cm^2 and 5x3 cm^2 segments were delivered sequentially such that the leaves defining the Y1 and Y2 field edges propagate in the in-plane direction (Figure 5.13). Y1 field edge is defined by one leaf side and Y2 field edge defined by another leaf side a distance of 1 cm, 2 cm and 3 cm apart. Figure 5.12 shows the scan direction through leaf positions to assess the clinical impact of the tongue and groove effect. All measurements were performed using Kodak X-Omat V film 5 cm deep in RMI certified therapy grade solid water. All films were processed with a Kodak automatic processor used for medical imaging, providing constant chemistry conditions. All experimental films and corresponding calibration films were taken from a single batch, minimizing any variations between film batches. All films were digitized using a VIDAR VXR-16 Dosimetry Pro film scanner and analysed using the RIT113 film dosimetry software version 4.1. All experimental films were exposed perpendicular to the primary beam direction, and firmly sandwiched between the slabs of solid water.

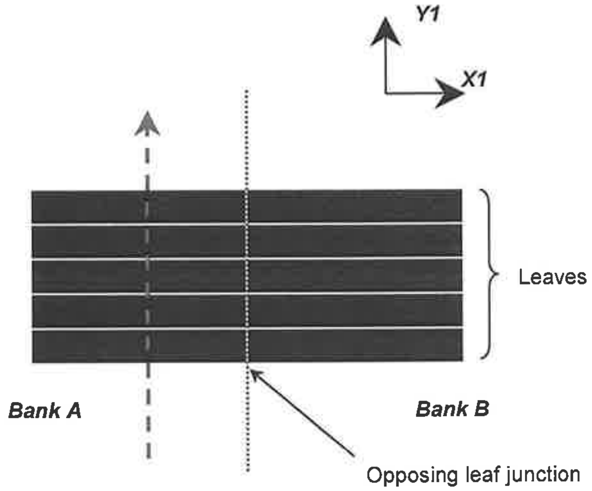

Figure 5.12: Schematic of the scan method for investigating the tongue-and-groove effect produced by the Varian 120-leaf Millennium multi-leaf collimator. The red line indicates the scan direction.

Segments were delivered both statically and via step-and-shot to compare the two delivery techniques. Secondary collimators were set to 5x12 cm^2 such that the leaves beyond the edges of the propagating segment were shielded to eliminate any unnecessary transmitted and scattered radiation.

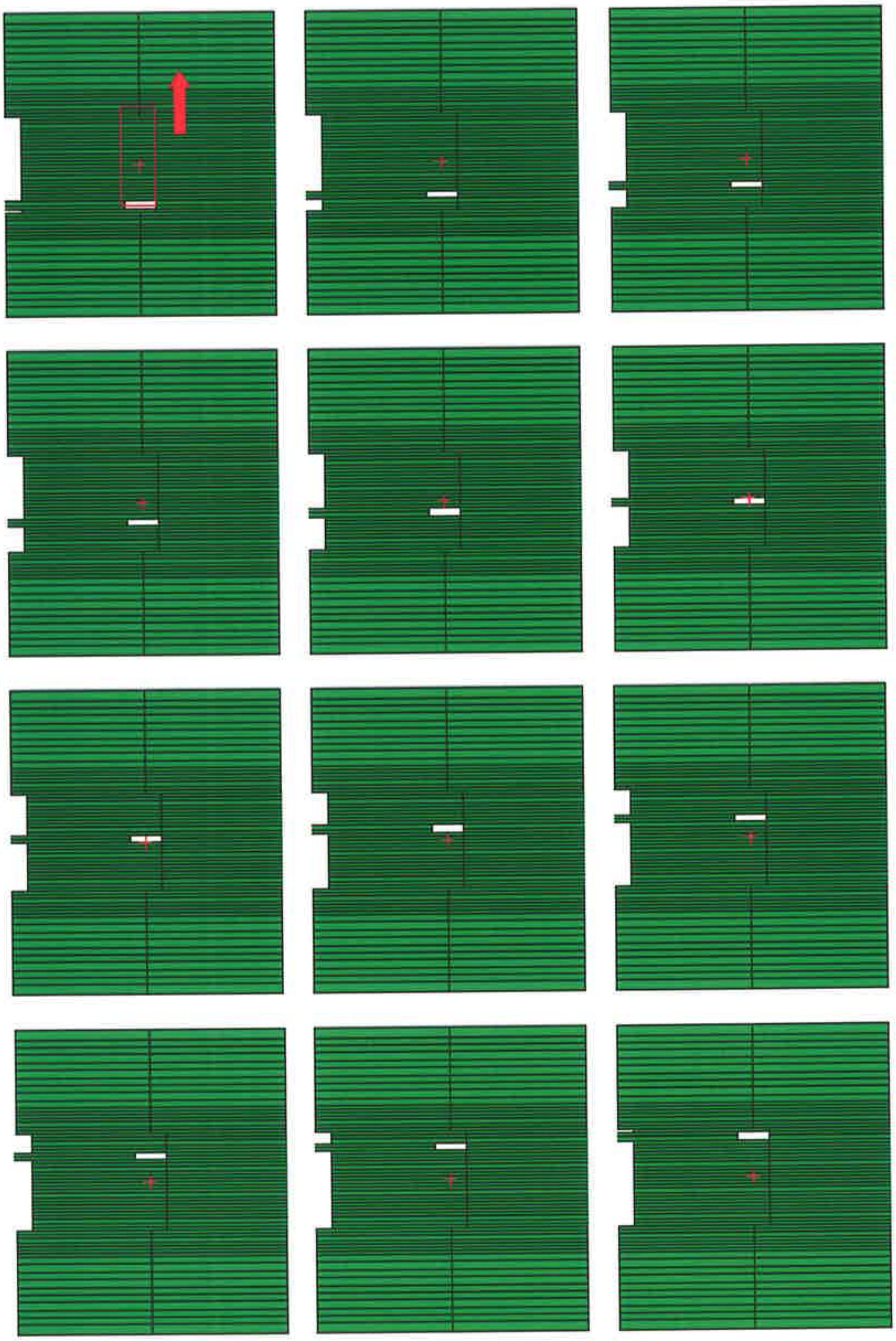

Figure 5.13: The MLC leaf positions to determine the tongue-and-groove leaf effect. The arrow indicates the direction of leaf propagation. The red rectangle on the first image represents the jaw settings.

5.4.2 Results and discussion

Films exposed to investigate the effect of the tongue-and-groove are shown in Figure 5.14. Figure 5.13 shows a profile measured at 5 cm deep displaying the dose reductions at the junctions formed by adjacent and opposite-adjacent leaves when 12 sequential 5x1 cm^2 segments are delivered via step-and-shoot. Appendix D (II) contains the results obtained from the profile data for scans performed at 5 cm, 10 cm and 20 cm for segments 5x1 cm^2, 5x2 cm^2 and 5x3 cm^2. The data collected for scans at the three depths and three segment sizes, is summarized in Table 5.9. Segments delivered statically were also measured to compare the segments delivered via step-and-shoot. As can be seen in Table 5.9 for segment size 1 cm propagating along CAX the dose reduction seen for all three depths is consistently low for segments delivered via step-and-shoot. For the 3 cm segment propagating along CAX the dose reduction for the three depths is consistently higher than statically delivered segments, and for the 2 cm segments, results show no real trend.

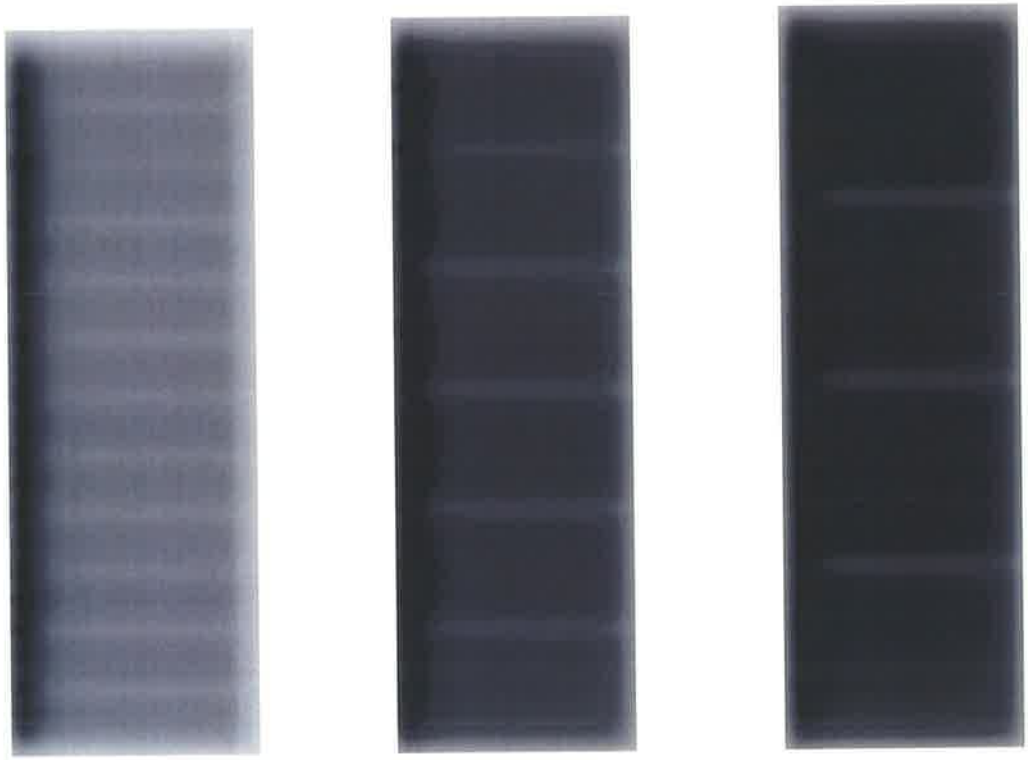

(a) (b) (c)

Figure 5.14: Film results showing the tongue-and-groove effect for (a) 5x1 cm^2 segments (b) 5x2 cm^2 segments (c) 5x3 cm^2 segments.

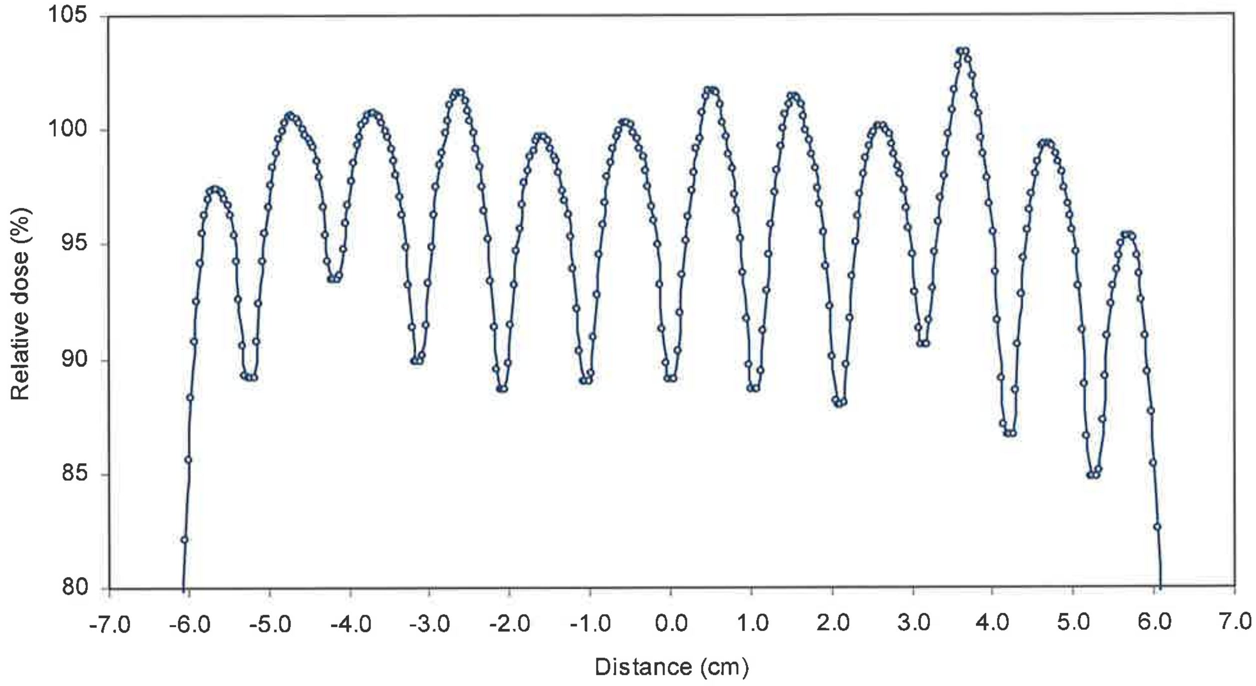

Figure 5.15: Profile showing the decreased dose as a result of the tongue-and-groove effect measured for 6 MV photons at 5 cm deep in water. Profile generated by delivering 12 sequential 5x1cm^2 segments dynamically (step-and-shoot).

Segment size (cm)	Delivery technique	Depth (cm)		
		5	10	20
5x1	static	-11.8%	-11.0%	-9.5%
	± standard deviation	1.86	2.06	2.59
	step & shoot	-10.8%	-10.4%	-8.9%
	± standard deviation	2.18	1.69	2.44
5x2	static	-13.0%	-11.3%	-9.6%
	± standard deviation	1.25	2.26	1.02
	step & shoot	-12.8%	-12.1%	-9.6%
	± standard deviation	3.06	1.05	0.98
5x3	static	-13.5%	-11.5%	-10.5%
	± standard deviation	1.99	0.51	1.79
	step & shoot	-13.6%	-12.6%	-10.9%
	± standard deviation	1.05	0.53	0.97

Table 5.9: Summary of the percent dose decrease as a result of the tongue-and-groove effect for the Varian 120 leaf Millennium MLC system and 6 MV.

With an increase in depth it is shown that the negative dose reduction increases, indicating that a higher dose is present at the segment junction defined by adjacent and opposite adjacent leaves. It would be thought that due to penumbra broadening the under dose spike would be seen to increase with increasing depth as was the case with the match-line effect. The dose is seen to increase at the junction as a result of an increase in scattered radiation at the increased depth. Penumbra broadening does however account for the increase in the dose reduction seen with an increasing segment size.

With limiting the tongue-and-groove effect through leaf sequencing techniques, Deng *et al.* has shown that the tongue-and-groove effect for the Varian MLC is insignificant (Deng, 2001). Using Monte Carlo dose calculations to produce fluence maps with and without tongue-and-groove effects, Deng *et al.* explain for multiple field IMRT plans were the number of fields is ≥ 5 the smearing effect of individual fields results in the tongue-and-groove effect being clinically insignificant (Deng, 2001). However, it was shown that for multiple field IMRT plans were the number of fields is < 5 the under dosage as a result of tongue-and-groove results in > 5% of maximum dose (Deng, 2001). The smearing effect was also seen for multiple gantry angles (≥ 5) with a 1.6% difference on the total dose (Deng, 2001).

5.4.3 Conclusion

The tongue-and-groove effect as a result of the construction of adjacent leaves has been investigated with results showing dose coldspots at the junctions of adjacent leaves. For the three small field sizes investigated the coldspot magnitude was shown to increase with field size, with the lowest coldspot of -13.6% found for the larger field size of 3x4 cm^2 at 5 cm deep. Much like the match-line effect, a change in depth showed little change in the magnitude of the coldspot for depths 5 cm and 10 cm, but at 20 cm depth the coldspot was shown to be higher by approximately 2% from that seen at 5 cm and 10 cm. Static delivery of the segments again showed a higher magnitude of the coldspot. The tongue-and-groove effect has been shown by Deng *et al.* to be insignificant due to the smearing effect when greater than 5 fields are delivered together. Generally for IMRT, more than 5 fields will be used; therefore, in this case the tongue-and-groove effect can be ignored, as it will be clinically insignificant.

5.5 Varian 600CD characteristics and the "Overshoot" effect

5.5.1 Method

To investigate the limits of the Varian 600CD beam delivery system, small MUs per segment were delivered at a range of dose rates for MLC defined segments. Segments were delivered both statically and via step-and-shot to compare the two delivery techniques with dose rates ranging from 100 MU/min to 600 MU/min employed to deliver the set MU ranging from 1 MU to 5 MU. All measurements were performed using Kodak X-Omat V film 5 cm deep in RMI certified therapy grade solid water. All films were processed with a Kodak automatic processor used for medical imaging, providing constant chemistry conditions. All experimental films and corresponding calibration films were taken from a single batch, minimizing any variations between film batches. All films were digitized using a VIDAR VXR-16 Dosimetry Pro film scanner, and analysed using the RIT113 film dosimetry software version 4.1. All experimental films were exposed perpendicular to the primary beam direction, and firmly sandwiched between the slabs of solid water.

Secondary collimators were set to 10x10 cm^2 such that the leaves beyond the edges of the propagating segment were shielded to eliminate any unnecessary transmitted and scattered radiation.

Dynamic segments for generating overshoot were manually created in Pinnacle such that a 1x10 cm^2 strip propagated in the cross-plane and in-plane directions. Segments were also delivered statically using a dose rate of 300 MU/min to assess dose inaccuracies through profile comparisons.

5.5.2 Results and discussion

Figure 5.16 displays film exposures obtained for 1 cm strip segments delivered at a dose rate of 400 MU/min and 4 MU delivered per segment. As a result of the communication time delay between the linac beam control and the MLC workstation the darkened overdose and the lightened underdose regions at the first and final exposure positions respectively, are clearly visible.

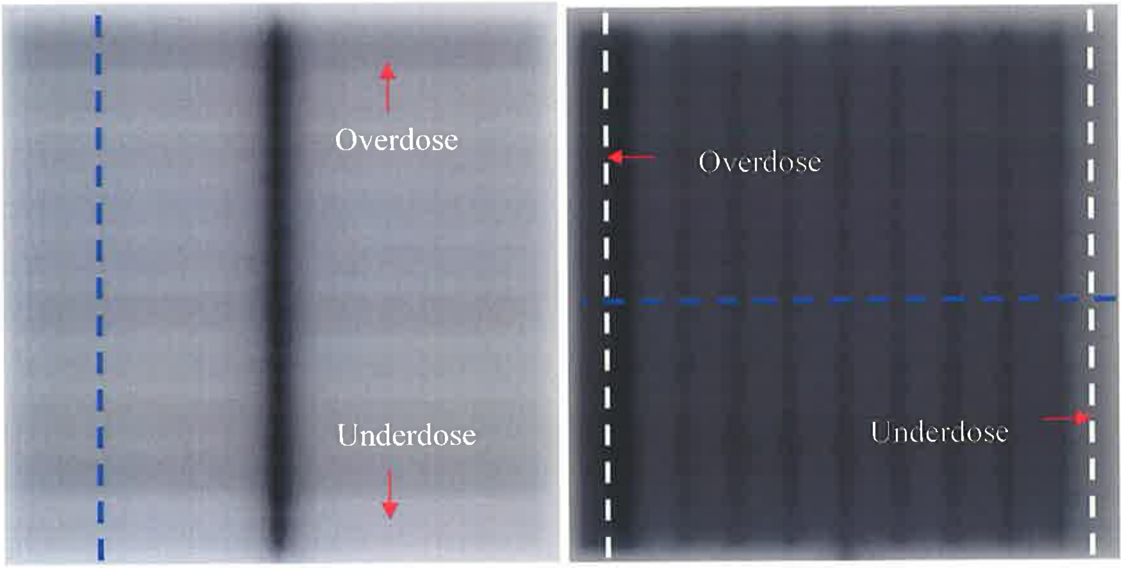

(a) (b)

Figure 5.16: Film results showing the overshoot effect resulting from delivering segments via step-and-shoot. (a) Segments propagating in-plane (b) Segments propagating cross-plane. Over dose and under dose sections at the outer most segments are clearly seen on both films. A dose rate of 400 MU/min and 4 MU per segment was used. The blue and dotted line represents the scan plane.

The film exposure seen in Figure 5.16 (a) resulted from the delivery of 4 MU to individual 1x10 cm^2 segments at a dose rate of 400 MU/min, with segment propagation occurring in the in-plane direction. The dark band seen at the centre of the film in Figure 5.16 (a) is a result of the dose transmitted through the junction of opposing leaves. Ideally this could have been eliminated by shifting the leaves such that the junction between the opposing leaf banks was shielded by the secondary collimators, however as the profile obtained from this film exposure is located approximately 3 cm off-axis, and shown as the blue dotted line in Figure 5.16 (a), the junction dose will have little effect on the dose off-axis. The light horizontal bands separating subsequent segments are a result of the tongue-and-groove effect which was discussed in Chapter 5.4. Figure 5.16 (b) shows the exposure for the same conditions as Figure 5.16 (b), but with segment propagation occurring in the cross-plane direction. Clearly visible on the film is the dark vertical dose bands that follow each segment and are a result of the increased dose due to the opposing leaf junctions as the segment propagates across the film. Also visible is the horizontal dose bands as a consequence of the transmitted radiation through the edges of adjacent leaves.

Figure 5.17 displays profiles taken in the direction of segment propagation, and shown in Figure 5.16 (a) and (b) as the blue dotted line. Appendix E displays the complete set of in-plane profiles for the range of MU/segment and machine dose rates investigated. Step-and-shoot profiles have been overlayed with a profile collected for identical segments delivered statically at a dose rate of 300 MU/min and 4MU/segment. The difference in intensity for the two outer most segments seen in the film exposure in Figure 5.16 (a) is a result of the overshoot effect, with the dark dose band and the light dose band corresponding to the first and last delivered segments respectively. All intermediate segments have an approximately identical magnitude. Assuming that there is zero error in the delivery of the intermediate segments, the first delivered segment is 22.7% higher than expected and the last segment is 27.5% lower. Combining these differences show a 2.4% decrease in the dose delivered for these two segments only, which corresponds to an overall dose decrease of 0.48% for all combined segments. Table 5.10 summarizes the percent differences determined between the sum of the percent dose for the first and last segments and that of the expected percent dose for the two segments.

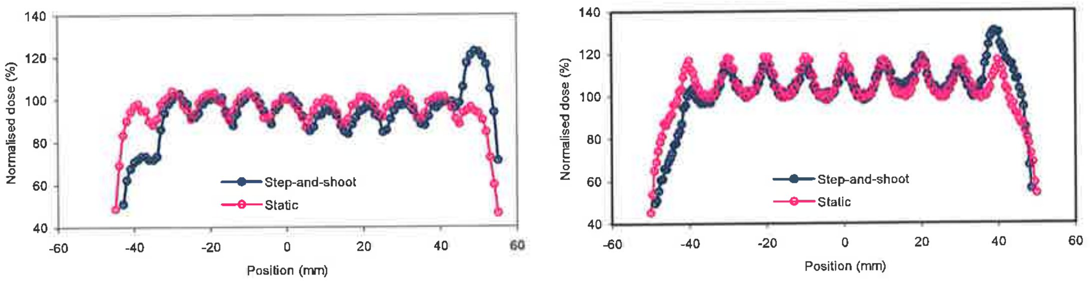

(a) (b)

Figure 5.17: Step-and-shoot profile overlaid with static profile to demonstrate the overshoot effect seen for the Varian 600CD Linac, for scan direction (a) In-plane (b) Cross-plane. Step-and-shoot profiles for both scan directions, was delivered with dose rate 400 MU/min and 4 MU/segment, and 300 MU/min and 4 MU/segment for the static profiles. The blue dotted line in Figure 5.16 represents the scan planes.

Dose rate (MU/min)	Monitor units delivered per segment			
	2 MU	3 MU	4 MU	5 MU
100	-10.3%	-6.3%	-6.6%	-4.4%
200	-6.2%	-4.7%	-8.8%	-5.0%
300	-9.8%	-8.8%	-4.8%	-6.8%
400	-12.5%	-6.0%	-1.9%	-7.2%
500	-	2.8%	1.0%	-6.0%
600	-	-10.4%	-8.0%	-4.2%

Table 5.10: Summary of percent difference seen for the sum of the first and last segments and that of the expected dose for both segments.

Ezzell *et al.* have stated that the total MU delivered will always be correct (Ezzell, 2001) and that by applying Equation 2.22 the sum of the first and last segments in all combinations of dose rate and MU per segment will be equal to two times the prescribed dose delivered to each individual intermediate segment. In this investigation the dose delivered to those segments was normalised to 100%, therefore, the sum of the first and last segments is expected to be approximately 200%. The differences displayed in Table 5.10 are significant and without a general trend other than an overall under dose seen for all combinations other than the 2.8% and 1% over dose seen for 3 MU and 4 MU respectively and delivered at a dose rate of 500 MU/min. Results from Grigorov *et al.* (Grigorov, 2006) show a similar result with 36.9% compared to 45.3% for this study for the difference between the measured percent dose for the last segment and that calculated using Equation 2.14 for 3 MU/segment delivered with a dose rate of 600 MU/min. Figure 5.18 displays the ratio of the calculated percent dose and measured percent dose for the last segment subtracted from unity as a function of dose rate. As is shown in the plot, for each MU setting an almost linear relationship is seen with a decrease in dose fraction with an increasing dose rate. For Equation 2.22 to be true the dose fraction plotted on the Y-axis in Figure 5.18 would be equal to zero. This is shown to be not the case for all combinations of MU per segment and machine dose rate. With 45.3% being the lowest difference between measured and calculated percent dose for the last segment for 3 MU/segment delivered at 600 MU/min.

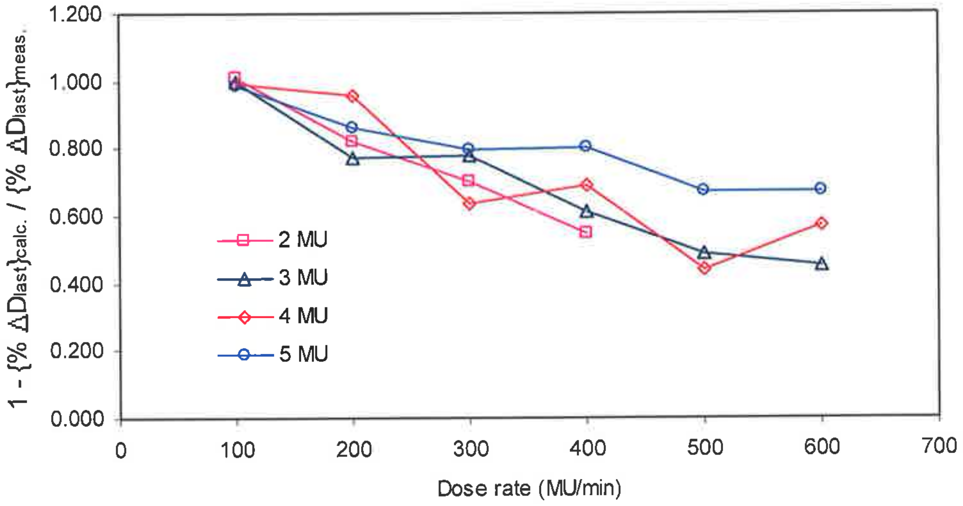

Figure 5.18: The ratio of the calculated percent dose of the last segment delivered and the measured percent dose of the last segment subtracted from unity as a function of machine dose rate.

Assuming the machine is delivering the set MU accurately for all intermediate segments, it can be stated that the total difference in MU delivered (ΔMU) as a result of the overshoot effect is given by,

$$\Delta MU = \frac{MU}{100} \times (\Delta D_{first} - \Delta D_{last}) \qquad (5.3)$$

where, MU is the monitor units delivered to individual segments, and ΔD_{first} and ΔD_{last} are the differences in the percent dose delivered for the first and last segments, and are given by the following expressions:

$$\Delta D_{first} = \%D_{first} - 100 \tag{5.4}$$

$$\Delta D_{last} = 100 - \%D_{last} \tag{5.5}$$

where, $\%D_{first}$ and $\%D_{last}$ are the total percent dose values for the first and last segments delivered respectively.

Figure 5.19 (b) shows the results obtained by applying Equation 5.3 for each MU setting and determining an average ΔMU over the range of machine dose rates.

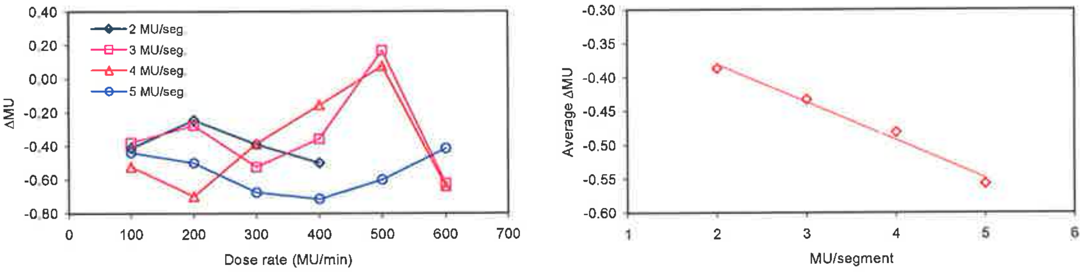

(a) (b)

Figure 5.19: (a) Change in MU delivered for all MU/segment settings as a function of machine dose rate. (b) Average change in the MU delivered for machine dose rates as a result of the overshoot effect.

Figure 5.19 (b) displays a linear decrease in the average MU missed as a result of the overshoot effect, and as the change in MU is negative indicates the dose difference for the last segment ΔD_{last} is greater than the first segment dose difference ΔD_{first}. The average ΔMU is shown to decrease with an increase in MU/segment delivered, indicating the magnitude of the overall underdose increases with increasing MU/segment. Figure 5.19 (a) shows no relationship was found between ΔMU and the machine dose rate, a contradiction of the assumption of Ezzell *et al.* who state a linear relationship, with ΔMU decreasing with decreasing dose rate (Ezzell, 2001).

For segments propagating in the cross-plane direction as displayed in Figure 5.17 (b) the dose transmitted as a result of the rounded leaf design obscures the overshoot effect for the first and last segments. The effect is not completely eliminated as the magnitude of the first and last dose peaks resulting from the rounded leaves are respectively greater and lower as is expected, but to accurately analyse the overshoot for the first and last segments the effect of the rounded leaves needs to be removed.

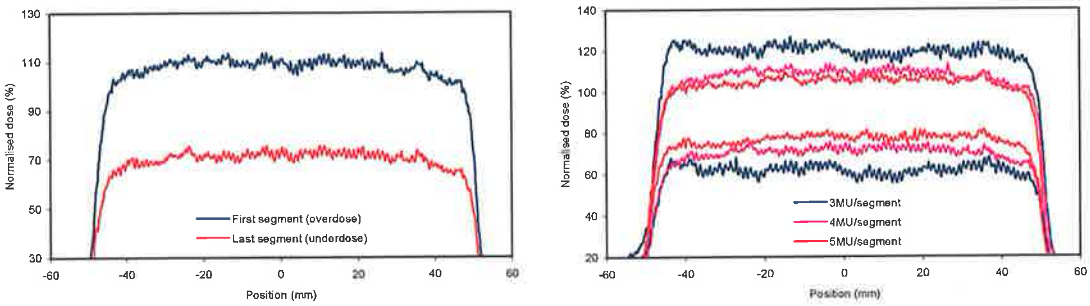

(a) (b)

Figure 5.20: (a) Normalised dose profiles in the cross-plane direction through the overdose and under dose regions, shown by the white dotted lines in Figure 5.16b. (b) Normalised dose profiles in the cross-plane direction through the overdose and underdose regions for dose rate 400 MU/min with different delivered MU/segment. Each MU setting has an upper and lower profile corresponding to overdose and underdoes respectively.

To investigate the overshoot effect for segments propagating in the cross-plane direction profiles were plotted through the first and last segments perpendicular to the direction of segment propagation. The profile directions are shown as the white dotted lines in Figure 5.16 (b). The resultant profiles for 4 MU/segment delivered at 400 MU/min are shown in Figure 5.20 (a) and show the difference between the first and last segments. Both profiles were normalised to the average of the intermediate segments. The average ΔD_{first} seen for the first segment is lower for the cross-plane direction with a percent dose difference of 13.5% between that for in-plane scans. The ΔD_{last} for in-plane and cross-plane are very similar with a percent dose difference of 1.8%, with cross-plane seen to be slightly higher than in-plane.

Figure 5.20 (b) displays normalised dose profiles for varying MU delivered at a dose rate of 400 MU/min. Comparisons of the profiles indicate that the dose gap between over- and underdose decreases with an increasing MU/segment setting, however, with this decrease in the dose gap, calculations show an approximate 9.1% ± 0.6% difference between the expected dose for the combined first and last segments for the three MU settings. In comparison the difference between the expected dose for the combined first and last segments for the in-plane scans was calculated to be 5.0% ± 2.7%.

To determine the optimum number of MU/segment and machine dose rate to employ for IMRT treatment, γ with dose and distance tolerances set to 3% and 3mm respectively, was calculated for the overlay of the step-and-shoot and static profiles. The percent $\gamma < 1$ was then used as a guide to find the best fit, with greater than 50% γ less than one considered a pass on goodness of fit. A visual inspection of the overlays also provided a quick method of determining the fit of the profile overlays. Linearity measurements could have also been performed. This would have provided information on a single point on the profile, but not an overall picture of the beam delivered for multiple segments and the actual uniformity of the beams delivered via step-and-shoot. Table 5.11 displays the γ results obtained, whereby green numbers indicate a reasonable fit between the static and step-and-shoot overlays, and the red indicating an unacceptable fit. A visual inspection of all the profiles displayed in Appendix E seems to agree with the γ calculations. The γ calculations were not performed for 1 MU/segment for all dose rates as shown in the plots in Appendix E, the profiles obtained for the step-and-shoot delivered fields provided little in the way of uniformity. It would be unrealistic to deliver IMRT with a dose rate lower than 400 MU/min due to the timing issues involved and patient workload; therefore, the results in Table 5.11 seem to suggest 3 MU/segment delivered at a dose rate of 400 MU/min would be the minimum machine requirement.

Dose rate (MU/min)	MU/segmet				
	1	2	3	4	5
100	X	32.5%	56.8%	44.4%	59.8%
200	X	75.0%	44.4%	27.2%	66.7%
300	X	50.6%	51.9%	25.0%	46.9%
400	X	38.3%	63.0%	57.5%	53.1%
500	X	11.3%	13.6%	33.8%	61.7%
600	X	5.0%	26.3%	40.0%	58.8%

Table 5.11: $\gamma < 1$ for the comparison of profile overlays of static and step-and-shoot profiles for the determination of optimum machine settings for IMRT delivery.

5.5.3 Conclusion

Through the delivery of multiple sequential segments via step-and-shoot, the communication time delay between the Linac beam control and the MLC workstation was simulated to produce the overshoot effect. Results acquired confirm an overdose and underdose for the first and last delivered segments respectively. For segments propagating in the in-plane direction, an overall underdose was found for all dose rate and MU/segment combinations with a change in the total delivered MU (ΔMU) averaged over all dose rates showing an increase in the magnitude of ΔMU with increasing MU/segment. Results deduce the underdose from the dose overshoot decreases with an increase in the number of segments delivered, suggesting when multiple segments are delivered the dose discrepancy becomes insignificant. The optimum machine parameters were determined from the γ calculations and visual inspecting of static and step-and-shot profiles of multiple delivered small segments. Results show that 3 MU/segment delivered at a dose rate of 400 MU/min will provide the required accuracy, and for dose rates greater than 400 MU/min, 5 MU/segment is required for uniform dose delivery between segments.

5.6 Machine limits applied to IMRT planning

5.6.1 Method

To assess the machine limits determined from this investigation and possible plan outcomes from the various MLC properties discussed previously, a relatively simple 8 field IMRT plan was generated using the Pinnacle treatment planning system. A patient CT data set was imported into Pinnacle and target and critical structure ROI were delineated. The isocentre was defined at the target volume centre and the beams were placed 45° apart. A 0.3 cm dose grid was used and DVHs were set up for the ROIs to specify dose objectives and constraints. Intensity modulation was chosen as the optimization type for each beam, which basically performs optimization on the individual ODMs. Following optimization of the ODMs the ideal ODMs were converted to a physical MLC segment using the K-means clustering method discussed in Chapter 2. Following conversion a final dose calculation was performed, and the 8

IMRT beams were copied to a standard IMRT phantom which consisted on 20 cm of solid water. All beams were set to a SSD of 95 cm and 0 gantry angles, and the plan re-calculated and exported to the treatment Linac.

At the Linac, Kodak EDR-2 film was employed for all the film measurements. Films were placed at 5 cm depth and the planned MUs delivered for each field using separate films for each beam using a dose rate of 400 MU/min. All films were scanned using the Vidar VXR-16 scanner analysed using the RIT113 dosimetry software, with a film calibration required, and obtained as discussed in Chapter 3. Films were exposed for settings outlined in Table 5.12 and labelled *Limits* and *No limits*, which signifies limits set for the minimum segment area and MUs per segment. The number of segments was also minimized for plans labelled *Limits* compared to the minimizing of the tongue-and-groove effect selected for the plan labelled *No limits*. Deng *et al.* (Deng, 2001) has stated that the tongue-and-groove effect becomes insignificant for plans with >5 fields due to the smearing effect, therefore, a comparison can be made between the two plans to see if the tongue-and-groove effect is insignificant by setting the minimize option to tongue-and-groove for plan *No limits*.

Pinnacle conversion settings	Trial name	
	LIMITS	NO LIMITS
ODM converter	K-means clustering	
Error tolerance	3%	
Minimum segment area	4 cm^2	1 cm^2
Minimum equivalent square	2 cm	1 cm
Leaf/Field edge overlap	0.5 cm	
Minimize	Number of segments	Tongue-and-groove effect
Filter ODM prior to conversion	Yes	
Correct for head scatter	Yes (Simplex)	
Minimum segment MUs	4 MU	1 MU
Compute ODM difference after conversion	No	

Table 5.12: Pinnacle settings for optimal IMRT delivery.

5.6.2 Results and discussion

Table 5.13 shows a summary of the data collected from the delivery of the Pinnacle generated IMRT plan delivered with and without set machine limits. Results clearly display a decrease in the number of segments required to deliver the optimum ODM from 221 to 149 segments when applying the limits outlined in Table 5.11. The overall decrease in segments is 72 in total, a 33% decrease. Also significant is the decrease in the total MU required for each field, 1624 MU reduced to 1179 MU for no limits and limits respectively. This is a 28% decrease in the total MU required. As the same prescription was applied to both plans, it could be assumed that as lower MU are delivered to produce a similar outcome, a larger dose could be prescribed when machine limits are incorporated, therefore providing a possible increase in tumour cell death. The change in the number of segments and the MU delivered for each individual beam also decreased with setting of limits. The minimum MU/segment was also shown to increase and be greater than the minimum MU/segment set, for example the worst case of the minimum MU/segment for the POST field increased from approximately 1 MU to approximately 4 MU. These results are significant in that a very similar ODM can be delivered with a reduced amount of both segments and MU. This would provide a more economical way to treat without compromising the accuracy that can be achieved through IMRT. Machine wear will also reduce in the long term through the delivery of fewer segments and MU. Patient treatment times would also be reduced, providing patients with less time spent being treated, as well as providing relief to ever growing patient waiting lists.

Field ID	Trial name					
	LIMITS			NO LIMITS		
	Total number of segments	Total MUs delivered	Minimum MUs	Total number of segments	Total MUs delivered	Minimum MUs
ANT	25	190	4.33	37	254	2.56
LT LAT	17	124	4.98	25	164	2.44
RT LAT	13	106	5.15	25	184	1.53
LTPO	16	166	4.77	20	183	1.81
RTPO	16	196	4.35	24	289	5.54
POST	25	178	3.99	35	227	1.00
RT ANT OB	17	107	4.00	27	164	3.66
LT ANT OB	20	112	4.02	28	160	2.90

Table 5.13: Summary of the impact on IMRT planning when machine limits are applied.

Figure 5.21 (a) and (c) displays the film exposure for plans delivered without machine limits and those delivered with limits are shown in Figure 5.21 (b) and (d). What is noticeable about the films exposed with limits is the overall "smoother" looking distribution, which could be attributed to the larger size segments and higher MUs being delivered. With the delivery of larger segments it would be thought the presence of low and high dose areas resulting from leaf junction effects would be less noticeable. This is shown to be correct in the films obtained, and Figure 5.21 (a) and (c) do display a more "striped" pattern over Figures 5.21 (b) and (d) in certain areas of the exposure.

The match-line effect has been shown to be an unavoidable limitation of the Varian Millennium MLC system due to the construction of the ends of each leaf. It has been shown in this investigation that the magnitude of this effect is significant, and limiting it is essential for accurate IMRT delivery. The match-line effect is shown to be present in the films exposed without limits and are highlighted by the red circles in Figures 5.21 (a) and (c). The dark dose bands corresponding to the effect in Figures 5.21 (a) and (c) are not present in the films exposed with machine limits. The removal of the effect is therefore dependent on the setting of machine limits. Figures 5.22 and 5.23 show overlayed profiles, indicated by the blue dotted lines in Figures 5.21, of the films with and without machine limits. Profiles have been taken through the area affected by the rounded leaf design and show clear spikes corresponding to the effect. On the film taken with limits the spike is no longer present.

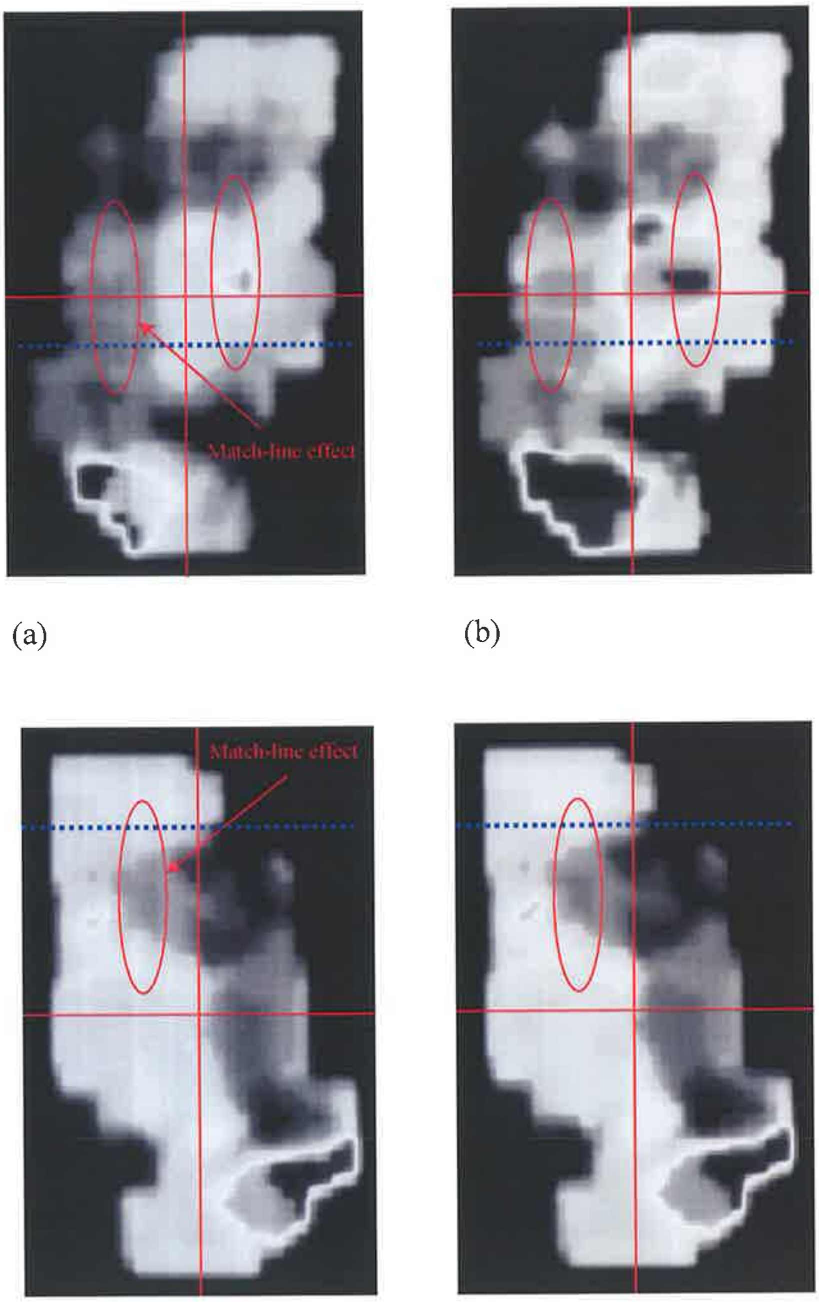

(a) (b)

(c) (d)

Figure 5.21: Example IMRT fields delivered (a) and (c) without limits (b) and (d) with limits (Table 5.13). It is shown that by setting machine limits the match-line effects has been removed and the tongue-and-groove effects have been reduced.

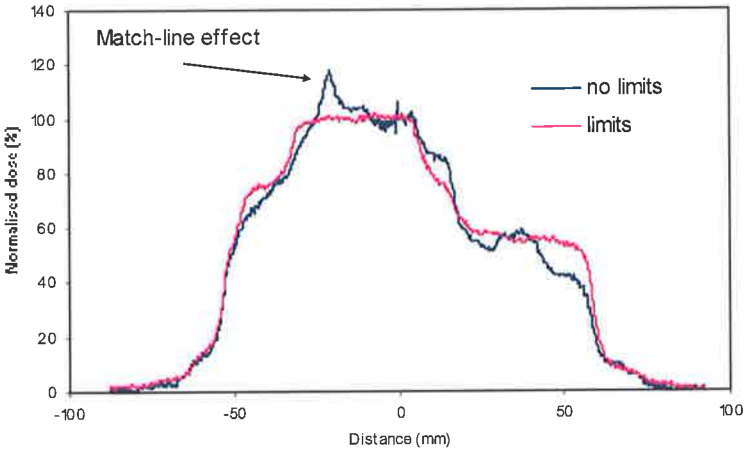

Figure 5.22: Profiles through IMRT example shown in Figures 5.21 (a) and (b). The blue dotted line displayed in the Figures is the scan plane.

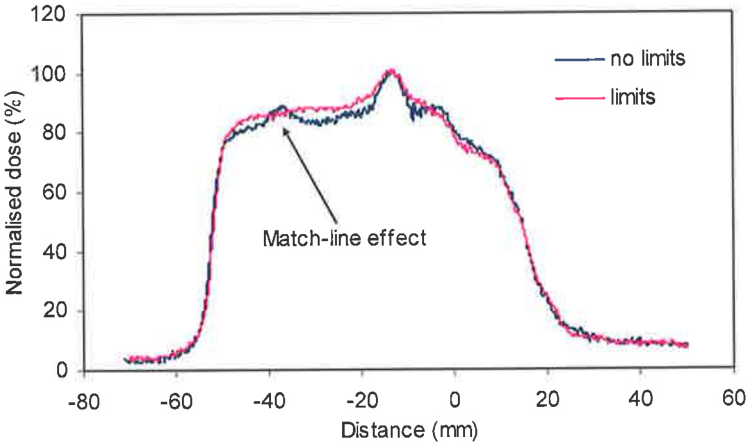

Figure 5.23: Profile through IMRT example shown in Figures 5.21 (c) and (d). The blue dotted line displayed in the Figures is the scan plane.

5.6.3 Conclusion

It has been shown that by setting machine limits for MU/segment and segment equivalent size, as well as minimizing the number of segments per beam, results in an overall decrease of 28% in the total MU required and 33% decrease in the number of segments required to deliver an ideal ODM. The overall impact on these findings is quicker treatment times, resulting in less machine downtime as wear-and-tear on the Linac is reduced, more patient throughput, thereby relieving the build-up in patient waiting lists, and the possibility of higher doses being prescribed. All of these outcomes as a result of applying simple machine limits are beneficial to both patient outcomes and overall wellbeing.

Chapter 6

6.1 Summary/Conclusion

Patient care is the ultimate goal in radiotherapy. IMRT is one area of radiotherapy that can provide, for certain cases, the ability to increase the probability of cancer eradication through dose escalation to cancer cells. The investigation of IMRT as an accurate technique for the treatment of cancer is an ongoing process with new developments being made in areas such as imaging, planning techniques, dose algorithms and computing power. All of these areas have a huge impact on the ability of accurate IMRT implementation.

This thesis has outlined the properties inherent to the MLC as a shielding device and the limitations resulting from these unavoidable structural properties. Measured has been compared to calculated, through the comparisons of data generated by the Pinnacle planning software and that delivered by the Varian 600CD linac. This has provided a way of setting machine limits that will provide optimum delivery of the small segments required in IMRT delivery.

Conclusions based on this investigation:

- Small fields modelled in Pinnacle show good comparison with measured data. However, it was shown that at greater depth the comparison fails the acceptance criteria, especially at the profile edges, and has been attributed to ion chamber over response to low energy radiation.

- Output factors for MLC defined fields are higher than fields defined by the secondary collimators. Results suggest radiation transmission through the leaves and differing scatter conditions may be the cause.

- With small MLC defined fields blocking large secondary collimator settings it was shown the error between the blocked outputs and outputs for fields defined by the secondary collimators was 2%, and 4% for secondary fields blocked greater than 99%. The 1x1 cm^2 field did show higher errors with 10% and 12.5% for 75% and 99.8% blocked fields respectively.

- The errors shown for the difference between Pinnacle calculated outputs and that of those measured are 8% and 12.3% for a 1x1 cm^2 segment size at 20 cm depth with secondary collimator settings of 10x10 cm^2 and 15x15 cm^2 respectively. For segment sizes 2x2 cm^2 and 3x3 cm^2 errors reduced to 4% and 2% respectively, and for both secondary collimator settings. These results highlight the unsuitability of a 1x1 cm^2 field size for accurate IMRT treatment.

- The overall MLC leaf transmission was measured to be 1.53%. With 1.07% and 1.01% measured for inter- and intra-leaf transmission respectively.

- Penumbra broadening due to the rounded leaf construction was shown to worsen with an increasing depth, but no significant change with field size. Good agreement was shown for scans performed in-plane.

- The match-line effect resulting from the rounded leaf design showed dose hotspots at the field junctions defined by abutting leaves. The magnitude of the hotspots is significant, and showed an increase with increasing field size. A 23.3% increase in dose was seen for a 3x4 cm^2 field at 5 cm deep. A change in depth had very little impact on the hotspot magnitude.

- The tongue-and-groove effect resulting from the leaf design showed dose coldspots at the field junctions. The magnitude of the coldspots is significant, and like the match-line, the magnitude of the coldspot increased with an increasing field size. A -13.3% decrease in dose was seen for a 3x4 cm^2 field at 5 cm deep. A change in depth also had very little impact on the coldspot magnitude.

- Static delivery over step-and-shoot resulted in slightly higher match-line and tongue-and-groove effects.

- The communication lag between the MLC and beam controllers was shown to produce the overshoot effect. It has been shown that the overshoot effect is only of concern when small numbers of MUs are delivered at high dose rates. The overshoot effect has been shown to decrease with a decreasing dose rate and increasing MUs. This makes sense as the lower the dose rate the longer the beam has to deliver set MUs.

- Overshoot results show that 3 MU/segment delivered at 400 MU/min is the ideal combination for IMRT delivery.

- The comparison of IMRT fields delivered with and without machine limits shows a decrease of 28% in the total MUs required and a 33% decrease in the total number of segments required to deliver an ideal ODM. Also, match-line effects were also shown to be removed when applying treatment limits.

6.2 Future work

- The large dose increases seen at the junction of abutting leaves will be clinically significant, and therefore further work is required to investigate the impact of introducing leaf shifts to account for the effect.

- Investigate the "blurring" of the tongue-and-groove effect associated with the number of beams used.

- Pinnacle v7.0 has been released during this investigation, whereby the rounded leaf design is accounted for in the modelling process. A thorough investigation of v7.0 is required to determine the accuracy of this new modelling feature.

- Comparison of match line and tongue-and-groove effects for Pinnacle v7.0 and Linac delivered IMRT fields.

References

ACPSEM, Absorbed dose determination in photon and electron beams: An adaption of the IAEA international codes of practice, 2nd Edition, Australasian College of Physical Scientists and Engineers in Medicine, 1998.

Philips, Physics Guide – External Beam and Brachytherapy Physics, Version 6.0, 2001.

Philips, P^{3}IMRT User Guide – Inverse Planning and IMRT for Pinnacle, Version 1.2, 2002.

Ahnesjö A, Collapsed cone convolution of radiant energy for photon dose calculation in heterogeneous media, *Med.Phys.*, 1989; **16**(4): 577-592.

AAPM, Basic applications of mulitleaf collimators, Report of task group No. 50, American Association of Physicists in Medicine Report No. 72, 2001.

Arnfield M. R, Siebers J. V, Kim J. O, Wu Q, Keall P. J and Mohan R, A method for determining multileaf collimator transmission and scatter for dynamic intensity modulated radiotherapy, *Med. Phys.*, 2000; **27**(10): 2231-2241.

Arnfield M. R, Mohan R and Siebers J. V, Specific IMRT delivery issues: Leaf design effects on IMRT delivered dose, ACMP annual meeting and workshops, Hershey, 2001.

Bomford C. K and Kunkler I. H., Textbook of Radiotherapy, Churchill Livingstone, 2004.

Bortfeld T. R, Kahler D. L, Waldron T. J and Boyer A, X-ray field compensation with multileaf collimators, *Int. J. Radiation Oncology Biol. Phys.*, 1994; **28**(3): 723-730.

Boyer A and Mok E, A photon dose distribution model employing convolution calculations, *Med. Phys.*, 1985; **12**(2): 169-177.

Boyer A, Ochran T. G, Nyerick C. E, Waldron T. J and Huntzinger C. J, Clinical dosimetry for implementation of a multileaf collimator, *Med. Phys.*, 1992; **19**(5): 1255-1261.

Boyer A and Shidong L, Geometrical analysis of light-field position of a multileaf collimator with curved ends, *Med. Phys.*, 1997; **24**(5): 757-762.

Boyer A, Biggs P, Galvin J, Klein E, LoSasso T, Low D, Mah K and Yu C, Basic Applications of Mulitleaf Collimators, *AAPM Report No. 72*, USA (2001).

Bragg W. H, Studies in radioactivity, New York, MacMillan Publishing, 1912.

Burch S. E, Kearfott K. J, Trueblood J. H, Sheils W. C, Yeo J. I and Wang C. K, A new approach to film dosimetry for high-energy photon beams: lateral scatter filtering, *Med. Phys.*, 1997; **24**: 775-83.

Butson M. J, Yu P. K. N and Cheung T, Rounded end multi-leaf penumbral measurements with radiochromic film, *Phys. Med. Biol.*, 2003; **48**: N247-N252.

Cadman P, Bassalow *R,* Sidhu N. P. S, Ibbott G and Nelson A, Dosimetric considerations for validation of a sequential IMRT process with a commercial treatment planning system, *Phys. Med. Biol.*, 2002; **47**(16): 3001-3010.

Chappell R. A, Evaluation of quality of model fit – Program MODFIT, Internal Document, Department of Radiation Oncology – W. P. Holman Clinic, Hobart, 2000.

Chow J.C.L, Seguin M and Alexander A, Dosimetric effect of collimating jaws for small multileaf collimated fields, *Med. Phys.*, 2005; **32**: 759-765.

Convery D. J and Rosenbloom M. E, The generation of intensity-modulated fields for conformal radiotherapy by dynamic collimation, *Phys. Med. Biol.*, 2006; **37**(6): 1359-1374.

Cormack A. M, Reconstruction of densities from their projections, with applications in radiological physics, *Phys. Med. Biol.*, 1973; **18**(2): 195-207.

Das I. J, Cheng C. W and Pai S, Basic film dosimetry, [Online], http://www.aapm.org/meetings/02AM/pdf/8321-71068.pdf (2002).

Deng J, Pawlicki T, Chen Y, Li J, Jiang S. B and Ma C. M, The MLC tongue-and-groove effect on IMRT dose distributions, *Phys. Med. Biol.*, 2001; **46**: 1039-1060.

Dogan N, Leybovich L. B and Sethi A, Comparitive evaluation of Kodak EDR2 and XV2 films for verification of intensity modulated radiation therapy, *Phys. Med. Biol.*, 2002; **47**: 4121-4130.

Dong L, Liu H, Wang X, Zhang X, Tu S, Mohan R and Wu Q, The effect of photon beam energy on the quality of IMRT plans, *Med. Phys.*, 2003; **30**: 1485.

Ezzell G. A and Chungbin S, The overshoot phenomenon in step-and-shoot IMRT delivery, *J. Appl. Clin. Med. Phys.*, 2001; **2**(3): 138-148.

Fraass B. A, The development of conformal radiation therapy, *Med. Phys.*, 1995; **22**(11): 1911-1921.

Gill P. E, Murray W, Saunders M. A and Wright M. H, User's Guide for NPSOL 5.0: A Fortran Package for Nonlinear Programming, Technical Report SOL 86-1, USA (1998).

Goiten M, Wittenberg J, Mendiondo M, Doucette J, Friedberg C, Ferrucci J, Gunderson L, Linggood R, Shipley W. U and Fineberg H. V, The value of CT scanning in radiation therapy treatment planning: A prospective study, *Int. J. Radiation Oncology Biol. Phys.*, 1979; **5**(10): 1787-1798.

Gray L. H, An ionization method for the absolute measurement of gamma-ray energy, *Proc R Soc*, 1936; A156:578.

Green D and Williams P. C., Linear accelerators for radiation therapy, Medical Science Series, Institute of Physics Publishing, 1997.

Grigorov G. N, Chow J. C. L and Barnett R. B, Dosimetry limitations and a dose correction methodology for step-and-shoot IMRT, *Phys. Med. Biol.*, 2006; **51**: 637-652.

Hårdemark B, Liander A, Rehbinder H and Löf J, P^3IMRT direct machine parameter optimization, Pinnacle^3 White Paper, Philips Medical Systems, 2004.

Harms W. B, Low D. A, Wong J. W and Purdy J. A, A software tool for the quantitative evaluation of 3D dose calculation algorithms, *Med. Phys.*, 1998; **25**(10): 1830-1836.

Hartigan J. A, Clustering Algorithms, John Wiley and Sons, New York, 1975.

Hoban P. W, Murray D. C, Metcalfe P. E and Round W. H, Superposition dose calculation in lung for 10MV photons, *J. Aust. Phys. Eng. Sci. Med.*, 1990; **13**(2): 81-92.

Hounsfield G. N, Computerized transverse axial scanning (tomography), *Br J Radiol*, 1973; **46**: 1016.

Hubbell J. H and Seltzer S. M, Tables of x-ray mass attenuation coefficients and mass energy-absorption coefficients (version 1.4) [Online], http://physics.nist.gov/xaamdi [Sept 2005], National Institute os Standards and Technology, Gaithersburge, MD 2004.

Hugo G. D, Dosimetric verification of respiratory gated IMRT, AAPM Newsletter, 2003; **13**(1): 1-5.

International Atomic Energy Agency, Absorbed Dose Determination in External Beam Radiotherapy, Technical Reports Series No. 398, IAEA, Vienna (2000).

Johns E. J and Cunningham J. R., The physics of radiology, Thomas, 1983.

Kahn F. M and Potish R. A., Treatment planning in radiation oncology, Williams and Wilkins, 1998.

Kilewski P. K, Chin L. M and Bjärngard B. E, Wedge-shaped dose distributions by computer-controlled collimator motion, *Med. Phys.*, 1978; **5**(5): 426-429.

Leavitt D. D, Martin M, Moeller J. H and Lee W. L, Dynamic wedge techniques through computer-controlled collimator motion and dose delivery, *Med. Phys.*, 1990; **17**(1): 87-91.

Leybovich L. B, Sethi A and Dogan N, Comparison of ionisation chambers of various volumes for IMRT absolute dose verification, *Med. Phys.*, 2003; **30**(2): 119-123.

Löf J and McNutt T, P^{3}IMRT inverse planning optimisation, Pinnacle^3 White Paper, Philips Medical Systems, 2003.

LoSasso T, Chen-Shou C and Ling C. C, Physical and dosimetric aspects of a multileaf collimation system used in the dynamic mode for implementing intensity modulated radiotherapy, *Med. Phys.*, 1998; **25**(10): 1919-1927.

Low D. A, Harms W. B, Mutic S and Purdy J. A, A technique for the quantitative evaluation of dose distributions, *Med. Phys.*, 1998; **25**(5): 656-661.

Lydon J, Theoretical and experimental validation of treatment planning for narrow MLC defined photon fields, *Phys. Med. Biol.*, 2005; **50**: 2701-2714.

Mackie T. R, Reckwerdt P. J, Olivera G. H, Shepard D and Zachman J. 3-D conformal and intensity modulated radiation therapy: clinical applications, Advanced Medical Publishing Inc., Madison, 2001, 179-190.

Martens C, De Wagter C and De Neve W, The value of the PinPoint chamber for characterization of small field segments used in intensity-modulated radiotherapy, *Phys. Med. Biol.*, 2000; **45**(9): 2519-2530.

Martens C, Claeys I, De Wagter and De Neve W, The value of radiographic film for the characterization of intensity-modulated beams, *Phys. Med. Biol.*, 2000; **47**: 2221-2234.

McShan D. L, Silverman A, Lanza D. M, Reinstein L. E and Glicksman A. S, A computerized three-dimensional treatment planning system utilizing interactive colour graphics, *Br J Radiol*, 1979; **52**: 478-481.

Metcalfe P. E, Hoban P. W, Murray D. C and Round W. H, Modelling polychromatic high-energy photon beams by superposition, *J. Aust. Phys. Eng. Sci. Med.*, 1989; **12**(3): 138-148.

Metcalfe P, Kron T and Hoban P., The Physics of Radiotherapy X-rays from Linear Accelerators, Medical Physics Publishing, 1997.

Milan J and Bentley R. E, The storage and manipulation of radiation dose data in a small digital computer, *Br J Radiol*, 1974; **47**: 115-121.

Murray D. C, Hoban P. W, Metcalfe P. E and Round W. H, 3-D superposition for radiotherapy treatment planning using fast fourier transforms, *J. Aust. Phys. Eng. Sci. Med.*, 1989; **12**(3): 128-137.

O'Brien P, Woo M and Nico A, Beam energy selection for intensity modulated radiation therapy, *Radiother. Oncol.*, **64** (Suppl.): S212.

Palm A, Kirov A. S, LoSasso T, Predicting energy response of radiographic film in a 6 MV x-ray beam using Monte Carlo calculated fluence spectra and absorbed dose, *Med.Phys.*, 1993; **31**(12): 3168-3178.

Podgorsak E. B, Review of radiation oncology physics: a handbook for teachers and students, IAEA Educational Report, Vienna 2003.

Pracy M, Private communication, Gamma analysis program presented in executable code, 2001.

PTW, Instruction Manual – PinPoint Chambers, 2002.

Sharpe M. B and Battista J. J, Dose calculations using convolution and superposition principles: The orientation of dose spread kernels in divergent x-ray beams, *Med.Phys.*, 1993; **20**(6): 1685-1694.

Sohn J. W, Dempsey J. F, Suh T. S, and Low D. A, Analysi of various beamlet sizes for IMRT with 6 MV photons, *Med.Phys.*, 2003; **30**(9): 2432-2435.

Sontag M. R, Battista J. J, Bronskill M. J and Cunningham J. R., Implications of computed tomography for inhomogeneity corrections in photon beam dose calculations, *Radiology*, 1976; **124**(1): 143-149.

Spencer L. V and Attix F. H, A theory of cavity ionization, *Radiat Res*, 1955; **3**: 239-358.

Stasi M, Baiotto B, Barboni G and Scielzo G, The behaviour of several microionization chambers in small intensity modulated radiotherapy fields, *Med. Phys.*, 2004; **31**: 2792-2795.

Suchowerska N, Davison A, Drew J and Metcalfe P, The validity of using radiographic film for radiotherapy dosimetry, *J. Aust. Phys. Eng. Sci. Med.*, 1997; **20**(1): 20-26.

Sykes J. R, James H. V and Williams P. C, How much does film sensitivity increase at depth for larger fields sizes?, *Med.Phys.*, 1997; **26**: 329-30.

Takahashi S, Conformation radiotherapy-rotation techniques as applied to radiography and radiotherapy of cancer, *Acta Radiol. Sippl.*, **242**: 1-142.

Tangboonduangjit P, Metcalfe P, Butson M, Quach K. Y and Rosenfield A, Matchline dosimetry in step and shoot IMRT fields: a film study, *Phys. Med. Biol.*, 2004; **49**: N287-N292.

Tatcher M and Palti S., Evaluation of Density Correction Algorithms for Photon-Beam Dose Calculations, *Radiology*, 1981; **141**: 201-205.

Tsien K. C, The Application of Automatic Computing Machines to Radiation Treatment Planning, *Br J Radiol*, 1955; **28**: 432-439.

Van Dyk J, Barnett R. B, Cygler J. E and Shragge P. C., Commissioning and Quality Assurance of Treatment Planning Computers, *Int. J. Radiation Oncology Biol. Phys.*, 1993; **26**(2): 261-273.

Varian, Primer on Dynamic Wedge and Lower Independent Jaws, Varian Associates, 1991.

Venencia C. D and Besa P, Commissioning and quality assurance for intensity modulated radiotherapy with dynamic multileaf collimator: Experience of the Pontificia Universidad Catolica de Chile, *J. Appl. Clin. Med. Phys.*, 2004; **5**(3): 37-54.

Webb S, Contemporary IMRT – Developing physics and clinical implementation, Institute of Physics Publishing, 2005.

Wierzbicki J and Blackmore L, Comparison of IMRT plans for different delivery systems, *Proc. World Congress in Medical Physics*, Sydeny, Australia, 2003.

Williams M. J and Metcalfe P, Verification of a rounded leaf-end MLC model used in a radiotherapy treatment planning system, *Phys. Med. Biol.*, 2006; **51**: N65-N78.

Williams J. R and Thwaites D. I., Radiotherapy physics in practice, Oxford Medical Publishing, 1993.

Williams J. R and Thwaites D. I., Radiotherapy physics in practice, Oxford Medical Publishing, 2004.

Williamson J. F, Khan F. M and Sharma S. C, Film dosimetry of megavoltage photon beams: a practical method of isodensity-to-isodose curve conversion, *Med.Phys.*, 1981; **8**: 94-98.

Wu Y, Yan D, Sharpe M. B, Miller B and Wong J. W, Implementing multiple field delivery for intensity modulated beams, *Med.Phys.*, 2001; **28**(11): 2188-2197.

Zhu X. R, Jursinic P. A, Grimm D. F, Lopez F, Rownd J. J and Gillin M. T, Evaluation of Kodak EDR2 film for dose verification of intensity modulated radiation therapy delivered by static multileaf collimator, *Med. Phys.*, 2002; **29**(8): 1687-1692.

Appendix A

Small field profile measurements for the Pinnacle model (Jaws only)

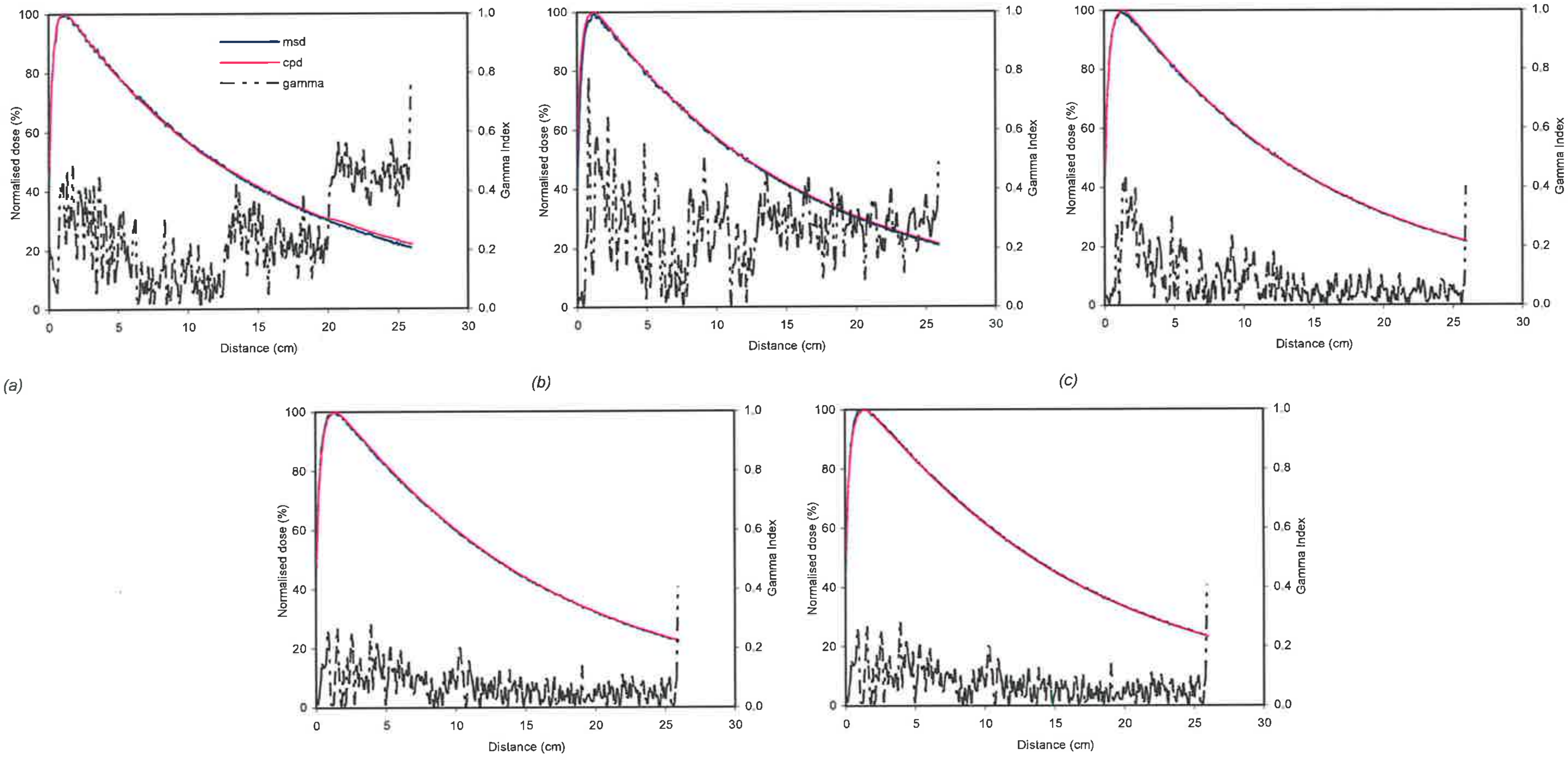

(a) (b) (c)

(d) (e)

Figure A.1: PinPoint ion chamber measured (msd) and Pinnacle computed (cpd) percentage depth dose curves with γ for (a) 1x1 cm^2 (b) 1.5x1.5 cm^2 (c) 2x2 cm^2 (d) 3x3 cm^2 (e) 4x4 cm^2. γ dose and distance tolerances set to 2% and 2 mm respectively.

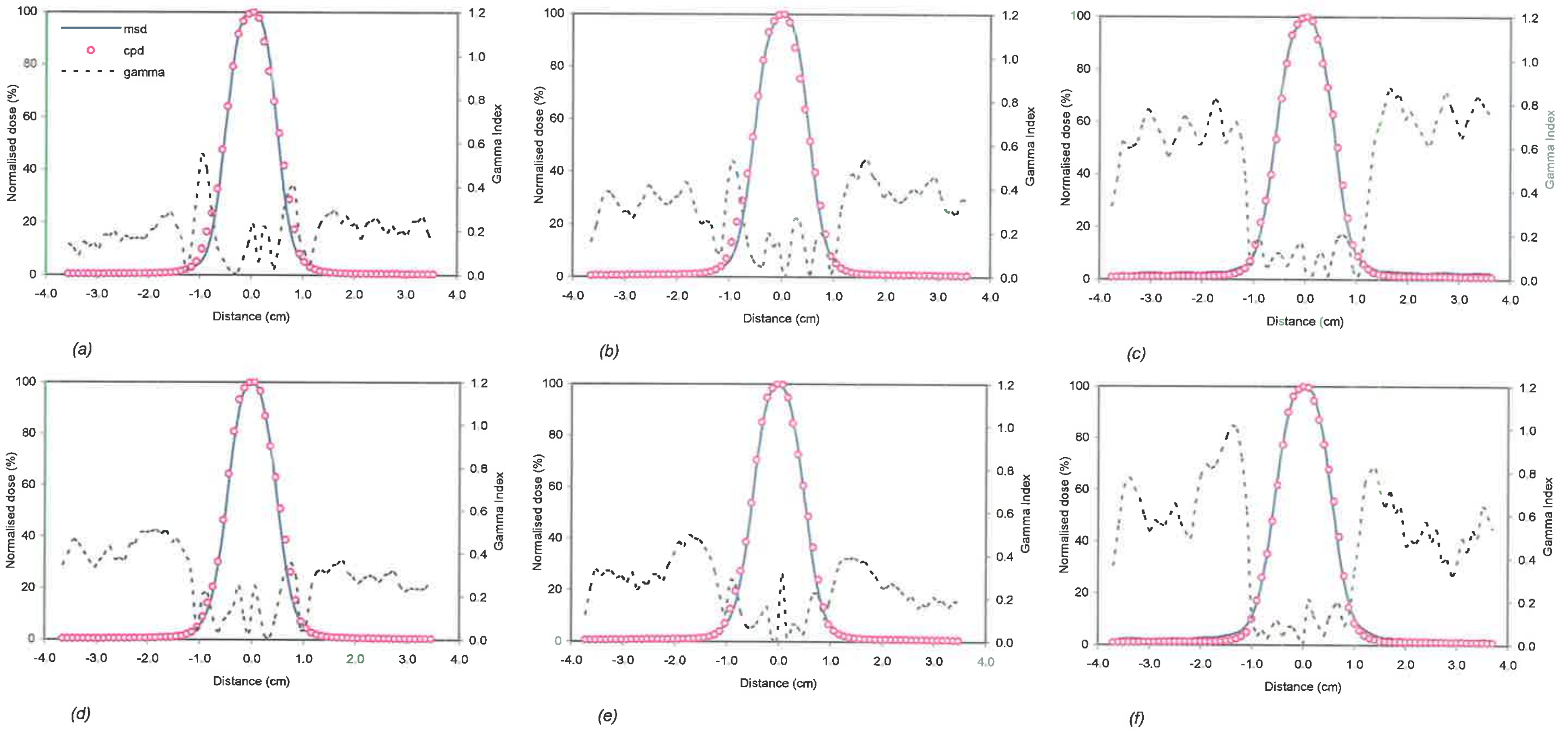

(a) (b) (c)

(d) (e) (f)

Figure A.2: PinPoint ion chamber measured (msd) and Pinnacle computed (cpd) 1x1 cm^2 profiles with γ for (a)(b)(c) Cross-plane at 5 cm, 10 cm and 20 cm respectively. (d)(e)(f) In-plane at 5 cm, 10 cm and 20 cm respectively. γ dose and distance tolerances set to 2% and 2 mm respectively.

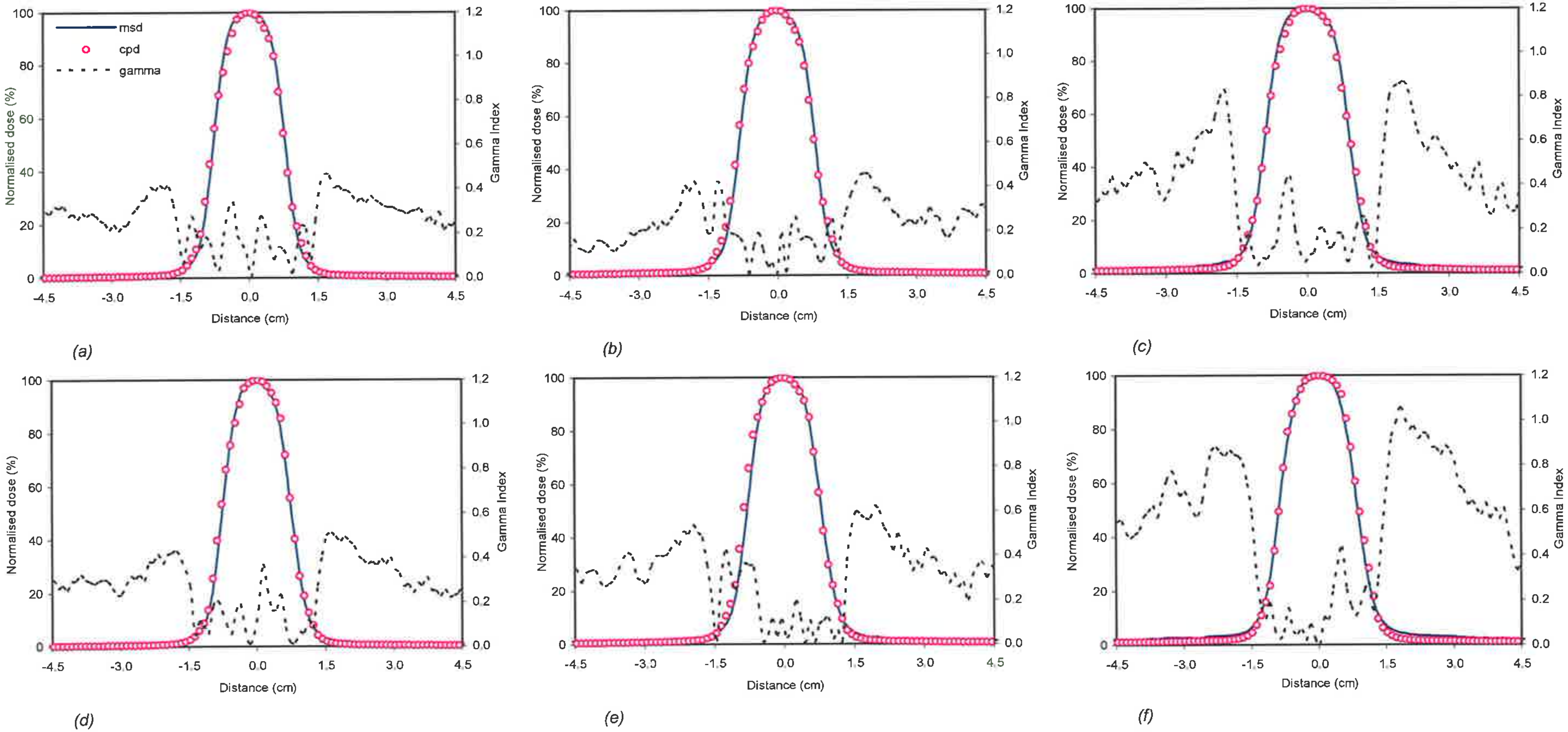

(a) (b) (c)

(d) (e) (f)

Figure A.3: PinPoint ion chamber measured (msd) and Pinnacle computed (cpd) 1.5x1.5 cm^2 profiles with γ for (a)(b)(c) Cross-plane at 5 cm, 10 cm and 20 cm respectively. (d)(e)(f) In-plane at 5 cm, 10 cm and 20 cm respectively. γ dose and distance tolerances set to 2% and 2 mm respectively.

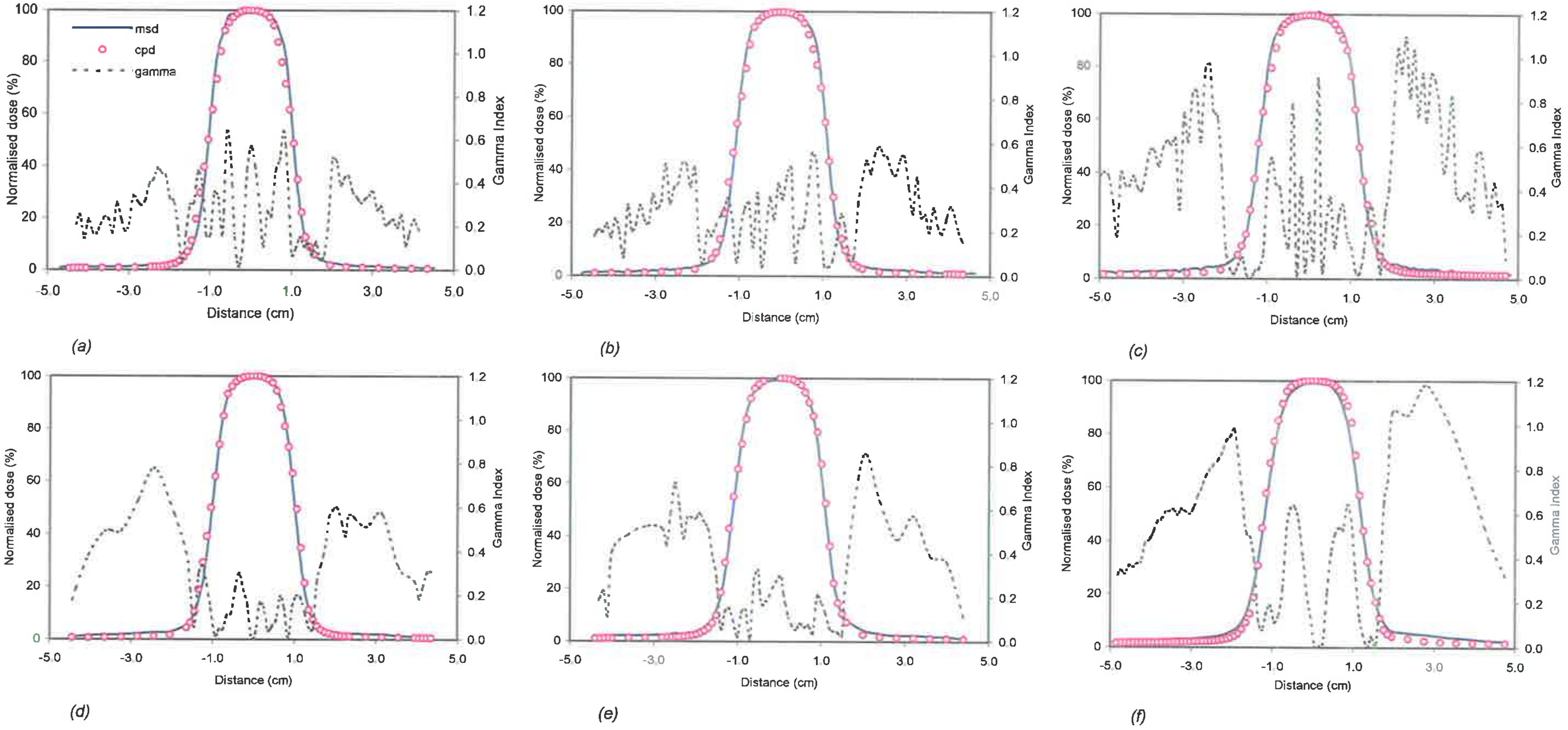

Figure A.4: PinPoint ion chamber measured (msd) and Pinnacle computed (cpd) 2x2 cm^2 profiles with γ for (a)(b)(c) Cross-plane at 5 cm, 10 cm and 20 cm respectively. (d)(e)(f) In-plane at 5 cm, 10 cm and 20 cm respectively. γ dose and distance tolerances set to 2% and 2 mm respectively.

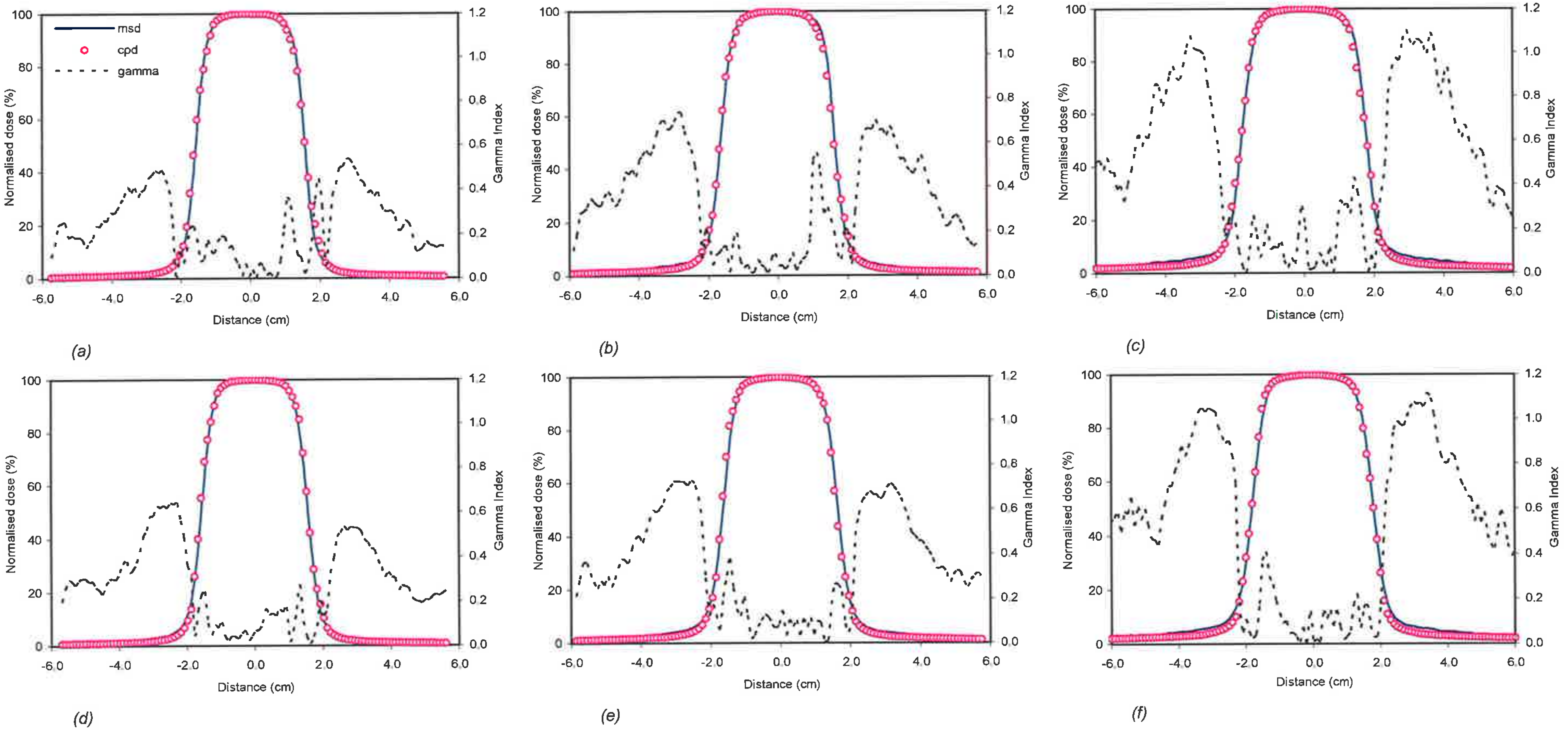

Figure A.5: PinPoint ion chamber measured (msd) and Pinnacle computed (cpd) 3x3 cm^2 profiles with γ for (a)(b)(c) Cross-plane at 5 cm, 10 cm and 20 cm respectively. (d)(e)(f) In-plane at 5 cm, 10 cm and 20 cm respectively. γ dose and distance tolerances set to 2% and 2 mm respectively.

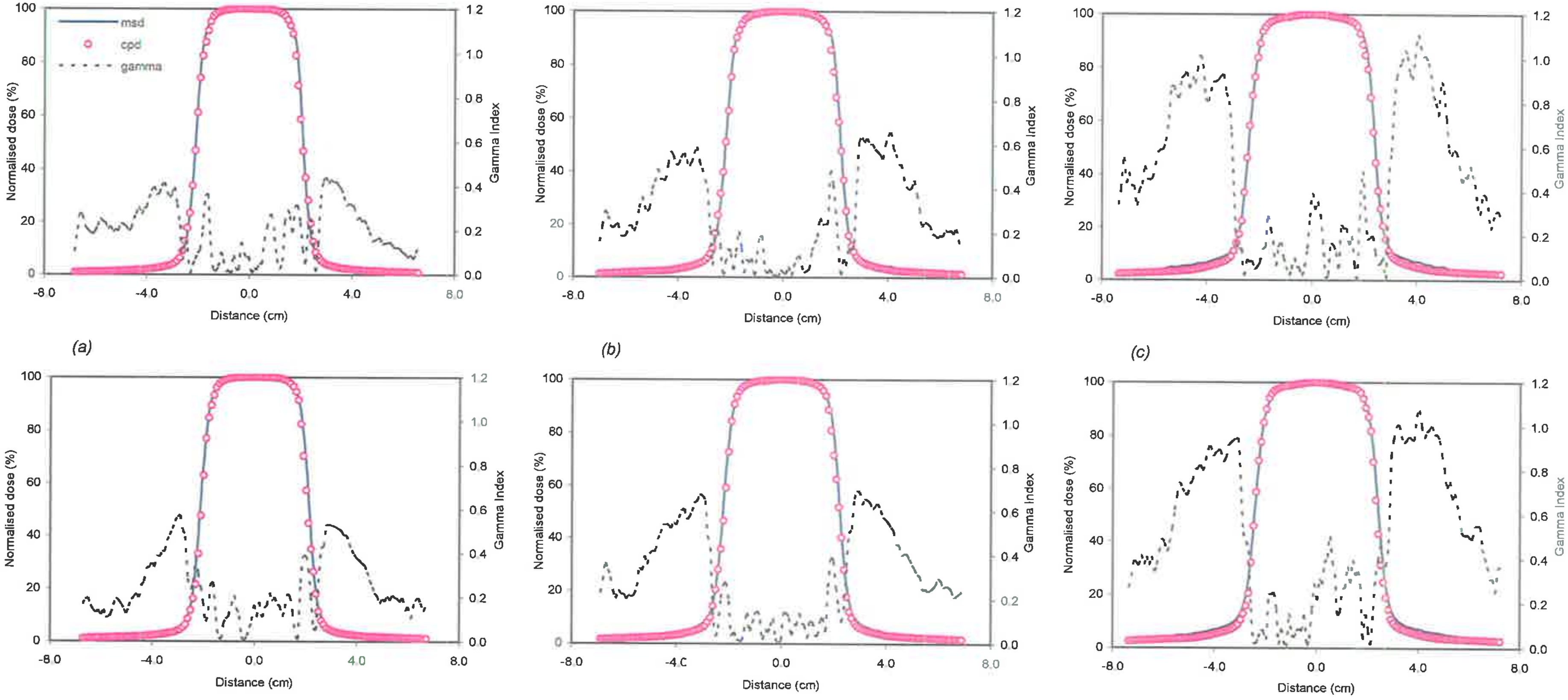

(a) (b) (c)

(d) (e) (f)

Figure A.6: PinPoint ion chamber measured (msd) and Pinnacle computed (cpd) 4x4 cm^2 profiles with γ for (a)(b)(c) Cross-plane at 5 cm, 10 cm and 20 cm respectively. (d)(e)(f) In-plane at 5 cm, 10 cm and 20 cm respectively. γ dose and distance tolerances set to 2% and 2 mm respectively.

Appendix B

Small field profile measurements (MLC only – off CAX)

I. Profile comparisons

Depth (cm)	50% penumbra (mm)						80% - 20% penumbra (mm)						90% - 10% penumbra (mm)					
	1x1 -ve	1x1 +ve	2x2 -ve	2x2 +ve	3x3 -ve	3x3 +ve	1x1 -ve	1x1 +ve	2x2 -ve	2x2 +ve	3x3 -ve	3x3 +ve	1x1 -ve	1x1 +ve	2x2 -ve	2x2 +ve	3x3 -ve	3x3 +ve
a	6.27	6.31	10.97	10.90	16.29	16.35	3.89	3.99	5.18	4.67	5.43	4.85	6.60	6.97	8.92	7.47	9.41	7.96
b	6.45	6.52	11.49	11.58	16.77	16.83	4.08	3.98	5.32	5.11	5.20	5.43	7.32	7.27	9.18	8.74	9.36	9.67
c	6.35	6.43	11.73	11.65	16.28	16.37	4.05	3.84	5.15	5.08	5.57	4.99	7.24	6.93	9.07	8.89	9.79	8.25
d	6.23	6.15	10.90	10.97	16.71	16.80	3.92	3.99	5.21	4.67	5.33	5.43	6.75	6.81	8.91	7.73	9.60	9.68
e	6.53	6.44	11.60	11.50	-	-	4.10	3.85	5.23	5.26	-	-	7.42	7.13	9.19	9.04	-	-
f	6.40	6.35	11.67	11.71	-	-	4.05	3.98	5.02	5.10	-	-	7.29	6.97	8.72	8.93	-	-
g	6.21	6.30	10.96	11.02	-	-	3.88	3.88	5.12	4.78	-	-	6.79	6.89	8.89	7.69	-	-
h	6.50	6.50	11.58	11.60	-	-	4.15	3.92	5.35	5.25	-	-	7.39	7.05	8.96	8.95	-	-
i	6.40	6.37	11.66	11.75	-	-	4.03	3.98	5.04	5.12	-	-	7.26	7.09	8.91	8.99	-	-

(a)

Depth (cm)	50% penumbra (mm)						80% - 20% penumbra (mm)						90% - 10% penumbra (mm)					
	1x1 -ve	1x1 +ve	2x2 -ve	2x2 +ve	3x3 -ve	3x3 +ve	1x1 -ve	1x1 +ve	2x2 -ve	2x2 +ve	3x3 -ve	3x3 +ve	1x1 -ve	1x1 +ve	2x2 -ve	2x2 +ve	3x3 -ve	3x3 +ve
a	5.16	5.22	10.29	10.34	15.56	15.59	3.25	3.33	3.52	3.77	3.68	3.88	5.34	5.47	6.31	6.76	6.85	7.15
b	5.22	5.19	10.32	10.33	15.61	15.61	3.21	3.17	3.68	3.79	3.77	3.88	5.17	5.42	6.97	7.03	7.12	7.24
c	5.21	5.24	10.31	10.40	15.71	15.65	3.19	3.29	3.63	3.79	3.95	3.80	5.25	5.56	6.73	6.84	7.47	7.09
d	5.31	5.31	10.23	10.21	15.66	15.71	3.05	3.36	3.68	3.59	4.01	3.85	5.38	5.77	6.28	6.61	7.64	7.05
e	5.35	5.29	10.23	10.21	-	-	3.28	3.34	3.68	3.59	-	-	5.50	5.80	6.28	6.61	-	-
f	5.37	5.29	10.19	10.26	-	-	3.13	3.40	3.82	3.72	-	-	5.50	5.80	6.92	6.99	-	-
g	5.27	5.28	10.36	10.29	-	-	3.13	3.39	3.70	3.61	-	-	5.36	5.70	6.70	6.24	-	-
h	5.23	5.22	10.41	10.40	-	-	3.18	3.36	3.69	3.62	-	-	5.58	5.61	6.88	6.60	-	-
i	5.23	5.32	10.42	10.33	-	-	3.25	3.36	3.80	3.65	-	-	5.56	5.56	7.20	6.73	-	-

(b)

Depth (cm)	50% penumbra (mm)						80% - 20% penumbra (mm)						90% - 10% penumbra (mm)					
	1x1 -ve	1x1 +ve	2x2 -ve	2x2 +ve	3x3 -ve	3x3 +ve	1x1 -ve	1x1 +ve	2x2 -ve	2x2 +ve	3x3 -ve	3x3 +ve	1x1 -ve	1x1 +ve	2x2 -ve	2x2 +ve	3x3 -ve	3x3 +ve
a	6.32	6.38	11.47	11.50	16.26	16.36	4.73	4.56	5.03	5.13	5.25	4.82	7.94	7.58	8.59	8.11	9.21	8.27
b	6.32	6.29	11.60	11.53	16.83	16.87	4.75	4.74	5.15	5.08	5.09	5.32	7.83	7.74	8.94	8.77	9.14	9.59
c	6.33	6.39	11.55	11.56	16.62	16.72	4.69	4.79	5.19	5.03	5.20	5.33	7.77	7.94	8.69	8.93	9.41	9.41
d	6.25	6.32	11.47	11.50	16.32	16.35	4.71	4.70	5.24	5.15	5.35	4.93	7.78	7.80	9.04	8.47	9.34	8.25
e	6.41	6.39	11.58	11.64	16.92	16.84	4.66	4.68	5.27	5.20	5.23	5.44	7.88	7.63	9.04	8.94	9.36	9.44
f	6.38	6.40	11.62	11.71	16.73	16.78	4.72	5.00	5.00	5.10	5.28	5.44	7.84	8.12	8.82	8.91	9.51	9.68
g	6.33	6.35	11.56	11.55	16.35	16.34	4.78	4.67	5.17	5.11	5.37	4.98	7.87	7.80	8.74	8.26	9.41	8.24
h	6.43	6.48	11.70	11.61	16.93	16.87	4.86	4.82	5.29	5.10	5.33	5.52	8.18	7.99	9.11	9.21	9.98	10.10
i	6.42	6.49	11.72	11.67	16.80	16.82	4.72	4.92	5.10	5.21	5.37	5.49	8.00	8.17	8.68	9.29	9.55	9.88

(c)

Depth (cm)	50% penumbra (mm)						80% - 20% penumbra (mm)						90% - 10% penumbra (mm)					
	1x1 -ve	1x1 +ve	2x2 -ve	2x2 +ve	3x3 -ve	3x3 +ve	1x1 -ve	1x1 +ve	2x2 -ve	2x2 +ve	3x3 -ve	3x3 +ve	1x1 -ve	1x1 +ve	2x2 -ve	2x2 +ve	3x3 -ve	3x3 +ve
a	5.23	5.15	10.16	10.24	15.45	15.52	3.16	3.27	3.71	3.39	3.68	4.06	5.29	5.57	6.68	6.23	6.92	7.05
b	5.15	5.11	10.24	10.19	15.53	15.48	3.30	3.56	3.77	3.41	3.76	4.01	5.47	-2.31	6.63	6.19	6.93	7.25
c	5.13	5.17	10.20	10.25	15.49	15.51	3.23	3.40	3.67	3.44	3.75	4.04	5.44	5.64	6.56	6.28	7.08	7.12
d	5.28	5.25	10.43	10.40	15.48	15.58	3.23	3.36	3.65	3.44	3.76	3.87	5.46	5.64	6.24	6.50	7.05	7.34
e	5.30	5.26	10.46	10.41	15.59	15.54	3.18	3.39	3.71	3.53	3.85	3.84	5.44	5.87	6.65	6.65	7.18	7.35
f	5.35	5.35	10.45	10.42	15.59	15.53	3.23	3.23	3.77	3.49	3.87	3.95	5.50	5.50	6.64	6.67	7.44	7.57
g	5.19	5.23	10.36	10.26	15.66	15.68	3.37	3.47	3.66	3.55	3.93	3.79	5.49	5.72	6.79	6.44	7.50	7.04
h	5.26	5.24	10.35	10.29	15.69	15.71	3.34	3.40	3.78	3.65	4.00	3.92	5.57	5.67	6.84	6.78	7.89	7.69
i	5.26	5.19	10.33	10.32	15.70	15.78	3.31	3.48	3.72	3.64	3.94	3.83	5.61	5.74	7.10	6.60	7.64	7.24

(d)

Table B.1: Penumbra results at 5 cm depth for 1x1 cm^2, 2x2 cm^2 and 3x3 cm^2 MLC defined segments off-axis with secondary collimators set to (a) Cross-plane10x10 cm^2 (b) In-plane 10x10 cm^2 (c) Cross-plane 15x15 cm^2 (d) In-plane 15x15 cm^2.

Depth (cm)	50% penumbra (mm)						80% - 20% penumbra (mm)						90% - 10% penumbra (mm)					
	1x1 -ve	1x1 +ve	2x2 -ve	2x2 +ve	3x3 -ve	3x3 +ve	1x1 -ve	1x1 +ve	2x2 -ve	2x2 +ve	3x3 -ve	3x3 +ve	1x1 -ve	1x1 +ve	2x2 -ve	2x2 +ve	3x3 -ve	3x3 +ve
a	6.71	6.73	11.53	11.56	17.14	17.17	4.16	4.14	5.51	4.97	5.90	5.18	7.13	7.39	9.88	8.14	10.69	8.97
b	6.79	6.75	12.20	12.27	17.68	17.65	4.29	4.21	5.74	5.40	5.82	6.04	7.54	7.54	9.77	9.73	10.81	11.03
c	6.76	6.78	12.23	12.28	17.14	17.22	4.28	4.25	5.47	5.24	6.10	5.31	7.93	7.76	9.91	9.54	11.12	9.34
d	6.55	6.64	11.52	11.49	17.68	17.62	4.03	4.16	5.48	4.87	5.77	6.03	7.00	7.18	9.60	8.01	10.85	11.11
e	6.78	6.84	12.13	12.18	-	-	4.42	4.28	5.70	5.49	-	-	7.70	7.72	10.00	9.99	-	-
f	6.78	6.71	12.23	12.31	-	-	4.37	4.21	5.39	5.38	-	-	7.74	7.62	9.55	9.73	-	-
g	6.60	6.53	11.45	11.50	-	-	4.08	4.14	5.69	5.10	-	-	6.92	7.37	9.84	8.47	-	-
h	6.90	6.86	12.24	12.20	-	-	4.20	4.33	5.56	5.44	-	-	7.47	7.64	9.77	9.86	-	-
I	6.73	6.83	12.29	12.24	-	-	4.48	4.17	5.39	5.44	-	-	7.87	7.55	9.70	9.72	-	-

(a)

Depth (cm)	50% penumbra (mm)						80% - 20% penumbra (mm)						90% - 10% penumbra (mm)					
	1x1 -ve	1x1 +ve	2x2 -ve	2x2 +ve	3x3 -ve	3x3 +ve	1x1 -ve	1x1 +ve	2x2 -ve	2x2 +ve	3x3 -ve	3x3 +ve	1x1 -ve	1x1 +ve	2x2 -ve	2x2 +ve	3x3 -ve	3x3 +ve
a	5.46	5.37	10.85	10.83	16.38	16.36	3.44	3.48	4.06	4.38	4.04	4.23	5.62	6.00	7.34	7.27	7.97	7.85
b	5.42	5.36	10.90	10.85	16.42	16.33	3.50	3.50	3.93	4.16	4.14	4.28	5.82	6.04	7.41	7.54	8.40	8.30
c	5.45	5.41	10.86	10.83	16.50	16.53	3.44	3.51	3.90	4.09	4.21	4.10	5.76	6.04	7.51	7.34	9.02	8.63
d	5.60	5.59	10.74	10.68	16.49	16.51	3.33	3.53	4.03	3.85	4.21	4.04	5.64	6.13	7.64	7.37	8.91	8.39
e	5.54	5.59	10.73	10.72	-	-	3.39	3.57	4.07	3.88	-	-	5.71	6.33	7.68	7.58	-	-
f	5.52	5.59	10.74	10.74	-	-	3.38	3.59	4.03	3.91	-	-	5.95	6.32	7.57	7.75	-	-
g	5.48	5.57	10.88	10.84	-	-	3.47	3.65	3.93	3.85	-	-	5.82	6.17	7.68	7.20	-	-
h	5.49	5.58	10.89	10.84	-	-	3.48	3.52	4.06	3.95	-	-	6.17	5.99	8.03	7.45	-	-
I	5.50	5.56	10.97	10.91	-	-	3.48	3.57	4.12	3.90	-	-	6.21	6.17	8.05	7.36	-	-

(b)

Depth (cm)	50% penumbra (mm)						80% - 20% penumbra (mm)						90% - 10% penumbra (mm)					
	1x1 -ve	1x1 +ve	2x2 -ve	2x2 +ve	3x3 -ve	3x3 +ve	1x1 -ve	1x1 +ve	2x2 -ve	2x2 +ve	3x3 -ve	3x3 +ve	1x1 -ve	1x1 +ve	2x2 -ve	2x2 +ve	3x3 -ve	3x3 +ve
a	6.78	6.68	12.12	12.20	17.10	17.19	4.91	4.91	5.36	5.23	5.61	5.22	8.27	8.14	9.53	8.94	10.37	9.05
b	6.68	6.64	12.19	12.10	17.83	17.75	4.77	4.92	5.66	5.41	5.55	5.68	8.46	8.35	9.77	9.86	10.55	10.90
c	6.76	6.73	12.15	12.22	17.52	17.61	5.03	5.13	5.42	5.26	5.63	5.84	8.49	8.53	9.60	9.44	10.53	10.96
d	6.65	6.63	12.18	12.21	17.14	17.23	4.99	4.99	5.49	5.43	5.71	5.24	8.64	8.56	9.87	9.07	10.42	9.09
e	6.66	6.76	12.25	12.19	17.83	17.75	4.91	5.00	5.67	5.50	5.58	5.76	8.60	8.32	9.94	10.07	10.54	10.81
f	6.73	6.79	12.22	12.19	17.70	17.61	4.92	5.22	5.48	5.37	5.82	5.99	8.71	8.82	9.91	9.67	10.96	11.09
g	6.67	6.66	12.25	12.16	17.17	17.21	5.12	4.91	5.46	5.42	5.76	5.34	8.48	8.41	9.98	9.21	10.74	9.16
h	6.83	6.76	12.19	12.26	17.84	17.83	5.11	5.02	5.67	5.61	5.77	6.03	8.72	8.63	9.96	10.23	11.40	11.79
I	6.75	6.79	12.26	12.29	17.65	17.71	5.07	5.30	5.40	5.56	5.87	6.10	8.52	8.89	9.77	9.98	10.93	11.34

(c)

Depth (cm)	50% penumbra (mm)						80% - 20% penumbra (mm)						90% - 10% penumbra (mm)					
	1x1 -ve	1x1 +ve	2x2 -ve	2x2 +ve	3x3 -ve	3x3 +ve	1x1 -ve	1x1 +ve	2x2 -ve	2x2 +ve	3x3 -ve	3x3 +ve	1x1 -ve	1x1 +ve	2x2 -ve	2x2 +ve	3x3 -ve	3x3 +ve
a	5.41	5.38	10.67	10.76	16.36	16.31	3.36	3.30	3.92	3.84	4.11	4.28	5.87	5.78	7.36	7.24	8.10	8.61
b	5.42	5.47	10.68	10.78	16.30	16.40	3.45	3.31	3.93	3.82	4.25	4.42	5.97	5.87	7.49	7.42	8.51	9.00
c	5.45	5.43	10.74	10.74	16.42	16.32	3.48	3.28	3.83	3.86	4.24	4.34	6.04	5.95	7.48	7.54	8.45	8.82
d	5.55	5.58	10.94	10.88	16.39	16.30	3.31	3.56	3.84	3.65	4.06	4.27	5.93	6.02	7.16	7.18	8.27	8.60
e	5.55	5.59	10.92	10.89	16.32	16.34	3.34	3.56	3.80	3.62	4.15	4.26	5.91	6.21	7.12	7.35	8.24	8.56
f	5.69	5.69	10.95	10.94	16.38	16.35	3.73	-3.73	3.92	3.78	4.26	4.34	6.26	-6.26	7.50	7.54	8.96	8.88
g	5.52	5.45	10.86	10.84	16.53	16.44	3.39	3.63	4.06	3.99	4.19	4.06	6.08	6.05	7.68	7.29	8.59	8.45
h	5.50	5.55	10.91	10.82	16.52	16.57	3.40	3.63	4.04	3.94	4.34	4.20	6.17	6.14	7.87	7.42	9.50	9.22
I	5.45	5.55	10.89	10.97	16.49	16.54	3.44	3.62	4.18	4.01	4.20	4.04	6.22	6.40	8.21	7.52	8.99	8.60

(d)

Table B.2: Penumbra results at 10 cm depth for 1x1 cm^2, 2x2 cm^2 and 3x3 cm^2 MLC defined segments off-axis with secondary collimators set to (a) Cross-plane10x10 cm^2 (b) In-plane 10x10 cm^2 (c) Cross-plane 15x15 cm^2 (d) In-plane 15x15 cm^2.

Depth (cm)	50% penumbra (mm)						80% - 20% penumbra (mm)						90% - 10% penumbra (mm)					
	1x1 -ve	1x1 +ve	2x2 -ve	2x2 +ve	3x3 -ve	3x3 +ve	1x1 -ve	1x1 +ve	2x2 -ve	2x2 +ve	3x3 -ve	3x3 +ve	1x1 -ve	1x1 +ve	2x2 -ve	2x2 +ve	3x3 -ve	3x3 +ve
a	7.42	7.46	12.66	12.57	18.77	18.87	4.58	4.79	6.12	5.50	6.53	5.69	7.69	8.35	11.66	9.05	12.90	10.65
b	7.65	7.58	13.32	13.39	19.40	19.46	5.12	4.91	6.05	6.14	6.67	6.85	9.03	8.90	11.23	11.13	13.42	13.84
c	7.39	7.35	13.39	13.45	18.82	18.92	4.77	4.86	6.06	5.82	6.76	5.92	8.35	8.79	11.18	11.27	14.06	11.76
d	7.41	7.35	12.64	12.62	19.42	19.40	4.66	4.72	5.83	5.36	6.68	6.84	7.97	8.71	10.91	9.09	12.58	13.11
e	7.38	7.48	13.36	13.33	-	-	4.80	4.90	6.23	6.11	-	-	8.62	9.14	11.31	11.06	-	-
f	7.37	7.39	13.41	13.42	-	-	4.89	4.84	5.98	5.93	-	-	8.71	8.61	11.20	12.23	-	-
g	7.35	7.32	12.64	12.70	-	-	4.76	4.64	5.92	5.28	-	-	8.21	8.49	11.13	9.36	-	-
h	7.49	7.48	13.33	13.35	-	-	4.75	4.82	6.12	6.12	-	-	8.52	8.86	11.08	11.67	-	-
I	7.51	7.45	13.44	13.45	-	-	5.05	4.77	5.93	6.01	-	-	8.91	8.73	10.99	11.84	-	-

(a)

Depth (cm)	50% penumbra (mm)						80% - 20% penumbra (mm)						90% - 10% penumbra (mm)					
	1x1 -ve	1x1 +ve	2x2 -ve	2x2 +ve	3x3 -ve	3x3 +ve	1x1 -ve	1x1 +ve	2x2 -ve	2x2 +ve	3x3 -ve	3x3 +ve	1x1 -ve	1x1 +ve	2x2 -ve	2x2 +ve	3x3 -ve	3x3 +ve
a	5.88	5.93	11.82	11.91	17.94	17.99	3.83	3.78	4.76	4.83	4.62	4.79	6.37	6.66	8.92	8.74	10.32	10.03
b	5.91	5.99	11.80	11.75	18.01	17.95	3.83	3.78	4.69	4.62	4.65	4.94	6.61	6.50	9.42	8.90	10.94	10.09
c	5.96	5.96	11.88	11.81	18.04	18.08	3.76	3.79	4.75	4.50	4.96	4.83	6.58	6.55	9.23	8.51	12.76	11.71
d	6.11	6.05	11.79	11.75	18.02	18.03	3.78	4.04	4.38	4.52	4.70	4.59	6.69	7.11	8.51	8.69	11.09	10.55
e	6.07	6.14	11.83	11.82	-	-	3.82	4.20	4.55	4.49	-	-	6.90	7.51	9.32	9.09	-	-
f	6.03	6.10	11.85	11.83	-	-	3.79	4.02	4.55	4.41	-	-	6.81	7.05	9.37	9.29	-	-
g	6.06	6.02	11.96	11.86	-	-	3.81	4.01	4.67	4.31	-	-	6.92	7.01	9.15	8.57	-	-
h	6.05	6.14	11.86	11.93	-	-	3.61	3.84	4.49	4.32	-	-	6.51	6.86	8.89	7.98	-	-
I	6.07	6.05	11.89	11.93	-	-	3.84	3.91	4.71	4.35	-	-	7.01	7.07	9.35	8.55	-	-

(b)

Depth (cm)	50% penumbra (mm)						80% - 20% penumbra (mm)						90% - 10% penumbra (mm)					
	1x1 -ve	1x1 +ve	2x2 -ve	2x2 +ve	3x3 -ve	3x3 +ve	1x1 -ve	1x1 +ve	2x2 -ve	2x2 +ve	3x3 -ve	3x3 +ve	1x1 -ve	1x1 +ve	2x2 -ve	2x2 +ve	3x3 -ve	3x3 +ve
a	7.35	7.33	13.30	13.27	18.80	18.71	5.33	5.27	5.94	5.68	6.47	5.72	9.34	8.80	11.22	9.59	13.12	10.48
b	7.22	7.29	13.39	13.32	19.48	19.45	5.59	5.34	6.13	6.00	6.45	6.61	9.71	9.27	11.28	11.31	13.24	13.28
c	7.46	7.44	13.32	13.32	19.35	19.30	5.45	5.59	5.79	5.84	6.56	6.63	9.60	9.49	10.81	11.12	12.83	13.61
d	7.41	7.40	13.33	13.35	18.85	18.77	5.36	5.42	6.15	5.66	6.25	5.57	9.10	9.31	11.16	9.40	12.55	10.71
e	7.43	7.40	13.40	13.40	19.52	19.43	5.49	5.36	6.17	5.90	6.31	6.68	9.36	9.32	11.52	11.31	12.82	12.89
f	7.49	7.55	13.41	13.46	19.37	19.38	5.52	5.67	5.95	5.97	6.84	6.81	9.90	9.92	11.12	11.70	13.10	14.54
g	7.39	7.30	13.34	13.37	18.77	18.80	5.36	5.34	6.12	5.74	6.43	5.66	9.52	9.09	11.17	9.79	12.95	10.26
h	7.38	7.48	13.45	13.40	19.62	19.58	5.51	5.40	6.34	6.07	6.76	7.02	9.72	9.53	11.39	11.49	15.84	15.11
I	7.39	7.47	13.44	13.54	19.45	19.39	5.48	5.82	5.97	6.06	6.63	7.06	10.21	10.25	10.90	11.70	14.17	13.93

(c)

Depth (cm)	50% penumbra (mm)						80% - 20% penumbra (mm)						90% - 10% penumbra (mm)					
	1x1 -ve	1x1 +ve	2x2 -ve	2x2 +ve	3x3 -ve	3x3 +ve	1x1 -ve	1x1 +ve	2x2 -ve	2x2 +ve	3x3 -ve	3x3 +ve	1x1 -ve	1x1 +ve	2x2 -ve	2x2 +ve	3x3 -ve	3x3 +ve
a	5.78	5.88	11.80	11.72	17.93	17.97	3.74	3.98	4.44	4.66	4.75	4.75	6.44	7.09	8.78	8.64	10.86	10.36
b	5.80	5.79	11.88	11.82	18.04	17.94	3.77	3.97	4.35	4.61	4.76	4.75	6.42	7.07	8.85	9.11	11.22	10.65
c	5.90	5.83	11.79	11.86	17.99	17.95	3.72	4.05	4.38	4.59	4.78	4.72	6.78	7.06	8.61	8.46	10.71	9.87
d	6.10	6.13	11.92	11.93	17.91	17.90	3.95	3.74	4.22	4.19	4.46	4.78	6.87	6.93	8.43	8.67	10.22	11.20
e	6.13	6.08	11.96	11.93	17.91	17.96	3.92	3.82	4.35	4.41	4.53	4.77	6.92	6.70	9.02	8.74	10.69	11.09
f	6.16	6.16	11.99	11.98	17.93	18.02	3.91	3.83	4.49	4.41	4.68	4.84	7.20	7.00	9.95	9.23	11.88	11.87
g	5.99	5.95	11.96	11.87	17.94	18.03	3.84	4.07	4.76	4.45	4.62	4.69	6.76	7.01	9.67	8.73	11.11	10.67
h	6.08	5.99	11.90	11.96	18.05	18.09	3.77	3.93	4.63	4.36	4.99	4.84	6.89	7.09	9.52	8.75	13.25	14.88
I	6.11	6.04	11.95	11.97	17.96	18.05	3.72	3.95	4.68	4.33	4.81	4.69	7.15	7.14	9.91	9.01	11.07	11.07

(d)

Table B.3: Penumbra results at 20 cm depth for 1x1 cm^2, 2x2 cm^2 and 3x3 cm^2 MLC defined segments off-axis with secondary collimators set to (a) Cross-plane10x10 cm^2 (b) In-plane 10x10 cm^2 (c) Cross-plane 15x15 cm^2 (d) In-plane 15x15 cm^2.

II. Output factor measurement

Secondary collimator (cm^2)	Segment size (cm^2)	Water depth (cm)	Segment #	X offset (cm)	Y offset (cm)	Total offset	Dose / MU (PP)	Dose / MU (P^3)	Error
10x10	1x1	5	*a*	4.2	4.2	5.9	0.679	0.700	**2.9%**
			b	2.1	4.2	4.7	0.675	0.713	**5.3%**
			c	0.0	4.2	4.2	0.672	0.702	**4.2%**
			d	4.2	2.1	4.7	0.676	0.701	**3.5%**
			e	2.1	2.1	3.0	0.670	0.713	**6.0%**
			f	0.0	2.1	2.1	0.666	0.701	**5.1%**
			g	4.2	0.0	4.2	0.677	0.695	**2.6%**
			h	2.1	0.0	2.1	0.667	0.706	**5.5%**
			i	0.0	0.0	0.0	0.661	0.690	**4.1%**
		10	*a*	4.4	4.4	6.2	0.480	0.507	**5.3%**
			b	2.2	4.4	4.9	0.480	0.513	**6.4%**
			c	0.0	4.4	4.4	0.479	0.510	**6.1%**
			d	4.4	2.2	4.9	0.483	0.510	**5.3%**
			e	2.2	2.2	3.1	0.480	0.516	**7.0%**
			f	0.0	2.2	2.2	0.479	0.512	**6.3%**
			g	4.4	0.0	4.4	0.487	0.505	**3.5%**
			h	2.2	0.0	2.2	0.482	0.510	**5.4%**
			i	0.0	0.0	0.0	0.478	0.503	**4.9%**
		20	*a*	4.8	4.8	6.8	0.243	0.271	**10.2%**
			b	2.4	4.8	5.4	0.248	0.275	**9.6%**
			c	0.0	4.8	4.8	0.249	0.273	**8.7%**
			d	4.8	2.4	5.4	0.250	0.273	**8.3%**
			e	2.4	2.4	3.4	0.253	0.277	**8.5%**
			f	0.0	2.4	2.4	0.253	0.275	**7.9%**
			g	4.8	0.0	4.8	0.255	0.271	**5.9%**
			h	2.4	0.0	2.4	0.256	0.275	**6.7%**
			i	0.0	0.0	0.0	0.255	0.271	**5.9%**

Table B4: Results for the % error between Pinnacle calculated and ion chamber measured output factors for 1x1 cm^2 MLC segments off-axis with secondary collimators at 10x10 cm^2 plotted as a function of X and Y at 5 cm, 10cm, and 20 cm depth.

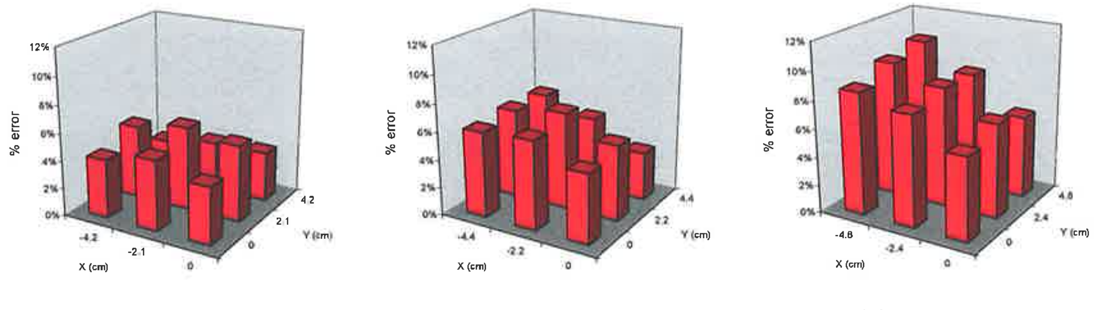

(a) (b) (c)

Figure B1: % error between Pinnacle calculated and ion chamber measured output factor for 1x1 cm^2 MLC segments off-axis with secondary collimators at 10x10 cm^2 plotted as a function of X and Y at (a) 5 cm (b) 10cm (c) 20 cm depth.

Secondary collimator (cm^2)	Segment size (cm^2)	Water depth (cm)	Segment #	X offset (cm)	Y offset (cm)	Total offset	Dose / MU (PP)	Dose / MU (P^3)	Error
15x15	2x2	5	*a*	4.2	4.2	5.9	0.763	0.791	3.5%
			b	2.1	4.2	4.7	0.766	0.793	3.4%
			c	0.0	4.2	4.2	0.763	0.793	3.7%
			d	4.2	2.1	4.7	0.763	0.789	3.3%
			e	2.1	2.1	3.0	0.761	0.789	3.5%
			f	0.0	2.1	2.1	0.757	0.788	3.9%
			g	4.2	0.0	4.2	0.761	0.788	3.3%
			h	2.1	0.0	2.1	0.757	0.786	3.7%
			i	0.0	0.0	0.0	0.750	0.781	3.9%
		10	*a*	4.4	4.4	6.2	0.549	0.569	3.5%
			b	2.2	4.4	4.9	0.552	0.573	3.6%
			c	0.0	4.4	4.4	0.552	0.573	3.6%
			d	4.4	2.2	4.9	0.551	0.570	3.4%
			e	2.2	2.2	3.1	0.551	0.574	3.9%
			f	0.0	2.2	2.2	0.548	0.572	4.1%
			g	4.4	0.0	4.4	0.548	0.569	3.6%
			h	2.2	0.0	2.2	0.547	0.570	4.0%
			i	0.0	0.0	0.0	0.543	0.566	4.1%
		20	*a*	4.8	4.8	6.8	0.289	0.300	3.5%
			b	2.4	4.8	5.4	0.291	0.302	3.3%
			c	0.0	4.8	4.8	0.291	0.302	3.6%
			d	4.8	2.4	5.4	0.290	0.300	3.0%
			e	2.4	2.4	3.4	0.292	0.302	3.3%
			f	0.0	2.4	2.4	0.290	0.302	3.8%
			g	4.8	0.0	4.8	0.290	0.300	3.1%
			h	2.4	0.0	2.4	0.291	0.301	3.3%
			i	0.0	0.0	0.0	0.289	0.299	3.4%

Table B5: Results for the % error between Pinnacle calculated and ion chamber measured output factors for 2x2 cm^2 MLC segments off-axis with secondary collimators at 10x10 cm^2 plotted as a function of X and Y at 5 cm, 10cm, and 20 cm depth.

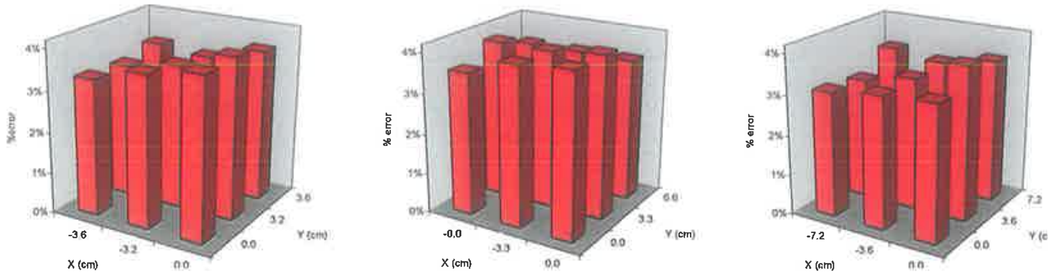

(a) (b) (c)

Figure B2: % error between Pinnacle calculated and ion chamber measured output factor for 2x2 cm^2 MLC segments off-axis with secondary collimators at 10x10 cm^2 plotted as a function of X and Y at (a) 5 cm (b) 10cm (c) 20 cm depth.

Secondary collimator (cm^2)	Segment size (cm^2)	Water depth (cm)	Segment #	X offset (cm)	Y offset (cm)	Total offset	Dose / MU (PP)	Dose / MU (P^3)	Error
15x15	3x3	5	*a*	3.7	3.7	5.2	0.795	0.811	1.9%
			b	0.0	3.7	3.7	0.794	0.813	2.3%
			c	3.7	0.0	3.7	0.794	0.809	1.8%
			d	0.0	0.0	0.0	0.785	0.804	2.3%
		10	*a*	3.9	3.9	5.5	0.580	0.592	2.0%
			b	0.0	3.9	3.9	0.581	0.593	2.0%
			c		0.0	3.9	0.579	0.592	2.1%
			d	0.0	0.0	0.0	0.574	0.588	2.3%
		20	*a*	4.2	4.2	5.9	0.309	0.317	2.5%
			b	0.0	4.2	4.2	0.310	0.319	2.6%
			c	4.2	0.0	4.2	0.309	0.316	2.4%
			d	0.0	0.0	0.0	0.307	0.315	2.4%

Table B6: Results for the % error between Pinnacle calculated and ion chamber measured output factors for 3x3 cm^2 MLC segments off-axis with secondary collimators at 10x10 cm^2 plotted as a function of X and Y at 5 cm, 10cm, and 20 cm depth.

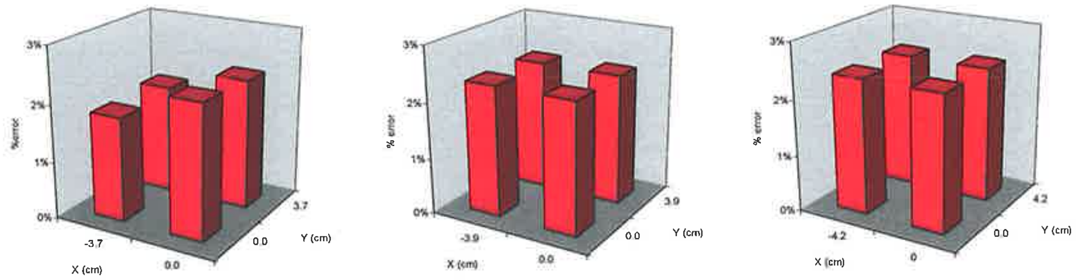

(a) (b) (c)

Figure B3: % error between Pinnacle calculated and ion chamber measured output factor for 3x3 cm^2 MLC segments off-axis with secondary collimators at 10x10 cm^2 plotted as a function of X and Y at (a) 5 cm (b) 10cm (c) 20 cm depth.

Secondary collimator (cm^2)	Segment size (cm^2)	Water depth (cm)	Segment #	X offset (cm)	Y offset (cm)	Total offset	Dose / MU (PP)	Dose / MU (P^3)	Error
10x10	1x1	5	*a*	4.2	4.2	5.9	0.679	0.706	3.9%
			b	2.1	4.2	4.7	0.682	0.704	3.2%
			c	0.0	4.2	4.2	0.679	0.711	4.6%
			d	4.2	2.1	4.7	0.683	0.710	3.8%
			e	2.1	2.1	3.0	0.678	0.708	4.2%
			f	0.0	2.1	2.1	0.674	0.713	5.5%
			g	4.2	0.0	4.2	0.684	0.712	3.8%
			h	2.1	0.0	2.1	0.673	0.707	4.8%
			i	0.0	0.0	0.0	0.668	0.707	5.5%
		10	*a*	4.4	4.4	6.2	0.480	0.512	6.3%
			b	2.2	4.4	4.9	0.479	0.514	6.8%
			c	0.0	4.4	4.4	0.482	0.519	7.1%
			d	4.4	2.2	4.9	0.482	0.514	6.2%
			e	2.2	2.2	3.1	0.486	0.515	5.5%
			f	0.0	2.2	2.2	0.483	0.519	6.9%
			g	4.4	0.0	4.4	0.483	0.519	6.9%
			h	2.2	0.0	2.2	0.486	0.516	5.7%
			i	0.0	0.0	0.0	0.477	0.515	7.3%
		20	*a*	4.8	4.8	6.8	0.219	0.273	19.7%
			b	2.4	4.8	5.4	0.233	0.274	14.7%
			c	0.0	4.8	4.8	0.234	0.276	15.1%
			d	4.8	2.4	5.4	0.239	0.275	13.1%
			e	2.4	2.4	3.4	0.251	0.277	9.4%
			f	0.0	2.4	2.4	0.251	0.279	10.0%
			g	4.8	0.0	4.8	0.244	0.276	11.3%
			h	2.4	0.0	2.4	0.253	0.277	8.6%
			i	0.0	0.0	0.0	0.254	0.277	8.5%

Table B7: Results for the % error between Pinnacle calculated and ion chamber measured output factors for 1x1 cm^2 MLC segments off-axis with secondary collimators at 15x15 cm^2 plotted as a function of X and Y at 5 cm, 10cm, and 20 cm depth.

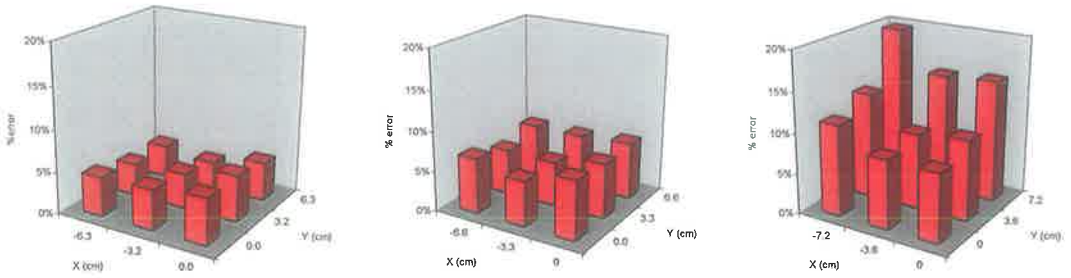

(a) (b) (c)

Figure B4: % error between Pinnacle calculated and ion chamber measured output factor for 1x1 cm^2 MLC segments off-axis with secondary collimators at 15x15 cm^2 plotted as a function of X and Y at (a) 5 cm (b) 10cm (c) 20 cm depth.

Secondary collimator (cm^2)	Segment size (cm^2)	Water depth (cm)	Segment #	X offset (cm)	Y offset (cm)	Total offset	Dose / MU (PP)	Dose / MU (P^3)	Error
15x15	2x2	5	*a*	4.2	4.2	5.9	0.775	0.795	**2.5%**
			b	2.1	4.2	4.7	0.775	0.801	**3.2%**
			c	0.0	4.2	4.2	0.775	0.802	**3.4%**
			d	4.2	2.1	4.7	0.776	0.798	**2.8%**
			e	2.1	2.1	3.0	0.771	0.803	**3.9%**
			f	0.0	2.1	2.1	0.766	0.801	**4.3%**
			g	4.2	0.0	4.2	0.775	0.799	**3.1%**
			h	2.1	0.0	2.1	0.765	0.802	**4.5%**
			i	0.0	0.0	0.0	0.752	0.793	**5.0%**
		10	*a*	4.4	4.4	6.2	0.554	0.575	**3.5%**
			b	2.2	4.4	4.9	0.556	0.579	**4.0%**
			c	0.0	4.4	4.4	0.557	0.581	**4.1%**
			d	4.4	2.2	4.9	0.557	0.577	**3.4%**
			e	2.2	2.2	3.1	0.556	0.581	**4.3%**
			f	0.0	2.2	2.2	0.553	0.581	**4.7%**
			g	4.4	0.0	4.4	0.558	0.578	**3.4%**
			h	2.2	0.0	2.2	0.553	0.580	**4.7%**
			i	0.0	0.0	0.0	0.545	0.575	**5.1%**
		20	*a*	4.8	4.8	6.8	0.289	0.301	**3.9%**
			b	2.4	4.8	5.4	0.291	0.305	**4.3%**
			c	0.0	4.8	4.8	0.292	0.305	**4.1%**
			d	4.8	2.4	5.4	0.293	0.305	**3.7%**
			e	2.4	2.4	3.4	0.295	0.310	**4.6%**
			f	0.0	2.4	2.4	0.294	0.308	**4.5%**
			g	4.8	0.0	4.8	0.294	0.303	**3.0%**
			h	2.4	0.0	2.4	0.294	0.306	**3.8%**
			i	0.0	0.0	0.0	0.291	0.303	**4.1%**

Table B8: Results for the % error between Pinnacle calculated and ion chamber measured output factors for 2x2 cm^2 MLC segments off-axis with secondary collimators at 15x15 cm^2 plotted as a function of X and Y at 5 cm, 10cm, and 20 cm depth.

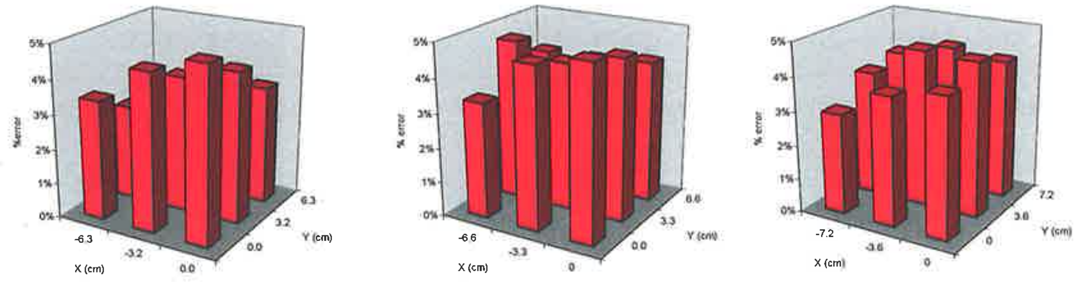

(a) (b) (c)

Figure B5: % error between Pinnacle calculated and ion chamber measured output factor for 2x2 cm^2 MLC segments off-axis with secondary collimators at 15x15 cm^2 plotted as a function of X and Y at (a) 5 cm (b) 10cm (c) 20 cm depth.

Secondary collimator (cm^2)	Segment size (cm^2)	Water depth (cm)	Segment #	X offset (cm)	Y offset (cm)	Total offset	Dose / MU (PP)	Dose / MU (P^3)	Error
15x15	3x3	5	*a*	4.2	4.2	5.9	0.805	0.815	1.1%
			b	2.1	4.2	4.7	0.808	0.822	1.6%
			c	0.0	4.2	4.2	0.807	0.824	2.0%
			d	4.2	2.1	4.7	0.808	0.818	1.1%
			e	2.1	2.1	3.0	0.807	0.823	1.9%
			f	0.0	2.1	2.1	0.801	0.822	2.4%
			g	4.2	0.0	4.2	0.807	0.818	1.3%
			h	2.1	0.0	2.1	0.800	0.820	2.5%
			i	0.0	0.0	0.0	0.787	0.813	3.2%
		10	***a***	4.4	4.4	6.2	0.582	0.595	2.1%
			b	2.2	4.4	4.9	0.593	0.600	1.1%
			c	0.0	4.4	4.4	0.587	0.601	2.3%
			d	4.4	2.2	4.9	0.587	0.597	1.6%
			e	2.2	2.2	3.1	0.590	0.601	1.9%
			f	0.0	2.2	2.2	0.586	0.600	2.4%
			g	4.4	0.0	4.4	0.586	0.598	1.9%
			h	2.2	0.0	2.2	0.584	0.600	2.5%
			i	0.0	0.0	0.0	0.576	0.594	3.0%
		20	***a***	4.8	4.8	6.8	0.307	0.317	3.1%
			b	2.4	4.8	5.4	0.311	0.321	3.0%
			c	0.0	4.8	4.8	0.312	0.322	2.9%
			d	4.8	2.4	5.4	0.310	0.319	2.7%
			e	2.4	2.4	3.4	0.314	0.323	2.7%
			f	0.0	2.4	2.4	0.313	0.322	2.8%
			g	4.8	0.0	4.8	0.310	0.319	2.7%
			h	2.4	0.0	2.4	0.313	0.321	2.6%
			i	0.0	0.0	0.0	0.308	0.319	3.2%

Table B9: Results for the % error between Pinnacle calculated and ion chamber measured output factors for 3x3 cm^2 MLC segments off-axis with secondary collimators at 15x15 cm^2 plotted as a function of X and Y at 5 cm, 10cm, and 20 cm depth.

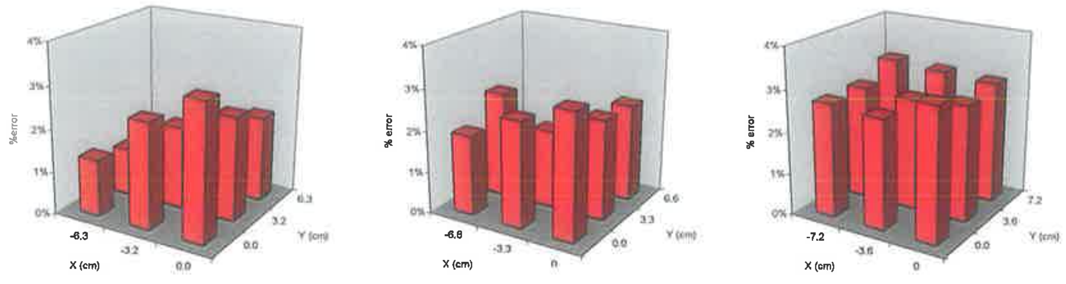

(a) (b) (c)

Figure B6: % error between Pinnacle calculated and ion chamber measured output factor for 3x3 cm^2 MLC segments off-axis with secondary collimators at 15x15 cm^2 plotted as a function of X and Y at (a) 5 cm (b) 10cm (c) 20 cm depth.

Appendix C

Small field profile measurements (MLC only – on CAX)

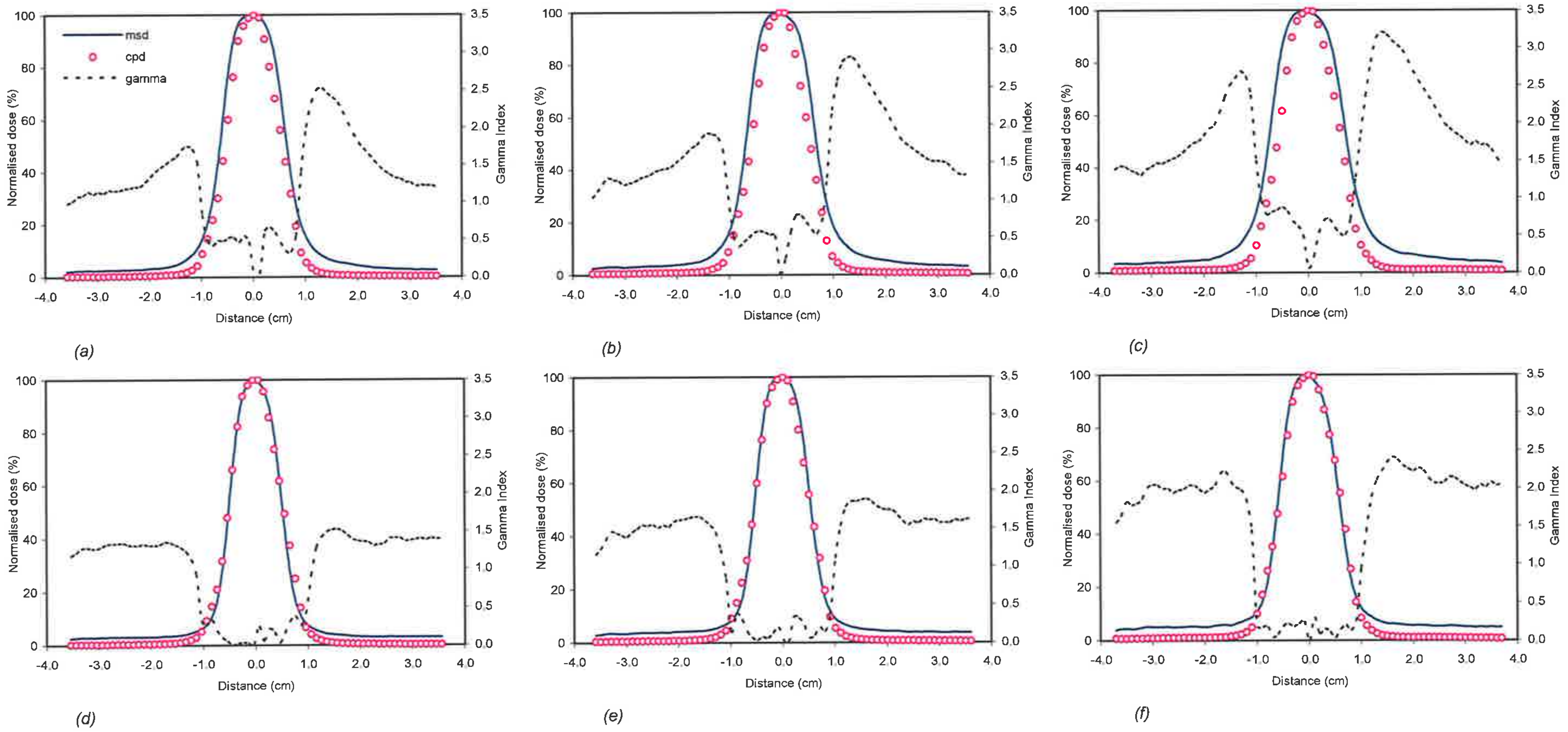

Figure C.1: PinPoint ion chamber measured (msd) and Pinnacle computed (cpd) 1x1 cm^2 profiles with γ for (a)(b)(c) Cross-plane at 5 cm, 10 cm and 20 cm respectively. (d)(e)(f) In-plane at 5 cm, 10 cm and 20 cm respectively. γ dose and distance tolerances set to 2% and 2 mm respectively.

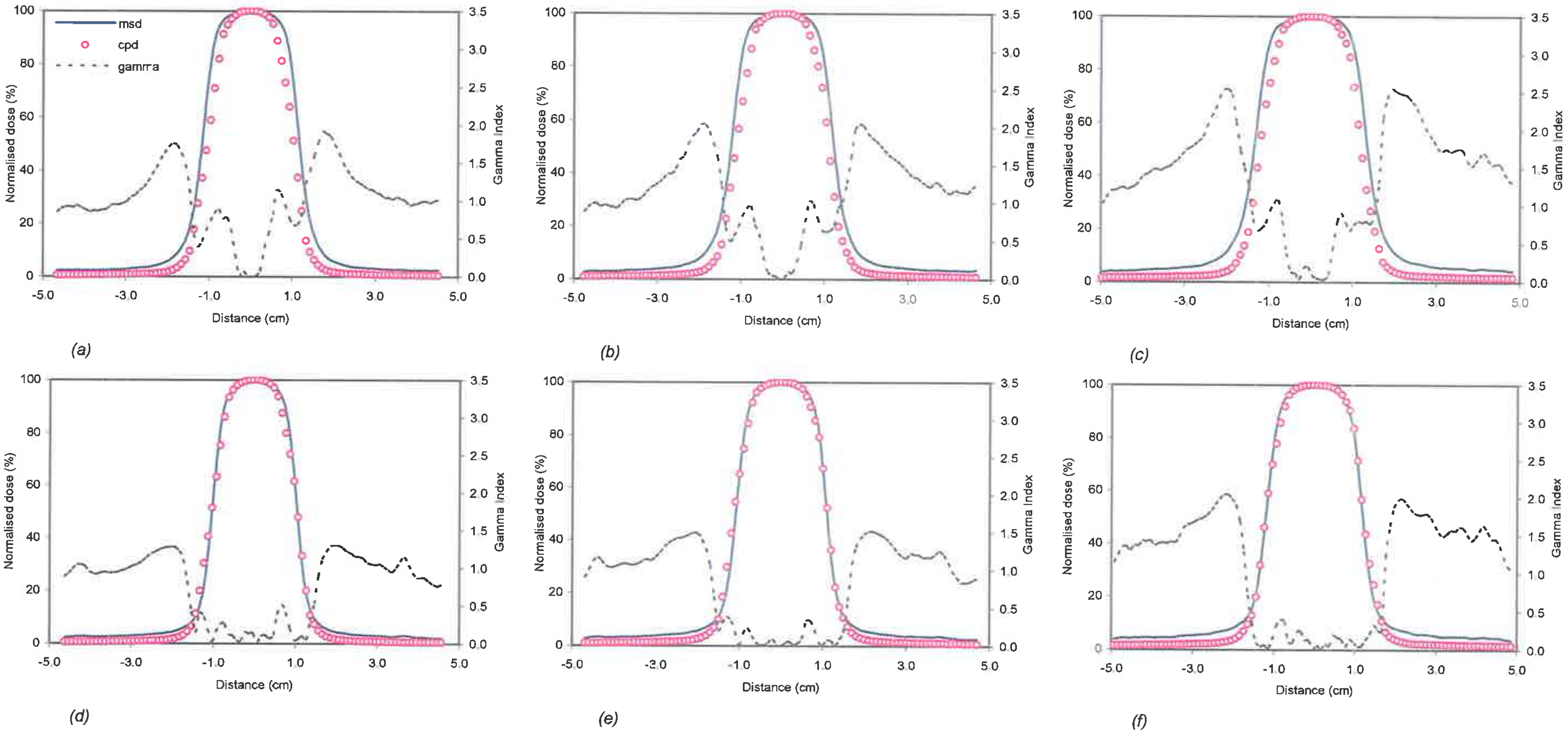

Figure C.2: PinPoint ion chamber measured (msd) and Pinnacle computed (cpd) 2x2 cm^2 profiles with γ for (a)(b)(c) Cross-plane at 5 cm, 10 cm and 20 cm respectively. (d)(e)(f) In-plane at 5 cm, 10 cm and 20 cm respectively. γ dose and distance tolerances set to 2% and 2 mm respectively.

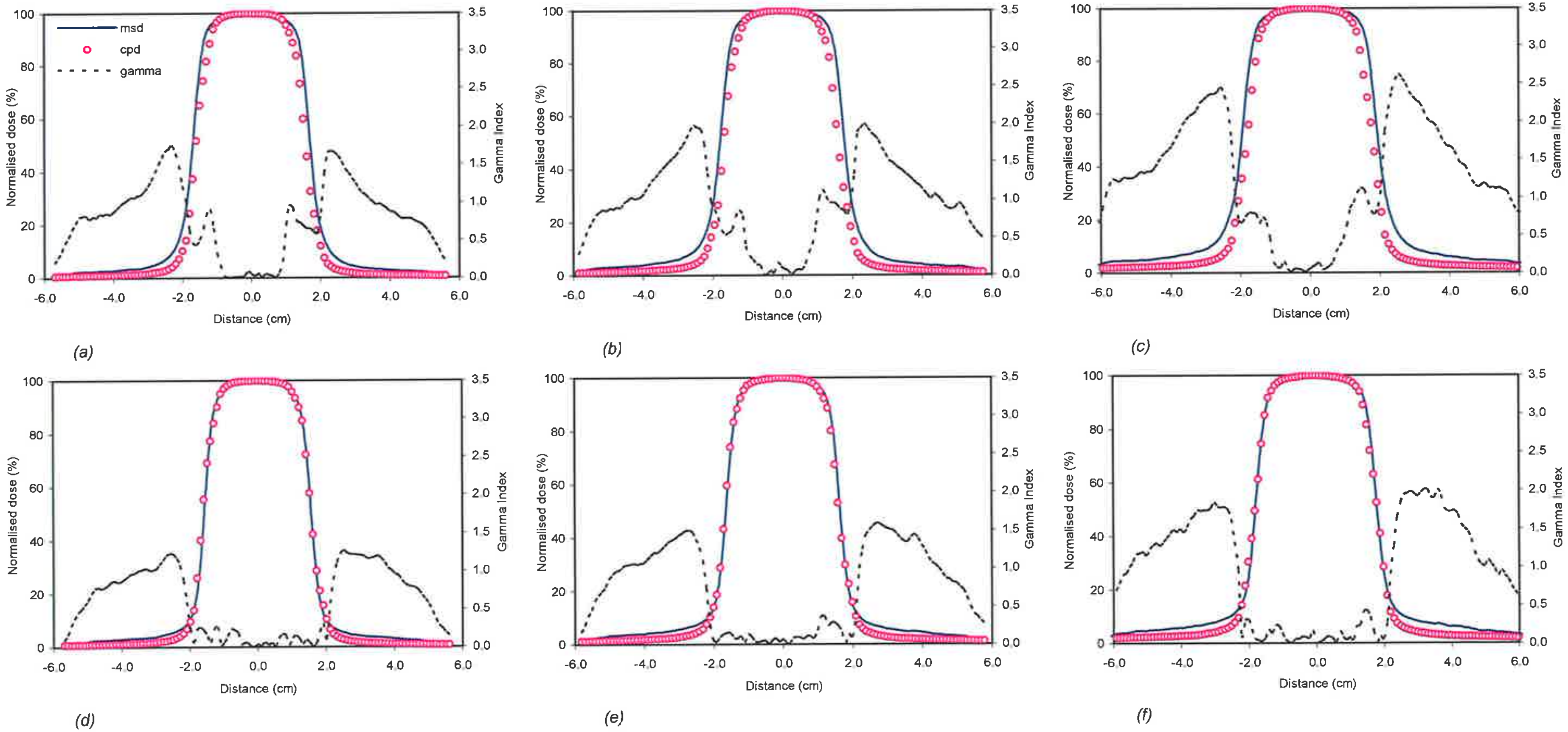

Figure C.3: PinPoint ion chamber measured (msd) and Pinnacle computed (cpd) 3x3 cm^2 profiles with γ for (a)(b)(c) Cross-plane at 5 cm, 10 cm and 20 cm respectively. (d)(e)(f) In-plane at 5 cm, 10 cm and 20 cm respectively. γ dose and distance tolerances set to 2% and 2 mm respectively.Appendix D.

Appendix D

Multi-leaf collimator characterisation measurements

I. Match-line effect

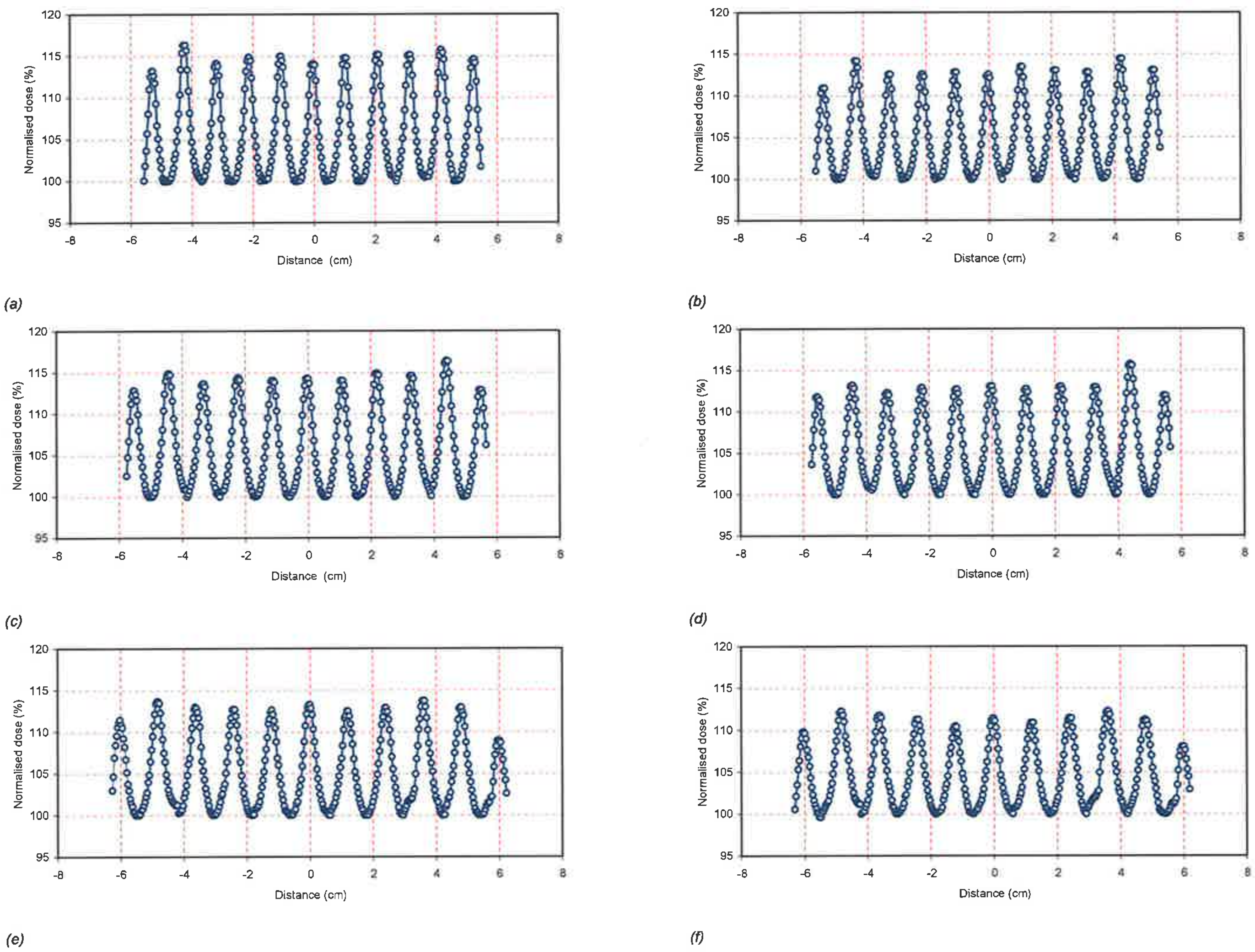

Figure D.1: (a) (c) (e) Normalised hotspots due to rounded leaf junction as a function of distance from central axis, with segments delivered statically, and profile through the junction of 4 leaves for 11 5x1 cm^2 segments at 5 cm, 10 cm and 20 cm respectively. (a) (d) (f) Normalised hotspots due to rounded leaf junction as a function of distance from central axis, with segments delivered statically, and profile through the junction of 2 leaves for 11 5x1 cm^2 segments at 5 cm, 10 cm and 20 cm respectively.

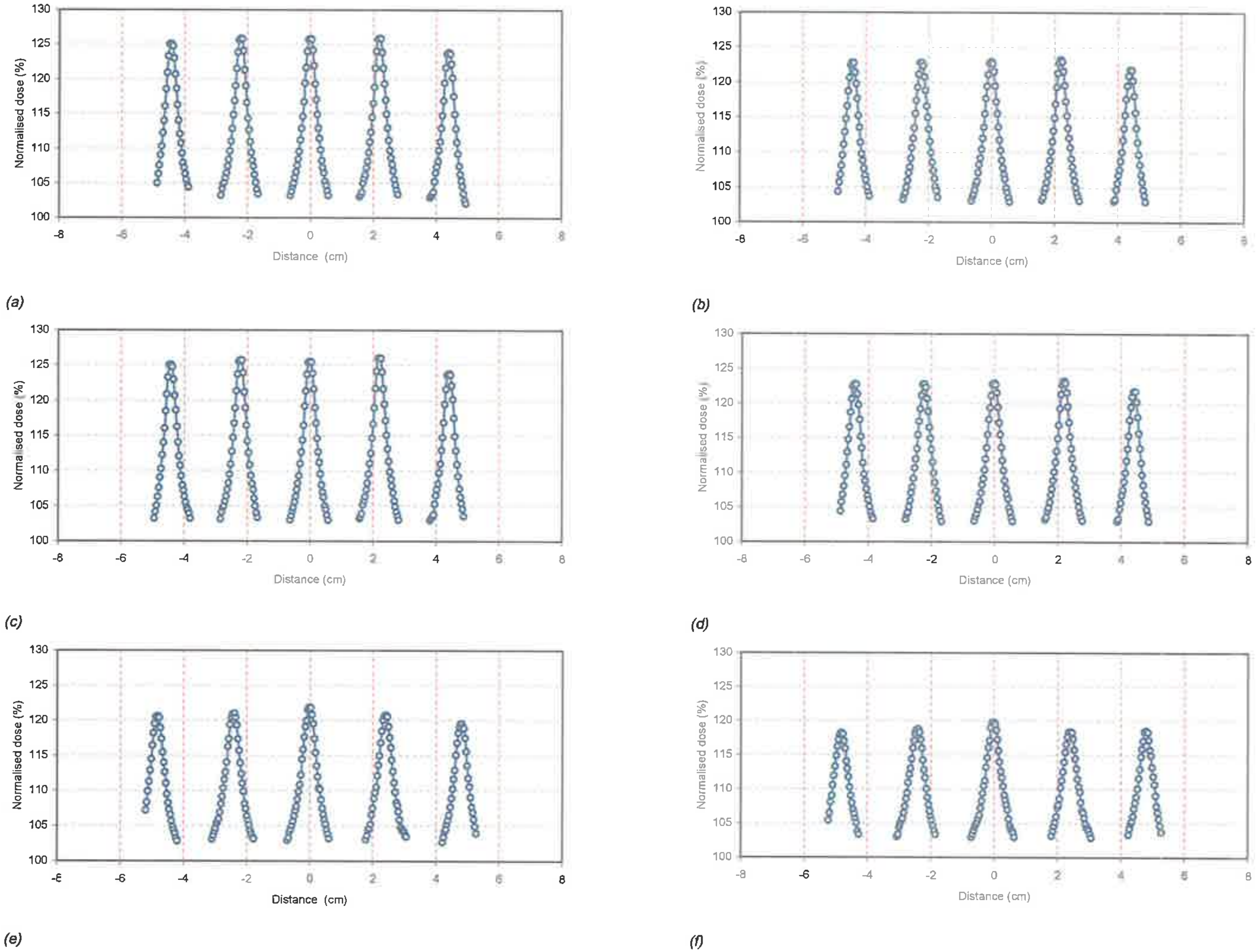

Figure D.2: (a) (c) (e) Normalised hotspots due to rounded leaf junction as a function of distance from central axis, with segments delivered dynamically, and profile through the junction of 4 leaves for 11 5x1 cm^2 segments at 5 cm, 10 cm and 20 cm respectively. (a) (d) (f) Normalised hotspots due to rounded leaf junction as a function of distance from central axis, with segments delivered dynamically, and profile through the junction of 2 leaves for 11 5x1 cm^2 segments at 5 cm, 10 cm and 20 cm respectively.

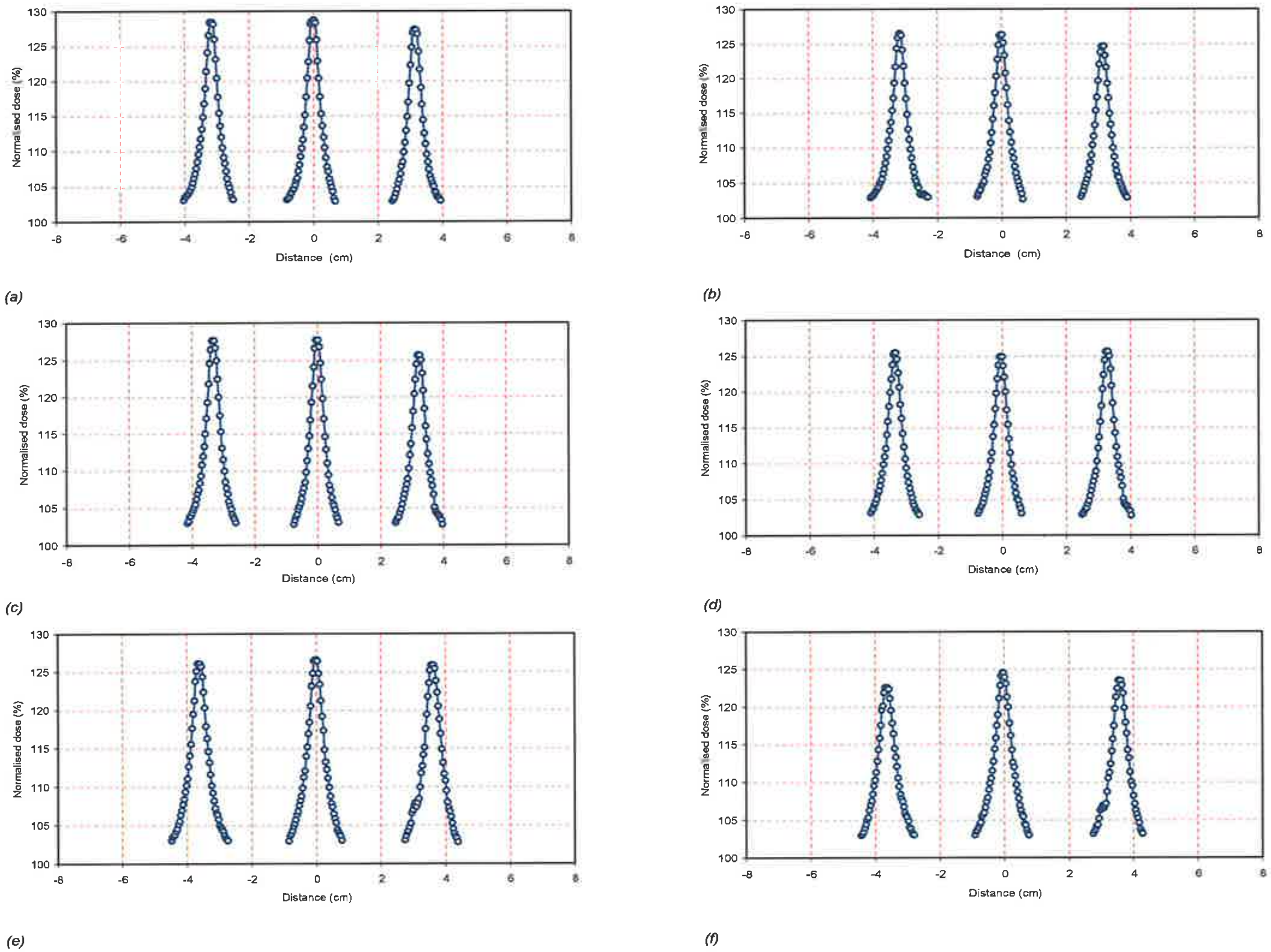

Figure D.3: (a) (c) (e) Normalised hotspots due to rounded leaf junction as a function of distance from central axis, with segments delivered statically, and profile through the junction of 4 leaves for 5 5x2 cm^2 segments at 5 cm, 10 cm and 20 cm respectively. (a) (d) (f) Normalised hotspots due to rounded leaf junction as a function of distance from central axis, with segments delivered statically, and profile through the junction of 2 leaves for 5 5x2 cm^2 segments at 5 cm, 10 cm and 20 cm respectively.

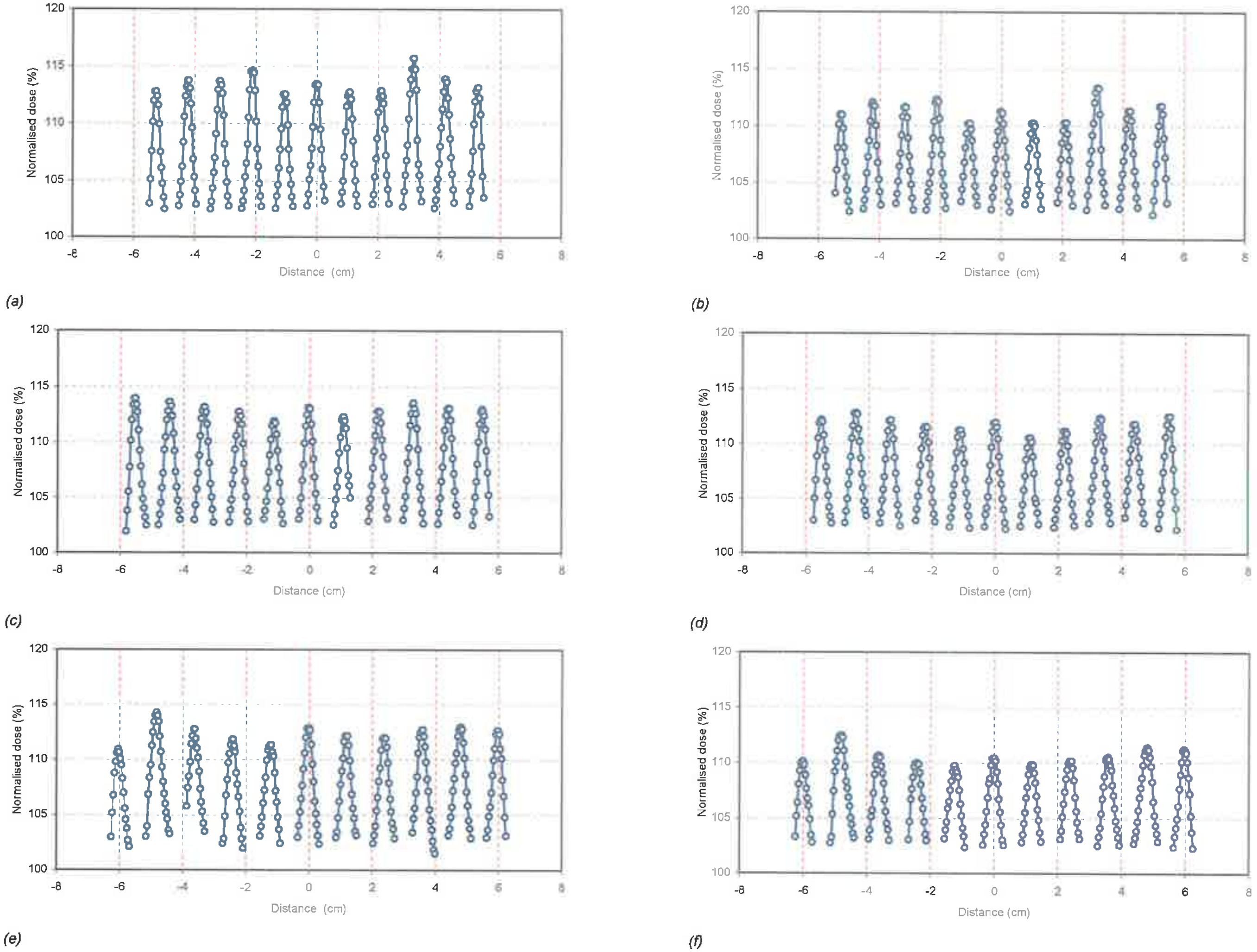

(a) (b) (c) (d) (e) (f)

Figure D.4: (a) (c) (e) Normalised hotspots due to rounded leaf junction as a function of distance from central axis, with segments delivered dynamically, and profile through the junction of 4 leaves for 11 5x1 cm^2 segments at 5 cm, 10 cm and 20 cm respectively. (a) (d) (f) Normalised hotspots due to rounded leaf junction as a function of distance from central axis, with segments delivered dynamically, and profile through the junction of 2 leaves for 11 5x1 cm^2 segments at 5 cm, 10 cm and 20 cm respectively.

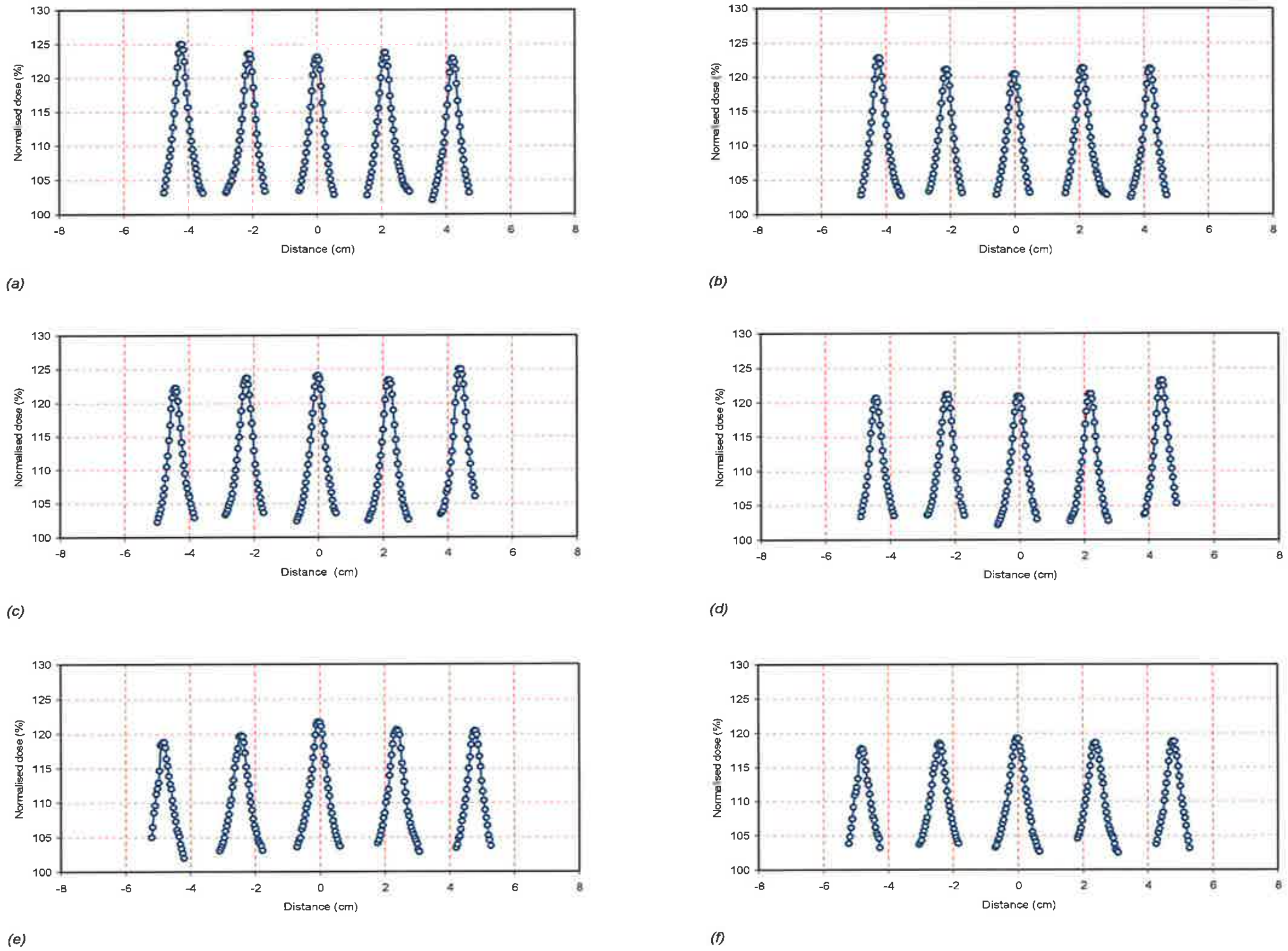

(a) (b) (c) (d) (e) (f)

Figure D.5: (a) (c) (e) Normalised hotspots due to rounded leaf junction as a function of distance from central axis, with segments delivered dynamically, and profile through the junction of 4 leaves for 5 5x2 cm^2 segments at 5 cm, 10 cm and 20 cm respectively. (a) (d) (f) Normalised hotspots due to rounded leaf junction as a function of distance from central axis, with segments delivered dynamically, and profile through the junction of 2 leaves for 5 5x2 cm^2 segments at 5 cm, 10 cm and 20 cm respectively.

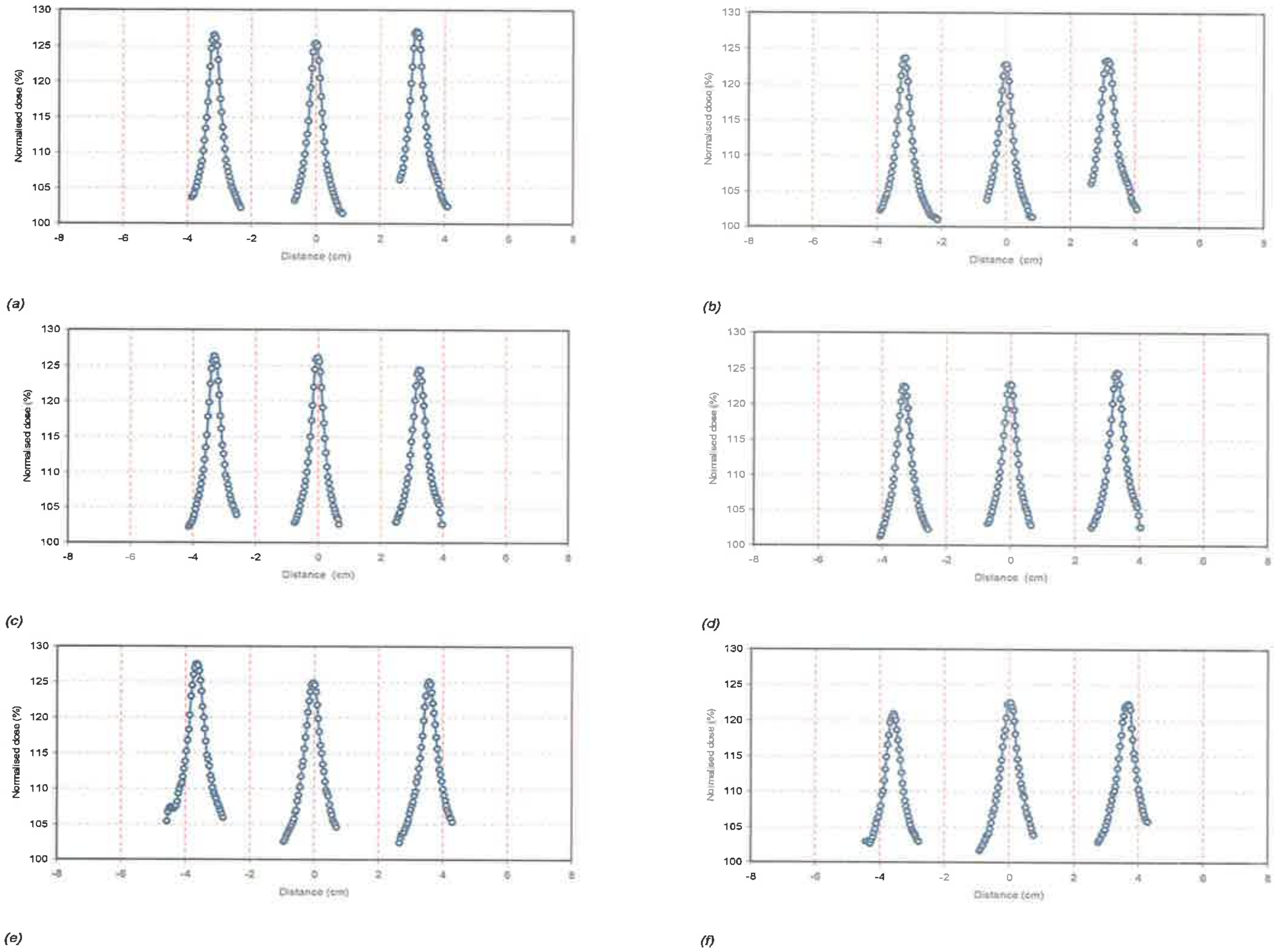

Figure D.6: (a) (c) (e) Normalised hotspots due to rounded leaf junction as a function of distance from central axis, with segments delivered dynamically, and profile through the junction of 4 leaves for 3 5x3 cm^2 segments at 5 cm, 10 cm and 20 cm respectively. (a) (d) (f) Normalised hotspots due to rounded leaf junction as a function of distance from central axis, with segments delivered dynamically, and profile through the junction of 2 leaves for 3 5x3 cm^2 segments at 5 cm, 10 cm and 20 cm respectively.

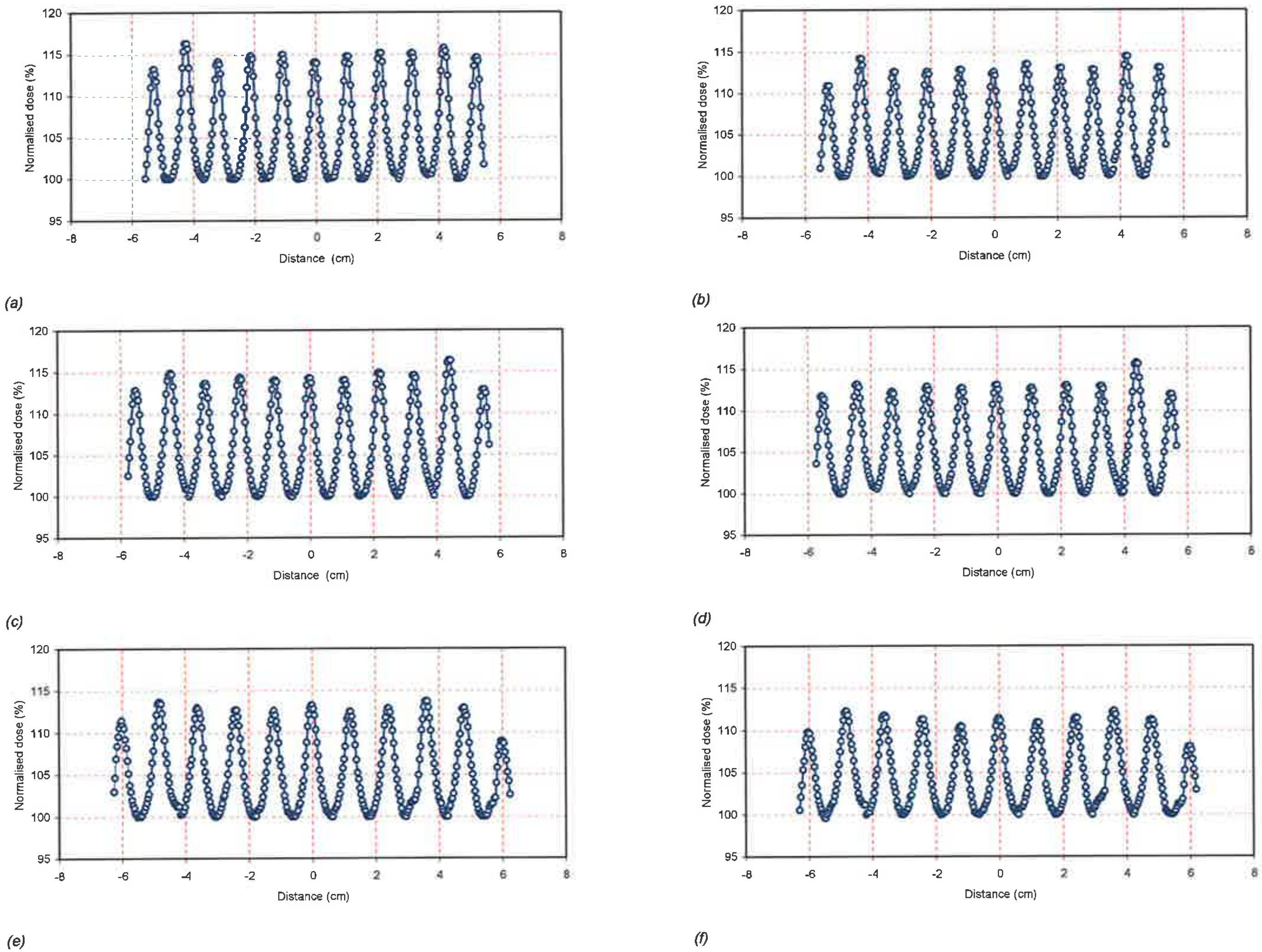

Figure D.1: (a) (c) (e) Normalised hotspots due to rounded leaf junction as a function of distance from central axis, with segments delivered statically, and profile through the junction of 4 leaves for 11 5x1 cm^2 segments at 5 cm, 10 cm and 20 cm respectively. (a) (d) (f) Normalised hotspots due to rounded leaf junction as a function of distance from central axis, with segments delivered statically, and profile through the junction of 2 leaves for 11 5x1 cm^2 segments at 5 cm, 10 cm and 20 cm respectively.

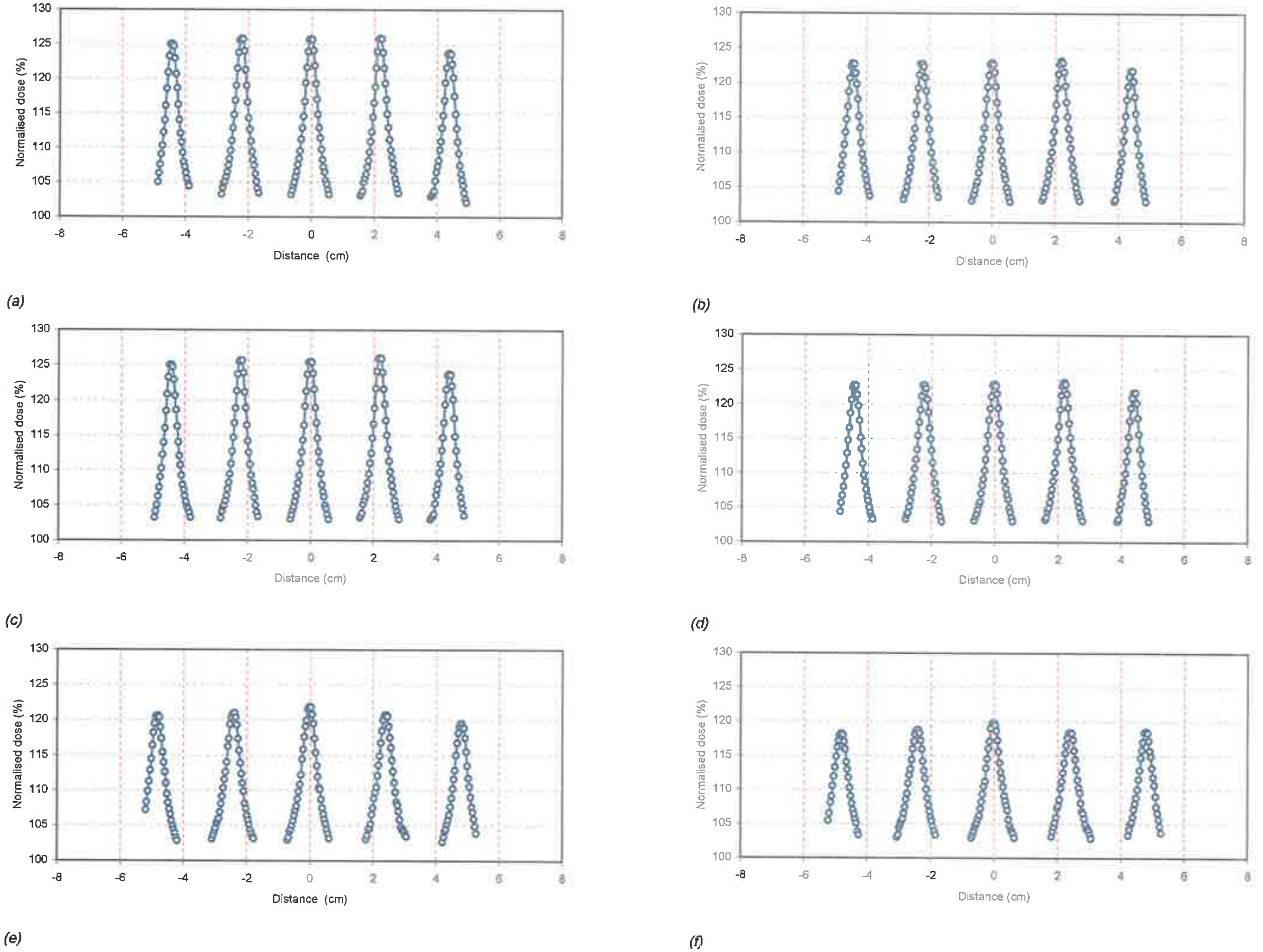

Figure D.2: (a) (c) (e) Normalised hotspots due to rounded leaf junction as a function of distance from central axis, with segments delivered dynamically, and profile through the junction of 4 leaves for 11 5x1 cm^2 segments at 5 cm, 10 cm and 20 cm respectively. (a) (d) (f) Normalised hotspots due to rounded leaf junction as a function of distance from central axis, with segments delivered dynamically, and profile through the junction of 2 leaves for 11 5x1 cm^2 segments at 5 cm, 10 cm and 20 cm respectively.

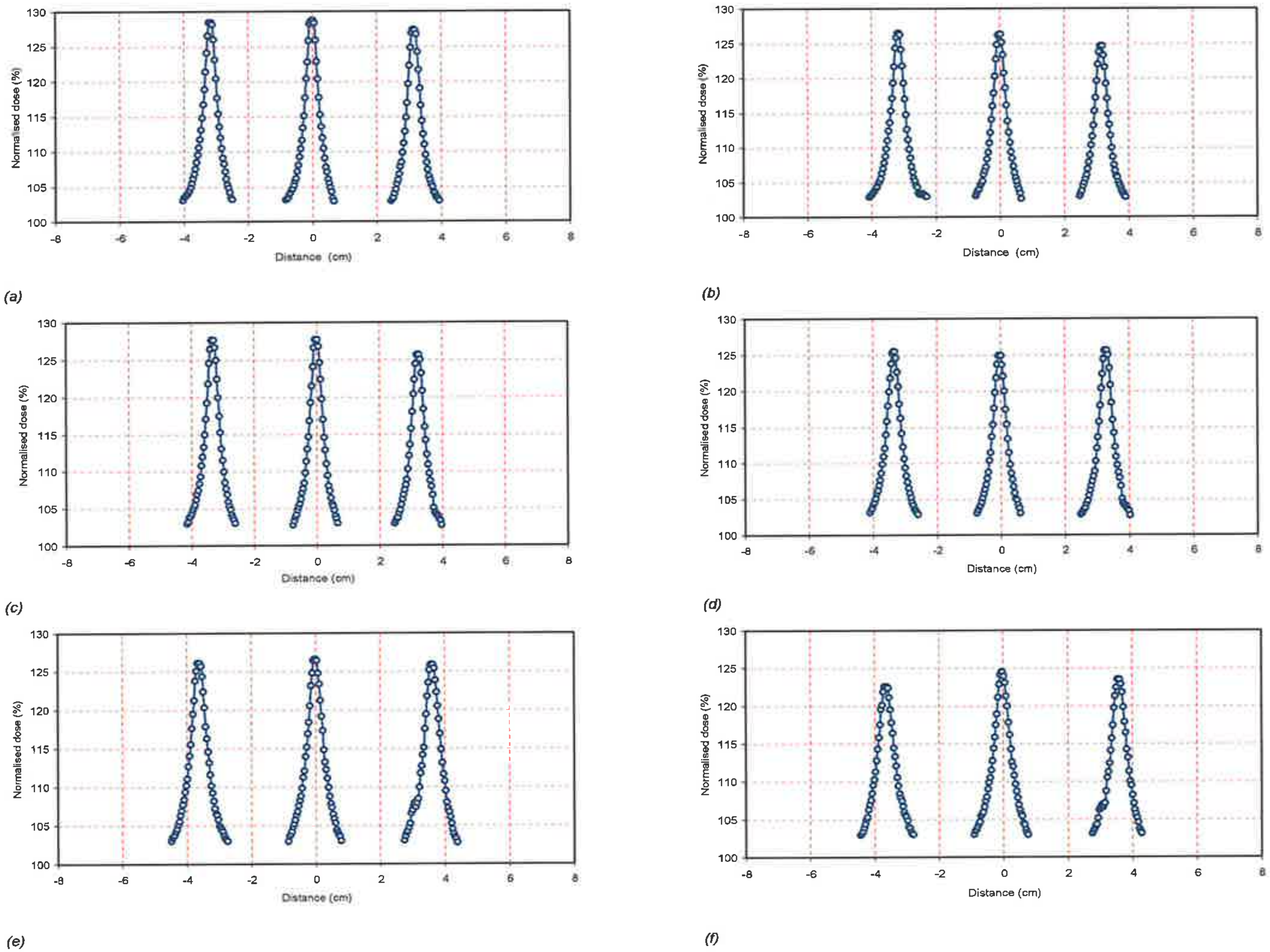

Figure D.3: (a) (c) (e) Normalised hotspots due to rounded leaf junction as a function of distance from central axis, with segments delivered statically, and profile through the junction of 4 leaves for 5 5x2 cm^2 segments at 5 cm, 10 cm and 20 cm respectively. (a) (d) (f) Normalised hotspots due to rounded leaf junction as a function of distance from central axis, with segments delivered statically, and profile through the junction of 2 leaves for 5 5x2 cm^2 segments at 5 cm, 10 cm and 20 cm respectively.

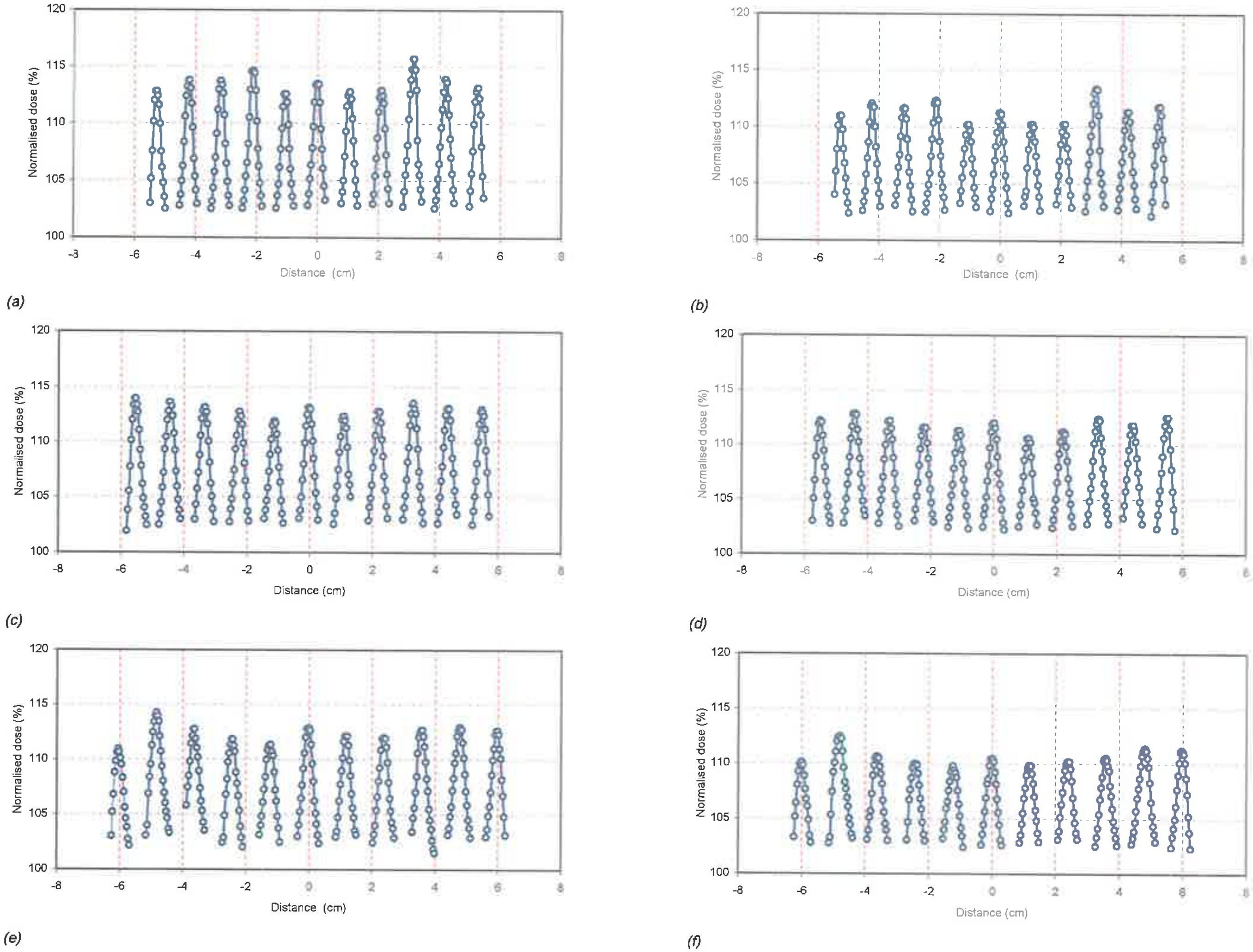

Figure D.4: (a) (c) (e) Normalised hotspots due to rounded leaf junction as a function of distance from central axis, with segments delivered dynamically, and profile through the junction of 4 leaves for 11 5x1 cm^2 segments at 5 cm, 10 cm and 20 cm respectively. (a) (d) (f) Normalised hotspots due to rounded leaf junction as a function of distance from central axis, with segments delivered dynamically, and profile through the junction of 2 leaves for 11 5x1 cm^2 segments at 5 cm, 10 cm and 20 cm respectively.

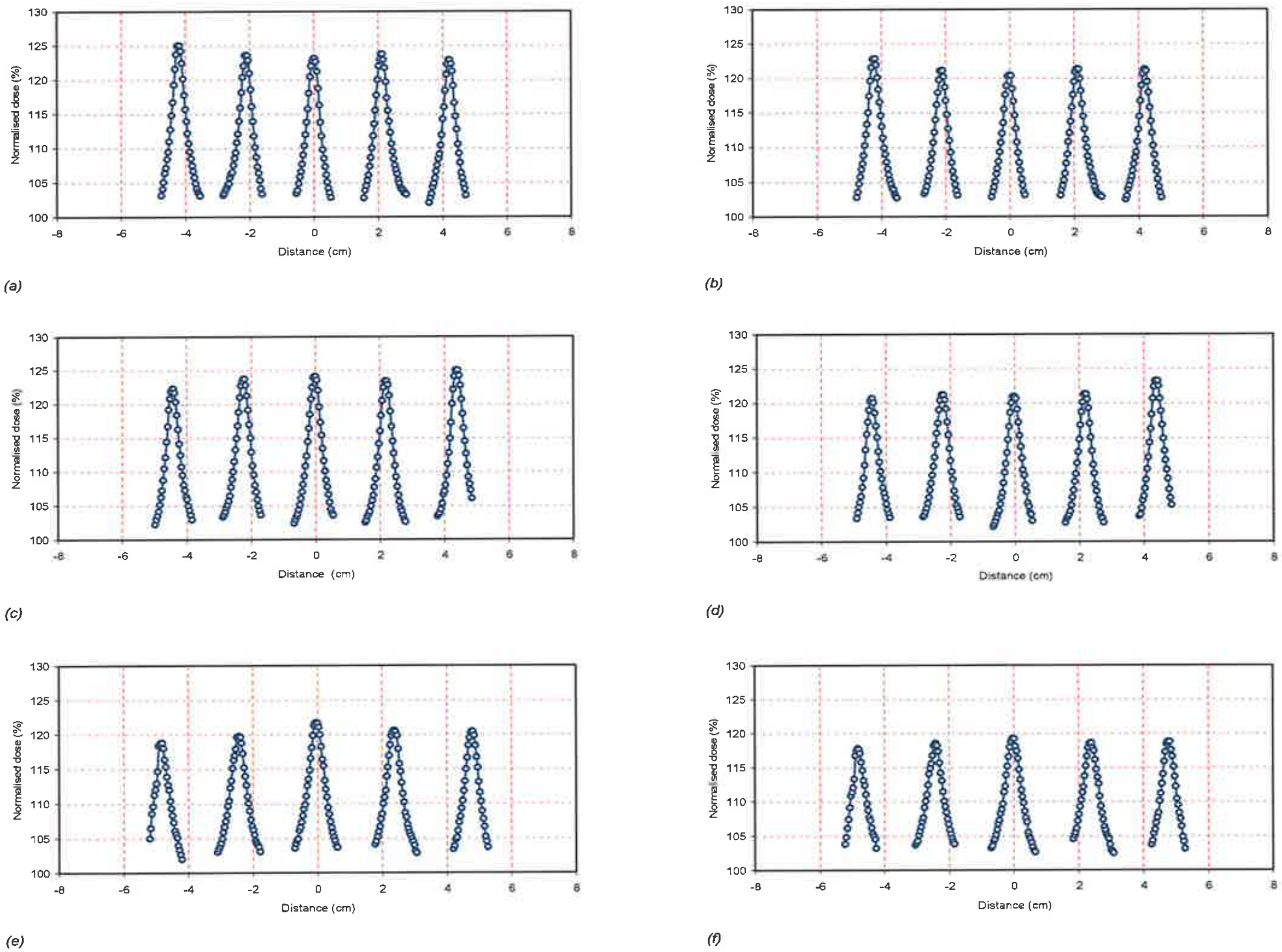

Figure D.5: (a) (c) (e) Normalised hotspots due to rounded leaf junction as a function of distance from central axis, with segments delivered dynamically, and profile through the junction of 4 leaves for 5 5x2 cm^2 segments at 5 cm, 10 cm and 20 cm respectively. (a) (d) (f) Normalised hotspots due to rounded leaf junction as a function of distance from central axis, with segments delivered dynamically, and profile through the junction of 2 leaves for 5 5x2 cm^2 segments at 5 cm, 10 cm and 20 cm respectively.

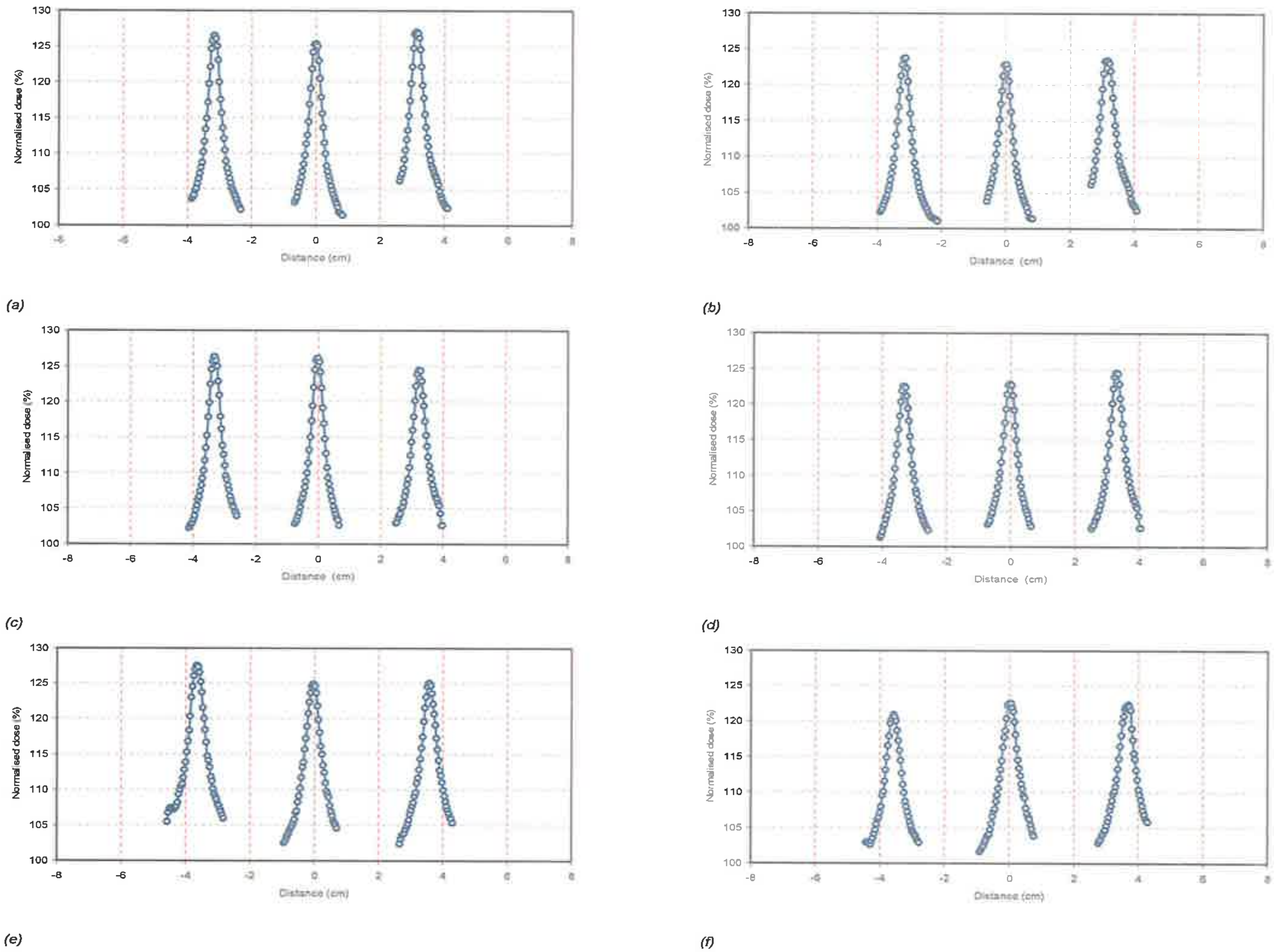

Figure D.6: (a) (c) (e) Normalised hotspots due to rounded leaf junction as a function of distance from central axis, with segments delivered dynamically, and profile through the junction of 4 leaves for 3 5x3 cm^2 segments at 5 cm, 10 cm and 20 cm respectively. (a) (d) (f) Normalised hotspots due to rounded leaf junction as a function of distance from central axis, with segments delivered dynamically, and profile through the junction of 2 leaves for 3 5x3 cm^2 segments at 5 cm, 10 cm and 20 cm respectively.

II. Tongue-and-groove effect

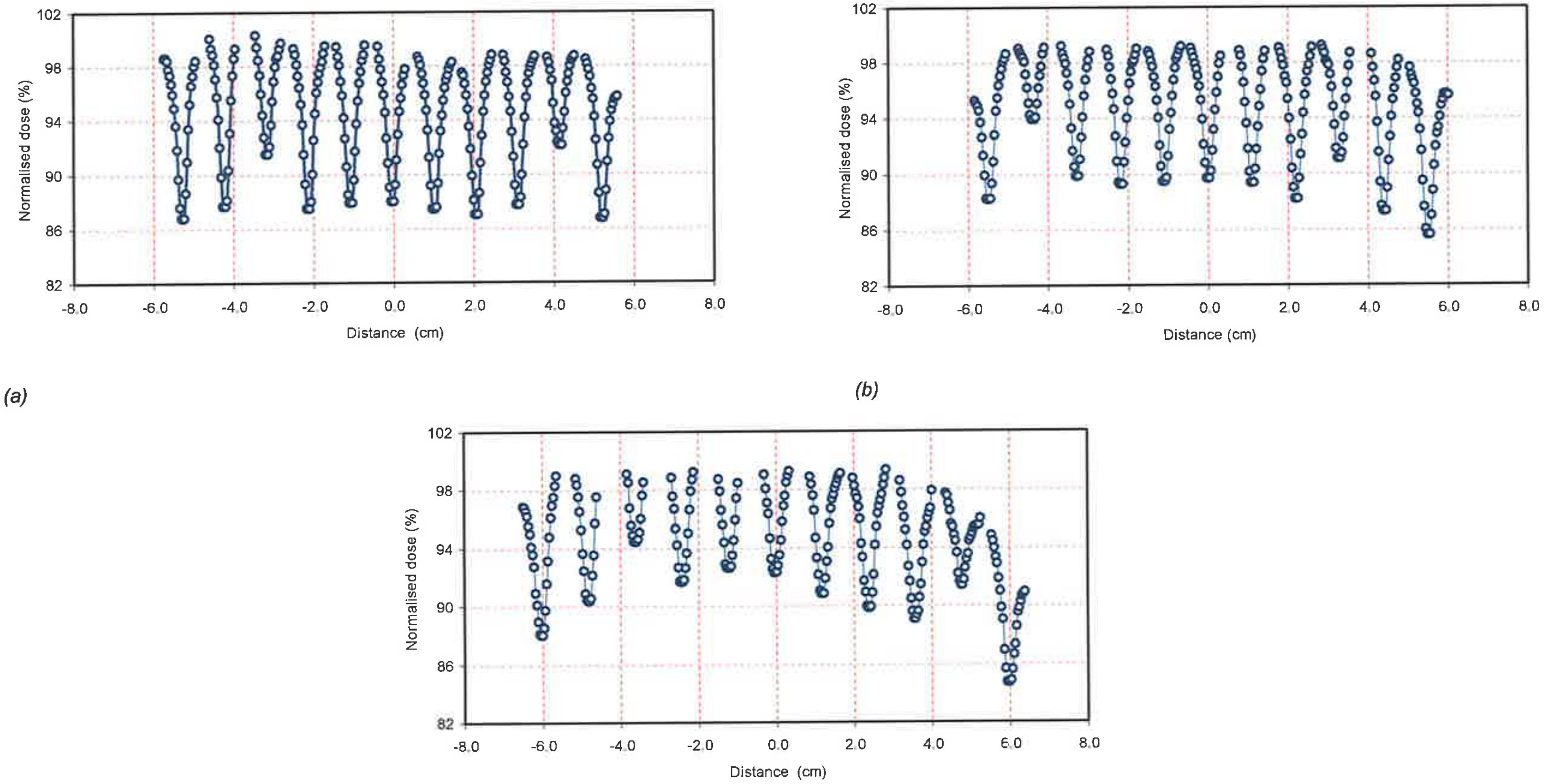

(a)

(b)

(c)

Figure D.7: 1x1 cm^2 segments (a) Normalised cold spots due to the tongue-and-groove effect as a function of distance from central axis, with segments delivered statically and at 5 cm deep. (b) Normalised cold spots due to the tongue-and-groove effect as a function of distance from central axis, with segments delivered statically ant at 10 cm deep. (c) Normalised cold spots due to the tongue-and-groove effect as a function of distance from central axis, with segments delivered statically and at 20 cm deep.

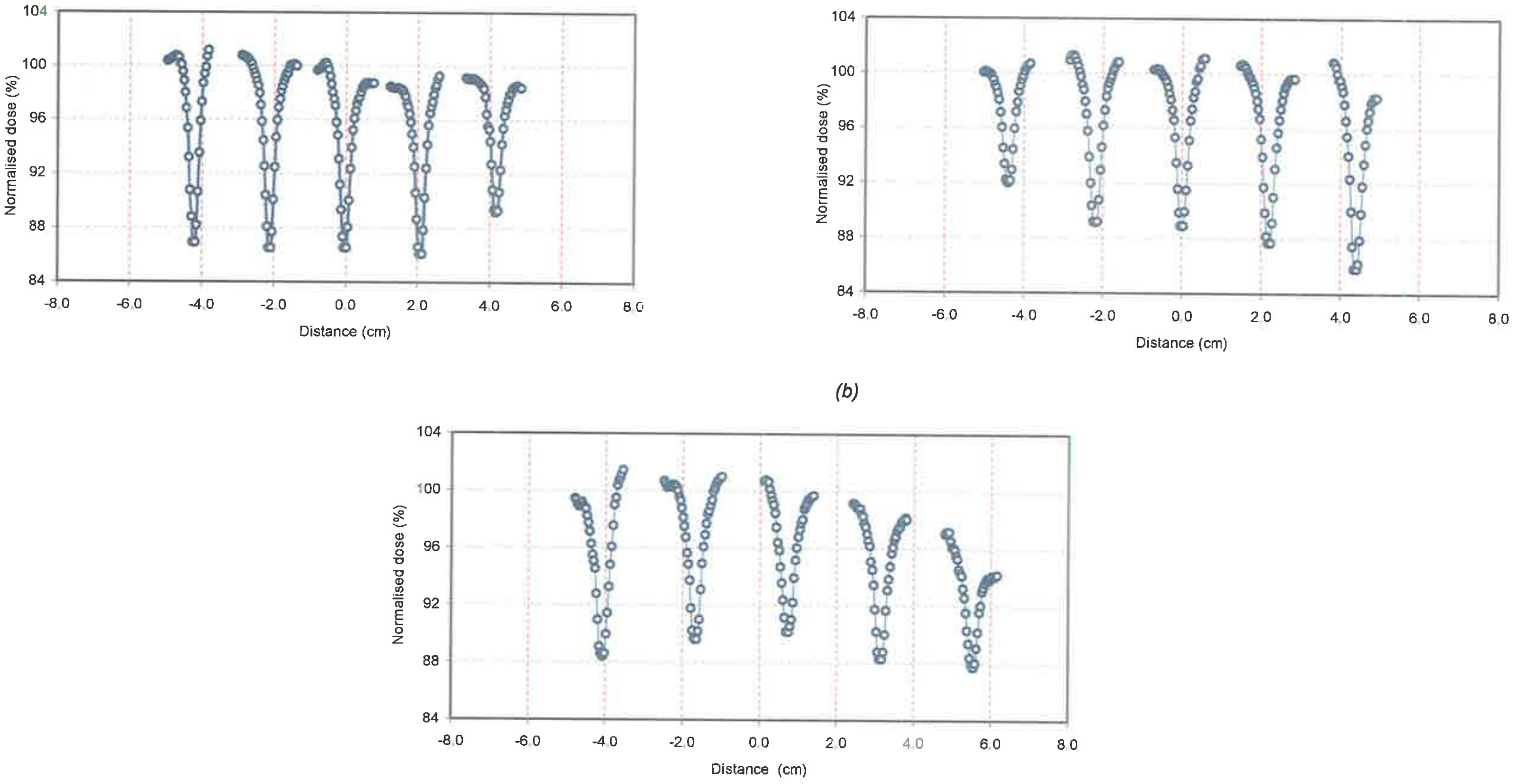

(a)

(b)

(c)

Figure D.8: 2x2 cm^2 segments (a) Normalised cold spots due to the tongue-and-groove effect as a function of distance from central axis, with segments delivered statically and at 5 cm deep. (b) Normalised cold spots due to the tongue-and-groove effect as a function of distance from central axis, with segments delivered statically ant at 10 cm deep. (c) Normalised cold spots due to the tongue-and-groove effect as a function of distance from central axis, with segments delivered statically and at 20 cm deep.

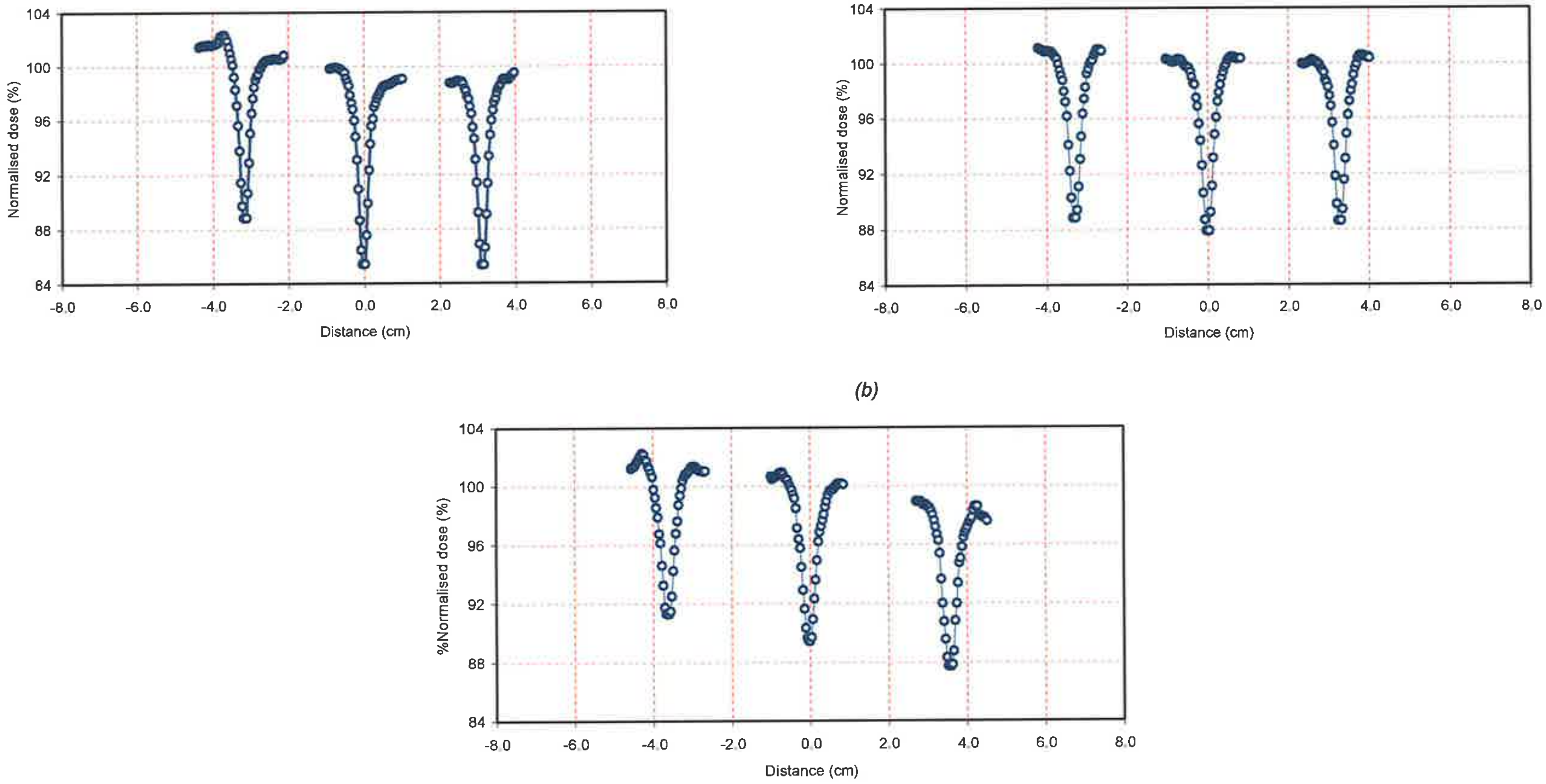

(a)

(b)

(c)

Figure D.9: 3x3 cm^2 segments (a) Normalised cold spots due to the tongue-and-groove effect as a function of distance from central axis, with segments delivered statically and at 5 cm deep. (b) Normalised cold spots due to the tongue-and-groove effect as a function of distance from central axis, with segments delivered statically ant at 10 cm deep. (c) Normalised cold spots due to the tongue-and-groove effect as a function of distance from central axis, with segments delivered statically and at 20 cm deep.

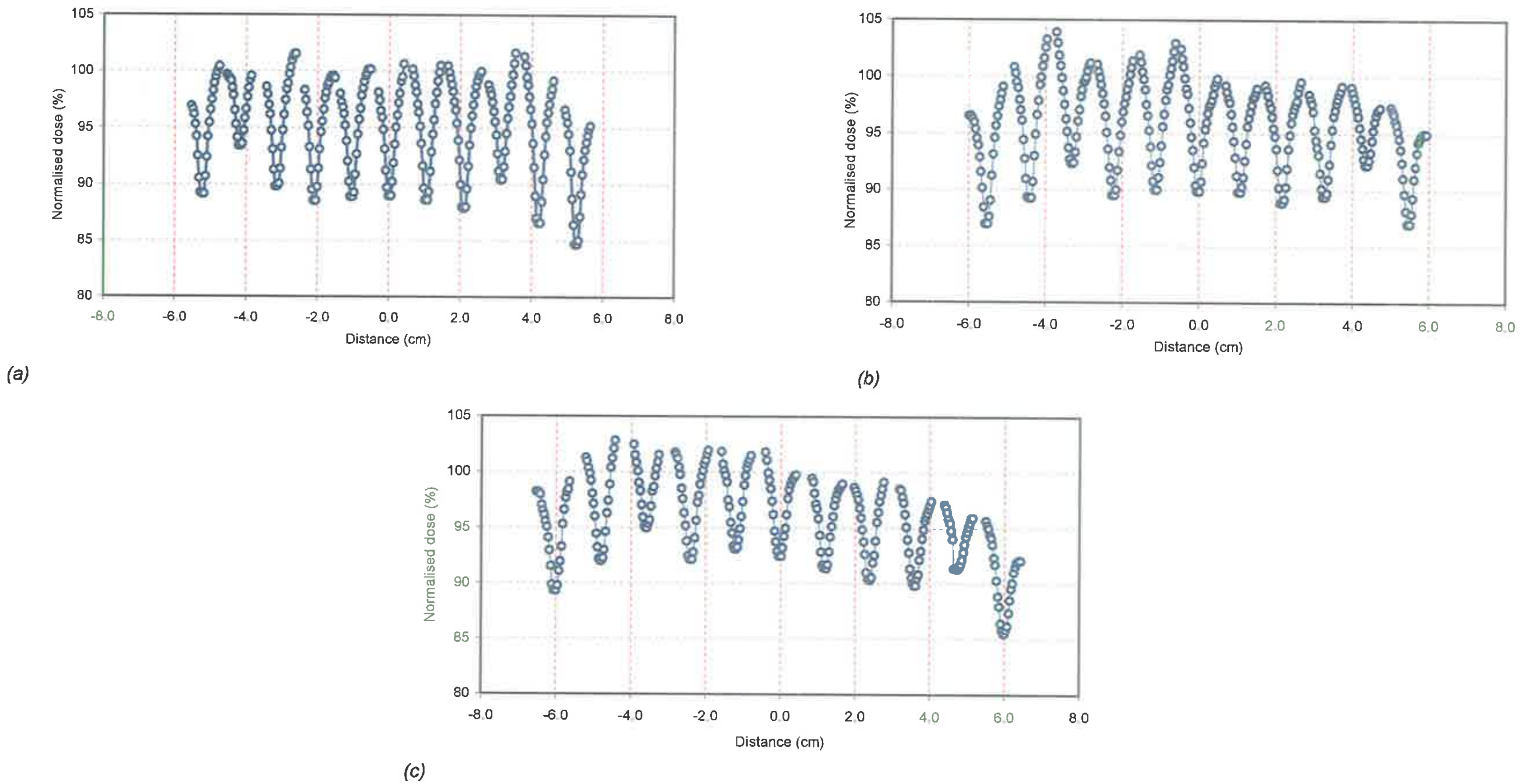

Figure D.10: 1x1 cm^2 segments (a) Normalised cold spots due to the tongue-and-groove effect as a function of distance from central axis, with segments delivered dynamically and at 5 cm deep. (b) Normalised cold spots due to the tongue-and-groove effect as a function of distance from central axis, with segments delivered dynamically ant at 10 cm deep. (c) Normalised cold spots due to the tongue-and-groove effect as a function of distance from central axis, with segments delivered dynamically and at 20 cm deep.

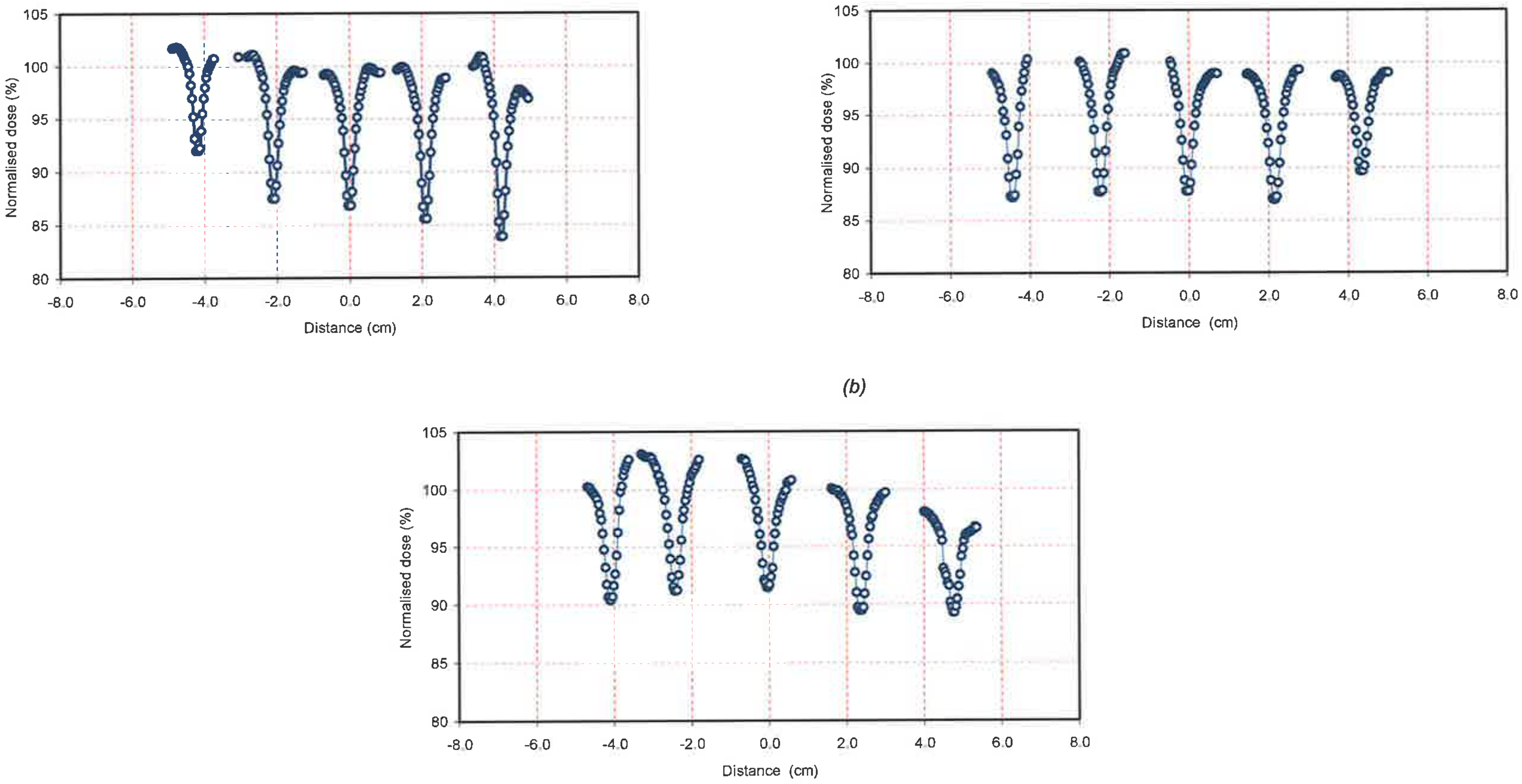

(a)

(b)

(c)

Figure D.11: 2x2 cm^2 segments (a) Normalised cold spots due to the tongue-and-groove effect as a function of distance from central axis, with segments delivered dynamically and at 5 cm deep. (b) Normalised cold spots due to the tongue-and-groove effect as a function of distance from central axis, with segments delivered dynamically ant at 10 cm deep. (c) Normalised cold spots due to the tongue-and-groove effect as a function of distance from central axis, with segments delivered dynamically and at 20 cm deep.

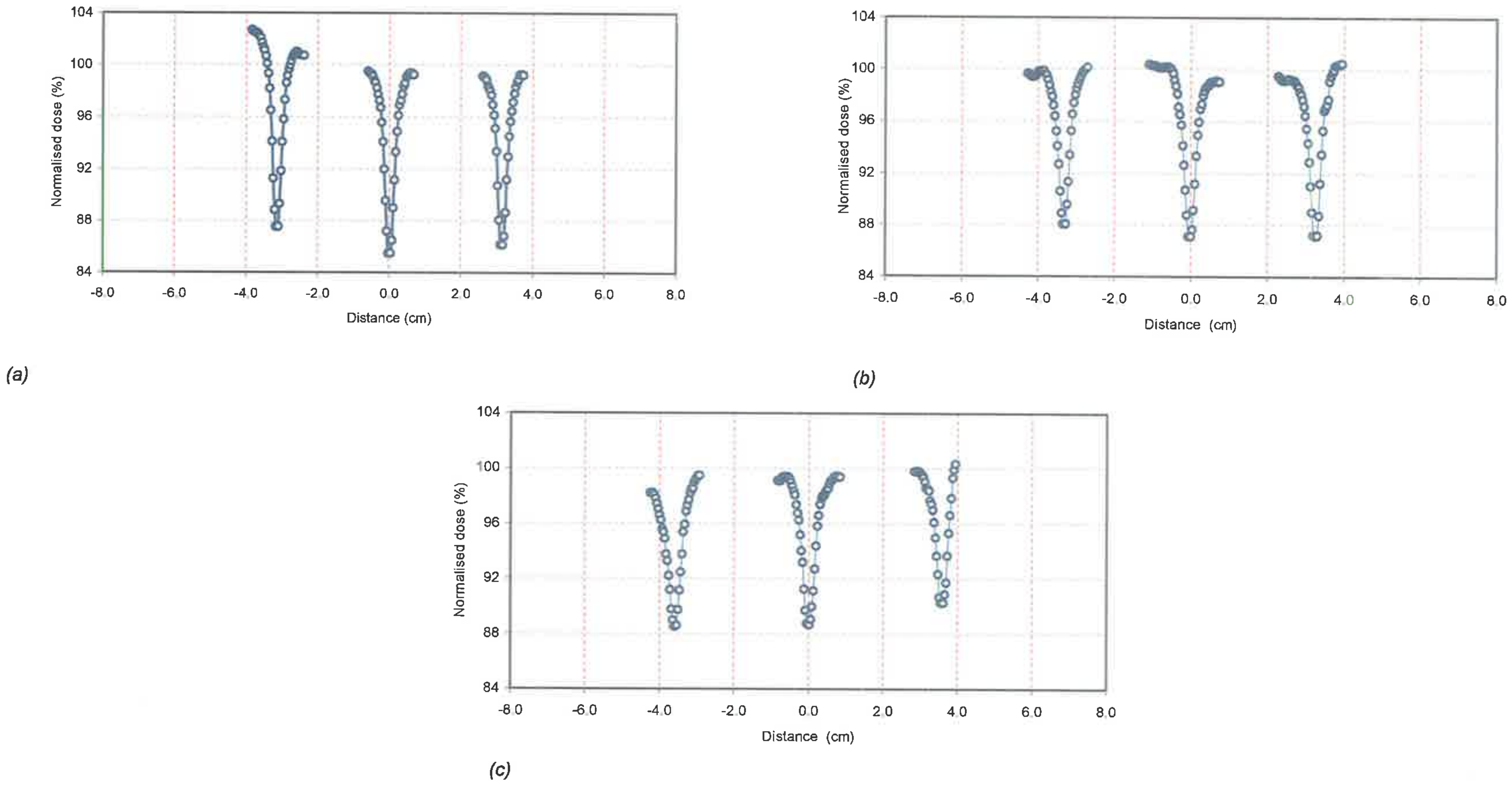

Figure D.12: 2x2 cm^2 segments (a) Normalised cold spots due to the tongue-and-groove effect as a function of distance from central axis, with segments delivered dynamically and at 5 cm deep. (b) Normalised cold spots due to the tongue-and-groove effect as a function of distance from central axis, with segments delivered dynamically ant at 10 cm deep. (c) Normalised cold spots due to the tongue-and-groove effect as a function of distance from central axis, with segments delivered dynamically and at 20 cm deep.

Appendix E

600CD characterisation measurements

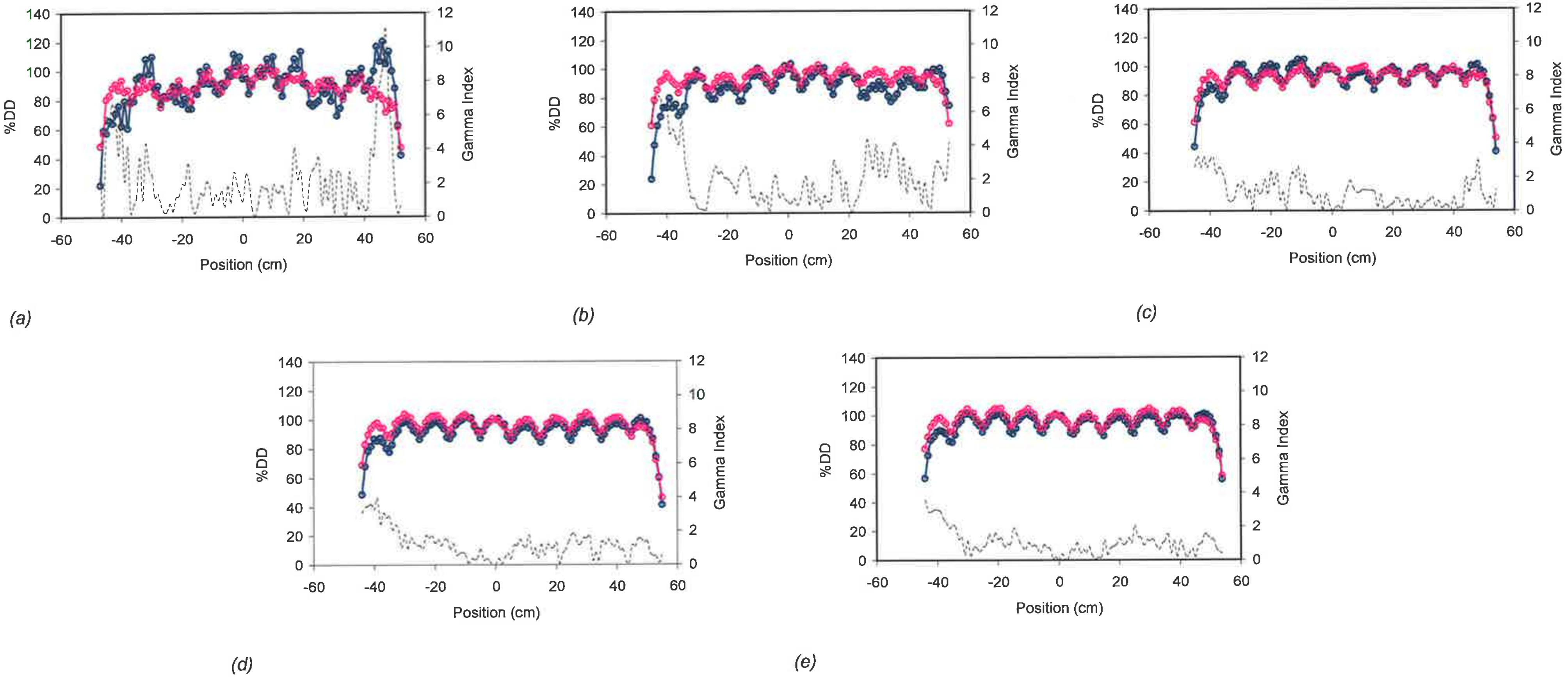

(a) (b) (c)

(d) (e)

Figure E.1: Profile of 10 4x1 cm^2 segments propagating in the in-plane direction and delivered via step-and-shoot with dose rate 100 MU/min overlayed with the profile of 10 4x1 cm^2 segments delivered statically at a dose rate of 300 MU/min. (a) 1 MU/segment (b) 2 MU/segment (c) 3 MU/segment (d) 4 MU/segment (e) 5 MU/segment.

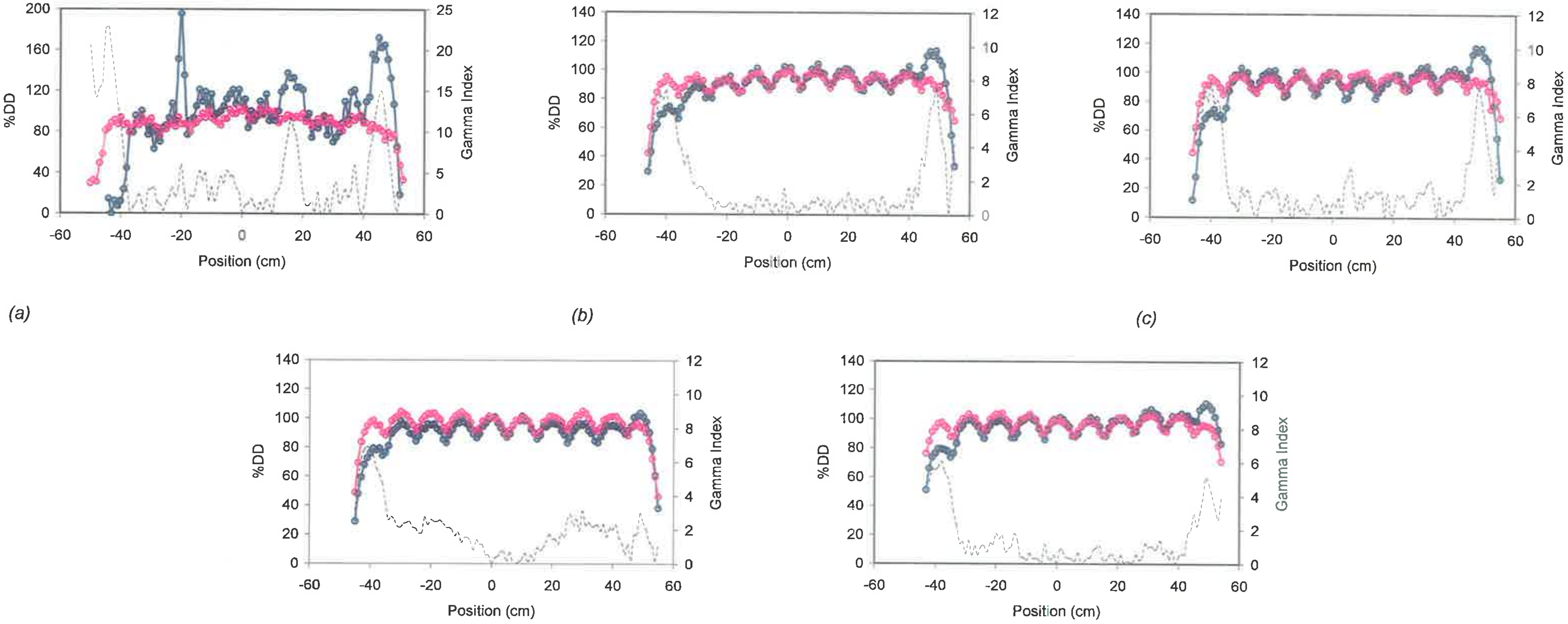

(a)

(b)

(c)

(d)

(e)

Figure E.2: Profile of 10 4x1 cm^2 segments propagating in the in-plane direction and delivered via step-and-shoot with dose rate 200 MU/min overlayed with the profile of 10 4x1 cm^2 segments delivered statically at a dose rate of 300 MU/min. (a) 1 MU/segment (b) 2 MU/segment (c) 3 MU/segment (d) 4 MU/segment (e) 5 MU/segment.

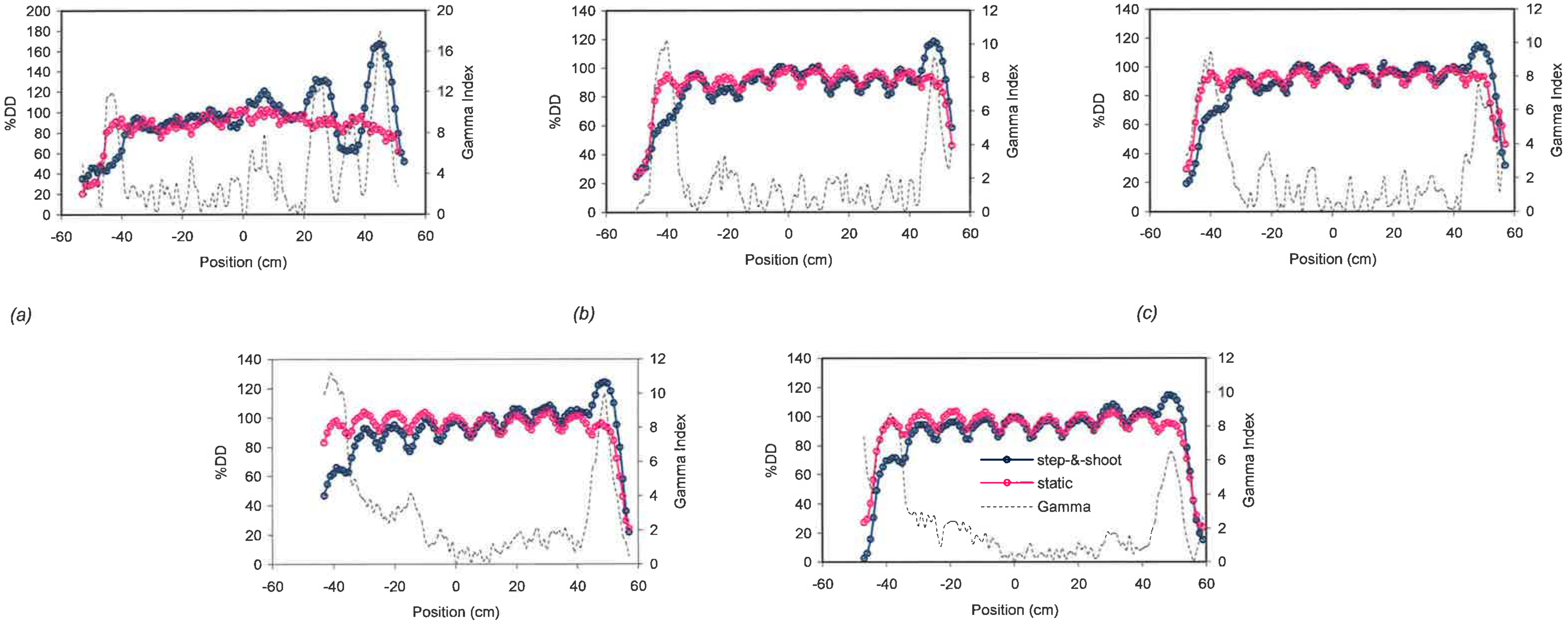

(a) (b) (c) (d) (e)

Figure E.3: Profile of 10 4x1 cm^2 segments propagating in the in-plane direction and delivered via step-and-shoot with dose rate 300 MU/min overlayed with the profile of 10 4x1 cm^2 segments delivered statically at a dose rate of 300 MU/min. (a) 1 MU/segment (b) 2 MU/segment (c) 3 MU/segment (d) 4 MU/segment (e) 5 MU/segment.

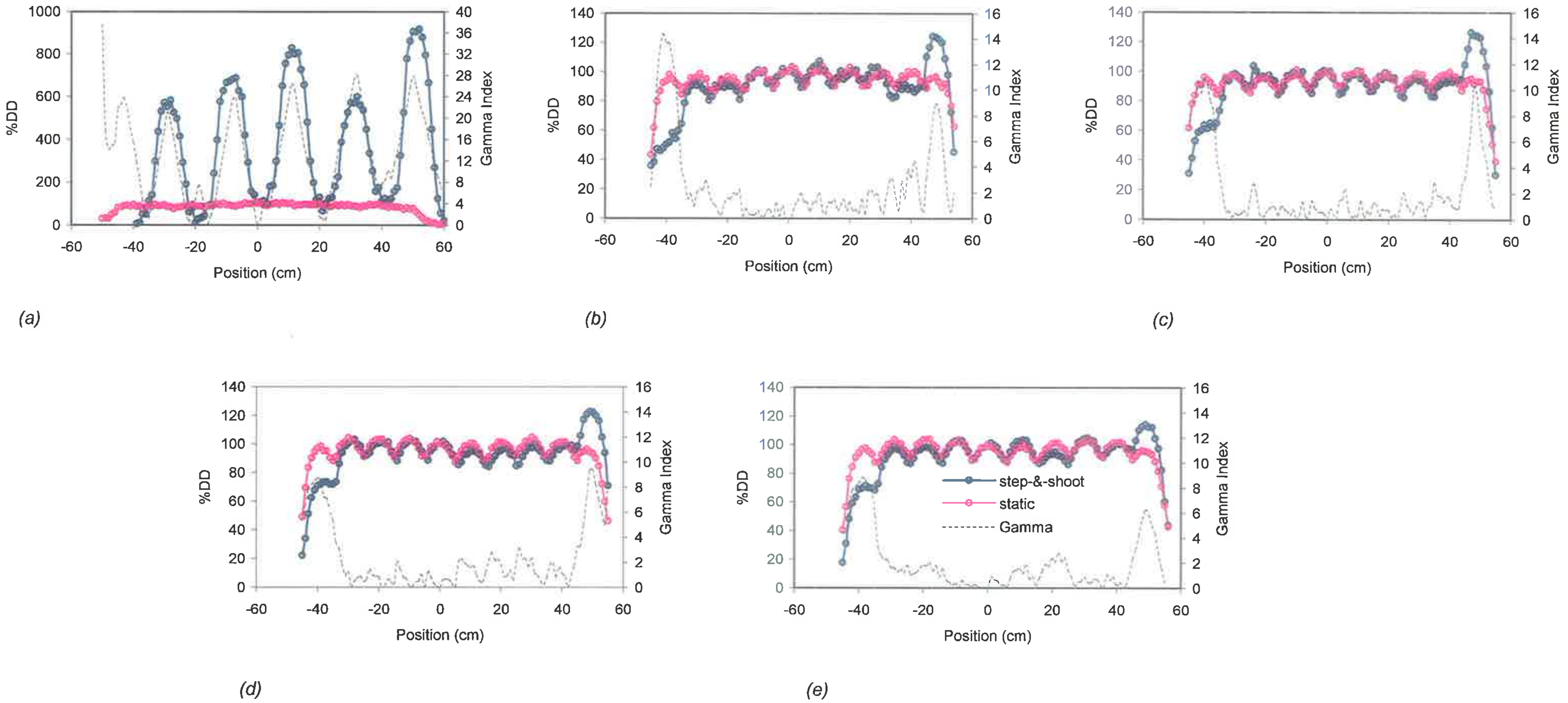

(a) (b) (c)

(d) (e)

Figure E.4: Profile of 10 4x1 cm^2 segments propagating in the in-plane direction and delivered via step-and-shoot with dose rate 400 MU/min overlayed with the profile of 10 4x1 cm^2 segments delivered statically at a dose rate of 300 MU/min. (a) 1 MU/segment (b) 2 MU/segment (c) 3 MU/segment (d) 4 MU/segment (e) 5 MU/segment.

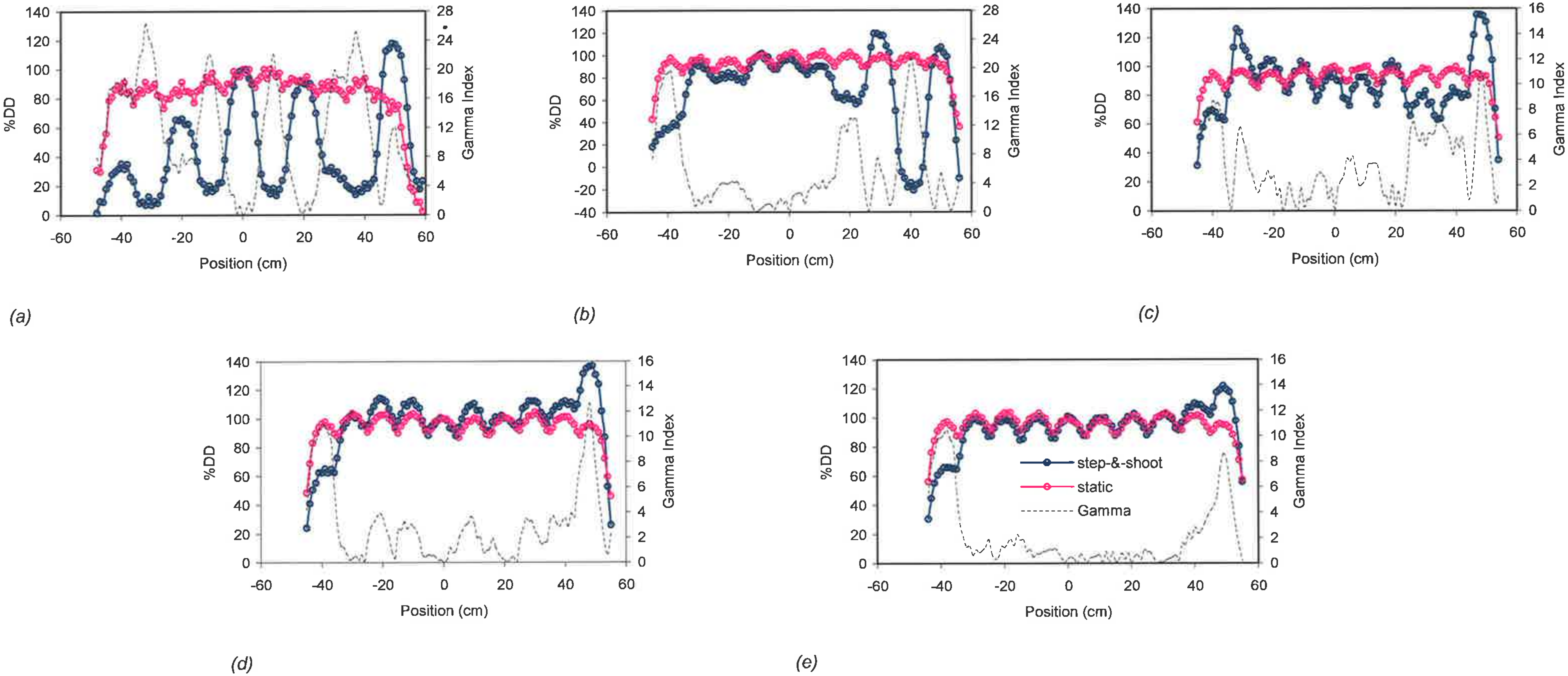

(a) (b) (c) (d) (e)

Figure E.5: Profile of 10 4x1 cm^2 segments propagating in the in-plane direction and delivered via step-and-shoot with dose rate 500 MU/min overlayed with the profile of 10 4x1 cm^2 segments delivered statically at a dose rate of 300 MU/min. (a) 1 MU/segment (b) 2 MU/segment (c) 3 MU/segment (d) 4 MU/segment (e) 5 MU/segment.

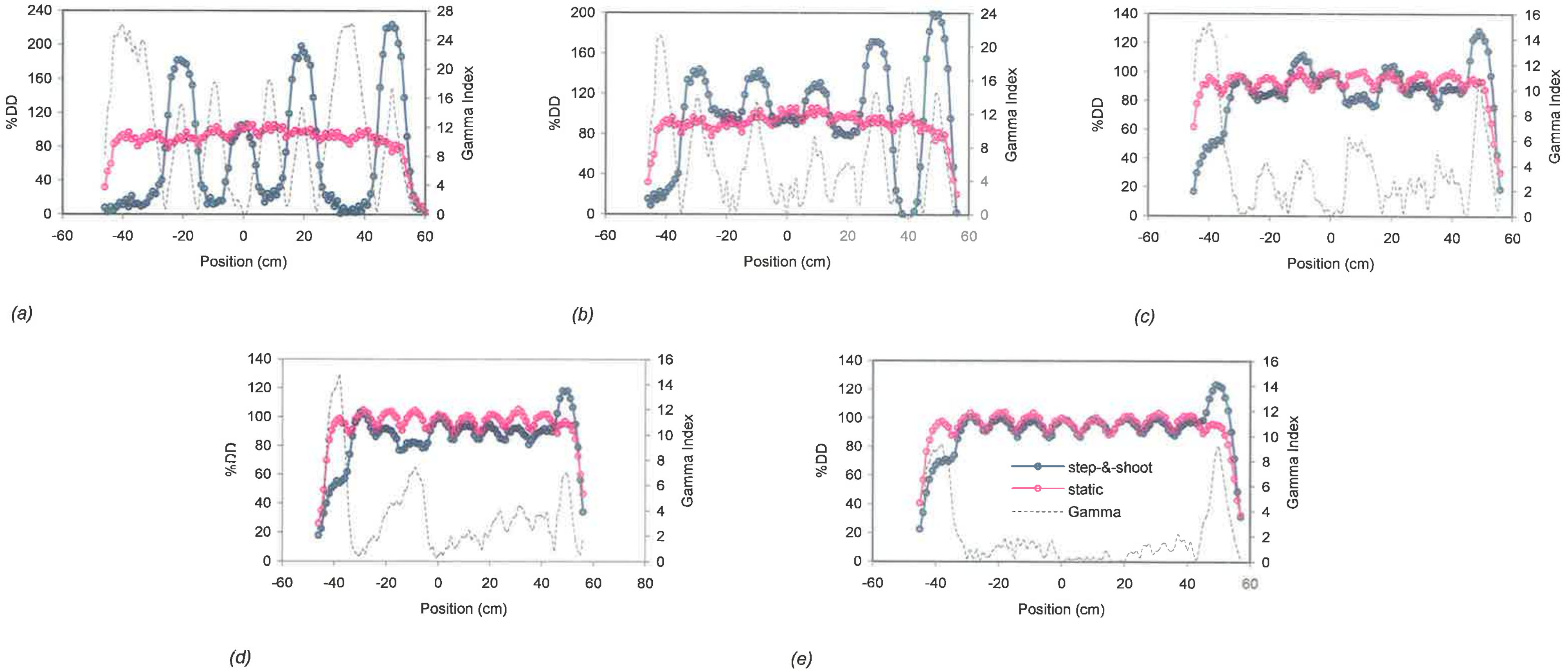

Figure E.6: Profile of 10 4x1 cm^2 segments propagating in the in-plane direction and delivered via step-and-shoot with dose rate 600 MU/min overlayed with the profile of 10 4x1 cm^2 segments delivered statically at a dose rate of 300 MU/min. (a) 1 MU/segment (b) 2 MU/segment (c) 3 MU/segment (d) 4 MU/segment (e) 5 MU/segment.